AN ABSTRACT OF THE DISSERTATION OF

Theresa Fritz-Endres for the degree of Doctor of Philosophy in Ocean, Earth, and Atmospheric Sciences presented on November 12, 2021.

Title: New Foraminifera-Based Proxies to Trace Changes to the Organic and Inorganic Carbon System Since the Last Glacial Maximum.

Abstract approved: _____
Jennifer Fehrenbacher

The production of carbon and export to deep ocean sediments is linked to carbon partitioning between the ocean and atmosphere and is a key driver of climate change over the glacial-interglacial transition. Yet conflicting reconstructions create barriers to understanding changes to the carbon system over this important climate transition. Production reconstructions conflict in part because commonly used production proxies may be subject to water column and seafloor diagenetic alterations that overprint primary oceanographic signals. In addition, reconstructions of deep ocean carbonate chemistry are complicated by the variable ways that dissolution/preservation affects the proxy. This dissertation explores the utility of new proxies recorded in the shells of planktic foraminifera that have the potential to reconstruct parameters of the carbon system and can be carefully assessed for signs of diagenesis. Proxy developments and reconstructions are made using foraminifera from equatorial Pacific Ocean sediments that span a gradient in surface ocean carbon production and deep ocean carbon preservation.

This research establishes new foraminiferal-based proxies that support existing surface ocean production and deep ocean carbonate chemistry reconstructions and add utility in regions where such reconstructions may be complicated by diagenetic

alterations. In chapter 2, I show that trace elements in foraminiferal calcite (i.e., Ba/Ca, Mn/Ca) that have traditionally been interpreted as diagenetic overprints are bound within the shells of non-spinose foraminifera and likely reflect a primary signal. I suggest these trace elements, when carefully derived with new cleaning methods, have utility in paleoceanographic reconstructions. In chapter 3, I explore using Ba/Ca bound within the shells of non-spinose foraminifera as a proxy for surface ocean organic matter production (production). The equatorial Pacific is used as an ideal environment to test the utility of the foraminifera Ba/Ca proxy because production follows a natural gradient across the basin. I compare the foraminifera-based LGM-Holocene reconstruction to other regional production reconstructions over this time period. The foraminifera Ba/Ca proxy supports the hypothesis that conditions in the equatorial Pacific responded to global atmospheric and oceanic reorganizations during the deglacial transition and hydrographic changes resulted in an increase in surface ocean organic carbon production. The foraminifera Ba/Ca proxy agrees with other reconstructions that also account for diagenetic processes. In chapter 4, I investigate the use of microCT scans of foraminifera shells as a proxy for calcite preservation/dissolution in the deep ocean. I establish calibrations that link foraminiferal shell density to deep ocean calcite saturation and use this information to explore changes in preservation in the deepest equatorial Pacific since the LGM. The foraminifera-based reconstruction supports the hypothesis that deep ocean carbonate conditions improved during the deglaciation linked to CO_2 leakage to the atmosphere. Because of poor preservation, few reconstructions have been conducted at this depth and our dataset adds valuable information about the bottom ocean calcite preservation state since the last glacial. Foraminifera-based proxies are a useful tool because they can be carefully assessed for signs of diagenesis, and the work of this dissertation supports the use of foraminiferal proxies alongside established proxies for more accurate interpretations of paleo-production and deep ocean carbonate chemistry changes.

New Foraminifera-Based Proxies to Trace Changes to the Organic and Inorganic Carbon System Since the Last Glacial Maximum

by

Theresa Fritz-Endres

A DISSERTATION

submitted to

Oregon State University

in partial fulfillment of
the requirements for the
degree of

Doctor of Philosophy

Presented November 12, 2021
Commencement June 2022

Doctor of Philosophy dissertation of Theresa Fritz-Endres presented on November 12, 2021

APPROVED:

Major Professor, representing Ocean, Earth, and Atmospheric Sciences

Dean of the College of Ocean, Earth, and Atmospheric Sciences

Dean of the Graduate School

I understand that my dissertation will become part of the permanent collection of Oregon State University libraries. My signature below authorizes release of my dissertation to any reader upon request.

Theresa Fritz-Endres, Author

ACKNOWLEDGEMENTS

The research presented in this dissertation was possible only with the support of my advisors, mentors, and peers. Foremost, I would like to thank my advisor, Jennifer Fehrenbacher, for her support every step of the way. Her love and enthusiasm for science and for being a mentor have kept me motivated through a series of challenges that have included not one but multiple disasters. The excellence of her mentorship is in the big things: providing me with the opportunities to pursue new questions, sharing her expertise to point me in the right direction, and going to bat for me when faced with challenges. But perhaps most importantly it is in the day-to-day interactions that continue to make me a better scientist. Her door has always been open to me and there is always excellent advice on the other side of that door, and for this, I am truly grateful.

To my many mentors in CEOAS, I am so grateful for your investment in my education and my development as an independent researcher. Laurie Juranek, Joe Stoner, and Ann Russell have contributed to my growth and to this dissertation since the very beginning. Chris Russo, the godfather of the ICP, has taught me bundles in the Keck Lab, and Chris and Brian Haley have been incredibly generous with their time as we troubleshot new methods. Andy Ross, June Padman, and Jennifer McKay in the Stable Isotope Lab have shared their guidance, a love of forams, and a love of baked goods. Teresa Sawyer helped me acquire beautiful images in the Electron Microscopy Facility. Dorthe Wildenschild, Doug Meisenheimer, Maoz Dor helped with all things microCT. Members of the Foraminarium (Julia Fontana, Brenna McBride, Jim Kelly, Faith Shell, Grace Meyer, and Brittany Hupp) have been a community and a lab home for me, especially Kelsey Lane Loftus, who has been a partner in crime through the Ph.D. journey. And finally, my CEOAS cohort has been a support group and an inspiration.

Outside of OSU, I thank Howie Spero for his guidance on the IRMS and for his thoughts on the data, and I thank Cate Davis, Oscar Branson, and Spider Vetter for thoughts that improved chapters of this dissertation. I am grateful for the 2019 Green Island Crew, and the many ship crews and science parties (R/Vs Oceanus, Sikuliaq, Shimada, Meteor) from which I learned how to conduct research in the field and have acquired precious samples.

Finally, I thank my husband, Alex, and my family, for believing that I could do this, even when I didn’t believe it myself. I love you.

CONTRIBUTION OF AUTHORS

Chapter 2:

The study was conceived of and designed by T. Fritz-Endres and J. Fehrenbacher. T. Fritz-Endres performed the laboratory and data analysis, with the guidance of J. Fehrenbacher. T. Fritz-Endres wrote the first draft of the manuscript. J. Fehrenbacher provided significant edits and contributions to manuscript drafts and to the final version of the manuscript. Chapter 2, in full, is a reprint of the publication in *Geochemistry, Geophysics, Geosystems*, 2020, Fritz-Endres, T., and Fehrenbacher, J.

Chapter 3:

The study was conceived of and designed by T. Fritz-Endres and J. Fehrenbacher. T. Fritz-Endres performed the laboratory and data analysis, with the guidance of J. Fehrenbacher, and with assistance from Julia Fontana, Brenna McBride, and Grace Meyer. T. Fritz-Endres wrote the first draft of the manuscript. J. Fehrenbacher and A. Russell provided significant edits and contributions to manuscript drafts and to the final version of the manuscript. H. Cynar provided edits to the final version of the manuscript. Chapter 3, in full, is submitted for review to *Paleoceanography and Paleoclimatology*, 2021, Fritz-Endres, T., Fehrenbacher, J. S., Russell, A. D., Cynar, H.

Chapter 4:

The study was conceived of and designed by T. Fritz-Endres and J. Fehrenbacher. T. Fritz-Endres performed the laboratory and data analysis, with assistance from Jim Kelly and Faith Schell. T. Fritz-Endres wrote the first draft of the manuscript. J. Fehrenbacher provided significant edits and contributions to manuscript drafts and to the final version of the manuscript.

TABLE OF CONTENTS

TABLE OF CONTENTS (continued)

LIST OF FIGURES

LIST OF FIGURES (continued)

Page

LIST OF TABLES

DEDICATION

This dissertation is dedicated to my son, Riley, for whom I wish scientific curiosity and a belief that he may achieve his goals.

CHAPTER 1: INTRODUCTION

1.1. Background

It is well established that the partitioning of carbon between the ocean and atmosphere is an important driver of global climate changes over glacial-interglacial transitions (review in Archer et al., 2000 and Sigman and Boyle, 2000). The ocean is the largest carbon reservoir, holding about 60 times the amount of carbon held in the atmosphere (Broecker, 1982). The result is that even small changes in ocean carbon chemistry over thousand-year time scales (in which the ocean carbon reservoir equilibrates with the atmosphere) can produce large changes in atmospheric CO_2 (foundation in Berger et al., 1989). Atmospheric CO_2 fluctuations have been correlated with climate on thousand-year time scales and because CO_2 is a greenhouse gas, atmospheric CO_2 fluctuations likely caused or amplified climate changes (Lisiecki and Raymo, 2005; Jouzel et al., 2007; Lüthi et al., 2008). Thus, resolving the reasons for glacial-interglacial atmospheric CO_2 fluctuations is essential for understanding the mechanisms that control the global climate system.

One important mechanism by which the ocean can change its ability to hold atmospheric carbon is a change in marine primary production in the surface ocean (Broecker, 1982; Broecker and Peng, 1986; Geider et al., 2001). The fixation and export of organic carbon from the photic zone acts as a "biological pump" that lowers the partial pressure of seawater CO_2 (pCO_2) and facilitates an exchange between the two reservoirs. Fluctuations in production and the export of particulate organic carbon (POC) to the deep ocean result in corresponding fluctuations in atmospheric CO_2 over thousand-year timescales (Berger et al., 1989; Kohfield et al., 2005; Lopes et al., 2015).

Another critical mechanism is the rain of particulate inorganic carbon (PIC) precipitated to form the hard parts of marine micro-plankton in the surface ocean that acts as a "carbonate counter pump", generally increasing seawater pCO_2. Over thousand-year time periods, an increase in $CaCO_3$ burial lowers global ocean alkalinity via the removal of carbonate ions (CO_3^{2-}). Everything else being equal, the removal of CO_3^{2-} shifts the

dissolved inorganic carbon (DIC) pool toward aqueous CO_2, decreasing CO_2 solubility in seawater, and increasing atmospheric CO_2 (Zeebe and Wolf-Gladrow, 2001). A decrease in the $[CO_3^{2-}]$ of the deep ocean eventually causes a shoaling of the calcite saturation horizon and increase in calcite dissolution, which acts as a negative feedback to changes in ocean carbon chemistry and restores alkalinity and pCO_2 to a new steady-state (i.e., carbonate compensation, Broecker and Peng, 1987; Boudreau et al., 2018). Because of these effects, variations in the lysocline (the depths over which calcite dissolution in sediments intensifies) are linked to glacial-interglacial changes in atmospheric CO_2, which was ~80 ppm lower during the Last Glacial Maxima (LGM) than the deglaciation that followed (Jouzel et al., 2007; Lüthi et al., 2008).

The equatorial Pacific is a region that has high organic and inorganic carbon production and is therefore an important region for global carbon partitioning. Primary production in this region is fueled by nutrients delivered to the surface ocean by strong equatorial upwelling. High primary production and particle export from the surface ocean drive high burial efficiency in the equatorial Pacific. It is estimated that the equatorial Pacific has the highest area integrated POC export of any oceanographic region and equates to nearly one fifth of global POC export (Dunne et al., 2007). In terms of inorganic carbon, in the equatorial Pacific the depth of the lysocline reflects the balance between extensive calcite production in the surface ocean and widespread calcite dissolution in deep waters. The equatorial Pacific exports ~10-20 g $CaCO_3/m^2/yr$, nearly twice that of higher latitude regions (Milliman, 1993); yet the lysocline of the equatorial Pacific is shallow (~3.5 km, Key et al., 2004) relative to the rest of the global ocean. Therefore, even small fluctuations in lysocline depth from the LGM to Holocene produce large changes in calcite preservation and corresponding shifts in global alkalinity and atmospheric CO_2 (Barnola et al., 1987; Sigman et al., 1998).

Over the past several decades there has been significant effort by the oceanographic community to understand the relationship between production, ocean chemistry, and atmospheric CO_2 (Arrhenius, 1952; Broecker, 1982; Gottschalk et al., 2019). The outcome from studies focused on the equatorial Pacific have alternately stated that production was greater during glacial periods (e.g., Herguera and Berger, 1991;

Perks et al., 2002) or that production was greater during interglacial periods (e.g., Loubere, 2000; Bradmiller et al., 2006; Richaud et al., 2007; Dubois et al., 2011; Costa et al., 2017). A necessary task required to explain atmospheric CO_2 changes over glacial transitions is to reconstruct components of the biological pump by providing information about the relevant organic carbon pools: POC of the surface ocean, POC export, and POC accumulation at depth. Together reconstructions of these pools quantify organic carbon burial efficiency. Equally important in describing atmospheric CO_2 changes of glacial-interglacial transitions is reconstructing the depth of the lysocline (which is coupled to the calcite saturation horizon; Broecker and Takahashi, 1978). $[CO_3^{2-}]$ of the deep ocean determines the calcite saturation state and changes in $[CO_3^{2-}]$ results in a shoaling/deepening of the lysocline and dissolution/preservation of calcite on the seafloor, which alters global ocean alkalinity. Therefore, reconstruction of $[CO_3^{2-}]$ can inform critical processes in past changes to the global carbon cycle (Yu et al., 2010).

Glacial-interglacial climate history has been reconstructed with an array of proxies derived from marine sediment archives. Information about paleo-production is largely derived from flux proxies that record a fraction of the organic matter delivered to the seafloor (e.g., organic carbon fluxes), or nutrient proxies that record information about the nutrient content of the surface ocean that feeds primary production (e.g., $\delta^{13}C$ and $\delta^{15}N$) (Berger et al., 1994). Each proxy records different aspects of production and can provide useful information about parts of the biological pump. In addition, each contains its own assumptions, making proxy comparisons difficult, and nearly all production proxies can be subject to alteration in the water column and on the seafloor that hinder the use of production proxies by dampening or overprinting the surface ocean signal. However, if production proxies can be carefully assessed for signs of diagenesis, the proxy may be useful in reconstructing surface ocean processes.

Alternatively, the effect of deep ocean processes on the proxy may be used to reconstruct conditions of the deep ocean. For example, information about changes in the lysocline depth have been estimated from deep ocean $[CO_3^{2-}]$ reconstructions that assess calcite preservation/dissolution in sediments (e.g., Crowley, 1983; Farrell and Prell, 1989; Le and Shackleton, 1992; Anderson and Archer, 2002). In addition, the fossilized

shells of foraminifera, which are marine protists that build calcite shells, reflect the preservation state of the deep water in which they lay and have been used to facilitate reconstruction of deep ocean [CO_3^{2-}] (e.g., Arrhenius, 1952; Broecker and Clark, 2001; Qin et al., 2017).

Foraminiferal calcite hosts geochemical proxies that offer valuable insights to the reconstruction of oceanographic conditions. Planktic foraminifera form their shells primarily from Ca^{2+} and CO_3^{2-} ions, and also incorporate some trace elements of the seawater of the surface ocean in which they grow, retaining these trace elements as shells are deposited on the seafloor. The geochemistry of planktic foraminifera shells is a critical tool that has been used for decades as one of the most common proxies for reconstructing paleotemperature (using Mg/Ca; Lea et al., 1999; Elderfield and Ganssen, 2000; Anand et al., 2003) and the $\delta^{18}O$ of seawater (using calcite $\delta^{18}O$; Emiliani, 1955; Shackleton, 1967) in ancient water masses. More recently, trace elements in planktic foraminifera have been used for an array of new proxies, including to reconstruct redox conditions (using Mn/Ca; Klinkhammer et al., 2009; Glock et al., 2012; Groeneveld et al., 2018; Skinner et al., 2018; Petersen et al., 2019), freshwater flux and salinity (using Ba/Ca; Hall and Chan, 2004; Weldeab et al., 2007, 2014; Bahr et al., 2013; Hoffman et al., 2014; Evans et al., 2015; Setiawan et al., 2017), and nutrients (using Mn/Ca; Zn/Ca; Ba/Ca; Marr et al., 2013). The geochemistry of benthic foraminifera has been used to reconstruct carbonate chemistry of the deep ocean, including deep ocean pH and [CO_3^{2-}] (using $\delta^{11}B$, Zn/Ca, or B/Ca; Sanyal et la., 1995; Marchitto et al., 2000; Yu et al., 2008, 2010; Rickaby et al., 2010; Raitzsch et al., 2011).

The research efforts described in this dissertation were motivated by the lack of consensus among existing proxies on relative changes in the organic (Costa et al., 2017) and inorganic carbon (Yu et al., 2017) systems over the glacial-interglacial transition. I investigate new proxies measured in planktic foraminifera that shed light on changes in paleo-production in the past and preservation on the seafloor. Foraminiferal proxies may offer an advantage to existing proxies because they can be carefully assessed to separate out surface vs. diagenetic signals. I investigate the effect of diagenetic alterations and cleaning on the trace element geochemistry of non-spinose foraminifera proxies for the

purpose of preserving a surface ocean signal in the proxy. I then investigate the utility of trace element proxies of non-spinose foraminifera for reconstructions of surface ocean production. Finally, I explore the use of microCT methods to reconstruct foraminifera shell density and reflect calcite preservation conditions of the deep ocean. I focus on reconstructions in the equatorial Pacific where high primary production results in high POC and PIC export, yet corrosive conditions in deep waters result in poor burial conditions, and changes in burial conditions through glacial-interglacial time.

1.2. Chapters overview

In chapter 2, I investigate the effect of cleaning procedures on the trace element composition of non-spinose foraminifera. Non-spinose foraminifera are underutilized in paleoceanographic studies, and the trace element composition of their shell calcite is often markedly different compared to the spinose species (i.e., Ba/Ca, Mn/Ca, and Zn/Ca ratios; Eggins et al., 2003; Hathorne et al., 2009; Kunioka et al., 2006; Jonkers et al. 2016; Sadekov et al., 2005; Fehrenbacher and Martin, 2010). Higher than expected trace element values have traditionally been interpreted as shell surface contaminations that mask the surface ocean signal and a series of cleaning steps – including a reductive step to remove metal contaminants and the use of the chelating agent DTPA to remove contaminants such as barite crystals – are often used to remove high trace elements (Boyle, 1981, 1983; Boyle and Keigwin, 1985). However, aggressive cleaning steps are also corrosive to calcite, dissolve portions of the shells, and lower trace element values (Lea and Boyle, 1991; Martin and Lea, 2002; Yu et al., 2007; Vetter et al., 2013). I show that the trace elements Ba, Mn, and Zn are lattice bound and are incorporated during the foraminifera's early ontogeny and likely represent a surface ocean signal. The corrosive cleaning steps lower trace element concentrations by preferentially removing early ontogenetic portions of the shell that contain high trace element values. This may alter the foraminifera's geochemical signal, particularly in locations and during time periods when trace elements are high in early ontogenetic calcite. I advise using modified cleaning procedures for non-spinose deeper dwelling foraminifera that prevent the

removal of the ontogenetic portions of the shell for future trace element/Ca investigations.

Chapter 3 builds on the methods and lessons learned from the previous work to establish the utility of Ba/Ca in non-spinose foraminifera. While Ba/Ca in spinose foraminifera species can reflect freshwater flux and changes in salinity, the Ba/Ca in non-spinose foraminifera likely reflects the Ba-enriched conditions within their particulate microhabitats (POM; Fehrenbacher et al., 2018) and are a promising new proxy for paleo-production reconstructions. We test this hypothesis in non-spinose species obtained from cores along a production gradient in the equatorial Pacific. We find that non-spinose species have much higher Ba/Ca ratios than values measured in spinose species from the same sediment material, confirming that high trace element values are not due to contamination. We reconstruct changes in the Ba/Ca proxy from the LGM to the Holocene and interpret our results alongside published paleo-production and climatological proxies from the same region. Our data agree with several paleo-production proxies that reflect a peak in production during the deglaciation. Our data supports the interpretation that a deglacial increase in production was a response to the entrainment of southern-sourced nutrients upwelled to locations of the equatorial Pacific by the equatorial undercurrent. In addition, our careful analysis of the Ba/Ca proxy in regions with post-depositional sediment re-distribution and regions with dissolution indicate the Ba/Ca proxy may be a useful tool in locations where other production proxies are poorly preserved.

In chapter 4, I assess the impact of deepwater [CO_3^{2-}] on individual foraminifera shell density using microCT imaging techniques. These techniques can resolve micro-scale changes to the shell interior (Iwasaki et al., 2015, 2019) and reflect shell density changes as a response to variable [CO_3^{2-}] (Johnstone et al., 2010). These techniques are applied for the first time to fossil foraminifera to reconstruct conditions of the glacial deep ocean. I generate calibrations relating foraminifera shells density to [CO_3^{2-}] of the deep ocean using a suit of equatorial Pacific core-tops that span saturated to under-saturated conditions with respect to calcite. I apply the calibrations to explore changes in preservation since the LGM using specimens obtained from a core located in very

corrosive deep waters of the central Pacific. I find that interior calcite of foraminifera specimens is better preserved during deglacial periods and less well preserved in the Holocene and LGM. In Holocene specimens, fragile interior calcite is thin or absent, and blocky exterior calcite crystals appear to be reprecipitated on the surface and is structurally and geochemically distinct from primary calcite. In contrast, the interior calcite is better preserved in deglacial specimens. These results suggest diagenetic alterations of foraminifera shells are impacted by changes since the LGM and can be used to determine relative changes in deep water calcite conditions. The foraminifera-based proxy adds to a suit of proxies that record deep ocean [CO_3^{2-}] conditions and contributes valuable information in regions where calcite is heavily dissolved and proxies are complicated by diagenetic alterations.

1.3. References

Archer, D., Winguth, A., Lea, D., and Mahowald, N. (2000). What caused the glacial/interglacial atmospheric pCO2 cycles?. *Reviews of Geophysics*, *38*(2), 159-189. doi.10.1029/1999RG000066

Bahr, A., Schönfeld, J., Hoffmann, J., Voigt, S., Aurahs, R., Kucera, M., ... and Gerdes, A. (2013). Comparison of Ba/Ca and $\delta^{18}O_{WATER}$ as freshwater proxies: A multi species core-top study on planktonic foraminifera from the vicinity of the Orinoco River mouth. *Earth and Planetary Science Letters*, *383*, 45-57. doi.10.1016/j.epsl.2013.09.036

Boudreau, B. P., Middelburg, J. J., and Luo, Y. (2018). The role of calcification in carbonate compensation. *Nature Geoscience*, *11*(12), 894-900. doi.10.1038/s41561-018-0259-5

Boyle, E. A. (1981). Cadmium, zinc, copper, and barium in foraminifera tests. *Earth and Planetary Science Letters*, *53*(1), 11-35.

Boyle, E. A. (1983). Manganese Carbonate Overgrowths on Foraminifera Tests. *Geochimica Et Cosmochimica Acta* 47.10, 1815-819.

Boyle, E. A., and Keigwin, L. D. (1985). Comparison of Atlantic and Pacific paleochemical records for the last 215,000 years: Changes in deep ocean circulation and chemical inventories. *Earth and Planetary Science Letters*, *76*(1-2), 135-150.

Bradtmiller, L. I., Anderson, R. F., Fleisher, M. Q., and Burckle, L. H. (2006). Diatom production in the equatorial Pacific Ocean from the last glacial period to the present: A test of the silicic acid leakage hypothesis. *Paleoceanography*, *21*(4). doi.10.1029/2006PA001282

Broecker, W. (1982). Glacial to interglacial changes in ocean chemistry. *Progress in*

Oceanography 2:151–197, doi.0.1016/0079-6611(82)90007-6.

Broecker, W., and Clark, E. (2001). An evaluation of Lohmann's foraminifera weight dissolution index. Paleoceanography, 16(5), 531–534. doi.10.1029/2000PA000600

Costa, K. M., Jacobel, A. W., McManus, J. F., Anderson, R. F., Winckler, G., and Thiagarajan, N. (2017). Production patterns in the equatorial Pacific over the last 30,000 years. *Global Biogeochemical Cycles*, *31*(5), 850-865. doi.10.1002/2016GB005579

Dubois, N., Kienast, M., Kienast, S., Normandeau, C., Calvert, S. E., Herbert, T. D., and Mix, A. (2011). Millennial-scale variations in hydrography and biogeochemistry in the Eastern Equatorial Pacific over the last 100 kyr. *Quaternary Science Reviews*, *30*(1-2), 210-223. doi.10.1016/j.quascirev.2010.10.012

Eggins, S., De Deckker, P., and Marshall, J. (2003). Mg/Ca variation in planktonic foraminifera tests: Implications for reconstructing paleoseawater temperature and habitat migration, *Earth and Planetary Science Letters*, 212(3–4), 291–306, doi.10.1016/s0012–821x(03)00283-8.

Evans, D., Erez, J., Oron, S., and Müller, W. (2015). Mg/Ca-temperature and seawater test chemistry relationships in the shallow-dwelling large benthic foraminifera Operculina ammonoides. *Geochimica et Cosmochimica Acta*, *148*, 325-342. doi.10.1002/2015GC005822

Fehrenbacher, J**. S.** and Martin, P. A. (2010). A comparison of intrashell Mg/Ca variability of the planktonic foraminifera *G. ruber*, *G. sacculifer*, and *N. dutertrei* determined by electron microprobe image mapping, 2010 *IOP Conference Series: Earth and Environmental Science.* doi.10.1088/1755-1315/9/1/012018

Geider, R. D. J. et al. Primary production of planet earth: biological determinants and physical constraints in terrestrial and aquatic habitats. *Glob. Change Biol.* **7**, 849–882 (2001). doi.10.1.1.564.5935

Gottschalk, J., Battaglia, G., Fischer, H., Frölicher, T. L., Jaccard, S. L., Jeltsch -Thömmes, A., ...and Stocker, T. F. (2019). Mechanisms of millennial-scale atmospheric CO_2 change in numerical model simulations. *Quaternary science reviews*, *220*, 30-74. doi.10.1016/j.quascirev.2019.05.013

Hall, J. M., and Chan, L. H. (2004). Ba/Ca in *Neogloboquadrina pachyderma* as an indicator of deglacial meltwater discharge into the western Arctic Ocean, *Paleoceanography*, 19, PA1017, doi.10.1029/2003PA000910.

Hathorne, E. C., James, R. H., and Lampitt, R. S. (2009). Environmental versus biomineralization controls on the intratest variation in the trace element composition of the planktonic foraminifera *G. inflata* and *G. scitula*. *Paleoceanography*, *24*(4). doi.10.1029/2009PA001742

Hoffmann, J., Bahr, A., Voigt, S., Schönfeld, J., Nürnberg, D., and Rethemeyer, J. (2014). Disentangling abrupt deglacial hydrological changes in northern South America: Insolation versus oceanic forcing. *Geology*, *42*(7), 579-582. doi.10.1130/G35562.1

Iwasaki, S. et al. Observation of the dissolution process of *Globigerina bulloides* tests (planktic foraminifera) by X-ray microcomputed tomography. Paleoceanography

30, 317–331 (2015). https://doi.org/10.1002/2014PA002639

Iwasaki, S., Kimoto, K., Okazaki, Y., and Ikehara, M. (2019). Micro-CT Scanning of Tests of Three Planktic Foraminiferal Species to Clarify DissolutionProcess and Progress. *Geochemistry, Geophysics, Geosystems*, *20*(12), 6051-6065.

Johnstone, H. J., Schulz, M., Barker, S., and Elderfield, H. (2010). Inside story: An X-ray computed tomography method for assessing dissolution in the tests of planktonic foraminifera. *Marine Micropaleontology*, *77*(1-2), 58-70.

Jonkers, L., Buse, B., Brummer, G. J. A., and Hall, I. R. (2016). Chamber formation leads to Mg/Ca banding in the planktonic foraminifer *Neogloboquadrina pachyderma*. *Earth and Planetary Science Letters*, *451*, 177-184. doi.10.1016/j.epsl.2016.07.030

Jouzel, J., V. Masson-Delmotte, O. Cattani, G. Dreyfus, S. Falourd, G. Hoffmann, B. Minster, J. Nouet, J.M. Barnola, J. Chappellaz, and others. 2007. Orbital and millennial Antarctic climate variability over the past 800,000 years. *Science* 317:793–797, doi.10.1126/science.1141038.

Key, R.M., A. Kozyr, C.L. Sabine, K. Lee, R. Wanninkhof, J.L. Bullister, R.A. Feely, F.J. Millero, C. Mordy, and T.H. Peng. 2004. A global ocean carbon climatology: Results from Global Data Analysis Project (GLODAP). *Global Biogeochemical Cycles* 18, GB4031, doi.10.1029/2004GB002247.

Kunioka, D., Shirai, K., Takahata, N., Sano, Y., Toyofuku, T., and Ujiie, Y. (2006). Microdistribution of Mg/Ca, Sr/Ca, and Ba/Ca ratios in *Pulleniatina obliquiloculata* test by using a NanoSIMS: Implication for the vital effect mechanism. *Geochemistry, Geophysics, Geosystems*, *7*(12). doi.10.1029/2006GC001280

Lea, D. W., and Boyle, E. A. (1991). Barium in planktonic foraminifera, *Geochim. Cosmochim. Acta*, 55(11), 3321–3331.

Lopes, C., Kucera, M., and Mix, A. C. (2015). Climate change decouples oceanic primary and export production and organic carbon burial. *Proceedings of the National Academy of Sciences*, *112*(2), 332-335. doi.10.1073/pnas.1410480111

Lutze, G.F., and Thiel, H. (1989). Epibenthic foraminifera from elevated microhabitats: *Cibicidoides wuellerstorfi* and *Planulina ariminensis*. *Journal of Foraminiferal Research* 19:153–158.

Marchitto Jr, T. M., Curry, W. B., and Oppo, D. W. (2000). Zinc concentrations in benthic foraminifera reflect seawater chemistry. *Paleoceanography*, *15*(3), 299-306. doi:10.1029/1999PA000420

Marr, J. P., Carter, L., Bostock, H. C., Bolton, A., and Smith, E. (2013). Southwest Pacific Ocean response to a warming world: Using Mg/Ca, Zn/Ca, and Mn/Ca in foraminifera to track surface ocean water masses during the last deglaciation. *Paleoceanography*, *28*(2), 347-362.

Martin, P. A., and Lea, D. W. (2002). A simple evaluation of cleaning procedures on fossil benthic foraminiferal Mg/Ca. *Geochemistry, Geophysics, Geosystems*, *3*(10), 1-8. doi.10.1029/2001GC000280

Qin, B., Li, T., Xiong, Z., Algeo, T. J., and Chang, F. (2017). Deepwater carbonate

ion concentrations in the western tropical Pacific since 250 ka: Evidence for oceanic carbon storage and global climate influence. Paleoceanography, 32(4), 351–370. doi.10.1002/2016PA003039

Raitzsch, M., E.C. Hathorne, H. Kuhnert, J. Groeneveld, and T. Bickert. 2011. Modern and late Pleistocene B/Ca ratios of the benthic foraminifer *Planulina wuellerstorfi* determined with laser ablation ICP-MS. *Geology* 39:1,039–1,042, doi.org/10.1130/G32009.1.

Richaud, M., Loubere, P., Pichat, S., and Francois, R. (2007). Changes in opal flux and the rain ratio during the last 50,000 years in the equatorial Pacific. *Deep Sea Research Part II: Topical Studies in Oceanography*, *54*(5-7), 762-771. doi.10.1016/j.dsr2.2007.01.012

Rickaby, R.E.M., H. Elderfield, N. Roberts, C.-D. Hillenbrand, and A. Mackensen. 2010. Evidence for elevated alkalinity in the glacial Southern Ocean. *Paleoceanography* 25, PA1209, http://dx.doi.org/10.1029/2009PA001762.

Sanyal, A., N.G. Hemming, G.N. Hanson, and W.S. Broecker. 1995. Evidence for a higher pH in the glacial ocean from boron isotopes in foraminifera. *Nature* 373:234–236, doi.10.1038/373234a0.

Sigman, D. M., and Boyle, E. A. (2000). Glacial/interglacial variations in atmospheric carbon dioxide. *Nature*, *407*(6806), 859-869. https://doi.org/10.1038/35038000

Vetter, L., Spero, H. J., Russell, A. D. and Fehrenbacher, J. S. (2013). LA-ICP-MS depth profiling perspective on cleaning protocols for elemental analyses in planktic foraminifers. *Geochem. Geophys. Geosyst.* 14, 2916–2931. doi.10.1002/ggge.20163

Yu, J., R.F. Anderson, and E.J. Rohling. 2014. Deep ocean carbonate chemistry and glacial-interglacial atmospheric CO2 changes. *Oceanography* 27(1):16–25, doi.10.5670/oceanog.2014.04.

Yu, J., W. Broecker, H. Elderfield, Z.D. Jin, J. McManus, and F. Zhang. 2010. Loss of carbon from the deep sea since the Last Glacial Maximum. *Science* 330:1,084–1,087, doi.10.1126/science.1193221.

Yu, J.M., H. Elderfield, and A. Piotrowski. 2008. Seawater carbonate ion-$\delta^{13}C$ systematics and application to glacial-interglacial North Atlantic ocean circulation. *Earth and Planetary Science Letters* 271:209–220, doi.10.1016/j.epsl.2008.04.010.

Preferential loss of high trace element bearing inner calcite in foraminifera during physical and chemical cleaning

Theresa Fritz-Endres[1]; Jennifer Fehrenbacher[1]

[1]Oregon State University, College of Earth, Ocean, and Atmospheric Sciences, Corvallis, OR 97330

Fritz-Endres, T., and Fehrenbacher, J. (2020). Preferential loss of high trace element bearing inner calcite in foraminifera during physical and chemical cleaning. *Geochemistry, Geophysics, Geosystems*, 22, e2020GC009419. https://doi.org/10.1029/2020GC009419

2. Preferential loss of high trace element bearing inner calcite in foraminifera during physical and chemical cleaning

2.1. Abstract

Trace elements in the calcite shells of foraminifera are widely used in paleoceanographic reconstructions. Nearly all trace element analytical protocols include cleaning to remove contaminant phases. Understanding how the trace element composition is altered during physical and chemical cleaning is of utmost importance in ensuring the accuracy of paleoclimate reconstructions. Aggressive cleaning steps that include corrosive reagents are commonly used to clean shells with elevated Ba/Ca and Mn/Ca ratios, under the assumption that these elements are elevated due to diagenetic overprinting. We provide evidence that elevated intra-shell Ba/Ca, Mn/Ca, and Zn/Ca ratios are lattice bound and a primary signal incorporated into inner calcite during calcification in the non-spinose species *Neogloboquadrina dutertrei* and *Pulleniatina obliquiloculata*. We first demonstrate, using laser ablation depth profiling analyses, that aggressive cleaning following the full cleaning protocol traditionally used to eliminate Mn and Ba contamination, preferentially removes inner (ontogenic) calcite and favors the low Ba/Ca, Mn/Ca, Zn/Ca, and Mg/Ca crust/cortex calcite. In a separate experiment, we demonstrate that mechanical fragmentation of bulk shells prepared for solution analysis also preferentially removes inner calcite and favors the low trace element crust/cortex calcite. Preferential loss of the ontogenic calcite decreases Ba/Ca, Mn/Ca, and Zn/Ca ratios by 50 - 90% in *N. dutertrei* and *P. obliquiloculata* shells. This biases foraminiferal trace element results toward lower values and may yield data that is problematic for the interpretation of downcore records.

Plain Language Summary

Elements (including barium and magnesium) measured inside microscopic fossil shells are higher than expected and could reflect contamination or could reflect key

information about the ancient surface ocean. For example, barium may reflect how much organic carbon is produced in the surface ocean, some of which is sunk to the deep ocean and thus removed from exchange with the atmosphere, affecting climate. Previous studies have attributed higher concentrations of these elements to contamination that forms on shells and have established harsh chemical cleaning techniques to remove the contamination. However, these cleaning techniques also remove parts of the shell that contain key information about past ocean conditions. We determine that high concentrations of these elements are not due to contamination in our samples and likely reflect conditions of the surface ocean. In future work, we suggest using techniques that measure at the micro-scale to confirm that there is no contamination and we suggest using more careful cleaning that preserves these elements. Preserving these elements in fossil shells may provide key information about organic carbon production and cycling in the surface ocean, which is critical to reconstruct carbon exchange between the atmosphere and ocean.

2.2. Introduction

The geochemistry of planktic foraminifera shells is a critical tool used to reconstruct paleotemperature (Mg/Ca) (Lea et al., 1999; Anand et al., 2003; Dekens et al., 2002; von Langen et al., 2005), redox conditions (Mn/Ca) (Klinkhammer et al., 2009; Glock et al., 2012; Groeneveld et al., 2018; Skinner et al., 2018; Petersen et al., 2019), freshwater flux and salinity (Ba/Ca) (Hall and Chan, 2004; Weldeab et al., 2007; 2014; Bahr et al., 2013; Hoffman et al., 2014; Evans et al., 2015; Setiawan et al., 2017), and nutrients (Mn/Ca; Zn/Ca; Ba/Ca) (Marr et al., 2013) in ancient water masses. Together, mixed layer dwelling and deeper dwelling planktic foraminifera species reconstruct the entire upper water column (e.g., Mulitza et al. 1997; Chaisson and Ravelo, 2000; Spero et al., 2003).

Trace element (TE) to Ca ratios, including Ba/Ca, Mn/Ca, and Zn/Ca, in many non-spinose deeper dwelling foraminifera species are higher, and Ba/Ca, Mn/Ca, Zn/Ca,

and Mg/Ca are more variable as compared to mixed layer dwelling foraminifera, and their utility in paleoceanographic reconstructions is less straight-forward (Hathorne et al., 2009; Kunioka, 2006; Branson et al., 2015; Jonkers et al. 2016; Jonkers et al., 2012; Sadekov et al., 2005; Fehrenbacher and Martin, 2010). Often, the TEs in non-spinose foraminifer shells are elevated in the ontogenic calcite with distinct high and low TE bands, and TEs are low and relatively invariable within the outer crust or cortex of the shell (Eggins et al., 2003; Hathorne et al., 2009; Steinhardt et al., 2015). High intra-shell TE/Ca bands are often correlated in non-spinose foraminifera (Eggins et al., 2003; Hathorne et al., 2009), suggesting similar environmental or biological control on incorporating these TEs. High TE/Ca bands may reflect the environmental conditions at the time of calcification. For example, high Mn/Ca and Zn/Ca ratios in foraminiferal calcite are thought to reflect increasing concentrations of these metals from low values in surface waters to higher values at depth and may be used to trace surface waters and nutrient stratification (Boyle, 1981; Marr et al., 2013). While few studies have been done evaluating Zn/Ca in planktic foraminifera, Zn/Ca ratios in benthic foraminifera may be used with other TE/Ca ratios to trace changes in deep water carbonate chemistry (Marchitto et al., 2000) and, in shallow water cores, changes in the nutricline (Bryan and Marchitto, 2010). Dissolved Mn is additionally modified by redox conditions, and high Mn/Ca ratios in benthic foraminifera have been used to reflect oxygenation of hypoxic deep water and pore water (Glock et al., 2012; Groeneveld et al., 2018; Skinner et al., 2018; Petersen et al., 2019). In regions with intense oxygen minimum zones, comparing the Mn/Ca ratio of species of planktic foraminifera that calcified in the mixed layer to those that calcified in the thermocline and benthic foraminifera may be used as a proxy for changing terrestrial input of Mn and oxidation reduction reactions in the water column (Klinkhammer et al., 2009) and Mn/Ca in sediment trap derived planktic foraminifera may in part reflect changing conditions within an oxygen minimum zone (Davis et al., 2020).

High Ba/Ca ratios in surface dwelling foraminifera reflect freshwater flux and salinity changes in regions with high freshwater input (Edmond et al., 1978; Bahr et al., 2013; Weldeab et al., 2007; 2014; Evans et al., 2015). High Ba/Ca ratios in non-spinose

deeper dwelling foraminifera may in part reflect higher Ba concentrations in deeper water; however, Ba/Ca ratios are often much higher than in surface dwelling species and higher than can be attributed to the Ba composition of any seawater location (Lea and Boyle, 1991; Hall and Chan, 2004; Hathorne et al., 2009; Bahr et al., 2013). High Ba/Ca ratios measured in *Neogloboquadrina dutertrei*, and likely in other non-spinose foraminifera, may reflect conditions within a Ba enriched microenvironment, such as within marine snow particulates or other organic detritus in the water column (Fehrenbacher et al., 2018; Greco et al., 2019; Tagaki et al., 2019). Within particles, the desorption of Ba from Fe hydroxides and the degradation of organic matter can enrich Ba and SO_4 enough to support Ba supersaturation and the formation of barium enriched amorphous particles and barite crystals ($BaSO_4$; Stroobants et al., 1991; Sternberg et al., 2005; Martinez-Ruiz et al., 2018), despite widespread barite undersaturation in bulk seawater (Monnin et al., 1999; Rushdi et al., 2000). The complicated geochemistry of particulates may also permit higher dissolved Mn within the particulate microhabitat (due to lower oxygen and pH (Alldredge, 2000; Alldredge and Cohen, 1987)), which may help to explain the elevated and variable Mn in non-spinose foraminifers.

Elevated Ba/Ca and Mn/Ca ratios in foraminiferal calcite have also been attributed to contaminants or diagenetic alteration in the water column or on the seafloor (Boyle, 1981, 1983; Boyle and Keigwin, 1985; Lea and Boyle, 1991; Haley and Klinkhammer, 2002; Gibson et al., 2016; Pena et al., 2005, 2008). Although Ba is thought to substitute in place of Ca in inorganic calcite (Kitano et al., 1971) and inside the lattice of a foraminifera shell (Lea and Boyle, 1991; Lea and Spero, 1994), Ba-rich sediment phases can result in non-lattice bound Ba enrichment on shell surfaces and within pores that masks shell-bound Ba. Such sediment phases, including Ba-enriched detrital and fine-grained material, barite crystals, organic matter, and Mg-Mn and Fe oxide overgrowths, have been observed associated with foraminifer shells (Gibson et al., 2016; Pena et al., 2005, 2008). Mn-carbonate phases can precipitate under conditions where Mn is remobilized from oxidized organic matter (Pedersen and Price, 1982; Boyle, 1983) and may contaminate the Mn and Mg signal on foraminifera shell surfaces in the water column (Davis and Benitez-Nelson, 2020; Gibson et al., 2016) or on the seafloor

(Boyle, 1981; Pena et al., 2005, 2008; Branson et al., 2015). Contamination may also occur during chemical cleaning, as high TE values have also been attributed to TE reabsorption onto cleaned calcite prepared for solution analysis (Sholkovitz, 1989; Haley and Klinkhammer, 2002) such that contaminants cleaned away may still be erroneously measured as a primary signal. Aggressive cleaning procedures (including a reductive cleaning step and the use of the chelating agent DTPA) are traditionally employed to remove contaminant phases (e.g., Lea and Boyle, 1991). These procedures are highly corrosive to calcite, can lead to extensive sample loss due to dissolution, and may decrease TE concentrations (Lea and Boyle, 1991; Yu et al., 2007; Martin and Lea, 2002; Vetter et al., 2013, Regenberg et al., 2006; Rosenthal et al., 2004, Barker et al., 2003; Johnstone et al., 2016). For this reason, the reductive and DTPA steps are often excluded unless metal contaminant phases are observed or suspected (Yu et al., 2007; Johnstone et al., 2016), such as within redox sensitive basins (Pena et al., 2005; 2008).

In this study, we use laser ablation ICP-MS to investigate how cleaning procedures alter the TE composition of the non-spinose planktic foraminifer species *N. dutertrei* and *Pulleniatina obliquiloculata*. These species were chosen because studies have shown that the TE composition of the inner (ontogenic) calcite in these species is markedly higher than the outer calcite (Eggins et al., 2003; Sadekov et al., 2005; 2009; Kunioka, 2006; Jonkers et al., 2012; Fehrenbacher and Martin, 2010; Fehrenbacher et al., 2018) and the inner calcite of these species are more prone to dissolution on the seafloor (e.g., Johnstone et al., 2010), potentially altering TE concentrations. Laser ablation ICP-MS is an excellent tool for assessing intra-shell TE variability (Eggins et al., 2003; Hathorne et al., 2003, 2009; Sadekov et al., 2009; Wit et al., 2010; Fehrenbacher et al., 2015). It is minimally destructive to the shell and permits repeat analyses of each specimen before and between each cleaning step, allowing for a detailed assessment of how each cleaning step alters the TE composition. After each cleaning step, we measure intra-shell TE/Ca ratios of whole shells and shell fragments using low energy and low repetition rate laser settings, enabling us to resolve ‘inner’ vs ‘outer’ calcite (as defined in Table 1) and corresponding TE/Ca variability within the shell. In addition to the laser analyses, we also investigate how bulk (solution) cleaning methods alter the trace

element composition of *P. obliquiloculata*. We use Scanning Electron Microscope (SEM) imaging to investigate how bulk cleaning modifies shell fragments. We find that the aggressive cleaning steps often employed to remove contaminant phases also decrease or completely remove inner calcite in *N. dutertrei* and *P. obliquiloculata* and decrease the mean TE composition.

2.3. Methods

2.3.1. Individual shell laser ablation ICP-MS

Specimens of *N. dutertrei* and *P. obliquiloculata* were obtained from the 355-500 μm size fraction of the 79 - 80 cm interval of Eastern Equatorial Pacific (EEP) core ME0005A-43JC (7.86ºN, 83.6ºW, water depth 1368 m). This interval was chosen because preliminary laser ablation data indicate that *N. dutertrei* and *P. obliquiloculata* shells have high Ba/Ca and Mn/Ca ratios, and specimens display intra-shell TE banding (Supplemental Figure 1). Four *N. dutertrei* and one *P. obliquiloculata* were left whole and 14 *N. dutertrei* and 15 *P. obliquiloculata* were placed on a rubber stopper, wetted, and gently broken with a scalpel into four - five large fragments.

The whole shells and fragments were cleaned using the established cleaning procedures of Martin and Lea [2002], adapted for single shells (see Appendix A). They included the Cd-cleaning step employed by Boyle and Keigwin [1985] and Lea and Boyle [1989] and others (e.g., Lea and Boyle, 1991). The cleaning steps included rinses to remove finely adhering clays, an oxidative step to remove remnant organic matter, the reductive step to remove metal oxides, and finally, the DTPA step that is typically only used in settings where contaminant surface phases are problematic. Briefly, shell material was rinsed in methanol and sonicated (10 seconds) followed by four ultrapure water (18 MΩ) rinses. Rinses were followed by an oxidative cleaning step in which shells were bathed for 10 minutes in a warm (60°C) buffered hydrogen peroxide solution followed by four ultrapure water rinses. Shell material was then reductively cleaned with an anhydrous hydrazine/ammonium citrate solution warmed to 80-90°C for 30 minutes,

followed by four ultrapure water rinses. Shell material was finally cleaned with an alkaline chelating agent of weak (0.002 M) DTPA solution, which was buffered in 0.05 M NaOH, warmed to 100°C for five minutes. DTPA was then neutralized by additions of 0.01 M NaOH followed by rinsing shell material three times with ultrapure water. During the final rinse step, the foraminifers were bathed for 30 minutes at 100°C. The final step was followed by a dilute acid (0.001 M HNO_3) leach to remove any adsorbed contaminants from the shell material followed by ultrasonication and a final ultrapure water rinse. In between each cleaning step (rinses/sonication, oxidative, reductive, DTPA+acid leach), the whole shells and fragments were mounted onto aluminum stubs with carbon tape, analyzed on a laser, and imaged on an SEM.

Laser ablation depth profile analyses were conducted at Oregon State University (OSU) using a Teledyne/Photon Machines 193 nm ArF UV excimer laser ablation system with a HelEx laser ablation cell coupled to a Thermo Scientific X-series II quadrupole ICP-MS. Gas composition and flow rate were determined by adjusting the flow of Ar and He as necessary to achieve high count rates on the sample/standard while maintaining ThO^+/Th^+ ratios less than 0.4% (tuned daily). Whole shells were analyzed from the outside - in and shell fragments were analyzed from the inside - out. Samples were analyzed using a 50 - 70 μm diameter spot size at 4 Hz repetition rate and 1.0 - 1.5 J/cm^2 laser fluence. Data acquisition varied between 40 - 60 seconds per spot analysis. Repeat analyses were conducted on chambers large enough to permit multiple spots. Isotopes, including ^{137}Ba, ^{24}Mg, ^{25}Mg, ^{43}Ca, ^{44}Ca, ^{66}Zn, ^{88}Sr, ^{27}Al, and ^{55}Mn, were measured along with others not assessed in this study. ^{43}Ca was used as the internal standard, and ^{44}Ca was monitored for consistency.

Shell profile mean elemental concentrations were calculated using LAtools data reduction software, including screening for outliers and background correcting by subtracting average background counts (calculated with the laser off) from each data point (Branson et al., 2019). The mean TE/Ca ratio for each profile was then calculated by normalizing to the known TE concentration in the drift/background-corrected bracketed analyses of the NIST SRM 610 and 612 glass standards at 5 Hz and ~ 4.5 J/cm^2 laser fluence (Jochum et al., 2011). Ten repeat analyses gave a reproducibility of the

mean Ba/Ca, Mn/Ca, Zn/Ca, Mg/Ca ratios of 1594 ± 69 μmol/mol (± 4.3%; 1σ), 3885 ± 75 μmol/mol (± 1.9%; 1σ), 3446 ± 89 μmol/mol (± 2.6%; 1σ), and 9.655 ± 0.49 mmol/mol (± 5.0%; 1σ), respectively for NIST 610 and 139 ± 5.0 μmol/mol (± 3.7%; 1σ), 331 ± 14 μmol/mol (± 4.1%; 1σ), 296 ± 14 μmol/mol (± 4.6%; 1σ), and 1.289 ± 0.90 mmol/mol (± 7.0%; 1σ), respectively for NIST 612. Standard measurements are within 5.0% of published values for NIST 610 and 612 (Jochum et al., 2011).

After each laser ablation session, the whole shell and shell fragments were imaged on a Quanta 300 environmental SEM at OSU. Thickness was measured from profile images of each shell fragment and used to convert ablation time to distance (μm). The SEM images were used to visually assess the effect of cleaning on shell material and microstructure changes. Because shell fragments were fragile and easily lost, SEM analysis was skipped after the oxidative step and only done after the reductive step to reduce the number of times fragments were removed from and remounted on the tape. Thus, the images taken after reductive cleaning represent impacts to the shell material that occurred during both the oxidative and reductive cleaning.

2.3.2. Bulk shells prepared for solution analysis

The purpose of the bulk shell cleaning study is to assess the effect of sample cleaning on shell TE/Ca ratios. Specifically, we modify the shell cracking procedure and use two different settling times before aspirating the rinse/cleaning solutions. We then assess shell fragmentation using image analysis. Forty *P. obliquiloculata* shells were selected from the 8 - 10 cm (Holocene) and 40 from the 26 - 28 cm (deglacial) intervals from western equatorial Pacific core MW91-9-6GGC (2.02ºS, 156.93ºE, water depth 1625m). Shells were grouped into sets of 20 and gently cracked between two glass slides to open chambers to aid the removal of clays and other debris. Shell fragments were homogenized with a brush and were split into two aliquots for a total of 16 bulk groups (eight replicates from each interval). Four groups for each interval were subjected to the Mg-only cleaning protocol (Barker et al., 2003), which included rinses/sonication, oxidative cleaning, and a weak (0.001 M) HNO_3 leach and a one-minute settling time before aspirating the rinse/cleaning solution. Four groups from each interval were

cracked open more gently, and the settling time before aspirating the rinse/cleaning solution was increased from one minute to three minutes.

Before cleaning, shell fragments were imaged on a dark background at 0.8 and 10.0X zoom using a Leica M125 stereomicroscope with a DMC 4500 mounted camera system. Images were processed using the Fiji software package (Schindelin et al. 2012) to analyze and categorize shell fragments, as shown in Supplemental Figure 2. Two images of each group were used for each image analysis. Shell fragments were distinguished from the background using the Auto Threshold v1.17 Fiji plugin. Shell fragment surface area was calculated using the Analyze Particles tool and categorized as either large (> 6 μm^2) or small fragments (< 6 μm^2) for each sample (changing the categorization by ± 3 μm^2 changes the number of large or small fragments by < 5%).

Following cleaning, fragments were carefully mounted on their longest axis onto aluminum stubs with carbon tape and analyzed on an FEI Quanta 600F environmental SEM at OSU. Each sample was imaged at higher and lower magnification (horizontal field width ~1 mm and ~500 μm). Regions of shell fragments were visually interpreted as either 'inner' or 'outer' calcite (as defined in Table 1). The outer calcite of *P. obliquiloculata* is dominated by a shell cortex characterized by a smooth micro-perforate texture. The cortex is identifiable as a thin and finely crystalline layer that appears glassy under SEM (Johnstone et al., 2010), while the inner calcite can be thicker and coarsely crystalline and is identifiable by larger uniformly spaced pores and high ridges between pore spaces. The visual categorization of inner and outer calcite at higher magnification (~1 mm horizontal field width) was used to train Weka Trainable Segmentation (v.3.2.33), a Fiji plugin with machine learning techniques (Supplemental Figure 2). Using Weka Trainable Segmentation, machine learning algorithms classified each image pixel to a class (inner or outer calcite) for all SEM images and calculated the total inner calcite and outer calcite surface area present in each replicate. Inner calcite has a distinct SEM grayscale range compared to outer calcite (8-bit greyscale range 100 - 210 and 210 - 255, for the inner and outer calcite, respectively) as a result of the very different pore structure (e.g., micro-perforate outer calcite has lighter greyscale values), allowing for an accurate

classification (using standard Weka settings, out-of-bag error for a well-trained run was typically < 1%).

2.4. Results

2.4.1. Individual shells

2.4.1.1. Visual changes in shell texture

SEM images of the whole shell and shell fragments of *N. dutertrei* and *P. obliquiloculata* material taken after each cleaning step indicate progressive dissolution during cleaning with preferential loss of inner portions of the shell (Figure 1; micro-structure descriptions based on those presented in Dittert and Henrich (2000) and Regenberg et al. (2013)). After the initial rinses/sonication, all *N. dutertrei* fragments and whole shells appear well preserved. SEM images reveal regularly spaced outer pores surrounded by irregular ridges, preserved shell layers, smooth inter-pore areas, round to funneled pores, high to slightly reduced ridges, thick outer calcite, and sharp edges of euhedral crystal structures (Figure 1a and 1b). After the oxidative and reductive steps (to preserve fragile shell fragments, SEM analysis was skipped after the oxidative step and only done after the reductive step), *N. dutertrei* material show signs of dissolution with cracked and disintegrated inner calcite layers, funneled pores (Figure 1c and 1d), and slightly rounded crystal surfaces on the exterior of the shell (Figure 1d). After the DTPA step, *N. dutertrei* material show signs of substantial dissolution (Figure 1e and 1f). The inner calcite appears heavily dissolved, and the calcite of the inner chamber wall is eroded, and the exterior calcite crystals are heavily dissolved and rounded (Figure 1f). SEM images of *P. obliquiloculata* taken after the initial rinses/sonication reveal smooth outer calcite, intact calcite layers, smooth inner calcite with a round to funneled and evenly spaced pores, and smooth inter-pore areas (Figure 1g and 1h). Often in cracking open *P. obliquiloculata* shells, inner calcite layers delaminate from outer calcite and are sheeted away in one or many distinct layers (Figure 1j). Delamination occurs in a few fragments after just the initial rinses/sonication and before more corrosive cleaning steps

are conducted. After oxidative and reductive cleaning, the inner calcite separated from the cortex in two of 15 fragments (Figure 1j). In another two fragments, the inner calcite is completely missing, and just the cortex remains. After DTPA cleaning, *P. obliquiloculata* material shows clear divisions between cortex and inner calcite and shows separation and removal of portions of inner calcite layers, severely cracked inner calcite, and heavily funneled pores. For three of the shell fragments, inner calcite is completely absent after the DTPA step (Figure 1k and 1i).

2.4.1.2. Laser ablation results

2.4.1.2.1. Depth profiles after initial rinse/sonication

Laser ablation profiles of samples that have undergone just initial rinses contain high and variable TEs (Figures 2 and 3). Laser ablation profiles of nearly all (90%, N = 16) of *N. dutertrei* shells have distinct regions of high TEs within the inner calcite (e.g., Figure 2, blue lines). These regions are 10 - 30 µm thick and have two - four alternating high/low TE/Ca bands. Bands of high Mn/Ca, Zn/Ca, and Mg/Ca are variable from specimen-to-specimen and less reproducible from chamber-to-chamber than bands of high Ba/Ca. TE bands are often, but not always, correlated (e.g., Figure 2a vs. 2b). Most (80%, N = 13) of *P. obliquiloculata* shells have alternating high and low TE bands in inner calcite, like those observed in *N. dutertrei*. However, there are fewer bands (one - two) and they are more variable from chamber-to-chamber (e.g., Figure 3, blue lines). All profiles of *N. dutertrei* and *P. obliquiloculata* have a low and homogenous TE region on the outside that is 10 - 20 µm thick and likely represents crust/cortex calcite, which has been shown in other laser ablation studies with this species to have homogeneous TE ratios (e.g., Jonkers et al., 2012; Sadekov et al., 2009; Steinhardt et al., 2015).

The regions of high TE outer calcite are differentiated from low TE inner calcite at the point of greatest change in Ba/Ca, Mn/Ca, Zn/Ca, and Mg/Ca ratios from high and variable values to low and homogenous values (Figure 4). In *N. dutertrei,* 65% of the total calcite is high TE calcite, on average, and *P. obliquiloculata* contains 55% high TE calcite. This is consistent with other studies of *N. dutertrei* (Jonkers et al., 2012) and *P. obliquiloculata* (Sadekov et al., 2009; Steinhardt et al., 2015), and the low TE regions in

P. obliquiloculata correspond with the smooth micro-perforate cortex observed in SEM images. In both *N. dutertrei* and *P. obliquiloculata*, inner calcite Ba/Ca, Mn/Ca, and Zn/Ca ratios are 60 - 80% higher than the outer (low TE) calcite and have 40 - 90% greater variability (1σ) (Table 2). Mg/Ca ratios in the inner calcite are 30 - 40% higher than in the outer (low TE) regions.

2.4.1.2.2. Oxidative cleaning

After the oxidative cleaning step, *N. dutertrei* shell thickness decreased by an average of 15%, and one or more high TE bands were removed (e.g., Figure 2, orange lines). TE/Ca ratios decrease by 40, 8, 24, and 20% for Ba/Ca, Mn/Ca, Zn/Ca, and Mg/Ca ratios, respectively (Figure 5). The decrease in Ba/Ca and Zn/Ca is significant (student's t-test, two-tailed, $p < 0.05$), while Mn/Ca and Mg/Ca ratios are not significantly different (student's t-test, two-tailed, $p = 0.08$ and 0.16, respectively).

Pulleniatina obliquiloculata shell thickness decreased by an average of 10% and inner calcite is preferentially removed (e.g., Figure 3, orange lines). TE/Ca ratios decrease by 51, 50, 59, and 24% for Ba/Ca, Mn/Ca, Zn/Ca, and Mg/Ca ratios, respectively. The decrease in all Ba/Ca, Mn/Ca, and Zn/Ca ratios are statistically significant (student's t-test, two-tailed, $p < 0.05$), while the decrease is not significantly different for Mg/Ca ratios (student's t-test, two-tailed, $p = 0.22$).

2.4.1.2.3. Reductive cleaning

After the reductive step, *N. dutertrei* shell thickness decreased by an average of 30% and few high TE/Ca bands remain (e.g., Figure 2, yellow lines). Ba/Ca, Mn/Ca, and Zn/Ca ratios decrease by 75, 41, 89%, respectively, relative to values measured after the initial rinses. All three decreases are significant (student's t-test, two-tailed, $p < 0.05$). The Mg/Ca ratios decrease by 18% relative to values measured after the initial rinses, but this decrease is not significantly different (student's t-test, two-tailed, $p = 0.16$).

Like in *N. dutertrei*, few high TE bands remain in *P. obliquiloculata*, and shell thickness decreased by 20% (e.g., Figure 3, yellow lines). High TE calcite makes up just 15% of the total calcite, compared to 56% after the initial rinses/sonication. Ba/Ca,

Mn/Ca, Zn/Ca, and Mg/Ca ratios decrease by 64, 50, 81, and 26%, respectively, relative to values measured after the initial rinses. The decrease in Ba/Ca, Mn/Ca, and Zn/Ca ratios are statistically significant (student's t-test, two-tailed, $p < 0.05$), while the decrease in Mg/Ca is not significant (student's t-test, two-tailed, $p = 0.06$).

2.4.1.2.4. DTPA cleaning

After the DTPA cleaning step, calcite with TE banding in *N. dutertrei* has been removed (e.g., Figure 2, purple lines). Shell thickness decreased by an average of 30% and high TE calcite comprises only 40% of the total calcite. Ba/Ca, Mn/Ca, Zn/Ca, and Mg/Ca ratios decrease by 82, 49, 91, and 22%, respectively, relative to values measured after the initial rinses. The decrease in Ba/Ca, Mn/Ca, and Zn/Ca ratios are significant (student's t-test, two-tailed, $p < 0.01$), and Mg/Ca ratios are not significantly different (student's t-test, two-tailed, $p = 0.07$). In *P. obliqiuloculata* shells, nearly all calcite with high TE bands has been removed (e.g., Figure 3, purple lines). A few profiles contain only low TE ratio calcite, consistent with the removal of all inner calcite layers leaving behind only low TE cortex. The shell wall thickness decreases by 30% and high TE calcite makes up just 10% of the total calcite. Ba/Ca, Mn/Ca, Zn/Ca, and Mg/Ca ratios are reduced by 65, 59, 90, and 19%, respectively, relative to values measured after the initial rinses. The decrease in Ba/Ca, Mn/Ca, and Zn/Ca ratios are significant (student's t-test, two-tailed, $p < 0.05$), and Mg/Ca ratios are not significantly different (student's t-test, two-tailed, $p = 0.06$).

In summary, shells progressively thin through chemical cleaning, and high TE inner calcite is preferentially removed. We note that SEM analysis obtained before chemical cleaning indicate that EEP shells are well preserved, despite residing at a water depth of 1368 m in waters with a $\Delta[CO_3^{2-}]$ of ~1-2 μmol/kg, ~500 m above the regional lysocline (~2000 m water depth; GLODAP data set, Key et al., 2004). While dissolution may lower TE/Ca ratios in samples above the lysocline (Dekens et al., 2002; Regenberg et al., 2006), Mg/Ca SST estimates using the Anand et al. (2003) multispecies equation predict *N. dutertrei* and *P. obliquiloculata* calcified in 19.0ºC and 19.5ºC waters, consistent with these species depth habitat at the base of the thermocline (Farmer et al.,

2007; Elderfield and Ganssen, 2000), further suggesting that dissolution did not significantly impact TE/Ca ratios in these specimens. SEM image analysis after cleaning reveals that in a few specimens, none of the high TE/Ca inner calcite remains. Chemical dissolution is evident from SEM analysis (widened pores, cracked surfaces, and delaminating shell structure) and shells are likely further agitated by handling and laser ablation. We note that shell fragmentation can occur during laser ablation analysis, often when the laser first strikes the shell surface unevenly (i.e., not perpendicular). Laser ablation is unlikely to be the main factor contributing to inner calcite loss, as uneven ablation results in large irregular pits, which we did not observe during our analyses. It is likely that both chemical and mechanical breakdown of the shell contributes to the loss of high TE/Ca inner calcite. Through the full cleaning process for single shells analyzed via laser ablation, Ba/Ca, Mn/Ca, Zn/Ca values decrease by ~ 50 - 90%. Mg/Ca ratios are not significantly affected throughout the cleaning process, likely because the Mg/Ca ratios are not markedly different in the inner vs. outer calcite portions of the shell used in our study. Through the full cleaning process, Mg/Ca ratios decrease by 20 - 25%, from 2.2 to 1.7 mmol/mol in *N. dutertrei* and 2.1 to 1.7 mmol/mol in *P. obliquiloculata* shells. This Mg/Ca decrease would translate to an Mg/Ca SST estimate of 19.0ºC and 19.5ºC, decreasing to 16.6ºC. While the decrease in Mg/Ca is not significant, the Mg/Ca SST estimation suggests a lowering of several degrees that is likely an artifact of the cleaning process, as shells were initially observed to be well preserved, which is consistent with the reduction in Mg/Ca SST estimate observed by others (Martin and Lea, 2002; Regenberg et al., 2006; Rosenthal et al., 2004).

2.4.2. Bulk shells

Bulk *P. obliquiloculata* were prepared for solution ICP-MS analysis by cracking the shells open and subjecting shells to initial rinses/sonication and an oxidative cleaning step. We compare the effect of using different sample cracking methods and settling times after rinses/sonication. We refer to the cleaning process with the standard crushing process (which yielded smaller fragments) and one minute settling time after rapping the vials on the counter as the ‘traditional cleaning method’. For the ‘careful cleaning

method', the shells were cracked more gently such that the inside of shells were exposed while maximizing the size of shell fragments, and the amount of settling time after rapping the vials on the counter was increased from one to three minutes. The increased settling time was chosen to maximize the opportunity for small fragments to settle to the bottom of the vials before aspirating the rinse/cleaning solution.

Light microscope images were taken of bulk *P. obliquiloculata* fragments before and after cleaning and fragments were measured using image analysis techniques (Supplemental Figure 2a-c). We find that small shell fragments (< 6 μm^2) are preferentially removed during traditional cleaning (Supplemental Figure 3). The proportion of small fragments is reduced by 3% in Holocene samples during traditional cleaning, which is not significant (student's t-test, two-tailed, paired, $p = 0.07$). In deglacial samples, small fragments comprise 59% of the total calcite prior to traditional cleaning and comprise 28% after traditional cleaning steps, which is significantly different (student's t-test, two-tailed, paired, $p < 0.05$). In contrast, when careful cleaning methods are used that include longer particle settling time, there is no significant difference in the number of small fragments before and after cleaning in Holocene samples (student's t-test, two-tailed, paired, $p = 0.26$) nor in deglacial samples (student's t-test, two-tailed, paired, $p = 0.08$). For all samples that underwent careful cleaning, more small fragments are retained than with traditional cleaning methods.

SEM images of the *P. obliquiloculata* fragments were taken after cleaning, and machine learning software was trained to categorize each pixel of the image as inner calcite or outer calcite (Supplemental Figure 2d-f). Holocene samples cleaned by traditional means retain 65% inner calcite, while when cleaned with careful procedures, Holocene samples retain 71% inner calcite, although the two groups are not significantly different (student's t-test, two-tailed, paired, $p = 0.29$) (Supplemental Figure 4). Deglacial samples that underwent traditional cleaning steps retain just 25% inner calcite. In contrast, deglacial samples cleaned with careful procedures retain 70% inner calcite and are significantly different (student's t-test, two-tailed, paired, $p < 0.01$).

2.5. Discussion

Ideally, geochemical measurements in planktic foraminifera yield the primary signal incorporated during calcification and can be used to interpret sea surface conditions. Our results demonstrate that *N. dutertrei* and *P. obliquiloculata* from the EEP have high TE/Ca ratios in the inner calcite with large intra-shell TE variability (Figure 2 and 3; Table 2). Our TE/Ca measurements are higher and more variable compared to the range of values measured in surface dwelling species. These results are consistent with others that observed high and variable Ba/Ca, Mn/Ca, and Zn/Ca ratios in some deeper dwelling species compared to surface dwelling species (Eggins et al., 2003; Kunioka, 2006; Hathorne et al., 2009; Steinhardt et al., 2015; Fehrenbacher et al., 2018). In particular, the Ba/Ca ratios in our specimens are much higher than measurements in surface dwelling species, which are typically < 1 - 2 μmol/mol (Hall and Chan, 2004; Weldeab et al., 2007a,b; Sprovieri et al., 2008), and higher then values traditionally expected in planktic foraminifera (e.g., Lea and Boyle, 1991). However, few Ba/Ca, Mn/Ca, and Zn/Ca measurements have been made in deeper dwelling species and our results add to a growing collection that is needed to establish a range of expected values in foraminiferal species. High TE values — especially elevated Mg/Ca, Mn/Ca, and Ba/Ca — are traditionally attributed to non-lattice bound contaminants that should be removed before shell geochemistry can be accurately interpreted (Boyle, 1981, 1983; Boyle and Keigwin, 1985; Lea and Boyle, 1989, 1990, 1991; Haley and Klinkhammer, 2002; Gibson et al., 2016). We demonstrate that the efforts to remove shell contaminant phases with highly corrosive cleaning can also remove ontogenic calcite and lattice bound TEs.

Below, we first present the case that high TE values in our samples are lattice bound and are representative of conditions experienced by foraminifera during their ontogeny and argue against diagenesis governing the high TE values in our samples. We then describe the consequences of chemical and physical cleaning on inner calcite high in TEs and discuss implications for down core analysis. We use a simple mixing model to illustrate the consequences of overcleaning shells. Finally, we provide suggestions for

sample preparation and the careful interpretation of TE data in *N. dutertrei* and *P. obliquiloculata* and other deeper dwelling foraminifera that contain high intra-shell TEs.

2.5.1. Biogenic vs. abiotic high TE/Ca ratios

In this study, TEs are high and most variable within *N. dutertrei* and *P. obliquiloculata* inner shell calcite. High intra-shell variability is likely attributed to ontogenic incorporation of elevated TEs. Foraminifera grow by first forming relatively thinly calcified chambers during early-adult stages before thickening with additions of outer calcite and sometimes an outer gametogenic crust or cortex that covers pre-existing ontogenic chambers (Schiebel and Hemleben, 2017; Fehrenbacher et al., 2017). Laser ablation profiles sample the entire calcite wall and demonstrate clear transitions from inner calcite regions with elevated TEs and intra-shell TE variability to homogenous (and low) TE outer calcite. Our results corroborate earlier findings: high TE/Ca bands in deeper dwelling species are located within the inner part of the shell wall and may be associated with organic components linked to the early stages of shell growth (e.g., Kunioka et al., 2006; Hathorne et al, 2009), and possibly linked to early ontogenic growth in microhabitats (e.g., Fehrenbacher et al., 2018).

Aggressive cleaning procedures were established to remove contaminant phases (e.g., Lea and Boyle, 1991). Problematically, these procedures can remove primary calcite in addition to abiotic phases. For example, Lea and Boyle (1991) found high Ba/Ca ratios (up to 4.7 μmol/mol) in *N. dutertrei* shells from sediment traps that have never had contact with deep sea sediments, demonstrating the Ba in the shells was not a contaminant phase. Other researchers also clearly demonstrate elevated intra-shell Ba and Mn in the species *Globorotalia inflata*, *Globorotalia scitula* (Hathorne et al., 2009) and *Globorotalia menardii* (Davis et al., 2020). While Lea and Boyle (1991) demonstrated that highly corrosive cleaning steps significantly lowered Ba/Ca ratios in *N. dutertrei*, they were never able to decrease the TE/Ca ratios as low as the Ba/Ca ratios of surface dwelling species and postulated that these measurements reflect a primary TE source in some deeper dwelling foraminifera.

Our analyses rule out the possibility that contamination is responsible for the elevated TE/Ca ratios in our samples. In laser ablation profiles, surface contaminant phases or reabsorption of contaminants during cleaning (Elderfield and Boyle, 1986; Klinkhammer et al., 2009) typically yield a spike in Al/Ca and Mn/Ca ratios on the inside and/or outside of the laser profile and these surface contaminants are excluded during data processing (e.g., Fehrenbacher et al., 2015; Branson et al., 2019). Average Ba/Ca and Zn/Ca ratios in our study do not correlate with Al/Ca nor Mn/Ca ratios and Mn/Ca ratios do not correlate with Mg/Ca ratios in *N. dutertrei* ($R^2 < 0.05$) nor in *P. obliquiloculata* ($R^2 < 0.05$) (Supplemental Figure 5). Additionally, there is no abrupt enrichment in Mn/Ca and Mg/Ca ratios at the innermost (Pena et al., 2005, 2008; Gibson et al., 2016) or outermost (Boyle, 1981) part of the shell that would indicate Mn-Mg rich oxide coating contamination. Mg/Ca and Mn/Ca measurements in this study in both *N. dutertrei* and *P. obliquiloculata* are also far lower than those observed by Pena et al., (2005) and (2008) (Mg/Ca ratios up to 6 mmol/mol and Mn/Ca ratios up to 25 mmol/mol in *N. dutertrei*). High TE/Ca ratios intra-shell are likely not clay/contaminant infill in pore spaces because bands are consistent between laser profiles (Figure 2 and 3, solid and dashed blue lines), whereas contamination in pores would not be consistent from laser spot-to-spot. These rule out infill or metal overgrowths primarily controlling the high TE/Ca ratios observed in our shells. Finally, careful SEM observations rule out carbonate overgrowths or barite contamination governing high Ba/Ca ratios. We find no evidence of carbonate overgrowths that would appear under SEM as a layer of calcite precipitate on the shell surface, like those observed on a few EEP sediment trap (Gibson et al., 2016) and seafloor (Pena et al, 2005) foraminifera samples. The presence of barite crystals would appear under SEM as dense euhedral to subspherical crystals several microns on the longest axis, like those observed in core-top sediment from the EEP (Payten et al. 2002) and within the shells of benthic foraminifera (Bertram and Cowen, 1997). SEM images of shell surfaces and inner-pore spaces taken after the initial rinses/sonication show no evidence of barite crystals under high magnification (< 50 μm horizontal field width). This suggests that either barite crystals are not present in these samples or that they were removed with sonication in the initial rinses.

A biogenic origin of high TE inner calcite is supported by our microstructure analysis. Outer calcite appears as a smooth veneer with very fine tightly structured crystals and micropores in the case of *P. obliquiloculata* cortex (Figure 1l), or as larger blocky triangular prisms that often cover pore spaces in *N. dutertrei* crusts (Figure 1f). Outer calcite with this appearance is typically associated with a later foraminiferal life stage (Brown and Elderfield, 1996), and may be formed deeper in the water column or on the sea floor (Sautter, 1998; Fehrenbacher and Martin, 2010; Eggins et al., 2003; Sadekov et al., 2005; Jonkers et al., 2012). The nature of the inner calcite in our study is compositionally distinct from observations of manganese carbonates or Mn-Fe-oxides (see Figure 11 in Pena et al., 2005) and distinct from outer calcite cortex or crust. Inner calcite is composed of smaller and randomly oriented crystals and contains high irregular ridges between pore pits that appear in layers templated over one another in cross section (Figure 1j). Laminations with radial calcite crystals laying perpendicular to the lamination are likely formed as a thin veneer of calcite is added to the pre-existing shell during ontogeny (Erez, 2003; Panieri et al., 2017), prior to the formation of the final chamber and the addition of outer calcite and final shell thickening (Fehrenbacher et al., 2017).

2.5.2. Implications of preferential loss of high TE inner calcite during solution cleaning

We demonstrate that chemical and physical cleaning can preferentially remove inner calcite and significantly lower whole shell TE/Ca ratios. Because the inner calcite is enriched in some TEs relative to the outer calcite, the preferential loss of inner calcite has important implications for the interpretation of TE data. Here, we use a simple mixing model to demonstrate the effects of loss of high TE inner calcite. For the first model demonstration, we use mean *P. obliquiloculata* TE/Ca data obtained from the laser ablation analyses as the initial model parameters and estimate that the inner calcite represents ~ 70% of the shell wall (e.g., Steinhardt et al., 2015). The following equation is used to calculate the mean TE/Ca:

$$TE/Ca_{mean} = (f_1 * TE/Ca_{inner}) + (f_2 * TE/Ca_{outer})$$

where TE/Ca_{mean} is the mean TE/Ca value through the whole shell, TE/Ca_{inner} is the mean of high TE calcite values from the inner calcite, TE/Ca_{outer} is the mean of low TE calcite values from the outer calcite, f_1 is the proportion of high TE inner calcite, and f_2 is the proportion of low TE outer calcite. TE values used in the initial model demonstration (Ba/Ca, Mn/Ca, Zn/Ca, and Mg/Ca ratios for the inner and outer calcite) are summarized in Table 1 and shown in Figure 6a. To demonstrate the effect of inner calcite loss on mean TE/Ca values, f_1 and f_2 are scaled to simulate a decrease in inner calcite of 5%, which results in a decrease of mean Ba/Ca, Mn/Ca, and Zn/Ca ratios of 10, 4, and 6%, respectively, and a decrease in Mg/Ca ratios of 1%, which is less than 0.1 mmol/mol (Figure 6b). Conversely, a decrease in inner calcite of 25% results in a larger decrease of mean Ba/Ca, Mn/Ca, and Zn/Ca ratios (30, 18, and 30%, respectively) and a decrease in Mg/Ca ratios of just 11% or 0.3 mmol/mol (Figure 6c), and a decrease in inner calcite of 50% results in a decrease of mean Ba/Ca, Mn/Ca, and Zn/Ca ratios of 60, 37, and 60%, respectively, while average Mg/Ca ratios decrease of 22% or 0.6 mmol/mol (Figure 6d). A second demonstration illustrates the consequences of cleaning in shells with inner calcite with much higher TE/Ca ratios (50% higher, consistent with very high TE/Ca measurements made in inner calcite of *P. obliquiloculata* (e.g., Kunioka et al., 2006)). In this demonstration, a decrease in inner calcite of 5% results in a decrease of mean Ba/Ca, Mn/Ca, and Zn/Ca ratios of 8, 5, and 6%, respectively, and a loss of Mg/Ca of just 3% or 0.1 mmol/mol (Figure 6f). This decrease is modest, however, when more inner calcite is lost, consequences become severe. A decrease in inner calcite of 25% results in a decrease of mean Ba/Ca, Mn/Ca, and Zn/Ca ratios by 29, 24, and 31%, respectively (Figure 6g), and a decrease in Mg/Ca ratios of 26% or 0.7 mmol/mol, and a decrease in inner calcite of 50% results in a substantial decrease of mean Ba/Ca, Mn/Ca, and Zn/Ca ratios by 64, 47, 64%, respectively, and a loss of Mg/Ca of 52% or 1.4 mmol/mol (Figure 6h).

This conceptual model, in which mean shell values are determined by the proportion of inner and outer calcite, in part, explains the drastic reduction in mean shell TE concentrations after traditional cleaning. When inner calcite high in TE is removed, more of the low TE outer calcite contributes to the whole shell mean, significantly

decreasing the mean ratios of Ba/Ca, Mn/Ca, and Zn/Ca. Importantly, this simple mixing model also demonstrates why Mg/Ca ratios do not decrease as meaningfully as Ba/Ca, Mn/Ca, and Zn/Ca ratios, as the difference in Mg/Ca ratios between inner and outer calcite is not large enough to significantly alter mean Mg/Ca values when cleaning *P. obliquiloculata* shells. The model demonstrates that with much higher TEs in the inner calcite and substantial inner calcite loss (Figure 1g and 1h), cleaning does significantly impact mean Mg/Ca values.

The model also highlights the serious consequences of cleaning on downcore reconstructions. Traditional cleaning procedures remove a considerable portion of the inner calcite and decrease TE values significantly. However, when careful cleaning techniques are employed, less inner calcite is removed, and mean TE/Ca values are minimally impacted. Additionally, samples with very high inner calcite TE/Ca values can be highly impacted by inner calcite loss, while impacts are less important in samples with more uniform TE/Ca values. This may have implications for comparing TE reconstructions between time periods/regions that have markedly higher inner calcite TE/Ca ratios to time periods/regions with lower TE/Ca inner calcite; the relative difference is dampened by the fact that samples with higher TE/Ca are more impacted by inner calcite loss. Additionally, dissolution caused by shells residing in bottom waters/pore waters that are undersaturated with respect to calcite may have similar effects to cleaning on TE/Ca ratios and may yield preferential dissolution of the inner calcite (Johnstone et al., 2010). In samples from undersaturated waters, TE/Ca ratios may be dampened by both calcite dissolution in sediments and calcite dissolution during corrosive cleaning processes, particularly because samples that are already partly dissolved have weakened structures in inner calcite. Alternatively, in well preserved shell from cores well above the regional lysocline, dissolution and cleaning may not as severely impact shell structure nor TE/Ca ratios, as compared to shells that have been impacted by dissolution in sediments. As the calcite saturation state is variable through time in cores close to the calcite saturation horizon, the dissolution effect on inner calcite may also vary through time in such locations.

2.5.3. Suggestions for sample preparation and TE interpretation

No foraminifera cleaning technique is universally applicable, and few studies have addressed the effects of cleaning on the intra-shell variability of Ba/Ca, Mn/Ca, and Zn/Ca ratios. We show that avoiding caustic chemicals during cleaning and/or using a 'careful cleaning method' (with reduced shell cracking and increased settling times) of foraminifera shells retains more of the inner calcite high in TEs and preserves the primary TE/Ca signal incorporated during ontogeny. Furthermore, we demonstrate that elevated Ba/Ca, Mn/Ca, and Zn/Ca ratios are not always linked to diagenetic overprinting. In many cases, aggressive cleaning steps are not necessary to remove fragile inner calcite and reduce the mean TE signal. The removal of the inner calcite is particularly problematic in samples where TE/Ca ratios in inner calcite are high, which likely varies from region-region and through time.

Sample cleaning for geochemical analysis should be based on the nature of the material and the TEs of interest, and care should be taken to determine if high Ba/Ca, Mn/Ca, and Zn/Ca are the result of contaminant phases or if they were incorporated during ontogeny before selecting cleaning methods for TE analysis. For accurate downcore reconstructions, we suggest the use of high-resolution techniques such as laser ablation and/or SEM analysis that first resolve the origin of high TEs (i.e., ontogenic vs. abiotic). If metal contaminants/precipitates are observed, or the material is suspected of high TE of abiotic origin, such as material originating from redox sensitive basins (e.g. Pena et al., 2005, 2008), the use of reductive chemicals may be appropriate (Yu et al. 2007; Panieri et al., 2017; Wan et al. 2018). If remnant organic material is suspected, such as with material from recently living specimens or specimens from sediments with high organic matter content, the use of oxidative cleaning methods is recommended (e.g., Guo et al., 2019). The use of high-resolution sampling techniques (such as laser ablation depth profiling) in lieu of solution analyses could be employed for material of time slices of interest while still relying on bulk shell solution techniques for longer time-series reconstructions, considering that high-resolution techniques are costly and labor intensive. This would ensure that the contaminated portions of the shell wall are excluded (Pena et al., 2005, 2008; Koho et al., 2015; Gibson et al., 2016) without employing

corrosive cleaning steps that could remove the primary TE/Ca signal. Furthermore, downcore reconstructions that relied on solution analysis and samples cleaned using corrosive cleaning steps may be reevaluated using high-resolution sampling techniques. Such techniques may lead to reinterpretations of previously published deeper dwelling foraminifera Ba/Ca, Mn/Ca, or Zn/Ca data as well as contributions of additional deeper dwelling foraminifera TE/Ca analysis which may increase the utility of Ba/Ca, Mn/Ca, and Zn/Ca in paleo-reconstructions.

2.6. Conclusion

We demonstrated, using the high-resolution sampling technique laser ablation ICP-MS, that deeper dwelling non-spinose foraminifera *N. dutertrei* and *P. obliquiloculata* have high and variable trace elements in the inner (ontogenic) calcite. We further demonstrate that chemical and mechanical cleaning preferentially removes the inner calcite in samples prepared for both single shell laser analyses and bulk solution analyses and favors the low trace element outer (crust/cortex) calcite. The preferential removal of inner calcite biases foraminiferal trace element results toward lower values and can yield data that is problematic for downcore applications. Mn/Ca, Ba/Ca, and Zn/Ca ratios, often very high in the ontogenic calcite and low in crust/cortex calcite, are particularly susceptible to alterations during cleaning, while Mg/Ca ratios are often more homogenous and less impacted. Careful evaluation of cleaning methods, incorporating laser ablation depth profiling, increases the potential for using trace elements such as Mn, Ba, and Zn in paleoclimate reconstructions. Furthermore, downcore reconstructions that relied on samples cleaned using the corrosive cleaning steps could be reevaluated using time-slice reconstructions and laser-ablation ICP-MS analyses.

2.7. Appendix A. Summary of Individual Shell Cleaning

A1. Step 1: Rinse

- Place each individual shell or shell fragment in a microcentrifuge vial.
- Rinse 2 - 3 times with methanol, ultrasonicating* briefly (5 - 60 seconds in 5 second intervals).
- Aspirate methanol. Before aspirating, rap rack or tap vials to remove air bubbles caught in chambers.
- Rinse 3 times in ultrapure water (18 MΩ), ultrasonication* briefly (5 - 30 seconds).
- If shells appear unclean, repeat rinses above.

If clays remain, gently crack shells into larger fragments and repeat rinses without ultrasonication. Add ultrapure water 'energetically' (i.e., squirt into bottom/sides of microcentrifuge vials so ultrapure water suspends loose clay particles/fragments). Allow fragments to settle before aspirations.

A2. Step 2: Oxidative

- Prepare oxidative cleaning solution: 100 μL of 9.8 M (30%) H_2O_2 added to 30 mL of 0.1 M NaOH in fume hood.
- Add 100 μL of the solution to individual microcentrifuge vials.
- Close vials and screw rack lid down to prevent vials from opening during the heating step.
- Place sample rack in warm water bath (~65°C) for 10 minutes, flip and briefly (5 - 30 seconds) ultrasonicate* rack every 5 minutes.

- Allow samples to cool briefly (5 minutes), then rap rack to remove air bubbles caught in chambers.
- Aspirate solution, and rinse with ultrapure water 4 times (including vial caps); allow shells/fragments to settle to the bottom of the vial before aspirating water during rinses.

A2. Step 3: Reductive

Step is not recommended unless metal oxide contaminants/Mn-Mg carbonate overgrowths are suspected/observed.

- Prepare reductive solution: mix 750 μL of 31 M anhydrous hydrazine added to 10 mL of 0.25 M ammonium citrate and 10 mL of 14.6 M (30%) ammonium hydroxide in fume hood.
- Add 50 μL of solution to individual microcentrifuge vials.
- Close vials and screw rack lid down to prevent vials from opening during the heating step.
- Place sample rack in sub-boiling (~90°C) water bath for 30 minutes, flip and briefly ultrasonicate* (5 seconds) rack every 2 - 4 minutes.
- Allow to cool briefly (5 minutes), then rap rack to remove air bubbles caught in chambers.
- Aspirate solution, and rinse with ultrapure water 4 times (including vial caps); allow shells/fragments to settle to the bottom of the vial before aspirating water during rinses.

*if observe shells fragmenting, stop ultrasonication. For Step 1, stop ultrasonication, skip rest of methanol rinses and proceed to ultrapure water rinses.

2.8. Acknowledgements

MW91-9 6GGC core samples were obtained from Woods Hole Oceanographic Institute and ME0005A-43JC core samples from the Oregon State University (OSU) Marine and Geology Repository. We thank Teresa Sawyer and Peter Eschbach of the OSU Electron Microscopy Facility for their assistance with SEM imaging and Chris Russo for his assistance on OSU's Keck Collaboratory laser ablation ICP-MS. Grace Meyer assisted with sample mounting on SEM pegs. Finally, we thank Catherine Davis whose feedback improved an earlier version of this manuscript. This work was supported by NSF MG&G Award OCE-1737165. Data is available from https://doi.pangaea.de/10.1594/PANGAEA.922678.

2.9. References

Alldredge A. L. (2000). Interstitial dissolved organic carbon (DOC) concentrations within sinking marine aggregates and their potential contribution to carbon flux. *Limnology and Oceanography* 45, 1245–1253. doi.10.4319/lo.2000.45.6.1245

Alldredge A. L. and Cohen Y. (1987). Can microscale chemical patches persist in the sea – microelectrode study of marine snow, fecal pellets. *Science* 235, 689–691.

Anand, P., H. Elderfield, and M. H. Conte (2003), Calibration of Mg/Ca thermometry in planktonic foraminifera from a sediment trap time series, *Paleoceanography*, 18(2), 1050, doi.10.1029/2002PA000846.

Bahr, A., Schönfeld, J., Hoffmann, J., Voigt, S., Aurahs, R., Kucera, M., ... and Gerdes, A. (2013). Comparison of Ba/Ca and $\delta^{18}O_{WATER}$ as freshwater proxies: A multi species core-top study on planktonic foraminifera from the vicinity of the Orinoco River mouth. *Earth and Planetary Science Letters*, *383*, 45-57. doi.10.1016/j.epsl.2013.09.036

Barker, S., Greaves, M., and Elderfield, H. (2003). A study of cleaning procedures used for foraminiferal Mg/Ca paleothermometry. *Geochemistry, Geophysics, Geosystems*, *4*(9). doi.10.1029/2003GC000559

Bertram, M.A. and Cowen, J.P. (1997). Morphological and compositional evidence for biotic precipitation of marine barite. J. Mar. Res., 55, 577–593. doi.10.1357/0022240973224292

Boyle, E. A. (1981). Cadmium, zinc, copper, and barium in foraminifera tests. *Earth and Planetary Science Letters*, *53*(1), 11-35.

Boyle, E. A. (1983). Manganese Carbonate Overgrowths on Foraminifera Tests. *Geochimica Et Cosmochimica Acta* 47.10, 1815-819.

Boyle, E. A., and Keigwin, L. D. (1985). Comparison of Atlantic and Pacific paleochemical records for the last 215,000 years: Changes in deep ocean circulation and chemical inventories. *Earth and Planetary Science Letters*, *76*(1-2), 135-150.

Branson, O., Read, E., Redfern, S. A., Rau, C., and Elderfield, H. (2015). Revisiting diagenesis on the Ontong Java Plateau: Evidence for authigenic crust precipitation in *Globorotalia tumida*. *Paleoceanography*, *30*(11), 1490-1502. doi.10.1002/2014PA002759

Branson, O., Fehrenbacher, J. S., Vetter, L., Sadekov, A. Y., Eggins, S. M., and Spero, H. J. (2019). LAtools: A data analysis package for the reproducible reduction of LA-ICPMS data. *Chemical Geology*, *504*, 83-95. doi.10.1016/j.chemgeo.2018.10.029

Brown, S. J., and Elderfield, H. (1996). Variations in Mg/Ca and Sr/Ca ratios of planktonic foraminifera caused by postdepositional dissolution: Evidence of shallow Mg-dependent dissolution. *Paleoceanography*, *11*(5), 543-551. doi.10.1029/96PA01491

Bryan, S. P., and Marchitto, T. M. (2010). Testing the utility of paleonutrient proxies Cd/Ca and Zn/Ca in benthic foraminifera from thermocline waters. *Geochemistry, Geophysics, Geosystems*, *11*(1). doi.10.1029/2009GC002780

Chaisson, W. P., and Ravelo, A. C. (2000). Pliocene development of the east-west hydrographic gradient in the equatorial Pacific. *Paleoceanography*, *15*(5), 497-505. doi.10.1029/1999PA000442

Davis, C.V., Fehrenbacher, J.S., Benitez-Nelson, C.R., Thunell, R. (2020), Trace Element Heterogeneity Across Individual Planktic Foraminifera from the Modern Cariaco Basin. *Journal of Foraminiferal Research*; 50 (2): 204–218. doi.10.2113/gsjfr.50.2.204

Davis, C. V., and Benitez-Nelson, C. R. (2020). Evidence for rapid trace element alteration of planktic foraminiferal shells from the Panama Basin: Manganese adsorption during vertical transport. *Marine Micropaleontology*, 101872. doi.10.1016/j.marmicro.2020.101872

Dekens, P. S., Lea, D. W., Pak, D. K., and Spero, H. J. (2002). Core top calibration of Mg/Ca in tropical foraminifera: Refining paleotemperature estimation, *Geochemistry, Geophysics, Geosystems*, 3(4), 1–29, doi.10.1029/2001GC000200.

Dittert, N., and Henrich, R. (2000). Carbonate dissolution in the South Atlantic Ocean: evidence from ultrastructure breakdown in Globigerina bulloides. *Deep Sea Research Part I: Oceanographic Research Papers*, *47*(4), 603-620. doi.10.1016/S0967-0637(99)00069-2

Edmond, J.M., E. D. Boyle, D. Drummond, B. Grant,T. Mislick, Neth. J. Sea Res.12, 324 (1978).

Eggins, S., De Deckker, P., and Marshall, J. (2003). Mg/Ca variation in planktonic foraminifera tests: Implications for reconstructing paleoseawater temperature and habitat migration, *Earth and Planetary Science Letters*, 212(3–4), 291–306, doi.10.1016/s0012–821x(03)00283-8.

Elderfield, H., and Boyle, E. (1986). Rare earth elements in the shells of benthic foraminifera. *Eos*, *67*, 1064.

Elderfield, H., and Ganssen, G. (2000). Past temperature and $\delta^{18}O$ of surface ocean waters inferred from foraminiferal Mg/Ca ratios. *Nature*, *405*(6785), 442-445. doi.10.1038/35013033

Erez, J. (2003). The source of ions for biomineralization in foraminifera and their implications for paleoceanographic proxies. *Reviews in mineralogy and geochemistry*, *54*(1), 115-149. doi.10.2113/0540115

Evans, D., Erez, J., Oron, S., and Müller, W. (2015). Mg/Ca-temperature and seawater test chemistry relationships in the shallow-dwelling large benthic foraminifera Operculina ammonoides. *Geochimica et Cosmochimica Acta*, *148*, 325-342. doi.10.1002/2015GC005822

Farmer, E. C., Kaplan, A., de Menocal, P. B., and Lynch-Stieglitz, J. (2007). Corroborating ecological depth preferences of planktonic foraminifera in the tropical Atlantic with the stable oxygen isotope ratios of core top specimens. *Paleoceanography*, *22*(3). doi.10.1029/2006PA001361

Fehrenbacher, J. **S.** and Martin, P. A. (2010). A comparison of intrashell Mg/Ca variability of the planktonic foraminifera *G. ruber*, *G. sacculifer*, and *N. dutertrei* determined by electron microprobe image mapping, 2010 *IOP Conference Series: Earth and Environmental Science* doi.10.1088/1755-1315/9/1/012018

Fehrenbacher, J. S., Spero, H. J., Russell, A. D., Vetter, L., and Eggins, S. (2015). Optimizing LA-ICP-MS analytical procedures for elemental depth profiling of foraminifera shells. *Chemical Geology*, *407*, 2-9. doi.10.1015/j.chemgeol.2014.04.007.

Fehrenbacher, J. S., Russell, A. D., Davis, C. V., Gagnon, A. C., Spero, H. J., Cliff, J. B., ... and Martin, P. (2017). Link between light-triggered Mg-banding and chamber formation in the planktic foraminifera *Neogloboquadrina dutertrei*. *Nature communications*, *8*(1), 1-10. doi.10.1038/ncomms15441

Fehrenbacher, J. S., Russell, A. D., Davis, C. V., Spero, H. J., Chu, E., and Hönisch, B. (2018). Ba/Ca ratios in the non-spinose planktic foraminifer *Neogloboquadrina dutertrei*: Evidence for an organic aggregate microhabitat. *Geochimica et Cosmochimica Acta*, *236*, 361-372. doi.10.1016/j.gca.2018.03.008

Gibson, K. A., Thunell, R. C., Machain-Castillo, M. L., Fehrenbacher, J., Spero, H. J., Wejnert, K., ... and Tappa, E. J. (2016). Evaluating controls on planktonic foraminiferal geochemistry in the Eastern Tropical North Pacific. *Earth and Planetary Science Letters*, *452*, 90-103. doi.10.1016/j.epsl.2016.07.039

Glock, N., Eisenhauer, A., Liebetrau, V., Wiedenbeck, M., Hensen, C., and Nehrke, G. (2012). EMP and SIMS studies on Mn/Ca and Fe/Ca systematics in benthic foraminifera from the Peruvian OMZ: a contribution to the identification of

potential redox proxies and the impact of cleaning protocols. *Biogeosciences*, *9*(1), 341-359. doi:10.5194/bg-9-341-2012

Greco, M., Jonkers, L., Kretschmer, K., Bijma, J., and Kucera, M. (2019). Depth habitat of the planktonic foraminifera Neogloboquadrina pachyderma in the northern high latitudes explained by sea-ice and chlorophyll concentrations. *Biogeosciences*, *16*(17), 3425-3437. doi.10.5194/bg-16-3425-2019

Groeneveld, J., Filipsson, H. L., Austin, W. E., Darling, K., McCarthy, D., Krupinski, N. B. Q., ... and Schweizer, M. (2018). Assessing proxy signatures of temperature, salinity, and hypoxia in the Baltic Sea through foraminifera-based geochemistry and faunal assemblages. *Journal of Micropalaeontology*. doi.10.5194/jm-37-403-2018

Guo, X., Xu, B., Burnett, W. C., Yu, Z., Yang, S., Huang, X., ... and Sun, F. (2019). A potential proxy for seasonal hypoxia: LA-ICP-MS Mn/Ca ratios in benthic foraminifera from the Yangtze River Estuary. *Geochimica et Cosmochimica Acta*, *245*, 290-303. doi.10.1016/j.gca.2018.11.007

Haley, B. A., and Klinkhammer, G. P. (2002). Development of a flow-through system for cleaning and dissolving foraminiferal tests. *Chemical Geology*, *185*(1-2), 51-69. doi.10.1016/S0009-2541(01)00399-0

Hall, J. M., and Chan, L. H. (2004). Ba/Ca in *Neogloboquadrina pachyderma* as an indicator of deglacial meltwater discharge into the western Arctic Ocean, *Paleoceanography*, 19, PA1017, doi.10.1029/2003PA000910.

Hathorne, E.C., Alard, O., James, R.H., and Rogers, N.W. (2003). Determination of intra test variability of trace elements in foraminifera by laser ablation inductively coupled plasma mass spectrometry. *Geochemistry, Geophysics, Geosystems* 4 (12).

Hathorne, E. C., James, R. H., and Lampitt, R. S. (2009). Environmental versus biomineralization Controls on the intratest variation in the trace element composition of the planktonic foraminifera *G. inflata* and *G. scitula*. *Paleoceanography*, *24*(4). doi.10.1029/2009PA001742

Hoffmann, J., Bahr, A., Voigt, S., Schönfeld, J., Nürnberg, D., and Rethemeyer, J. (2014). Disentangling abrupt deglacial hydrological changes in northern South America: Insolation versus oceanic forcing. *Geology*, *42*(7), 579-582. doi.10.1130/G35562.1

Jochum, K. P., Weis, U., Stoll, B., Kuzmin, D., Yang, Q., Raczek, I., ... and Günther, D. (2011). Determination of reference values for NIST SRM 610–617 glasses following ISO guidelines. *Geostandards and Geoanalytical Research*, *35*(4), 397-429. doi.10.1111/j.1751-908X.2011.00120.x

Johnstone, H. J., Schulz, M., Barker, S., and Elderfield, H. (2010). Inside story: An X-ray computed tomography method for assessing dissolution in the tests of planktonic foraminifera. *Marine Micropaleontology*, *77*(1-2), 58-70. doi.10.1016/j.marmicro.2010.07.004

Johnstone, H. J., Lee, W., and Schulz, M. (2016). Effect of preservation state of planktonic foraminifera tests on the decrease in Mg/Ca due to reductive cleaning and on sample loss during cleaning. *Chemical Geology*, *420*, 23-36. doi.10.1016/j.chemgeo.2015.10.045

Jonkers, L., De Nooijer, L. J., Reichart, G. J., Zahn, R., and Brummer, G. J. (2012). Encrustation and trace element composition of *Neogloboquadrina dutertrei* assessed from single chamber analyses implications for paleotemperature estimates. *Biogeosciences*, *9*(11), 4851-4860. doi.10.5194/bg-9-4851-2012

Jonkers, L., Buse, B., Brummer, G. J. A., and Hall, I. R. (2016). Chamber formation leads to Mg/Ca banding in the planktonic foraminifer *Neogloboquadrina pachyderma*. *Earth and Planetary Science Letters*, *451*, 177-184. doi.10.1016/j.epsl.2016.07.030

Key, R. M., Kozyr, A., Sabine, C. L., Lee, K., Wanninkhof, R., Bullister, J. L., ... and Peng, T. H. (2004). A global ocean carbon climatology: Results from Global Data Analysis Project (GLODAP). *Global biogeochemical cycles*, *18*(4). doi:10.1029/2004GB002247

Kitano, Y., Kanamori, N., and Oomori, T. (1971). Measurements of distribution coefficients and barium between carbonate precipitate—abnormally high values of distribution measured at early stages of carbonate of strontium and solution coefficients formation. *Geochemical Journal*, *4*(4), 183-206.

Klinkhammer, G. P., Mix, A. C., and Haley, B. A. (2009). Increased dissolved terrestrial input to the coastal ocean during the last deglaciation. *Geochemistry, Geophysics, Geosystems*, *10*(3). doi.10.1029/2008GC002219

Koho, K. A., de Nooijer, L. J., and Reichart, G. J. (2015). Combining benthic foraminiferal ecology and shell Mn/Ca to deconvolve past bottom water oxygenation and paleoproduction. *Geochimica et Cosmochimica Acta*, *165*, 294-306. doi.10.1016/j.gca.2015.06.003

Kunioka, D., Shirai, K., Takahata, N., Sano, Y., Toyofuku, T., and Ujiie, Y. (2006). Microdistribution of Mg/Ca, Sr/Ca, and Ba/Ca ratios in *Pulleniatina obliquiloculata* test by using a NanoSIMS: Implication for the vital effect mechanism. *Geochemistry, Geophysics, Geosystems*, *7*(12). doi.10.1029/2006GC001280

Lea, D., and Boyle, E. (1989). Barium content of benthic foraminifera controlled by bottom-water composition. *Nature*, *338*(6218), 751-753.

Lea, D. W., and Boyle, E. A. (1990). Foraminiferal reconstruction of barium distributions in water masses of the glacial oceans. *Paleoceanography*, *5*(5), 719-742.

Lea, D. W., and Boyle, E. A. (1991). Barium in planktonic foraminifera, *Geochim. Cosmochim. Acta*, 55(11), 3321–3331.

Lea, D. W., Mashiotta, T. A., and Spero, H. J. (1999). Controls on magnesium and strontium uptake in planktonic foraminifera determined by live culturing, *Geochim. Cosmochim. Acta*, 63(16), 2369–2379, doi.10.1016/S0016–7037(99) 00197-0.

Lea, D.W. and Spero, H.J. (1994). Assessing the reliability of paleochemical tracers – barium uptake in the shells of planktonic foraminifera, *Paleoceanography*, 9, pp. 445-45

Marchitto Jr, T. M., Curry, W. B., and Oppo, D. W. (2000). Zinc concentrations in benthic foraminifera reflect seawater chemistry. *Paleoceanography*, *15*(3), 299-306. doi.10.1029/1999PA000420

Marr, J. P., Carter, L., Bostock, H. C., Bolton, A., and Smith, E. (2013). Southwest

Pacific Ocean response to a warming world: Using Mg/Ca, Zn/Ca, and Mn/Ca in foraminifera to track surface ocean water masses during the last deglaciation. *Paleoceanography*, *28*(2), 347-362.

Martin, P. A., and Lea, D. W. (2002). A simple evaluation of cleaning procedures on fossil benthic foraminiferal Mg/Ca. *Geochemistry, Geophysics, Geosystems*, *3*(10), 1-8. doi.10.1029/2001GC000280

Martinez-Ruiz, F., Jroundi, F., Paytan, A., Guerra-Tschuschke, I., del Mar Abad, M., and González Muñoz, M. T. (2018). Barium bioaccumulation by bacterial biofilms and implications for Ba cycling and use of Ba proxies. *Nature communications*, *9*(1), 1-9. doi.10.1038/s41467-018-04069-z

Monnin C., Jeandel C., Cattaldo T. and Dehairs F. (1999). The marine barite saturation state of the world's oceans. *Marine Chemistry* 65, 253–261.

Mulitza, S., Dürkoop, A., Hale, W., Wefer, G., and Stefan Niebler, H. (1997). Planktonic foraminifera as recorders of past surface-water stratification. *Geology*, *25*(4), 335-338. doi.10.1130/00917613(1997)025<0335:PFAROP>2.3.CO;2

Panieri, G., Lepland, A., Whitehouse, M. J., Wirth, R., Raanes, M. P., James, R. H., ... and Schneider, A. (2017). Diagenetic Mg-calcite overgrowths on foraminiferal tests in the vicinity of methane seeps. *Earth and Planetary Science Letters*, *458*, 203-212. doi.org/10.1016/j.epsl.2016.10.024

Paytan, A., Mearon, S., Cobb, K. and Kastner, M. (2002). Origin of marine barite deposits: Sr and S isotope characterization. *Geology*, 30, 747–750. doi.10.1130/0091-7613(2002)030<0747:OOMBDS>2.0.CO;2

Pedersen, T. F., and N. B. Price (1982). The geochemistry of manganese carbonate in Panama Basin sediments, *Geochim. Cosmochim. Acta*, 46, 69–74.

Pena, L. D., Calvo, E., Cacho, I., Eggins, S., and Pelejero, C. (2005). Identification and removal of Mn Mg rich contaminant phases on foraminiferal tests: Implications for Mg/Ca past temperature reconstructions. *Geochemistry, Geophysics, Geosystems*, *6*(9). doi.10.1029/2005GC000930

Pena, L. D., Cacho, I., Calvo, E., Pelejero, C., Eggins, S., and Sadekov, A. (2008). Characterization of contaminant phases in foraminifera carbonates by electron microprobe mapping. *Geochemistry, Geophysics, Geosystems*, *9*(7). doi.10.1029/2008GC002018

Petersen, J., Barras, C., Bézos, A., La, C., Slomp, C. P., Meysman, F. J., ... and Jorissen, F. J. (2019). Mn/Ca ratios of Ammonia tepida as a proxy for seasonal coastal hypoxia. *Chemical Geology*, *518*, 55-66. doi:10.1016/j.chemgeo.2019.04.002

Regenberg, M., Nürnberg, D., Steph, S., Groeneveld, J., Garbe-Schönberg, D., Tiedemann, R., and Dullo, W. C. (2006). Assessing the effect of dissolution on planktonic foraminiferal Mg/Ca ratios: Evidence from Caribbean core tops. *Geochemistry, Geophysics, Geosystems*, *7*(7). doi.10.1029/2005GC001019

Regenberg, M., Schröder, J. F., Jonas, A. S., Woop, C., and Gorski, L. (2013). Weight loss and elimination of planktonic foraminiferal tests in a dissolution experiment. *The Journal of Foraminiferal Research*, *43*(4), 406-414. doi.10.2113/gsjfr.43.4.406

Rosenthal, Y., Perron-Cashman, S., Lear, C. H., Bard, E., Barker, S., Billups, K., ... and

Elderfield, H. (2004). Interlaboratory comparison study of Mg/Ca and Sr/Ca measurements in planktonic foraminifera for paleoceanographic research. *Geochemistry, Geophysics, Geosystems*, *5*(4). doi.10.1029/2003GC000650

Rushdi A. I., McManus J. and Collier R. W. (2000). Marine barite and celestite saturation in seawater. Marine Chemistry 69, 19–31. doi.10.1016/S0304-4203(99)00089-4

Sadekov, A. Y., Eggins, S. M., and De Deckker, P. (2005). Characterization of Mg/Ca distributions in planktonic foraminifera species by electron microprobe mapping. *Geochemistry, Geophysics, Geosystems*, *6*(12). doi.10.1029/2005GC000973

Sadekov, A., Eggins, S. M., De Deckker, P., Ninnemann, U., Kuhnt, W., and Bassinot, F. (2009). Surface and subsurface seawater temperature reconstruction using Mg/Ca microanalysis of planktonic foraminifera *Globigerinoides ruber*, *Globigerinoides sacculifer*, and *Pulleniatina obliquiloculata*. *Paleoceanography*, *24*(3). doi.10.1029/2008PA001664

Sautter, L. R. (1998). Morphologic and stable isotopic variability within the planktic foraminiferal genus *Neogloboquadrina*. *The Journal of Foraminiferal Research*, *28*(3), 220-232.

Schiebel, R., and Hemleben, C. (2017). *Planktic foraminifers in the modern ocean* (pp. 1 -358). Berlin: Springer.

Schindelin, J.; Arganda-Carreras, I., … and Frise, E. (2012). Fiji: an open-source platform for biological image analysis, *Nature methods* 9(7): 676-682, PMID 22743772, doi.10.1038/nmeth.2019.

Schmidt, M. W., and Lynch-Stieglitz, J. (2011). Florida Straits deglacial temperature and salinity change: Implications for tropical hydrologic cycle variability during the Younger Dryas. *Paleoceanography*, *26*(4). doi.10.1029/2011PA002157

Setiawan, R. Y., Wirasatriya, A., Shaari, H. B., Setyobudi, E., and Rachman, F. (2017). Assessing the Reliability of Planktic Foraminifera Ba/Ca as a Proxy for Salinity off the Sunda Strait. *International Journal of Marine Sciences (IJMS)*, *22*(4), 201-212.

Sholkovitz, E. R. (1989). Artifacts associated with the chemical leaching of sediments for rare-earth elements. *Chemical Geology*, *77*(1), 47-51.

Skinner, L. C., Sadekov, A., Brandon, M., Greaves, M., Plancherel, Y., de La Fuente, M., ... and Scrivner, A. E. (2019). Rare Earth Elements in early-diagenetic foraminifer 'coatings': Pore-water controls and potential palaeoceanographic applications. *Geochimica et Cosmochimica Acta*, *245*, 118-132. doi.0.1016/j.gca.2018.10.027

Spero, H. J., Mielke, K. M., Kalve, E. M., Lea, D. W., and Pak, D. K. (2003). Multispecies approach to reconstructing eastern equatorial Pacific thermocline hydrography during the past 360 kyr. *Paleoceanography*, *18*(1), 1022. doi.10.1029/2002PA000814

Sprovieri, M., d'Alcalà, M. R., Manta, D. S., Bellanca, A., Neri, R., Lirer, F., ... and Sammartino, S. (2008). Ba/Ca evolution in water masses of the Mediterranean late Neogene. *Paleoceanography*, *23*(3). doi.10.1029/2007PA001469

Steinhardt, J., de Nooijer, L. L., Brummer, G. J., and Reichart, G. J. (2015). Profiling planktonic foraminiferal crust formation. *Geochemistry, Geophysics, Geosystems*, *16*(7), 2409-2430. doi.10.1002/2015GC005752

Sternberg, E., Tang, D., Ho, T. Y., Jeandel, C., and Morel, F. M. (2005). Barium uptake

and adsorption in diatoms. *Geochimica et Cosmochimica Acta*, *69*(11), 2745-2752. doi.10.1016/j.gca.2004.11.026

Stroobants N., Dehairs F., Goeyens L., Vanderheijden N. and Vangrieken R. (1991). Barite formation in the southern-ocean water column. *Marine Chemistry*. 35, 411–421.

Takagi, H., Kimoto, K., Fujiki, T., Saito, H., Schmidt, C., Kucera, M., and Moriya, K. (2019). Characterizing photosymbiosis in modern planktonic foraminifera. *Biogeosciences*, *16*(17). doi.10.5194/bg-16-3377-2019

Vetter, L., Spero, H. J., Russell, A. D. and Fehrenbacher, J. S. (2013). LA-ICP-MS depth profiling perspective on cleaning protocols for elemental analyses in planktic foraminifers. *Geochem. Geophys. Geosyst.* 14, 2916–2931. doi.10.1002/ggge.20163

von Langen, P. J., D. K. Pak, H. J. Spero, and D. W. Lea (2005). Effects of temperature on Mg/Ca in *neogloboquadrinid* shells determined by live culturing, *Geochemistry, Geophysics, Geosystems*, 6, Q10P03, doi.10.1029/2005GC 000989.

Wan, S., Feng, D., Chen, F., Zhuang, C., and Chen, D. (2018). Foraminifera from gas hydrate-bearing sediments of the northeastern South China Sea: proxy evaluation and application for methane release activity. *Journal of Asian Earth Sciences*, *168*, 125-136. doi.10.1016/j.jseaes.2018.04.036

Weldeab, S., Lea, D.W., Schneider, R. R., and Andersen, N. (2007a). 155,000 years of west African monsoon and ocean thermal evolution. Science 316, 1303–1307. doi.10.1126/science.1140461

Weldeab, S., Lea, D.W., Schneider, R.R., and Andersen, N. (2007b). Centennial scale climate instabilities in a wet early Holocene West African monsoon. Geophysical Research Letters 34, L24702. doi.10.1029/2007GL031898

Wit, J. C., Reichart, G. J., A Jung, S. J., and Kroon, D. (2010). Approaches to unravel seasonality in sea surface temperatures using paired single-specimen foraminiferal $\delta^{18}O$ and Mg/Ca analyses. *Paleoceanography*, *25*(4). doi.10.1029/2009PA001857

Yu, J., Elderfield, H., Greaves, M., and Day, J. (2007). Preferential dissolution of benthic foraminiferal calcite during laboratory reductive cleaning. *Geochemistry, Geophysics, Geosystems*, *8*(6). doi.10.1029/2006GC001571

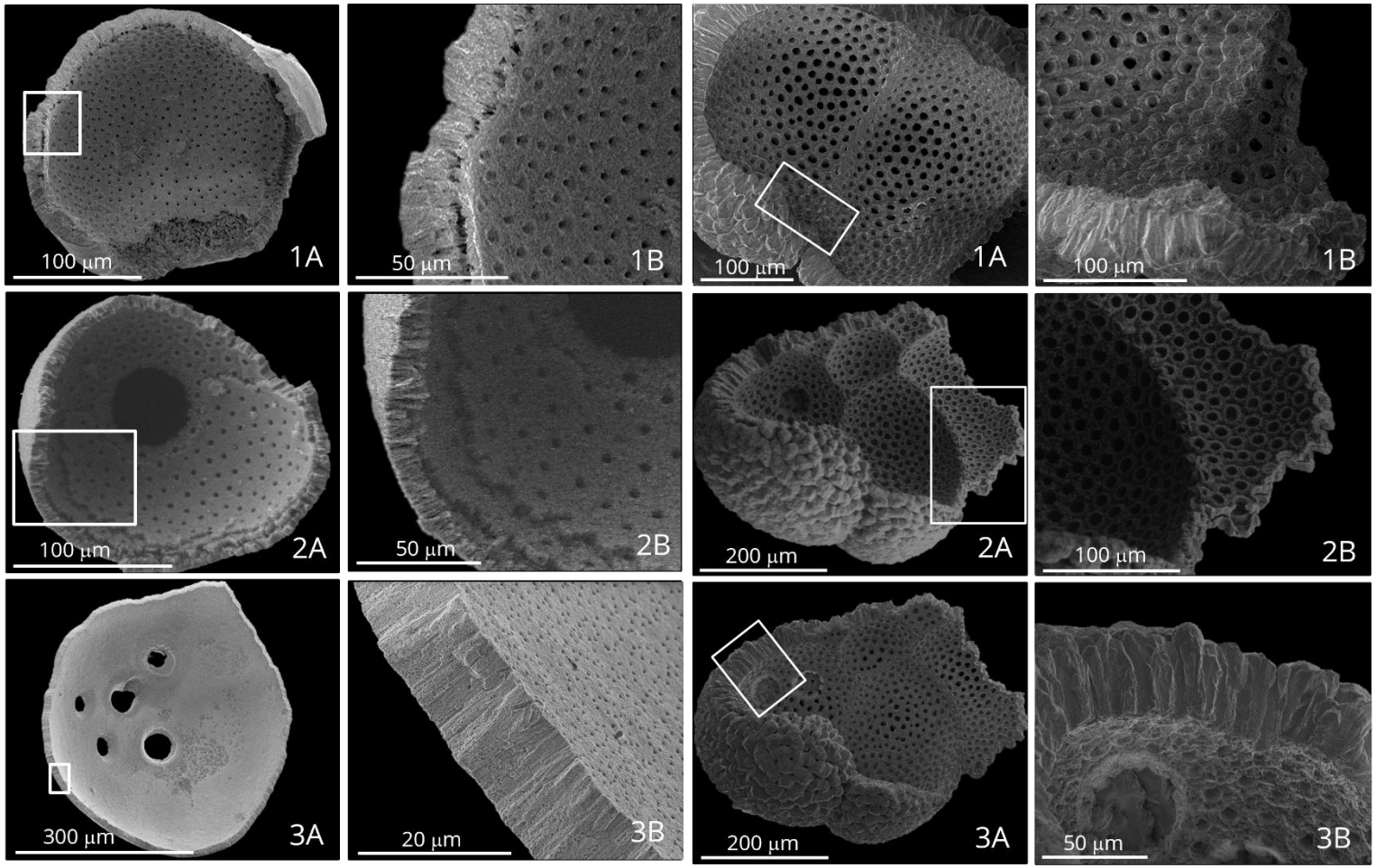

Figure 2.1. Scanning electron micrograph (SEM) images of examples of N. dutertrei (a-f) and P. obliquiloculata (g-l) shells that show progressive dissolution from initial rinses (a and g), to oxidative and reductive cleaning (c and i), and DTPA cleaning (e and k). White boxes show the area that is magnified in the corresponding panel.

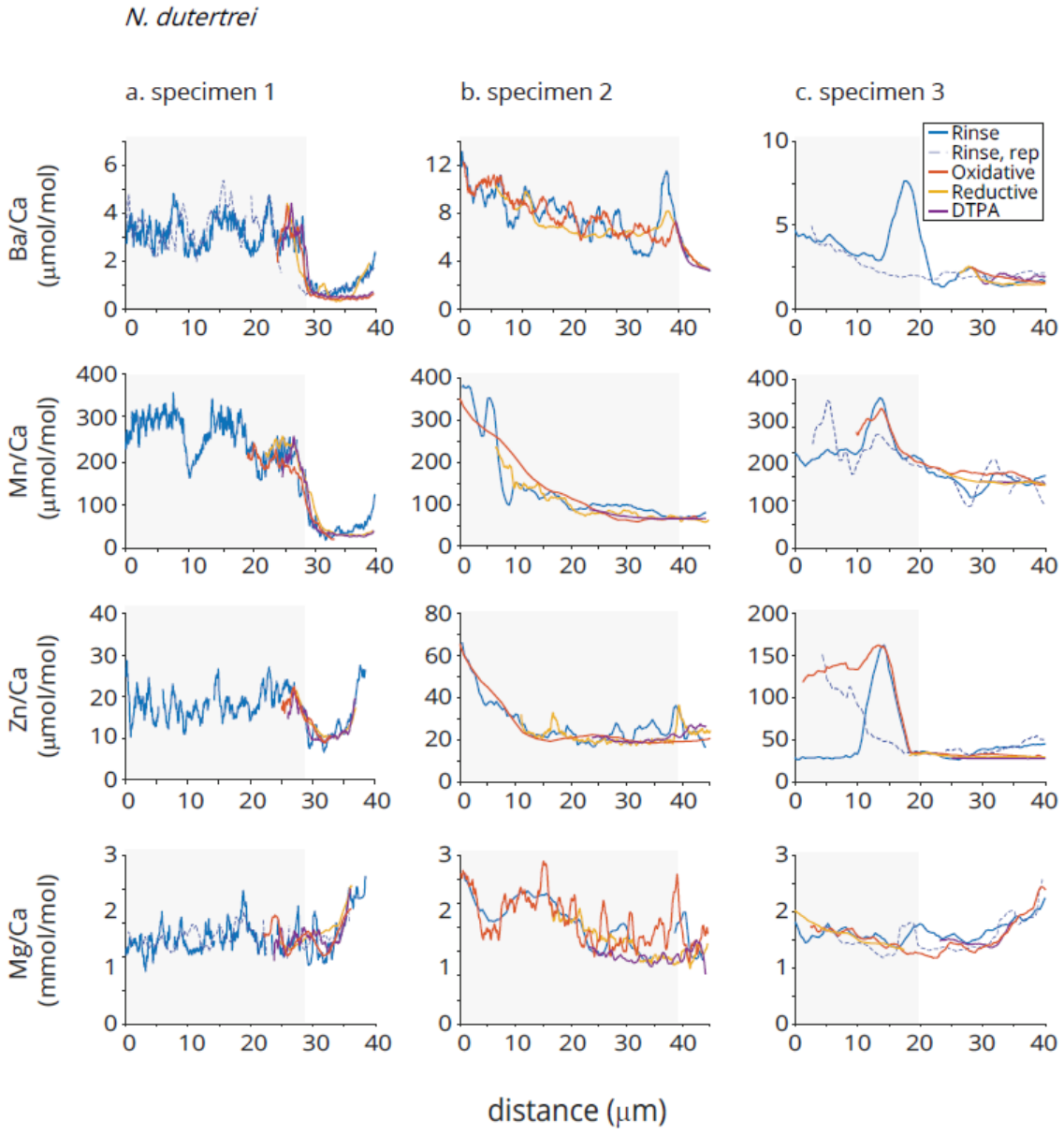

Figure 2.2. Laser ablation Ba/Ca, Mn/Ca, Zn/Ca, and Mg/Ca (µmol/mol, µmol/mol, µmol/mol, and mmol/mol, respectively) profiles of three example N. dutertrei specimens (a-c) subject to initial rinses/sonication (blue line, repeat analysis performed on some shells is shown as blue dashed line), oxidative cleaning (orange line), reductive cleaning (yellow line), and a DTPA+acid leach (purple line). High trace

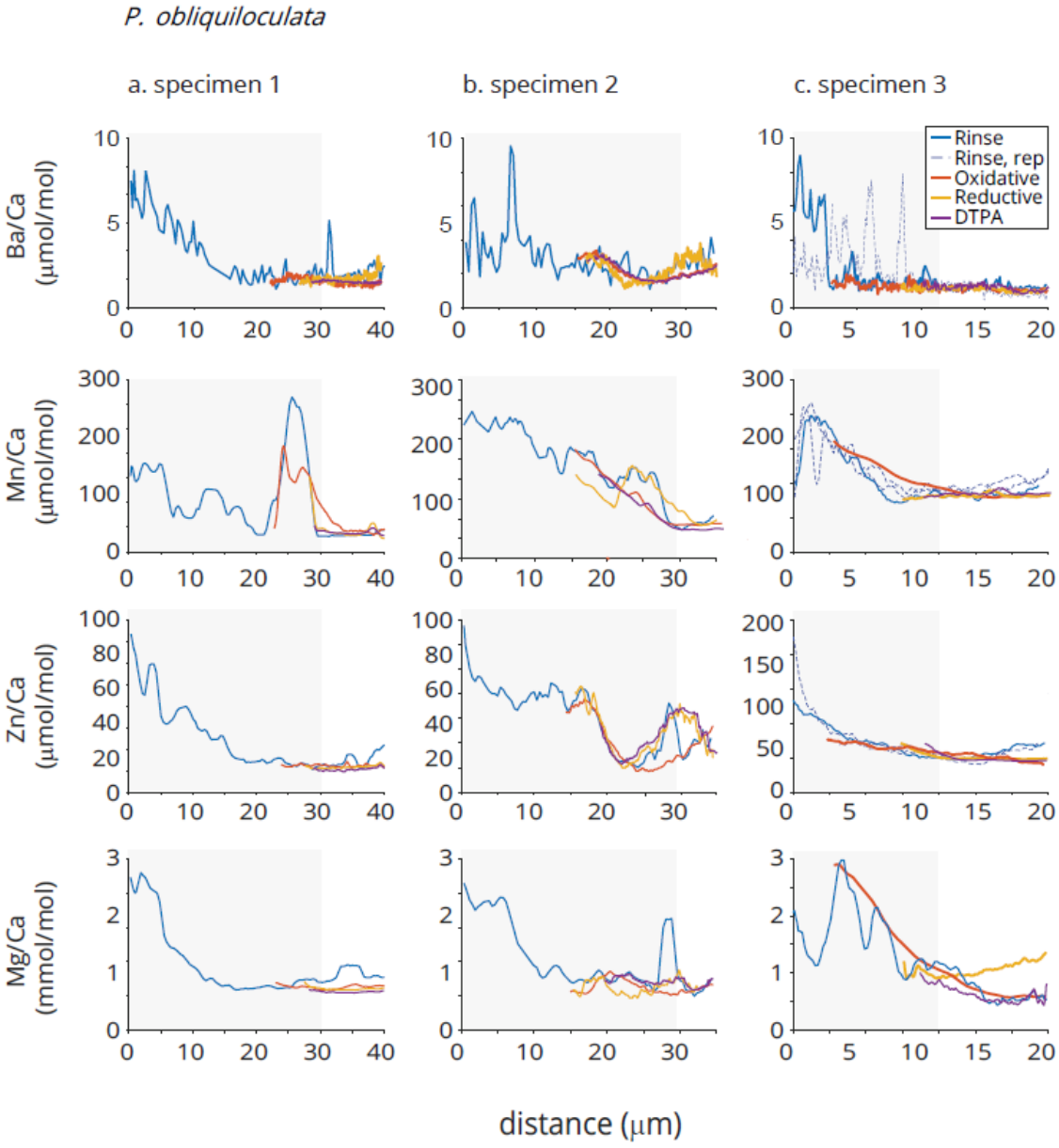

Figure 2.3. Figure is the same as Figure 2, but with three example *P. obliquiloculata* samples.

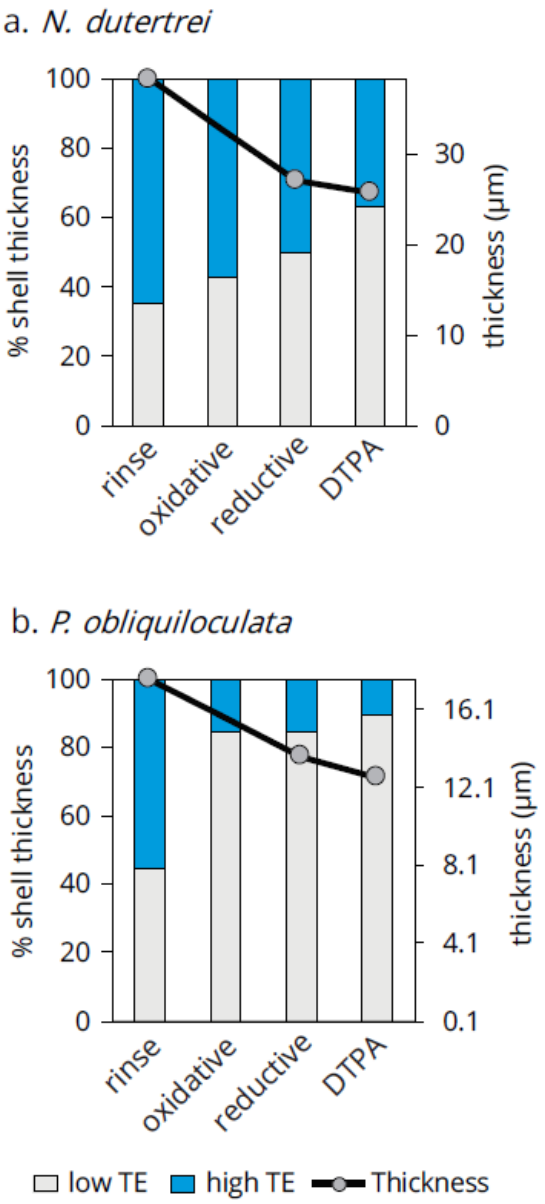

Figure 2.4. Shell thickness (µm; grey circles) and proportion of the shell thickness composed of low TE outer calcite (gray bar) and high TE inner calcite (blue bar) after initial rinses (rinse), oxidative, reductive, and DTPA cleaning for *N. dutertrei* (a) and *P. obliquiloculata* (b) material.

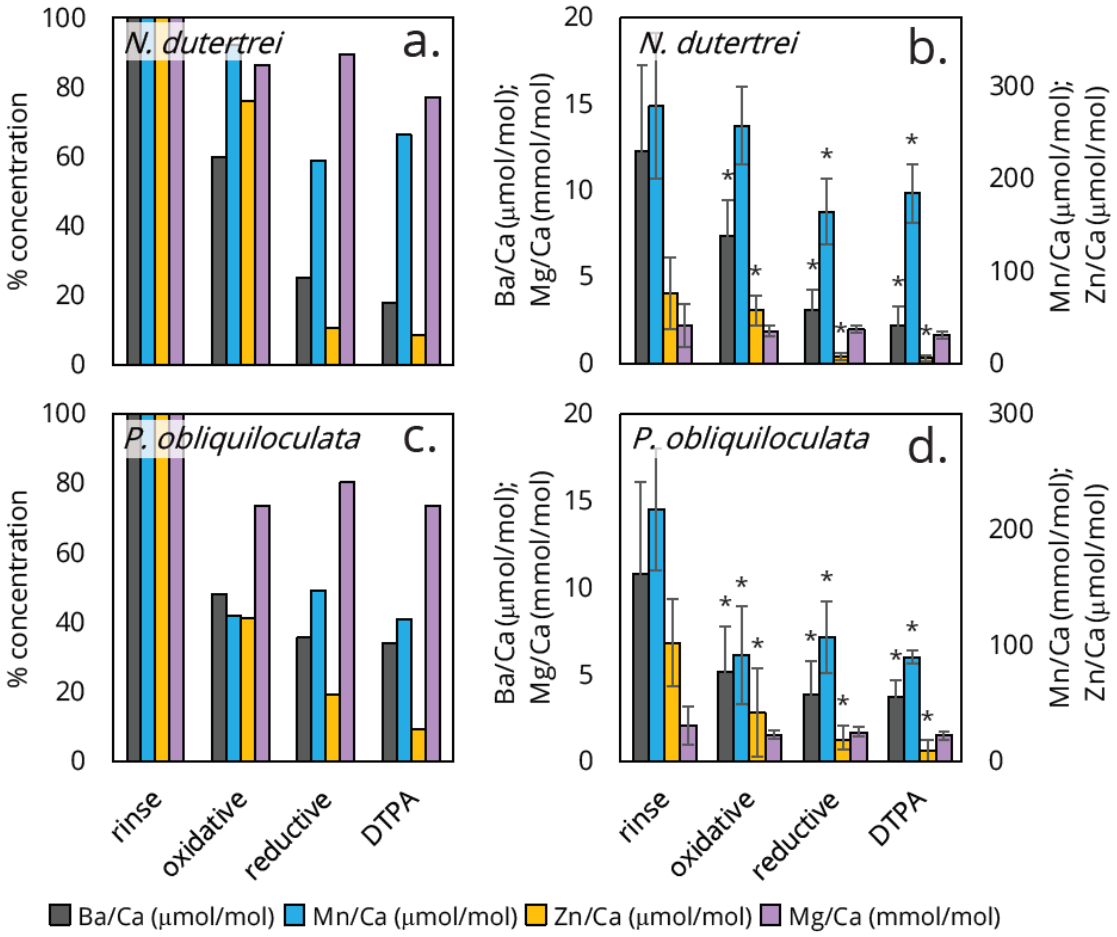

Figure 2.5. Laser ablation mean percent concentration of Ba/Ca (µmol/mol; grey bar), Mn/Ca (µmol/mol; blue bar), Zn/Ca (yellow bar; µmol/mol), and Mg/Ca (purple bar; mmol/mol) in *N. dutertrei* (a and b) and *P. obliquiloculata* (c and d) shell material after initial rinses (rinse), oxidative, reductive, and DTPA cleaning. Values are scaled to rinse measurements (a and c) and reported as mean and std dev (1σ) (b and d). Star indicates a statistically significance difference from initial rinse values (student's t-test, two-tailed).

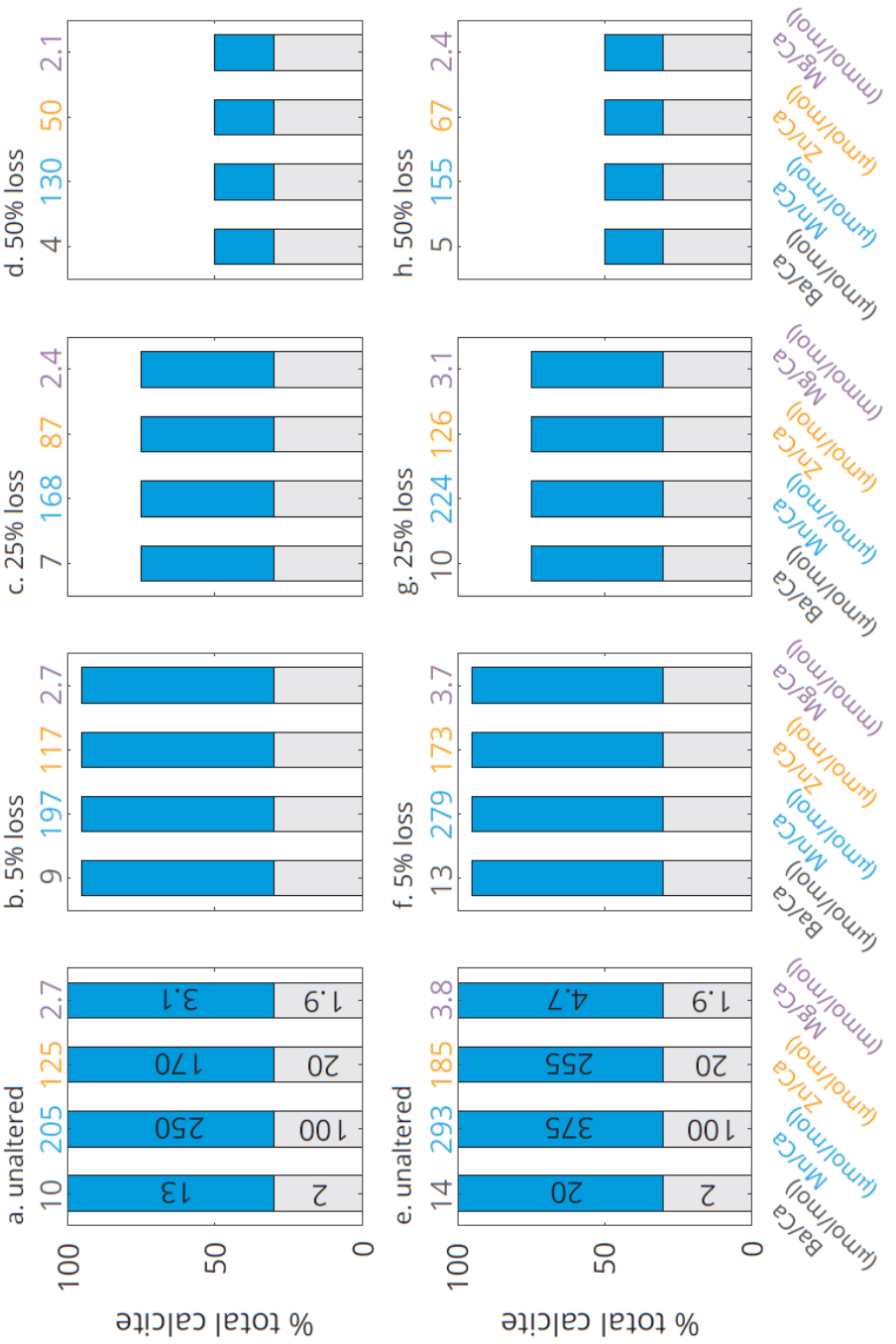

Figure 2.6. Simple mixing model results showing changing values when high TE inner calcite (a-d; inner and outer calcite Ba/Ca, Mn/Ca, Zn/Ca, and Mg/Ca concentrations in μmol/mol, μmol/mol, μmol/mol, and mmol/mol, respectively, overlay bar graph and calculated mean values are above each bar) is preferentially removed by 5% (b), 25% (c), and 50% (d) and higher TE inner calcite (e-h) is preferentially removed by 5% (f), 25% (g), and 50% (h).

Table 2.1 - Definition of inner vs. outer calcite after the definition of Brown and Elderfield (1996)

Inner calcite	Defines all chambers inside the shell as well as calcite of the inner part of the exterior shell wall.
Outer calcite	The outer part of the exterior shell wall that covers inner calcite layers. In the case of *N. dutertrei* and *P. obliquiloculata* species in this study, the outer calcite includes the crust/cortex calcite.
Cortex calcite	The smooth microperforate veneer that covers *P. obliquiloculata* inner calcite.
Crust calcite	Calcite layer that forms over inner calcite comprised of large blocky prismatic crystals that often cover inner calcite pore spaces.

Table 2.2. Mean and standard deviation (std dev, 1σ) through individual shells of all individual shells before chemical cleaning.

Species	Measurement	Ba/Ca (μmol/mol)		Mn/Ca (μmol/mol)		Zn/Ca (μmol/mol)		Mg/Ca (mmol/mol)	
		mean	std dev	mean	std dev	mean	std dev	mean	std dev
N. dutertrei	Whole shell	12.3	10.0	279.9	158.5	76.1	76.6	2.2	2.5
	High TE calcite	23.4	62.1	295.0	390.1	160.6	277.0	2.6	2.6
	Low TE calcite	1.6	0.8	102.2	54.2	39.9	41.8	1.7	0.5
P. obliquiloculata	Whole shell	10.7	10.6	218.0	105.3	102.7	73.9	2.1	2.1
	High TE calcite	13.0	37.1	250.0	386.5	168.0	91.3	2.1	2.1
	Low TE calcite	2.0	1.1	103.8	39.8	18.6	54.0	1.9	0.4

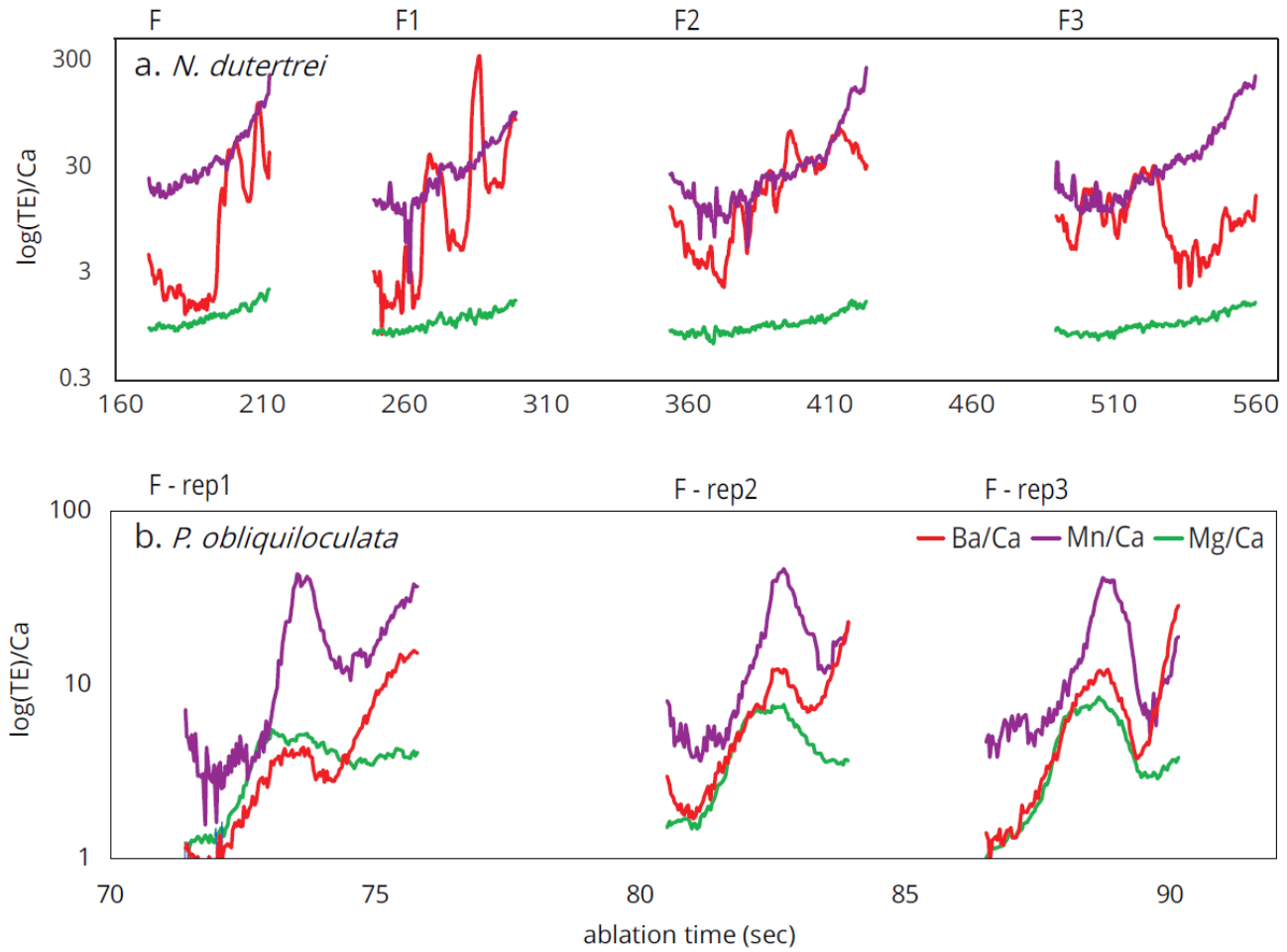

Figure S2.1. Representative laser ablation depth profile data exemplifying high trace element variability from a single *N. dutertrei* (a) that is reproducible between F, F1, F2, and F3 chamber and a single *P. obliquiloculata* (b) that is reproducible between repeat analysis F-rep1-3. Ba/Ca, Mn/Ca, Mg/Ca (mmol/mol, mmol/mol, mmol/mol, respectively) are plotted on a log scale vs. ablation time (sec).

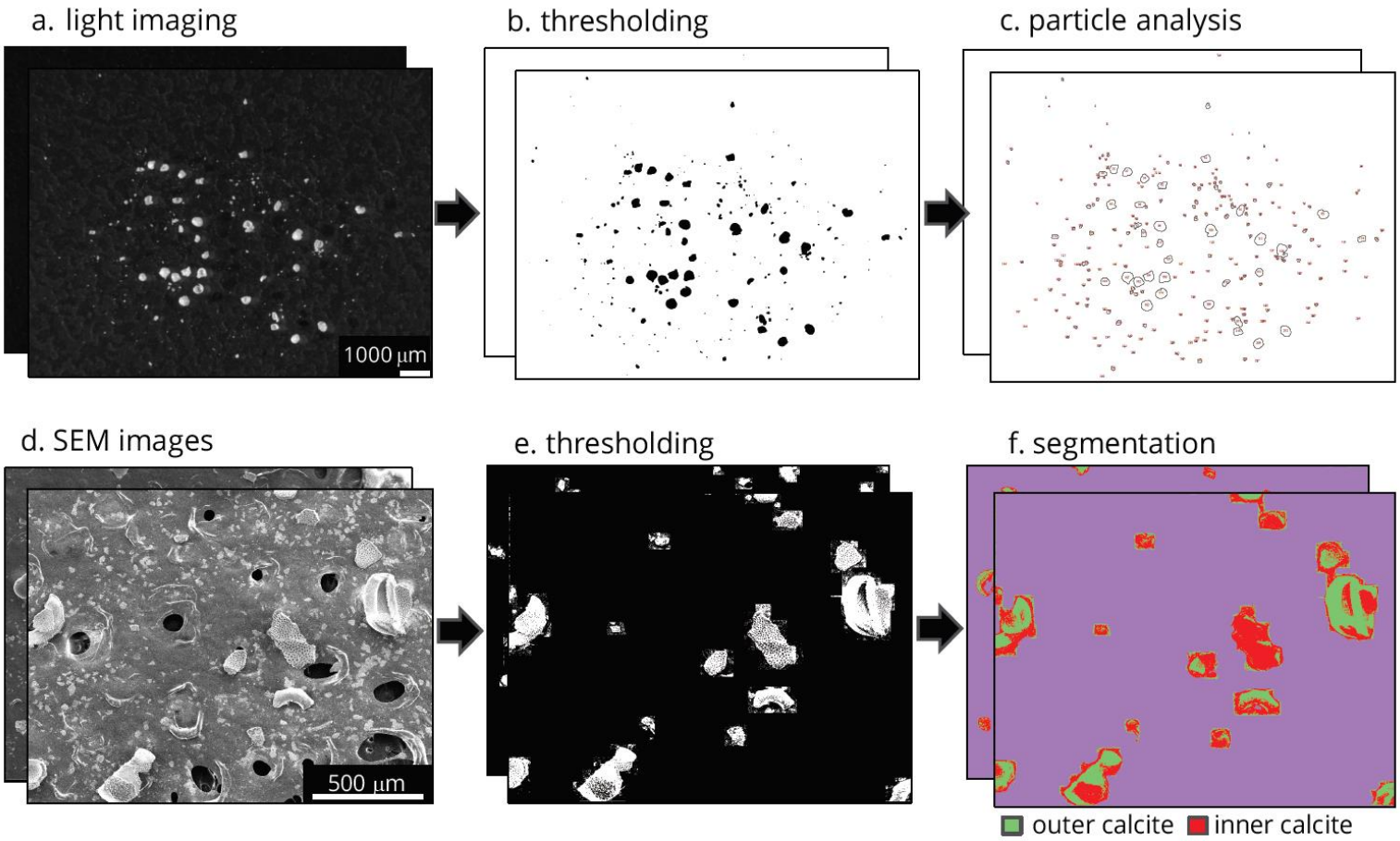

Figure S2.2. Scheme of image analysis procedure on light microscope images (a-c) processed to threshold background/object (b) and measure size and number of particles (c), and scanning electron micrograph images (d-f) processed to threshold background/object (e) and segmented to classify outer calcite/cortex (green) and inner calcite (red) using machine learning algorithms.

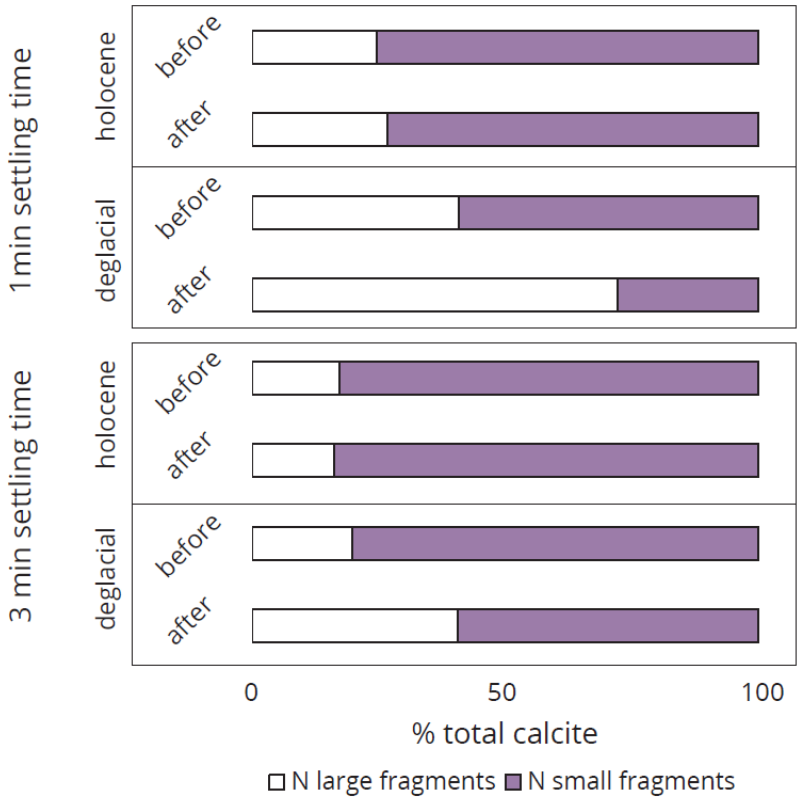

Figure S2.3. The number (N) of small (< 6 μm^2; purple bar) and large (> 6 μm^2; white bar) P. obliquiloculata fragments counted before and after preparation for bulk shell solution analysis with short ('1 min settling time') and long settling time ('3 min settling time') in Holocene (8-10 cm) and deglacial (26-28 cm) intervals of core MW91-9-6GGC.

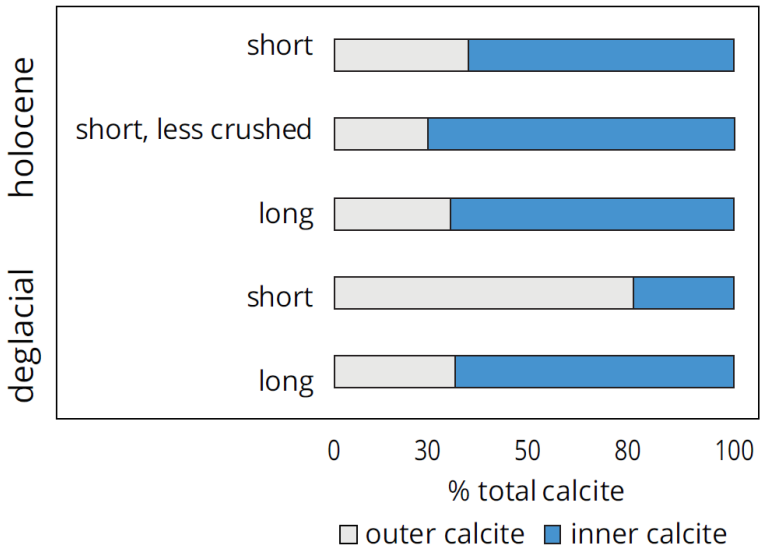

Figure S2.4. The proportion of total calcite in samples of *P. obliquiloculata* fragments classified as inner (blue bar) and outer (grey bar) calcite. Samples are analyzed after preparation for bulk solution analysis with short (one min) settling time (short), short settling time with less crushing of fragments (short, less crushed), and with long (three min) settling time (long).

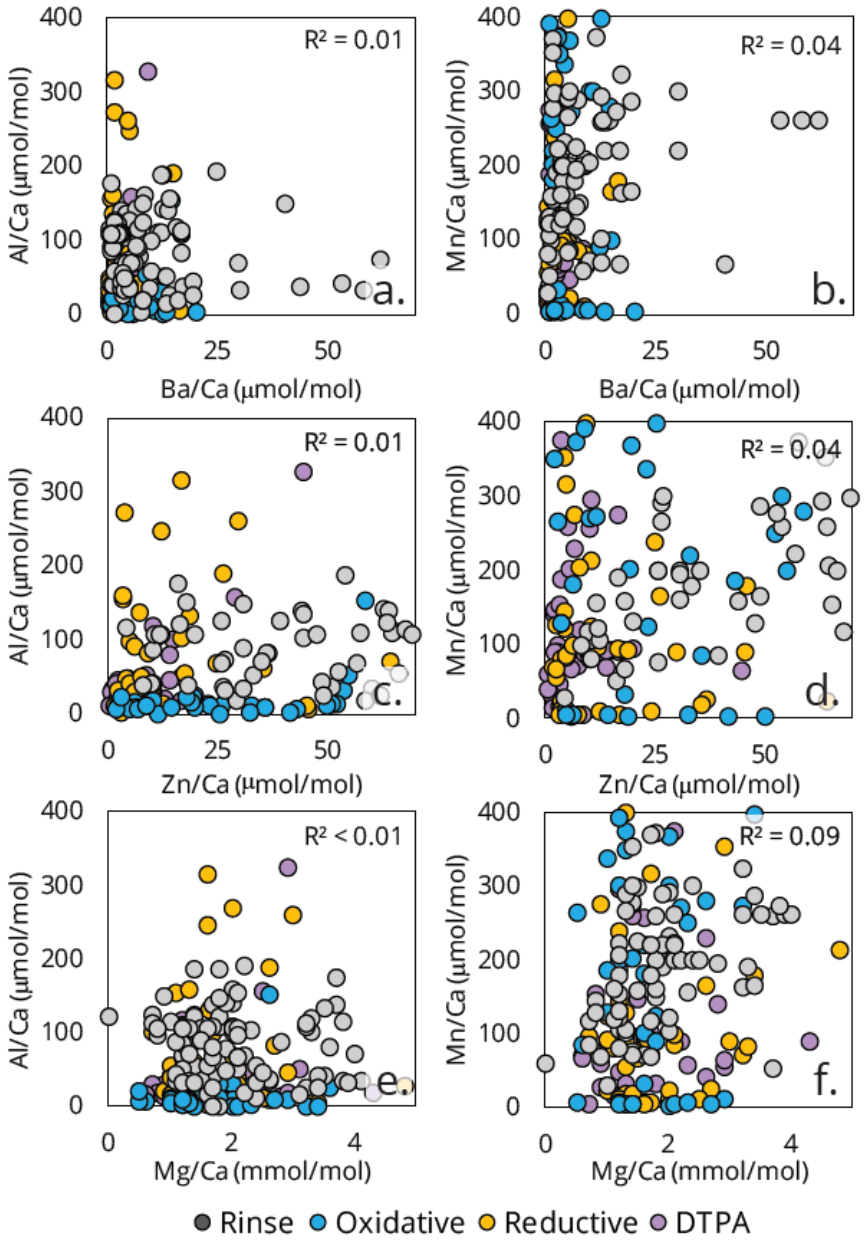

Figure S2.5. Regression between average shell Ba/Ca, Mn/Ca, Mg/Ca, and Al/Ca (mmol/mol, mmol/mol, mmol/mol, and mmol/mol, respectively) values measured via laser ablation ICP-MS after each cleaning step: initial rinses/sonication (grey circles), oxidation (blue circles), reductive (yellow circles), and DTPA (purple circles) cleaning. Coefficient of determination (R^2) value shown in top right corner of each panel.

Increased production in the equatorial Pacific during the deglaciation inferred from the Ba/Ca ratios of non-spinose planktic foraminifera

Theresa Fritz-Endres[1]; Jennifer Fehrenbacher[1], Ann Russell[2], Haley Cynar[1]

[1]Oregon State University, College of Earth, Ocean, and Atmospheric Sciences, Corvallis, OR 97330; [2]University of California, Davis, Department of Earth and Planetary Sciences, Davis, CA 95616

Submitted to: *Paleoceanograpy and Paleoclimatology*

3. Increased production in the equatorial Pacific during the deglaciation inferred from the Ba/Ca ratios of non-spinose planktic foraminifera

3.1. Abstract

The production and export of organic matter to deep ocean sediments is a critical driver in modulating glacial-interglacial carbon cycles. Yet, it remains unsettled whether production has increased or decreased over glacial-interglacial transitions, in part because common production proxies may be complicated by sediment re-deposition and diagenetic alterations.

We explore using non-spinose foraminifera Ba/Ca ratios as a proxy for surface ocean production. We analyze Ba/Ca ratios since the Last Glacial Maximum in three planktic foraminifera species sampled from cores that span a production gradient along the equatorial Pacific. Ba/Ca ratios are low and invariable in the spinose species *Trilobatus sacculifer*. In contrast, Ba/Ca ratios are higher and more variable in the non-spinose species *Neogloboquadrina dutertrei* and *Pulleniatina obliquiloculata*. Ba/Ca enrichment in non-spinose species is hypothesized to be linked to the degradation of organic matter within the species' particulate microhabitat and reflects surface ocean particulate organic matter production at the time of shell calcification (Fehrenbacher et al., 2018). We demonstrate that Ba/Ca ratios in core-top and sediment trap derived non-spinose foraminifera correlate with organic matter production. We generate downcore Ba/Ca results in the western and eastern equatorial Pacific and observe an increase in Ba/Ca ratios during the deglaciation. We suggest this may be linked to an increase in production, as observed in several other regional paleo-production records. The 16 - 17 ka BP peak in Ba/Ca is evident even in specimens obtained from a deep ocean core and from regions that experience sediment focusing, suggesting the Ba/Ca proxy may be useful in regions where samples are poorly preserved or complicated by sediment re-deposition.

Plain Language Summary

The production of organic matter in the surface ocean ('production') sequesters carbon from the atmosphere and transports and stores some of this carbon to the deep ocean for 1,000s of years. How much carbon is produced in the surface ocean as Earth's climate emerges from cold (glacial) time periods remains uncertain. One reason for this uncertainty is that production proxies derived from ocean sediments are often partially dissolved, or transported from their origin as they fall through the water column and settle on the seafloor. A promising new proxy is the barium content in the shells of non-spinose planktic foraminifera. Foraminifera are marine plankton that incorporate trace elements of the surface ocean within their shells and retain them as shells are deposited on the seafloor. The amount of barium bound within the shells of non-spinose planktic foraminifera species is linked to production because these species may build their shells within marine particles which contain high organic matter and high barium. It is hypothesized that when production is high in the surface ocean, non-spinose foraminifera Ba/Ca ratios will also be high and more variable from specimen to specimen, compared to low production regions/time periods. We measure barium in non-spinose species' shells from deep ocean sediment cores underneath low production and high production regions in the Pacific Ocean and find that shell-bound barium is closely correlated to surface ocean production. We use this relationship to reconstruct production since the Last Glacial Maximum, ~ 25,000 years ago, and find that the shell-bound barium significantly increased during the deglaciation, ~ 17,000 years ago. This suggests that the deglacial time period experienced higher surface ocean production in response to a changing climate. Reconstructing ocean production during climate transitions has implications for understanding the link between ocean-atmosphere carbon exchange and climate change.

3.2. Introduction

Records of export production from the surface ocean link primary production to burial and provide critical information about the strength of the biological pump and its relationship to carbon storage over climate transitions (see Sigman and Boyle,

2000 and references therein). However, changes in production over glacial-deglacial transitions are not yet well constrained (Loubere, 1999; Carter et al., 2020). Previous studies in the equatorial Pacific have alternately stated that production was greater during glacial periods (Pedersen, 1983; Lyle et al., 1988; Sarnthein et al., 1988; Pedersen et al., 1991; Herguera and Berger, 1991, 1994; Perks et al., 2002) or greater during interglacial periods (Pichat et al., 2004; Bradtmiller et al., 2006; Richaud et al., 2007; Costa et al., 2016). Other studies suggest a production maximum occurred during the deglaciation in response to a changing global climate that may have altered nutrient concentrations in upwelling waters in the equatorial Pacific (Loubere, 2001; Schwarz et al., 1996; Bradtmiller et al., 2006; Martínez et al., 2006; Kienast et al., 2007; Anderson et al., 2009; Zhang, 2007; Pichevin et al., 2009; Hayes et al., 2011; Rafter and Charles, 2012; Dubois et al., 2011; Costa et al., 2017).

Information about paleo-production is primarily derived from flux proxies that reconstruct the accumulation rate of biogenic materials in sediments (e.g., opal, excess Ba (Ba_{xs}), organic C fluxes), or nutrient proxies that record information about the nutrient content of the surface ocean that drives production (e.g., $\delta^{13}C$ and $\delta^{15}N$) (reviewed in Berger et al., 1994). Reconstructions disagree, in part, because different proxies record fundamentally different aspects of production, and all contain their assumptions. Additionally, nearly all production proxies are subject to alteration in the water column and on the seafloor. Therefore, they are linked to multiple counteracting processes such as export production and preservation in deep waters. For example, arguments for lower deglacial production in the equatorial Pacific have mainly focused on flux proxies (Pedersen, 1983; Pedersen et al., 1991; Lyle et al., 1988; Sarnthein et al., 1988; Payten et al., 1996); however, accumulation rates may be altered by dissolution in bottom waters and pore waters (e.g., Nelson et al., 1995; Lyle et al., 1992) and influenced by sediment re-distribution by bottom currents (re-deposition; Cochran and Osmond, 1976; Frank et al., 1999; Marcantonio et al., 2001; Loubere et al., 2004). Thus, accumulation rates may be sensitive to sediment focusing/winnowing that change over climate cycles and impact glacial-interglacial interpretations (Patterson and Farley, 1998; Higgins et al., 2002). Early work

suggested that an accumulation event in the eastern equatorial Pacific (EEP) during the Last Glacial Maximum (LGM) reflects an increase in surface ocean production (Pedersen, 1983; Lyle et al., 1988; Pedersen et al., 1991; Paytan et al., 1996; Lyle et al., 2005). However, constant flux proxies that correct for lateral sediment re-deposition have since been used to reassess these early studies (e.g., excess thorium-230 ($^{230}Th_{xs}$); Kienast et al., 2007; Winckler et al., 2016), and some have reevaluated the LGM accumulation event in the EEP as re-deposition rather than due to an increase in production (Loubere, 1999, 2001; Loubere et al., 2003, 2004; Francois et al., 2004; Pichat et al., 2004).

Foraminiferal proxies may offer an advantage over flux proxies because they are generally less prone to re-deposition than finer-grained material. Additionally, the geochemical signals in foraminifera shells are independent of mass accumulation rates. Foraminifera shells are also advantageous because individual foraminifera can be carefully assessed for signs of dissolution. Foraminifera are generally well preserved in sediments above the lysocline (Berger, 1979; Kucera, 2009), and some species (*Pulleniatina obliquiloculata* and *Neogloboquadrina dutertrei*) are preserved even when collected from sediment cores below the lysocline, making them available for paleo-reconstructions where other paleo-production proxies are poorly preserved (Berger, 1979). However, partial dissolution may impact shell-bound geochemical signals (Rosenthal and Lohmann, 2002; Rosenthal et al., 2004; Regenberg et al., 2006). For example, dissolution/preservation effects in the Ontong Java Plateau (OJP) have been shown to increase foraminiferal $\delta^{18}O$ and bias Mg/Ca temperature reconstructions to lower values (Berger et al. 1982; Brown et al., 1996; Dekens et al., 2002; Marchitto et al., 2005; Bonneau et al., 1980; Killingley et al., 1981; Wu and Berger, 1989; Wu et al., 1991; McCorkle and Keigwin, 1994; Zhang et al., 2007). Dissolution on the seafloor and in laboratory experiments resulted in ~ 15% preferential shell Mg loss (Regenberg et al., 2006; Rosenthal et al., 2004) and decreased Ba/Ca ratios (Lea and Boyle, 1991; Martin and Lea, 2002; Yu et al., 2007; Vetter et al., 2013; Fritz-Endres and Fehrenbacher, 2020). Individual shells in deep cores below the regional lysocline should be carefully assessed for signs of

dissolution, especially when using material derived from corrosive waters of the deep equatorial Pacific where changes in calcite preservation over climate transitions are dramatic (Murray et al., 2000).

This study explores the utility of Ba/Ca ratios in non-spinose foraminifera as a proxy for paleo-production. Laboratory studies with spinose species, including *Orbulina universa*, *Trilobatus sacculifer*, and *Globigerina bulloides*, show that Ba is incorporated into the shell calcite as a function of [Ba] of the seawater in which they calcified (Lea and Spero, 1994; Hönisch et al., 2011). Laboratory studies also confirm that shell Ba/Ca ratios are unaffected by temperature, pH, or algal symbiosis. In nearshore environments, Ba/Ca ratios may reflect changes in freshwater flux and salinity because of relatively high riverine [Ba] (Edmond et al., 1978; Bahr et al., 2013; Weldeab et al., 2007a,b; 2014; Evans et al., 2015; Gebregiorgis et al., 2016; Setiawan et al., 2017). Laboratory culture studies with the non-spinose foraminifera *Neogloboquadrina dutertrei* show the incorporation of Ba/Ca in this species also varies with bulk filtered seawater [Ba] (Fehrenbacher et al., 2018). However, Ba/Ca ratios in *N. dutertrei* and many other non-spinose foraminifera obtained from the open-ocean setting are higher and more variable than in spinose foraminifera (Lea and Boyle, 1991; Hall and Chan, 2004; Hathorne et al., 2009; Kunioka, 2006; Bahr et al., 2013), and higher than can be attributed to bulk seawater [Ba] alone. The elevated Ba/Ca ratios in the non-spinose foraminifera is hypothesized to reflect calcification within a microenvironment (Fehrenbacher et al., 2018), such as marine snow or other organic detritus in the water column (herein referred to as particulate organic matter (POM)) and reflect a Ba-enriched microhabitat (Dehairs et al., 1980; Stroobants et al., 1991; Gonzalez-Munoz et al., 2012). Ba/Ca ratios in the fossil shells of some non-spinose species offer the potential to reflect organic matter content within particulate aggregates. Ba/Ca data from sediment traps in the Pacific support this hypothesis. Mean Ba/Ca ratios in *P. obliquiloculata* from sediment traps from 5°S to 9°N along a 140°W JGOFS transect reflect zonal patterns of export production (Figure 1a). Intra-shell and population Ba/Ca mean and variability is greatest in sediment traps underlying high surface production, and Ba/Ca ratios at latitudes of high export are

significantly higher than Ba/Ca ratios at latitudes of low export ($p << 0.01$; Cynar, senior thesis, 2016). Individual foraminifera analysis (IFA) and bulk shell (solution) analysis mean Ba/Ca ratios in *N. dutertrei* and *P. obliquiloculata* are higher in core-tops beneath regions of high surface production (Figure 1b), and Ba/Ca ratios in the core-top and sediment trap derived foraminifera correlate with export production (Figure 1c). Ba/Ca ratios in non-spinose foraminifera likely record an increase/decrease in POM in the surface ocean and offer the opportunity to reconstruct production, perhaps more directly than flux proxies that record only the proportion of organic matter delivered to the seafloor.

We measure Ba/Ca ratios in *N. dutertrei* and *P. obliquiloculata* from cores from the western equatorial Pacific (WEP) and the EEP that span a production gradient (Figure 2a and b). We assess intra-shell and population variability at key time intervals (Holocene, deglaciation, and LGM) using laser ablation-based IFA. We also develop a continuous downcore record (~ 1 kyr resolution) from the core-top through the LGM using bulk shell analysis. We hypothesize that during periods of higher surface ocean production, Ba/Ca ratios of non-spinose foraminifera would be higher and more variable both intra-shell and among a population of specimens. In contrast, intra-shell Ba/Ca ratios of non-spinose foraminifera would be low during periods of low production, and population variability would decrease. Ba/Ca ratios of the spinose species *T. sacculifer* are used as a 'control,' as there is no evidence this species lives in association with POM, and this species should have low Ba/Ca values that reflect the [Ba] of bulk seawater. Foraminiferal Ba/Ca records are evaluated alongside established proxies for paleo-production and assessed in the context of hydrographic changes since the LGM. In addition, we evaluate the effect of dissolution by comparing data from cores on the OJP that span a calcite saturation gradient of ~ +14 to -20 μmol/kg (Figure 1c). We assess the impact of sediment re-deposition by comparing data from cores in the EEP located on a topographic high (atop the Cocos Ridge) and a topographic low (within the Panama Basin).

3.3. Methods

3.3.1. Sample location and oceanographic setting

Sediment samples were obtained from WEP cores MW91-9-6GGC (2.02ºS, 156.93ºE, water depth 1.6 km) and MW91-9-55GGC (0.01ºS, 161.77ºE, water depth 4.0 km), and EEP cores ME0005A-43JC (43JC; 7.86ºN, 83.6ºW, water depth 1.4 km) and ME0005A-24JC (0.01ºN, 86.3ºW, water depth 2.9 km). All cores are well above the regional lysocline (~ 3 km water depth; Global Ocean Data Analysis Project (GLODAP) data set, Key et al., 2004), except core 55GGC, which is ~ 1 km below the regional lysocline (Figure 2c). Cores are located along the path of the equatorial undercurrent (EUC) (Figure 2a). The EUC flows within the equatorial thermocline, shoaling from west to east, and is the source of nutrients upwelled along the equator. Nutrient delivery and production are relatively low in the WEP, while cores from the EEP underlay a region of higher surface ocean production (Table 1). EEP core 24JC is situated in the highly productive eastern equatorial cold tongue. Production in the cold tongue is driven by nutrients supplied by deep waters from the sub-Antarctic, brought to the surface by equatorial and coastal upwelling (Pennington et al., 2006). EEP core 43JC is located further north in the more stratified eastern Pacific warm pool and experiences slightly lower production than core 24JC.

3.3.2. Bulk shell analysis

3.3.2.1. Sample preparation for trace element and isotope analysis

Sediment samples were washed with DI water over a 63 μm sieve to remove fines. Approximately 20 - 30 shells of *T. sacculifer, N. dutertrei*, and *P. obliquiloculata* species were picked from the 250 - 355 μm size fraction at intervals spaced ~ 10 cm apart. The age model used for 6GGC and 55GGC cores is from Fehrenbacher and Martin (2011). The age model for the 43JC cores is from Benway et al. (2006), and for the 24JC core is from Kienast et al. (2007), updated by Dubois et al. (2011).

For the bulk shell trace element and isotope paired analyses, ~ 0.7 - 1.0 mg of shells were gently cracked open between glass plates, homogenized with a dry brush, and split into three aliquots. Fragments appeared free of infill and metal oxides under a light microscope. Two aliquots were loaded into acid-leached microcentrifuge vials under a Class-1000 laminar flow bench for solution-based trace element analyses. The third aliquot was set aside for stable isotope analyses (see Section 2.1.2).

Samples for trace elements were cleaned following the procedures of Martin and Lea (2002) (without the reductive step) modified to reduce sample loss during the cleaning process (Fritz-Endres and Fehrenbacher, 2020). The reductive step traditionally used to remove barite and other metal contamination (Boyle and Keiwin, 1985; Lea and Boyle, 1989, Lea and Boyle, 1991) was omitted because there is no evidence of metal contamination including manganese carbonate or Mn-oxide overgrowths (Martin and Lea, 2002; Pena et al., 2005; Pena et al., 2008; Panieri et al., 2017; Wan et al. 2018). Furthermore, the reductive step causes partial dissolution of shell material, and its use results in lower trace element values (Lea and Boyle, 1991; Barker et al., 2003; Sexton et al., 2006; Yu et al., 2007; Bian and Marin, 2010; Martin and Lea, 2002; Vetter et al., 2013, Regenberg et al., 2006; Rosenthal et al., 2004; Johnstone et al., 2016). The cleaning procedures were further modified by gently cracking open the shells (leaving fragments as large as possible) before chemical cleaning and using a three min (vs. one min) settling time between aspirations of the cleaning solution to retain more ontogenic inner calcite fragments. Taking steps to retain inner calcite regions of the shell is essential for trace element analysis in non-spinose foraminifera because these regions typically have higher trace element concentrations (Hathorne et al., 2009; Kunioka, 2006; Fehrenbacher et al., 2018; Fritz-Endres and Fehrenbacher, 2020). For example, Ba/Ca ratios in *P. obliquiloculata* that have undergone more intensive cleaning (greater cracking of the shells and less time between aspirations of the cleaning fluid) prior to solution analysis are far lower than laser ablation results, even though samples are from the same intervals and should record the same Ba/Ca values (Figure S1).

3.3.2.2. Bulk shell solution ICP-MS

Bulk trace element analyses were obtained on WEP samples using an XSeriesII ICP-MS at the University of California, Santa Cruz (UCSC) and on EEP samples using an iCAP RQ ICP-MS at Oregon State University (OSU) using a combination of techniques detailed in Yu et al. (2005). Samples were analyzed for a suite of minor and trace analytes, including ^{137}Ba, ^{24}Mg, ^{25}Mg, ^{43}Ca, ^{44}Ca, ^{86}Sr, ^{87}Sr, ^{27}Al, and ^{55}Mn and other analytes not presented in this study. High Al and/or Mn were used to assess the presence of sediment contaminations such as clay infill or metal surface contaminations, which may alter the Mg/Ca and/or Ba/Ca signal (e.g., Boyle, 1983; Martin and Lea, 2002). Twenty-five samples (~ 3%) were rejected due to anomalously high Al and/or Mn (> 400 μmol/mol). Two samples (< 1%) had average Trace Element/Ca ratios greater than two standard deviations higher than the average samples in adjacent intervals and were rejected as outliers.

Multielement stock standard mixtures were prepared at UCSC gravimetrically by spiking a 10,000 mg/ml Ca standard with Ba, Mg, Sr, Al, and Mn mono-elemental 1,000 mg/ml ICP-MS grade solution such that the final ratios of solutions span the natural ratio ranges expected in planktic foraminifera. Calibration standards were made by diluting the standard stock solutions with 0.075M Optima grade HNO_3 to give Ca concentrations of 100 ppm, within the range of expected sample Ca concentrations. Samples analyzed at OSU used a different standard approach. An 8,000 ppb Ca standard solution and a customized (based on expected foraminifera values) multi-elemental standard solution was used to create calibration standards within the elemental range of the samples. A 0.1 ppb indium standard was used as an internal standard to correct for variability between the calibration standards and the samples. A 0.1 ppb Ca standard was used to check for matrix effects that can cause signal suppression/enhancement in ICP-MS analysis (Jarvis et al., 1991). The long-term instrument precision (1σ) of Mg/Ca and Ba/Ca measurements is better than 5% at UCSC and better than 3% at OSU based on repeated analyses of in-house standards. Five consistency standards (treated as unknowns) from each of four runs at UCSC have a mean reproducibility (1σ) of better than 5% for Mg/Ca, and 8% for

Ba/Ca, and five consistency standards from each of five runs at OSU have a mean reproducibility (1σ) of better than 3% for Mg/Ca and 2% for Ba/Ca. Ten intra-lab comparison samples produced Mg/Ca and Ba/Ca values within 5%.

3.3.2.3. Bulk shell stable isotope analysis

Stable oxygen and carbon isotopes were measured in WEP samples using dual inlet isotope ratio mass spectrometry using a Kiel III carbonate device coupled to a MAT 252 Isotope Ratio Mass Spectrometer OSU Stable Isotope Laboratory. Oxygen and carbon isotope data were calibrated to the Vienna Pee Dee Belemnite (V-PDB) standard using an in-house Wiley standard. The international calcite standard NBS-19 was the consistency standard, and the $\delta^{18}O$ and $\delta^{13}C$ reproducibility (1σ) based on 26 measurements of NBS-19 in the same mass range as our samples were better than 0.03‰ and 0.02‰, respectively.

Stable oxygen and carbon isotopes were measured in EEP samples by reacting the specimens in supersaturated H_3PO_4 at 90ºC using an automated Isocarb common acid bath carbonate device and analyzing the resulting CO_2 using a Micromass Optima Isotope Ratio Mass Spectrometer at the University of California Davis (UCD) Stable Isotope Lab. Samples were first roasted at 375ºC for 30 min under vacuum to remove residual carbon tape/organic matter before being introduced to the common acid bath. Oxygen and carbon isotope data were calibrated to an in-house Carrara Marble standard (UCD-SM92) that had been previously calibrated against NBS-19. The internal calcite standard UCD-SM92 was run as a consistency standard (treated as an unknown), and the $\delta^{18}O$ and $\delta^{13}C$ reproducibility based on 35 measurements of UCD-SM92 in the same mass range as our samples were better than 0.03‰ and 0.05‰, respectively. Five large fragments of the same specimen of the spinose species *O. universa* were analyzed at both labs for inter-laboratory comparison. The $\delta^{18}O$ and $\delta^{13}C$ reproducibility was better than 0.04‰ and 0.06‰, respectively.

3.3.3. IFA

3.3.3.1. Sample preparation for IFA

IFA was performed to generate inter-population and intra-shell Ba/Ca data at key time intervals. Shells were cleaned using the established cleaning procedures of Martin and Lea (2002), adapted for individual foraminifera (Fritz-Endres and Fehrenbacher, 2020). In brief, shells were placed in individual microcentrifuge vials and subjected to milliQ/methanol rinses and brief sonication followed by an oxidative cleaning step. As with bulk shells (section 2.2.1), the reductive step was excluded; we did not observe evidence of metal contaminants on shell surfaces under Scanning Electron Microscope (SEM) nor within laser ablation profiles. We sought to avoid dissolution caused by the reductive cleaning steps.

3.3.3.1. IFA laser ablation ICP-MS

Cleaned shells were mounted onto aluminum stubs with carbon tape and analyzed on a Teledyne/Photon Machines 193 nm ArF UV excimer laser ablation system with an HelEx laser ablation cell coupled to a Thermo Scientific X-series II quadrupole ICP-MS at OSU. Gas composition and flow rate were tuned daily by adjusting the flow of Ar and He as necessary to achieve high count rates on the sample/standard while maintaining ThO^+/Th^+ ratios less than 0.2% (tuned daily). Shells were analyzed from the outside-in using a 50 - 110 µm diameter spot size, a 4 - 5 Hz repetition rate, and 1 - 1.5 J/cm^2 laser fluence. Data acquisition varied between 40 - 60 seconds per spot analysis. Repeat analyses were conducted on chambers large enough to permit multiple spots. Isotopes included ^{138}Ba, ^{24}Mg, ^{25}Mg, ^{43}Ca, ^{44}Ca, ^{66}Zn, ^{88}Sr, ^{87}Sr, ^{27}Al, and ^{55}Mn, along with others not presented in this study. ^{43}Ca was used as the internal standard, and ^{44}Ca was monitored for consistency. Al and Mn were monitored to assess clay and metal contamination that would appear as a spike in concentration at the beginning or end of the laser profile. Any correlation between Al and Mn and the trace element of interest is removed in preliminary data reduction by excluding an initial and terminal spike in Mn and Al that could be surface contamination or excess ablated material, following established protocols (Eggins et al. 2003; Fehrenbacher et al., 2015; Branson et al., 2019).

Average elemental concentrations were calculated using LAtools laser data reduction software, including screening for outliers and background correcting by subtracting average background counts (calculated with the laser off) from each data point (Branson et al., 2019). The mean trace element/Ca ratio for each profile was then calculated by normalizing to the known trace element concentration in the drift/background-corrected bracketed analyses of NIST SRM 610 and 612 glass standards at 5 Hz and ~ 4.5 J/cm^2 laser fluence (Jochum et al., 2011). Thirty-eight repeat analyses gave a reproducibility (1σ) of the mean Mg/Ca ratios of 9.5 ± 0.3 mmol/mol and 1.5 ± 0.05 mmol/mol and Ba/Ca ratios of 1594.1 ± 68.7 μmol/mol and 138.6 ± 5.1 μmol/mol for NIST 610 and 612, respectively. Standard measurements are within 5% of published values for NIST 610 and 612 (Jochum et al., 2011).

3.3.3.2. IFA stable isotope analysis

Following laser ablation, individual shells were carefully removed from the carbon tape with methanol for stable isotope analysis following the procedures outlined in section 2.1.3. The WEP samples were loaded into a Kiel IV carbonate device at OSU. EEP samples were roasted and loaded into a common acid bath carbonate device at UCD by dual inlet isotope ratio mass spectrometry. Because of the low weight of individual foraminifera (often < 12 μg), two shells were pooled together for all of the IFA isotope analyses. Pooled specimens had similar Mg/Ca ratios under the assumption that shells with similar Mg/Ca concentrations calcified under similar conditions (after Farmer et al., 2007). The $\delta^{18}O$ and $\delta^{13}C$ reproducibility (1σ), based on 22 measurements of NBS-19 at OSU, was better than 0.03‰ and 0.02‰, respectively, and based on 21 measurements of UCD-SM92 at UCD, was better than 0.06‰ and 0.05‰, respectively.

3.4. Results

3.4.1. Ba/Ca results for the WEP

3.4.1.1. Bulk shell Ba/Ca ratios

In the WEP, the bulk shell Ba/Ca ratios measured in the spinose species *T. sacculifer* are low and invariable through time from the LGM to the Holocene; In contrast, Ba/Ca ratios are elevated and vary through time in the non-spinose species *N. dutertrei* and *P. obliquiloculata* (Figure S6a). Ba/Ca ratios in *N. dutertrei* are moderately low during the LGM (5.2 μmol/mol and 1.0 μmol/mol), increase significantly into the deglaciation, and reach a maximum value at ~ 17 ky BP (9.0 μmol/mol and 12.7 μmol/mol at core sites 6GGC and 55GGC, respectively). Values then decrease into the Holocene, with a second smaller increase in the late Holocene (of ~ 4 and 3 μmol/mol at core sites 6GGC and 55GGC, respectively). Ba/Ca ratios in *P. obliquiloculata* follow a similar pattern; values are moderately low during the LGM (3.3 μmol/mol and 4.7 μmol/mol), peak during the deglaciation (7.7 μmol/mol and 11.6 μmol/mol at core sites 6GGC and 55GGC respectively), and then decrease into the Holocene with a small peak in Ba/Ca during the late Holocene (~ 3 μmol/mol increase in both cores). The Holocene peak coincides temporally with the peak in *N. dutertrei* Ba/Ca ratios.

To compare time interval results, bulk data is compiled into three intervals (Holocene ~ 5 - 11 ka BP, deglacial ~ 11 - 18 ka BP, and LGM ~ 18 - 25 ka BP; Figure 3, large symbols) and the mean and 95% confidence interval is plotted for each (Figure 3, shaded area). Ba/Ca data of *N. dutertrei* and *P. obliquiloculata* from deglacial time intervals are significantly different from Holocene and LGM time intervals within 95% confidence (confidence interval around deglacial mean does not intersect confidence interval around Holocene or LGM).

3.4.1.2. IFA Ba/Ca ratios

Like the bulk shell Ba/Ca results, IFA mean Ba/Ca in *T. sacculifer* are significantly lower than *N. dutertrei* and *P. obliquiloculata* Ba/Ca ratios at both 6GGC and 55GGC core sites (t-test, two-tailed, two-sample assuming unequal variances, all sample sets p-value < 0.01; Figure 4a-c). Sample-to-sample Ba/Ca variance in *T. sacculifer* is much lower (~ 1 μmol/mol, Figure 4d) compared to the

non-spinose species (always > 4 μmol/mol and as high as 173 μmol/mol; Figure 4e, f) and is significantly different from non-spinose species in all three time intervals of both core sites (F-test for equality of two variances, two-tailed, all sample sets p-value << 0.01).

In the LGM, Ba/Ca IFA mean and variance (1σ) among *N. dutertrei* (4.9 ± 19.0 μmol/mol and 9.3 ± 22.7 μmol/mol, in cores 6GGC and 55GGC, respectively) and *P. obliquiloculata* (5.0 ± 28.8 μmol/mol and 9.2 ± 19.0 μmol/mol, in cores 6GGC and 55GGC, respectively) is low compared to the deglacial values for *N. dutertrei* (9.8 ± 87.9 μmol/mol and 13.0 ± 173.0 μmol/mol, in cores 6GGC and 55GGC, respectively) and *P. obliquiloculata* (6.5 ± 116.9 μmol/mol and 9.6 ± 22.7 μmol/mol at 6GGC and 55GGC core sites, respectively). Ba/Ca mean and variance decreases from the deglacial into the Holocene for *N. dutertrei* (6.9 ± 12.5 μmol/mol and 9.0 ± 9.0 μmol/mol at core sites 6GGC and 55GGC, respectively) and *P. obliquiloculata* (2.9 ± 4.2 μmol/mol and 6.7 ± 16.5 μmol/mol at core sites 6GGC and 55GGC, respectively). Deglacial means are distinct from Holocene and LGM means within 95% confidence (confidence intervals shown as error bars in Figure 4a, top row), except in the case of deglacial vs. LGM values of *P. obliquiloculata* (not distinct within 95% confidence). Deglacial variances are significantly higher compared to Holocene and LGM variances (F-test for equality of two variances, two-tailed, all sample sets p-value < 0.01; Figure 4a, bottom row), except for *P. obliquiloculata* data at core site 55GGC, where time intervals do not have distinct variability (F-test for equality of two variances, two-tailed, all sample sets p-value > 0.50). Ba/Ca mean and variance in *N. dutertrei* and *P. obliquiloculata* in both WEP cores increase during the deglacial interval.

Notably, the results above demonstrate that higher deglacial Ba/Ca ratios are evident in both the shallow and deep cores, despite the differences in preservation and the well-documented effect of dissolution on foraminiferal proxies in the OJP. Core 6GGC has likely remained above the regional lysocline through the record and foraminifera geochemistry unaltered by dissolution, while core 55GGC lays below

the regional lysocline and has experienced dissolution (Wu et al., 1991; Marchitto et al., 2005; Fehrenbacher and Martin, 2011; Branson et al., 2013). Results suggest that even in locations that experience dissolution, Ba/Ca ratios in foraminifera remains a robust signal, provided that specimens are carefully cleaned to avoid preferential dissolution of the inner calcite (section 2.2.1; Figure S1).

3.4.2. Ba/Ca results for the EEP

3.4.2.1. Bulk shell Ba/Ca ratios

In the EEP, the bulk Ba/Ca ratios measured in *T. sacculifer* are low and have low variability (1σ) through the timeseries (2.7 ± 0.71 μmol/mol and 1.1 ± 1.05 μmol/mol) as compared to *N. dutertrei* (5.7 ± 4.3 μmol/mol and 13.9 ± 8.1 μmol/mol) and *P. obliquiloculata* data (6.2 ± 4.3 μmol/mol and 9.1 ± 7.7 μmol/mol, at the 43JC and 24JC core sites, respectively, Figure S6b). *N. dutertrei* Ba/Ca ratios are lower during the LGM (3.5 μmol/mol and 10.0 μmol/mol) relative to the timeseries and sharply increase at ~ 16 - 17 ka BP (28.5 μmol/mol and 13.7 μmol/mol at core sites 43JC and 24C, respectively). Values decrease at ~ 15 ka BP in core 24JC and decrease at ~ 11 ka BP in core 43JC. Ba/Ca ratios in *N. dutertrei* indicate a second smaller increase in the late Holocene (of ~ 10 μmol/mol at both core sites). As with the *N. dutertrei* record, Ba/Ca ratios in *P. obliquiloculata* are low during the LGM (2.7 μmol/mol and 8.9 μmol/mol at the 43JC and 24JC core sites, respectively), and increase sharply during the deglaciation (37.0 μmol/mol and 26.6 μmol/mol, at the 43JC and 24JC core sites, respectively). The deglacial Ba/Ca peak coincides temporally with the peak in the *N. dutertrei* Ba/Ca ratios. Values in both cores decrease into the Holocene at ~ 11 ka BP with a small peak in Ba/Ca at ~10 ka BP (of 10 μmol/mol).

Using the same statistical method described for bulk samples in the WEP, we observe that the deglacial interval is significantly higher than the LGM and Holocene intervals (interval means are distinct, within 95% confidence, Figure 3). These results

are consistent for both *N. dutertrei* and *P. obliquiloculata* Ba/Ca ratios in the two cores.

3.4.2.2. IFA Ba/Ca ratios

Mean IFA Ba/Ca is much lower for *T. sacculifer* and is significantly different from *N. dutertrei* and *P. obliquiloculata* Ba/Ca in both EEP cores (t-test, two-tailed, two-sample assuming unequal variances, all sample sets p-value < 0.01; Figure 4g-4i) and mean *T. sacculifer* Ba/Ca measured in all time intervals in cores 43JC and 24JC are not statistically different (t-test, two-tailed, two-sample assuming equal variances, p-value > 0.21). Specimen-to-specimen Ba/Ca variance in *T. sacculifer* is low compared to that of non-spinose species and is significantly different from non-spinose species in all time intervals of both core sites (F-test for equality of two variances, two-tailed, all sample sets p-value << 0.01).

IFA Ba/Ca mean and variance is significantly higher during the deglacial time interval for *N. dutertrei* (11.2 ± 136.6 μmol/mol and 22.0 ± 140.0 μmol/mol) and *P. obliquiloculata* (14.1 ± 43.3 μmol/mol and 11.5 ± 33.7 μmol/mol, for 43JC and 24JC core sites, respectively). Deglacial values are significantly higher compared to the LGM for *N. dutertrei* (7.6 ± 40.0 μmol/mol and 4.5 ± 0.7 μmol/mol) and *P. obliquiloculata* (4.3 ± 9.3 μmol/mol and 6.0 ± 1.2 μmol/mol) and compared to the Holocene (*N. dutertrei* values are 7.0 ± 1.3 μmol/mol and 15.8 ± 99.8 μmol/mol; *P. obliquiloculata* are 7.2 ± 5.4 μmol/mol and 9.0 ± 1.5 μmol/mol, for 43JC and 24JC core sites, respectively). Deglacial means are distinct from Holocene and LGM means within 95% confidence for both species and for both 43JC and 24JC core sites (confidence intervals shown as error bars in Figure 4g-4i, top row). Variances are significantly higher for the deglacial than the LGM and Holocene, for both core sites and species (F-test for equality of two variances, two-tailed, all sample sets p-value < 0.01; Figure 4j-4l, bottom row).

Sediment re-deposition can sometimes alter sediment core records and may impact paleo-production reconstructions, particularly in high depositional environments with high and low topographic features (e.g., the EEP; Loubere, 1999,

2001; Loubere et al., 2003, 2004; Francois et al., 2004; Pichat et al., 2004; Lyle et al., 2005). Despite potential issues with higher sediment focusing at core site 24JC, which is situated in a topographic low (Lyle et al., 2005), we find that the bulk non-spinose foraminifera Ba/Ca records of 43JC and 24JC core sites reflect the same patterns of abrupt increase at ~ 16 - 17 ka BP, followed by low values in the early Holocene. The similarity of the Ba/Ca records between both core sites suggests sediment re-deposition does not measurably impact the results.

3.5. Discussion

3.5.1 Mechanisms responsible for elevated Ba/Ca in non-spinose species

While the Ba/Ca ratios in *T. sacculifer* generally reflect seawater Ba (Ba_{SW}), the Ba/Ca in non-spinose foraminifera is higher and more variable than would be expected if ratios reflected Ba_{SW} alone. We demonstrate this by converting the bulk shell and IFA Ba/Ca ratios from the core-top intervals to Ba_{SW} (assuming [Ca] at 35 psu is 10.3 mmol/L) using established Ba distribution coefficients (D_{Ba}). We compare results to the modern Ba_{SW} at the average habitat depths for all three species determined using the Mg/Ca SST and $\delta^{18}O$ data that is shown to faithfully record species-specific oceanographic conditions (Text S1; Figure 1). For *T. sacculifer*, we convert the Ba/Ca ratios to Ba_{SW} using the spinose species D_{Ba} ($Ba/Ca_{calcite} = 0.13 \pm 0.004\ (Ba/Ca_{sw}) + 0.15 \pm 0.10$; Hönisch et al., 2011; Lea and Spero, 1994). We use the *N. dutertrei* D_{Ba} for both *N. dutertrei* and *P. obliquiloculata* because a *P. obliquiloculata* D_{Ba} has not yet been established ($Ba/Ca_{calcite} = 0.11 \pm 0.008\ (Ba/Ca_{sw}) + 0.03 \pm 0.10$; Fehrenbacher et al., 2018).

Bulk Ba/Ca ratios of *T. sacculifer* are ~ 1 μmol/mol and provide accurate estimates of Ba_{SW} of the upper thermocline in the EEP (44.0 and 52.0 nmol/L for 43JC and 24JC core sites, respectively, compared to Ba_{sw} of 43.0 nmol/L; Wolgemuth, 1970) and are higher than upper thermocline values in the WEP (99 nmol/L and 91 nmol/L for 6GGC and 55GGC core sites, respectively, vs. Ba_{sw} of 32.6 nmol/L; Schlitzer et al., 2018; Table 1). In contrast, bulk Ba/Ca ratios in the non-

spinose species are consistently over 2 μmol/mol in core-top samples from the WEP and EEP and reach as high as 15.7 μmol/mol in *N. dutertrei* from the 24JC core. The Ba_{SW} at the base of the thermocline would have to be as high as 1,200 nmol/L to explain these values, which is more than 20x higher than Ba_{sw} measured at the base of the thermocline in the EEP (50.0 nmol/L) or WEP (32.6 nmol/L). Furthermore, specimen-to-specimen variability is high ($1\sigma \sim 1$ μmol/mol up to 11 μmol/mol; Figure S2), and intra-shell Ba/Ca ratios in the non-spinose species (1 μmol/mol up to 120 μmol/mol; Figure S4) would imply calcifying in an environment with Ba_{sw} of ~ 60 nmol/L to nearly 9,500 nmol/L.

Measured seawater Ba at the base of the thermocline is relatively constant, and the Ba_{sw} range implied from the Ba/Ca ratios of non-spinose species is much larger than the range in Ba_{sw} recorded anywhere in the upper water column at our sites or anywhere in the equatorial Pacific (Schlitzer et al., 2018; Wolgemuth, 1970). Additionally, Ba_{sw} rarely exceeds 200 nmol/L in the open ocean (Jeandel et al., 1996; Monnin et al., 1999; Rushdi et al., 2000), and seawater would be supersaturated with respect to barite at about 250 nmol/L (at temperature, salinity, pressure, and $[SO_4]$ of the surface ocean; Monnin et al., 1999). Thus, another mechanism is required to explain elevated and variable Ba/Ca in the non-spinose species.

Possible Ba/Ca enrichment sources include contamination or diagenetic alteration in the water column or on the seafloor or calcification within a Ba-enriched environment. It is unlikely that our results are due to Ba contaminations because elevated Ba/Ca ratios are observed only in the non-spinose species in this study and not in *T. sacculifer* obtained from the same core intervals and prepared for analysis using the same cleaning procedures. It is possible that Ba/Ca is enriched by hydrothermal Ba sources, particularly in specimens from the 24JC core, which is located 80 km south of the Galapagos Spreading Center (Lonsdale, 1977; Corliss et al., 1978). However, there is no abrupt enrichment in Ba/Ca nor other trace elements associated with hydrothermal sources (Mg/Ca and Mn/Ca) at the innermost (Pena et al., 2005, 2008; Gibson et al., 2016) or outermost (Boyle, 1981) part of the shells. Furthermore, hydrothermal sources could only be attributed to elevated Ba samples in

core 24JC, which fails to explain the elevated Ba/Ca at core site 43JC and the core sites in the WEP.

We favor the hypothesis that the elevated Ba/Ca ratios in the non-spinose species are due to calcification in Ba-enriched POM. Non-spinose foraminifera are often found attached or embedded within POM (Fehrenbacher et al., 2018; Davis et al., 2020), perhaps as a feeding mechanism, as non-spinose species are believed to feed on sinking aggregates of phytoplankton remains (e.g., Anderson et al., 1979; Spindler et al., 1984; Greco et al., 2019, 2021; Takagi et al., 2019). Foraminifera likely inhabit a Ba-enriched environment for a portion of their lifecycle, perhaps while feeding, and spend a part of their lifecycle in seawater prior to gametogenesis when the rhizopodia they use to attach to the POM are retracted (Fehrenbacher et al., 2018; Shiebel and Hemleben, 2017). This behavior would explain the high intra-shell Ba/Ca variability and high specimen-to-specimen variability, as each specimen would be recording its own microhabitat.

Particulates provide an environment conducive to the enrichment of Ba, despite widespread barite undersaturation in seawater (Monnin et al., 1999; Rushdi et al., 2000). The degradation of organic matter within particles can enrich Ba enough to support barite supersaturation and the formation of barite crystals (Stroobants et al., 1991; Sternberg et al., 2005; Ganeshram et al., 2003; Martínez-Ruiz et al., 2019). POM can be enriched with Ba by > 2,000 nmol/L (Bernstein et al., 1992), and high [Ba] and barite supersaturation maintained within the particle (Zhen-Wu et al., 2016) could explain Ba/Ca ratios in non-spinose foraminifera of 20 μmol/mol or greater as is suggested by non-spinose population and intra-shell Ba/Ca ratios. It is hard to justify [Ba] of 1,000s of nmol/L in the calcifying fluid unless barite supersaturation is maintained. Barite supersaturation may be achieved by sulfate loss through reduction within particles (Alldredge, 2000), mediated by sulfate-reducing bacteria (Brumsack and Gieskes, 1983; Breheret and Brumsack, 2000; Dickens, 2001) and maintained by low oxygen and pH. Particulates have relatively low and variable oxygen and pH than surrounding seawater (Alldredge, 2000). Furthermore, foraminifera have a diurnal respiration cycle that likely contributes to changes in pH and oxygen in the POM

microhabitat, based on observations of significant diurnal changes around the shell surface of spinose species (Jørgensen et al., 1985; Rink et al., 1998). Barite formation may also be inhibited by organic chelators (Putnis et al., 2008) or trace elements such as Mg that are enriched in particles (Hebel et al., 1986) and can act as a crystallization inhibitor (Berner, 1975). Future work in geochemical modeling of conditions within particles may help explain the complicated and unique shell geochemistry.

The micro-environment habitat hypothesis provides a link between non-spinose foraminifera Ba/Ca and POM production (e.g., production in the surface ocean). It is already known that Ba concentrations in particles are closely linked to the abundance of POM (Martínez-Ruiz et al., 2020) and regional variability in surface ocean production (Payten and Griffith, 2007 and references therein). Ba/Ca results from the core-top non-spinose species reflect the longitudinal gradient in modern export production, with higher and more variable IFA and bulk shell Ba/Ca values in the higher production region of the EEP compared to the WEP (Figure 2b) and Ba/Ca in the core-top and sediment trap derived foraminifera are strongly correlated with export production (Figure 2c). We propose that the mean and variability of Ba/Ca ratios in *P. obliquiloculata* and *N. dutertrei* can serve as a proxy for surface ocean production.

3.5.2. Ba/Ca ratios in non-spinose foraminifera agree with production reconstructions

3.5.2.1. Production changes in the WEP

The dominant signal over the 25 kyr record is a sharp increase in the non-spinose foraminifera Ba/Ca ratios beginning at ~ 16 - 17 ka BP that coincides with the timing of increased export production based upon $^{230}Th_{xs}$-normalized Ba_{xs} flux, $^{230}Th_{xs}$-normalized opal flux, and $^{231}Pa_{xs}/^{230}Th_{xs}$ ratios measured in OJP cores (Schwarz et al., 1996; Winckler et al., 2016, Pichat et al., 2004; Bradmiller et al., 2006). Increased production is likely driven by an increase in nutrients in the EUC. Increased nutrients could result from increased interaction between the New Guinea Coastal Undercurrent and the Papua New Guinea continental shelf as sea-level rose, supplying iron to the EUC (Pichat et al., 2004; Mackey et al., 2002; Milliman et al.,

1999). A more common hypothesis is that nutrients in the EUC responded to deglacial nutrient enrichment in southern-sourced intermediate waters from which the deep part of the EUC originates (Sarmiento et al., 2004; Liu and Alexander, 2007; Pena et al., 2008; Rafter et al., 2012; Rafter and Sigman, 2016). During the deglacial, a southward shift in the southern hemisphere westerlies may have led to increased upwelling intensity and overturning of the Southern Ocean (Anderson et al., 2009; Toggweiler et al., 2006; Toggweiler and Lea, 2010; Denton et al., 2010; Dubois et al., 2011; Costa et al., 2017), as inferred from $^{230}Th_{xs}$-normalized opal flux and $^{231}Pa_{xs}/^{230}Th_{xs}$ records from the Pacific sector of the Southern Ocean (Figure 5d, Chase et al., 2003). This signal was likely transmitted into the thermocline of low latitudes by the EUC, increasing production (Anderson et al., 2009; Dubois et al., 2011). The Southern Ocean signal is recorded by depleted planktic foraminifera $\delta^{13}C$, which is attributed to the upwelling of old and $\delta^{13}C$-depleted deep water in the Southern Ocean (Shackleton et al., 1983; Oppo and Fairbanks, 1989; Spero and Lea, 2002; Anderson et al., 2009; Hayes et al., 2011; Pena et al., 2013; Poggemann et al., 2017). The deglacial Ba/Ca peak coincides with the decline of $\delta^{13}C$ values in the base of the thermocline and upper thermocline dwelling species at ~ 16 - 17 ka BP (decrease of ~ 10% from LGM to deglacial intervals; Figure 5b and e; Text S2), which supports the hypothesis of southern-sourced nutrient enrichment in the WEP.

3.5.2.2. Production changes in the EEP

The peak in Ba/Ca ratios in the EEP at ~ 16 - 17 ka BP coincides with a production maximum inferred from $^{230}Th_{xs}$-normalized calcite flux (Richaud et al., 2007), $^{230}Th_{xs}$-normalized opal flux (Anderson et al., 2009; Hayes et al., 2011), and $^{230}Th_{xs}$-normalized organic carbon flux at the same site as our study (24JC; Figure 5c; Kienast et al., 2006; Dubois et al., 2011) and elsewhere in the equatorial cold tongue (Pichevin et al., 2009). Additionally, foraminiferal assemblages transitioned to high production groups during the deglacial at sites underlaying the equatorial cold tongue, further suggesting that production was high during this time (Loubere, 2001; Martínez et al., 2005).

The higher resolution of cores 43JC and 24JC help resolve the timing of the deglacial increase in production in relation to northern and southern hemisphere climate events and support the hypothesis that the entrainment of high nutrient southern-sourced waters sparked a production increase at our sites. There is evidence for both a northern and a southern hemisphere climate influence on equatorial SST and production (Figure 5a), with some uncertainty as to which hemisphere exerts the dominant control. The Ba/Ca proxy suggests that the most dramatic increase in production occurred during Heinrich Stadial 1 (H1; ~ 16 ka BP; Figure 5, blue box). Northern hemisphere cooling and atmospheric and oceanic reorganization during both H1 and the Younger Dryas (YD; ~ 4.5 ka BP) are thought to have led to cooling in the equatorial cold tongue (Kienast et al., 2006; Pahnke et al., 2007; Koutavas and Sachs, 2008; Dubois et al., 2011). The cooling is evident by a decrease in Mg/Ca SST (Figure 6, red arrows) and an increase in $\delta^{18}O$ (Figure 6, blue arrows) at site 24JC and perhaps in the warm pool at site 43JC. The EEP surface ocean response to northern hemisphere cold events suggests a northern hemisphere influence. However, as with the WEP, we also observe a strong influence of the southern hemisphere: the depleted $\delta^{13}C$ signature of deeper Southern Ocean waters reaching the surface of the EEP simultaneous with an increase in the Ba/Ca ratios (Figure 5c and e; Text S2). Climate changes in the equatorial region likely reflect the link between high latitudes of both hemispheres: cooling of the northern hemisphere during H1 and the YD, and nutrient enrichments in the southern hemisphere.

3.5.2.3. Comparing results with cross-basin paleo-production reconstructions

The peak in Ba/Ca in both the WEP and EEP cores during the deglaciation agrees with $^{230}Th_{xs}$-normalized calcite fluxes from cores that span the equatorial Pacific region (Richaud et al., 2007) and somewhat agrees with a recent comprehensive study of $^{231}Pa_{xs}/^{230}Th_{xs}$ and $^{230}Th_{xs}$-normalized records that suggest an increase in production from the LGM to the deglacial (Costa et al., 2017). However, the Costa et al. (2017) study indicated that the deglacial peak in production was

isolated to the EEP, driven by the east-west asymmetry in nutrient delivery of La Niña-like thermocline conditions.

Our observations of cooler SSTs in the equatorial cold tongue (site 24JC) and higher production during H1 and the YD may suggest stronger upwelling during these periods either driven by a more La Niña-like state resulting in a shallower thermocline in the EEP and a deeper thermocline in the WEP, or due to enhanced coastal upwelling (Pena et al., 2008; bin Shaari et al., 2013). Reconstructions of EEP and WEP thermocline depth during the deglacial have generated conflicting results, with evidence for increased upwelling rates (McManus et al., 2004; Martínez et al., 2006; bin Sharri et al., 2013) and a shallower thermocline (DiNezio et al., 2011; Ford et al., 2015), while some records imply there is little evidence for dramatic thermocline changes that would impact production (Zhang et al., 2007). There is no clear trend in our Mg/Ca SST and $\delta^{18}O$ thermocline reconstructions that suggest upwelling dramatically changed at our EEP or WEP sites (Text S1; Figure S3). We also do not observe opposing production trends across the Pacific that would signify the east-west asymmetry typical of a La Niña-like state. Instead, we observe an increase in the Ba/Ca proxy simultaneously in the EEP and WEP (within the resolution of the age models).

Furthermore, stronger La Niña-like wind-driven upwelling is difficult to reconcile with atmospheric conditions during H1 in the EEP. H1 is associated with strengthened northeasterly trade winds, a southward position of the ITCZ, and suppressed easterlies (Liu and Yang, 2003; Jacobel et al., 2016; Benway et al., 2006; Kienast et al., 2006; Leduc et al., 2007), which would reduce, not enhance upwelling in the EEP (Clement et al., 1999; Koutavas and Lynch-Stieglitz, 2004; Zhang and Delworth, 2005; Dubois et al., 2009). Conditions of H1 instead favor the enhanced coastal upwelling hypothesis (Pena et al., 2008) as a more southerly ITCZ and strengthened northeasterly trade winds would drive enhanced coastal upwelling along Central America and deliver colder nutrient-rich waters to the equatorial cold tongue via the Peru current (Feldberg and Mix, 2003; Lyle et al., 1992; Kienast et al., 2006; Pahnke et al., 2007). However, this mechanism cannot fully explain our results, as we

observe cooling and increased production at the 43JC core site, which is north of the primary influence of the Peru Current. Our data support the hypothesis that intensification of intermediate water circulation during H1 and the YD increased the speed of the EUC and the delivery of southern-sourced nutrients to the equatorial thermocline, as opposed to upwelling changes (Dubois et al., 2011). Future cross-basin analysis in the equatorial Pacific may help resolve the pathway of nutrient delivery and substantiate the hypothesis favored by our data that southern-sourced nutrients sparked production changes.

3.6. Conclusions

In this study, we generate Ba/Ca data in three planktic foraminifera species and demonstrate that Ba/Ca ratios in non-spinose foraminifera increase during the deglacial attributable to a deglacial peak in primary production. *Neogloboquadrina dutertrei* and *Pulleniatina obliquiloculata* Ba/Ca ratios likely record the Ba-enriched conditions within particulate organic matter, which explains high Ba/Ca ratios and the high specimen-to-specimen and intra-shell variability, as each specimen records the chemistry of its microhabitat. Individual shell and bulk foraminifera analyses record a peak in Ba/Ca ratios at ~ 16 - 17 ka BP across the equatorial Pacific and suggest the Ba/Ca data reflects a significant change in production in this region. A deglacial increase in the Ba/Ca proxy is consistent with other paleo-production proxies that account for post-depositional processes (e.g., $^{230}Th_{xs}$-normalized sediment proxies). Careful analysis of non-spinose foraminifera Ba/Ca ratios in regions with sediment focusing and regions with dissolution indicates the Ba/Ca proxy may be a valuable tool in locations where other production proxies are poorly preserved.

3.7. References

Alldredge, A. L. (2000). Interstitial dissolved organic carbon (DOC) concentrations within sinking marine aggregates and their potential contribution to carbon flux. *Limnology and Oceanography*, *45*(6), 1245-1253. doi.10.4319/lo.2000.45.6.1245

Anand, P., Elderfield, H., and Conte, M. H. (2003). Calibration of Mg/Ca thermometry in planktonic foraminifera from a sediment trap time series. *Paleoceanography*, *18*(2). doi.10.1029/2002PA000846

Anderson, R. F., S. Ali, L. Bradtmiller, S. H. H. Nielson, M. Q. Fleisher, B. E. Anderson, and L. H. Burckle (2009), Wind-driven upwelling in the Southern Ocean and the deglacial rise in atmospheric CO_2, *Science*, 323, 1443-1448. doi.10.1126/science.1167441

Berger, W. H., Bonneau, M. C., and Parker, F. L. (1982). Foraminifera on the deep sea floor-lysocline and dissolution rate. *Oceanologica Acta*, *5*(2), 249-258.

Berger, W. H., Herguera, J. C., Lange, C. B., and Schneider, R. (1994) Paleoproduction: flux proxies versus nutrient proxies and other problems concerning the Quaternary production record. In *Carbon cycling in the glacial ocean: Constraints on the ocean's role in global change* (pp. 385-412). Springer, Berlin, Heidelberg.

Bernstein, R. E., and Byrne, R. H. (2004). Acantharians and marine barite. *Marine Chemistry*, *86*(1-2), 45-50. doi.10.1016/j.marchem.2003.12.003

Bijma, J., Spero, H. J., and Lea, D. W. (1999). Reassessing foraminiferal stable isotope geochemistry: Impact of the oceanic carbonate system (experimental results). In *Use of proxies in paleoceanography* (pp. 489-512). Springer, Berlin, Heidelberg. doi.10.1007/978-3-642-58646-0_20

bin Shaari, H., Yamamoto, M., and Irino, T. (2013). Enhanced upwelling in the eastern equatorial Pacific at the last five glacial terminations. *Palaeogeography, Palaeoclimatology, Palaeoecology*, *386*, 8-15. doi.10.1016/j.palaeo.2013.03.022

Bonneau, M. C., Vergnaudgrazzini, C., and Berger, W. H. (1980). Stable isotope fractionation and differential dissolution in recent planktonic-foraminifera from Pacific box-cores. *Oceanologica Acta*, *3*(3), 377-382.

Bradtmiller, L. I., Anderson, R. F., Fleisher, M. Q., and Burckle, L. H. (2006). Diatom production in the equatorial Pacific Ocean from the last glacial period to the present: A test of the silicic acid leakage hypothesis. *Paleoceanography*, *21*(4). doi.10.1029/2006PA001282

Brown, S. J., and Elderfield, H. (1996). Variations in Mg/Ca and Sr/Ca ratios of planktonic foraminifera caused by postdepositional dissolution: Evidence of shallow Mg-dependent dissolution. *Paleoceanography*, *11*(5), 543-551. doi.10.1029/96PA01491

Chase, Z., Anderson, R. F., Fleisher, M. Q., and Kubik, P. W. (2003). Accumulation

of biogenic and lithogenic material in the Pacific sector of the Southern Ocean during the past 40,000 years. *Deep Sea Research Part II: Topical Studies in Oceanography*, *50*(3-4), 799-832. doi.10.1016/S0967-0645(02)00595-7

Cochran, J. K., and Osmond, J. K. (1976). Sedimentation patterns and accumulation rates in the Tasman Basin. In *Deep Sea Research and Oceanographic Abstracts* (Vol. 23, No. 3, pp. 193-210). Elsevier. doi.10.1016/0011-7471(76)91324-3

Conroy, J. L., Thompson, D. M., Collins, A., Overpeck, J. T., Bush, M. B., and Cole, J. E. (2014). Climate influences on water and sediment properties of Genovesa Crater Lake, Galápagos. *Journal of Paleolimnology*, *52*(4), 331-347. doi.10.1007/s10933-014-9797-z

Costa, K. M., Jacobel, A. W., McManus, J. F., Anderson, R. F., Winckler, G., and Thiagarajan, N. (2017). Production patterns in the equatorial Pacific over the last 30,000 years. *Global Biogeochemical Cycles*, *31*(5), 850-865. doi.10.1002/2016GB005579

Corliss, J. B., Lyle, M., Dymond, J., and Crane, K. (1978). The chemistry of hydrothermal mounds near the Galapagos Rift. *Earth and Planetary Science Letters*, *40*(1), 12-24. doi.10.1016/0012-821X(78)90070-5

Clement, A. C., Seager, R., and Cane, M. A. (1999). Orbital controls on the El Nino/Southern Oscillation and the tropical climate. *Paleoceanography*, *14*(4), 441-456. doi.10.1029/1999PA900013

Davis, C. V., Livsey, C. M., Palmer, H. M., Hull, P. M., Thomas, E., Hill, T. M., and Benitez-Nelson, C. R. (2020). Extensive morphological variability in asexually produced planktic foraminifera. *Science Advances*, *6*(28), eabb8930. doi.10.1126/sciadv.abb8930

de Garidel-Thoron, T., Rosenthal, Y., Beaufort, L., Bard, E., Sonzogni, C., and Mix, A. C. (2007). A multiproxy assessment of the western equatorial Pacific hydrography during the last 30 kyr. *Paleoceanography*, *22*(3). doi.10.1029/2006PA001269

Dekens, P. S., Lea, D. W., Pak, D. K., and Spero, H. J. (2002). Core top calibration of Mg/Ca in tropical foraminifera: Refining paleotemperature estimation. *Geochemistry, Geophysics, Geosystems*, *3*(4), 1-29. doi.10.1029/2001GC000200

Denton, G. H., R. F. Anderson, J. R. Toggweiler, R. L. Edwards, J. M. Schaefer, and A. E. Putnam (2010), The last glacial termination, Science, 328, 1652–1656. doi.10.1126/science.1184119

Dickson, A. G., Sabine, C. L., and Christian, J. R. (2007). *Guide to best practices for ocean CO_2 measurements*. North Pacific Marine Science Organization.

DiNezio, P. N., Clement, A., Vecchi, G. A., Soden, B., Broccoli, A. J., Otto-Bliesner, B. L., and Braconnot, P. (2011). The response of the Walker circulation to Last Glacial Maximum forcing: Implications for detection in proxies. *Paleoceanography*, *26*(3). doi.10.1029/2010PA002083

Dubois, N., Kienast, M., Normandeau, C., and Herbert, T. D. (2009). Eastern

equatorial Pacific cold tongue during the Last Glacial Maximum as seen from alkenone paleothermometry. *Paleoceanography*, *24*(4). doi.10.1029/2009PA001781

Dubois, N., Kienast, M., Kienast, S., Normandeau, C., Calvert, S. E., Herbert, T. D., and Mix, A. (2011). Millennial-scale variations in hydrography and biogeochemistry in the Eastern Equatorial Pacific over the last 100 kyr. *Quaternary Science Reviews*, *30*(1-2), 210-223. doi.10.1016/j.quascirev.2010.10.012

Edmond, J. M., Boyle, E. D., Drummond, D., Grant, B., and Mislick, T. (1978). Desorption of barium in the plume of the Zaire (Congo) River. *Netherlands Journal of Sea Research*, (3-4).

Elderfield, H., and Ganssen, G. (2000). Past temperature and δ 18 O of surface ocean waters inferred from foraminiferal Mg/Ca ratios. *Nature*, *405*(6785), 442-445. doi.10.1038/35013033

Fairbanks, R. G., and Wiebe, P. H. (1980). Foraminifera and chlorophyll maximum: vertical distribution, seasonal succession, and palaeoceanographic significance. *Science*, *209*(4464), 1524-1526. doi.10.1126/science.209.4464.1524

Fairbanks, R. G., Sverdlove, M., Free, R., Wiebe, P. H., and Bé, A. W. (1982). Vertical distribution and isotopic fractionation of living planktonic foraminifera from the Panama Basin. *Nature*, *298*(5877), 841-844. doi.10.1038/298841a0

Farmer, E. C., Kaplan, A., de Menocal, P. B., and Lynch-Stieglitz, J. (2007). Corroborating ecological depth preferences of planktonic foraminifera in the tropical Atlantic with the stable oxygen isotope ratios of core top specimens. *Paleoceanography*, *22*(3). doi.10.1029/2006PA001361

Fehrenbacher, J. S., Russell, A. D., Davis, C. V., Spero, H. J., Chu, E., and Hönisch, B. (2018). Ba/Ca ratios in the non-spinose planktic foraminifer *Neogloboquadrina dutertrei*: Evidence for an organic aggregate microhabitat. *Geochimica et Cosmochimica Acta*, *236*, 361-372. doi.10.1016/j.gca.2018.03.008

Feldberg, M. J., and Mix, A. C. (2003). Planktonic foraminifera, sea surface temperatures, and mechanisms of oceanic change in the Peru and south equatorial currents, 0-150 ka BP. *Paleoceanography*, *18*(1). doi.10.1029/2001PA000740

Ford, H. L., Ravelo, A. C., and Polissar, P. J. (2015). Reduced El Niño–Southern oscillation during the last glacial maximum. *Science*, *347*(6219), 255-258. doi.10.1126/science.1258437

Francois, R., Frank, M., Rutgers van der Loeff, M. M., and Bacon, M. P. (2004). ^{230}Th normalization: An essential tool for interpreting sedimentary fluxes during the late Quaternary. *Paleoceanography*, *19*(1). doi.10.1029/2003PA000939

Frank, M., Gersonde, R., and Mangini, A. (1999). Sediment redistribution, $^{230}Th_{ex}$

normalization and implications for the reconstruction of particle flux and export paleoproduction. In *Use of proxies in paleoceanography* (pp. 409-426). Springer, Berlin, Heidelberg.

Ganeshram, R. S., François, R., Commeau, J., and Brown-Leger, S. L. (2003). An experimental investigation of barite formation in seawater. *Geochimica et Cosmochimica Acta*, *67*(14), 2599-2605. doi.10.1016/S0016-7037(03)00164-9

Greco, M., Jonkers, L., Kretschmer, K., Bijma, J., and Kucera, M. (2019). Depth habitat of the planktonic foraminifera *Neogloboquadrina pachyderma* in the northern high latitudes explained by sea-ice and chlorophyll concentrations. *Biogeosciences*, *16*(17), 3425-3437. doi.10.5194/bg-16-3425-2019

Greco, M., Morard, R., and Kucera, M. (2021). Single-cell metabarcoding reveals biotic interactions of the Arctic calcifier *Neogloboquadrina pachyderma* with the eukaryotic pelagic community. *Journal of Plankton Research*, *43*(2), 113-125. doi.10.1101/2020.10.20.347930

Jacobel, A. W., McManus, J. F., Anderson, R. F., and Winckler, G. (2016). Large deglacial shifts of the Pacific Intertropical Convergence Zone. *Nature communications*, *7*(1), 1-7. doi.10.1038/ncomms10449.

Jarvis, K. E., Gray, A. L., and Houk, R. S. (1991). *Handbook of inductively coupled plasma mass spectrometry*. Chapman and Hall.

Jochum, K. P., Weis, U., Stoll, B., Kuzmin, D., Yang, Q., Raczek, I., ... and Günther, D. (2011). Determination of reference values for NIST SRM 610-617 glasses following ISO guidelines. *Geostandards and Geoanalytical Research*, *35*(4), 397-429. doi.10.1111/j.1751-908X.2011.00120.x

Jonkers, L., and Kučera, M. (2015). Global analysis of seasonality in the shell flux of extant planktonic Foraminifera. *Biogeosciences*, *12*(7), 2207-2226. doi.10.5194/bg-12-2207-2015

Hayes, C. T., Anderson, R. F., and Fleisher, M. Q. (2011). Opal accumulation rates in the equatorial Pacific and mechanisms of deglaciation. *Paleoceanography*, *26*(1). doi.10.1029/2010PA002008

Hebel, D., Knauer, G. A., and Martin, J. H. (1986). Trace metals in large agglomerates (marine snow). *Journal of Plankton research*, *8*(4), 819-824. doi.10.1093/plankt/8.4.819

Hollstein, M., Mohtadi, M., Rosenthal, Y., Moffa Sanchez, P., Oppo, D., Martínez Méndez, G.,... and Hebbeln, D. (2017). Stable oxygen isotopes and Mg/Ca in planktic foraminifera from modern surface sediments of the Western Pacific Warm Pool: Implications for thermocline reconstructions. *Paleoceanography*, *32*(11), 1174-1194. doi.10.1002/2017PA003122

Jeandel, C., Dupre, B., Lebaron, G., Monnin, C., and Minster, J. F. (1996). Longitudinal distributions of dissolved barium, silica and alkalinity in the western and southern Indian Ocean. *Deep Sea Research Part I: Oceanographic Research Papers*, *43*(1), 1-31. doi.10.1016/0967-0637(95)00098-4

Jørgensen, B. B. (1977). Bacterial sulfate reduction within reduced microniches of oxidize marine sediments. *Marine Biology*, *41*(1), 7-17. doi.10.1007/BF00390576

Jørgensen, B. B., Erez, J., Revsbech, P., and Cohen, Y. (1985). Symbiotic photosynthesis in a planktonic foraminiferan, *Globigerinoides sacculifer (Brady),* studied with microelectrodes 1. *Limnology and Oceanography*, *30*(6), 1253-1267. doi.10.4319/lo.1985.30.6.1253

Key, R. M., Kozyr, A., Sabine, C. L., Lee, K., Wanninkhof, R., Bullister, J. L., ... and Peng, T. H. (2004). A global ocean carbon climatology: Results from Global Data Analysis Project (GLODAP). *Global biogeochemical cycles*, *18*(4). doi.10.1029/2004GB002247

Kienast, S. S., Kienast, M., Mix, A. C., Calvert, S. E., and François, R. (2007). Thorium-230 normalized particle flux and sediment focusing in the Panama Basin region during the last 30,000 years. *Paleoceanography*, *22*(2). doi.10.1029/2006PA001357

Killingley, J. S., Johnson, R. F., and Berger, W. H. (1981). Oxygen and carbon isotopes of individual shells of planktonic foraminifera from Ontong-Java Plateau, equatorial Pacific. *Palaeogeography, Palaeoclimatology, Palaeoecology*, *33*(1-3), 193-204. doi.10.1016/0031-0182(81)90038-9

Kim, S. T., and O'Neil, J. R. (1997). Equilibrium and nonequilibrium oxygen isotope effects in synthetic carbonates. *Geochimica et cosmochimica acta*, *61*(16), 3461-3475. doi.10.1016/S0016-7037(97)00169-5

Koutavas, A., and Lynch-Stieglitz, J. (2004). Variability of the marine ITCZ over the eastern Pacific during the past 30,000 years. In *The Hadley circulation: Present, past and future* (pp. 347-369). Springer, Dordrecht.

Koutavas, A., and Sachs, J. P. (2008). Northern timing of deglaciation in the eastern equatorial Pacific from alkenone paleothermometry. *Paleoceanography*, *23*(4). doi.10.1029/2008PA001593

Lea, D. W., and Boyle, E. A. (1991). Barium in planktonic foraminifera, *Geochim. Cosmochim. Acta*, 55(11), 3321–3331.

Lea, D. W., Pak, D. K., and Spero, H. J. (2000). Climate impact of late Quaternary equatorial Pacific sea surface temperature variations. *Science*, *289*(5485), 1719-1724. doi.10.1126/science.289.5485.1719

Leduc, G., Vidal, L., Tachikawa, K., Rostek, F., Sonzogni, C., Beaufort, L., and Bard, E. (2007). Moisture transport across Central America as a positive feedback on abrupt climatic changes. *Nature*, *445*(7130), 908-911. doi.10.1038/nature05578

Levitus, S., and Boyer, T. P. (1994). *World Ocean Atlas 1994*, *NOAA Atlas NESDIS* (Vol. 4, Temperature, 4, p. 129). Silver Spring, Md: NOAA.

Liu, Z., and Alexander, M. (2007). Atmospheric bridge, oceanic tunnel, and global climatic teleconnections. *Reviews of Geophysics*, *45*(2). doi.10.1029/2005RG000172.

Liu, Z., and Yang, H. (2003). Extratropical control of tropical climate, the atmospheric bridge and oceanic tunnel. *Geophysical Research Letters*, *30*(5). doi.10.1029/2002GL016492

Lonsdale, P. (1977). Deep-tow observations at the mounds abyssal hydrothermal field, Galapagos Rift. *Earth and Planetary Science Letters*, *36*(1), 92-110. doi.10.1016/0012-821X(77)90191-1

Loubere, P. (1999). A multiproxy reconstruction of biological production and oceanography in the eastern equatorial Pacific for the past 30,000 years. *Marine micropaleontology*, *37*(2), 173-198. doi.10.1016/S0377-8398(99)00013-4

Loubere, P. (2001). Nutrient and oceanographic changes in the eastern equatorial Pacific from the last full glacial to the present. *Global and Planetary Change*, *29*(1-2), 77-98. doi.10.1016/S0921-8181(00)00085-0

Loubere, P., Fariduddin, M., and Murray, R. W. (2003). Patterns of export production in the eastern equatorial Pacific over the past 130,000 years. *Paleoceanography*, *18*(2). doi.10.1029/2001PA000658

Loubere, P., Mekik, F., Francois, R., and Pichat, S. (2004). Export fluxes of calcite in the eastern equatorial Pacific from the Last Glacial Maximum to present. *Paleoceanography*, *19*(2). doi.10.1029/2003PA000986

Lyle, M., Murray, D. W., Finney, B. P., Dymond, J., Robbins, J. M., and Brooksforce, K. (1988). The record of late Pleistocene biogenic sedimentation in the eastern tropical Pacific Ocean. *Paleoceanography*, *3*(1), 39-59. doi.10.1029/PA003i001p00039

Lyle, M. W., Prahl, F. G., and Sparrow, M. A. (1992). Upwelling and production changes inferred from a temperature record in the central equatorial Pacific. *Nature*, *355*(6363), 812-815. doi.10.1038/355812a0

Lyle, M., Mitchell, N., Pisias, N., Mix, A., Martínez, J. I., and Paytan, A. (2005). Do geochemical estimates of sediment focusing pass the sediment test in the equatorial Pacific? *Paleoceanography*, *20*(1). doi.10.1029/2004PA001019

Mackey, D. J., O'Sullivan, J. O., and Watson, R. J. (2002). Iron in the western Pacific: a riverine or hydrothermal source for iron in the Equatorial Undercurrent?. *Deep Sea Research Part I: Oceanographic Research Papers*, *49*(5), 877-893. doi.10.1016/S0967-0637(01)00075-9

Malevich, S. B., Vetter, L., and Tierney, J. E. (2019). Global Core Top Calibration of $\delta^{18}O$ in Planktic Foraminifera to Sea Surface Temperature. *Paleoceanography and Paleoclimatology*, *34*(8), 1292-1315. doi.10.1029/2019PA003576

Marchitto, T. M., Lynch-Stieglitz, J., and Hemming, S. R. (2005). Deep Pacific $CaCO_3$ compensation and glacial-interglacial atmospheric CO_2. *Earth and Planetary Science Letters*, *231*(3-4), 317-336. doi.10.1016/j.epsl.2004.12.024

Martin, P. A., and Lea, D. W. (2002). A simple evaluation of cleaning procedures on fossil benthic foraminiferal Mg/Ca. *Geochemistry, Geophysics, Geosystems*, *3*(10), 1-8. doi.10.1029/2001GC000280

Martínez, I., Rincon, D., Yokoyama, Y., and Barrows, T. (2006). Foraminifera and coccolithophorid assemblage changes in the Panama Basin during the last deglaciation: Response to sea-surface production induced by a transient climate change. *Palaeogeography, Palaeoclimatology, Palaeoecology*, *234*(1), 114-126. doi.10.1016/j.palaeo.2005.10.022

Martínez-Ruiz, F., Paytan, A., Gonzalez-Muñoz, M. T., Jroundi, F., Abad, M. D. M., Lam, P. J.,... and Kastner, M. (2019). Barite formation in the ocean: Origin of amorphous and crystalline precipitates. *Chemical Geology*, *511*, 441-451. doi.10.1016/j.chemgeo.2018.09.011

Martínez-Ruiz, F., and González Muñoz, M. T. (2020). Barite precipitation on suspended organic matter in the mesopelagic zone. doi.10.3389/feart.2020.567714

McManus, J. F., Francois, R., Gherardi, J. M., Keigwin, L. D., and Brown-Leger, S. (2004). Collapse and rapid resumption of Atlantic meridional circulation linked to deglacial climate changes. *nature*, *428*(6985), 834-837. doi.10.1038/nature02494.

McCorkle, D. C., and Keigwin, L. D. (1994). Depth profiles of $\delta^{13}C$ in bottom water and core top *C. wuellerstorfi* on the Ontong Java Plateau and Emperor Seamounts. *Paleoceanography*, *9*(2), 197-208. doi.10.1029/93PA03271

Milliman, J. D., Farnsworth, K. L., and Albertin, C. S. (1999). Flux and fate of fluvial sediments leaving large islands in the East Indies. *Journal of Sea Research*, *41*(1-2), 97-107. doi.10.1016/S1385-1101(98)00040-9

Monnin, C., Jeandel, C., Cattaldo, T., and Dehairs, F. (1999). The marine barite saturation state of the world's oceans. *Marine Chemistry*, *65*(3-4), 253-261. doi.10.1016/S0304-4203(99)00016-X

Mohtadi, M., Steinke, S., Groeneveld, J., Fink, H. G., Rixen, T., Hebbeln, D., ... and Herunadi, B. (2009). Low-latitude control on seasonal and interannual changes in planktonic foraminiferal flux and shell geochemistry off south Java: A sediment trap study. *Paleoceanography*, *24*(1). doi.10.1029/2008PA001636

Moutin, T., Wagener, T., Caffin, M., Fumenia, A., Gimenez, A., Baklouti, M., ... and Verneil, A. D. (2018). Nutrient availability and the ultimate control of the biological carbon pump in the western tropical South Pacific Ocean. *Biogeosciences*, *15*(9), 2961-2989.

Murray, R. W., Knowlton, C., Leinen, M., Mix, A. C., and Polsky, C. H. (2000). Export production and carbonate dissolution in the central equatorial Pacific Ocean over the past 1 Myr. *Paleoceanography*, *15*(6), 570-592. doi.10.1029/1999PA000457

Nelson, D. M., Tréguer, P., Brzezinski, M. A., Leynaert, A., and Quéguiner, B. (1995). Production and dissolution of biogenic silica in the ocean: revised global estimates, comparison with regional data and relationship to biogenic sedimentation. *Global Biogeochemical Cycles*, *9*(3), 359-372. doi.10.1029/95GB01070

Oppo, D. W., and Fairbanks, R. G. (1989). Carbon isotope composition of tropical surface water during the past 22,000 years. *Paleoceanography*, *4*(4), 333-351. doi.10.1029/PA004i004p00333

Pedersen, T. F. (1983). Increased production in the eastern equatorial Pacific during the last glacial maximum (19,000 to 14,000 yr BP). *Geology*, *11*(1), 16-19. doi.10.1130/0091-7613(1983)11<16:IPITEE>2.0.CO;2

Pedersen, T. F., Nielsen, B., and Pickering, M. (1991). Timing of late Quaternary production pulses in the Panama Basin and implications for atmospheric CO_2. *Paleoceanography*, *6*(6), 657-677. doi.10.1029/91PA02532

Pennington, J. T., Mahoney, K. L., Kuwahara, V. S., Kolber, D. D., Calienes, R., and

Chavez, F. P. (2006). Primary production in the eastern tropical Pacific: A review. *Progress in oceanography*, *69*(2-4), 285-317. doi.10.1016/j.pocean.2006.03.012

Pena, L. D., Calvo, E., Cacho, I., Eggins, S., and Pelejero, C. (2005). Identification and removal of Mn Mg rich contaminant phases on foraminiferal tests: Implications for Mg/Ca past temperature reconstructions. *Geochemistry, Geophysics, Geosystems*, *6*(9). doi.10.1029/2005GC000930

Pena, L. D., Cacho, I., Calvo, E., Pelejero, C., Eggins, S., and Sadekov, A. (2008). Characterization of contaminant phases in foraminifera carbonates by electron microprobe mapping. *Geochemistry, Geophysics, Geosystems*, *9*(7). doi.10.1029/2008GC002018

Pena, L. D., Goldstein, S. L., Hemming, S. R., Jones, K. M., Calvo, E., Pelejero, C., and Cacho, I. (2013). Rapid changes in meridional advection of Southern Ocean intermediate waters to the tropical Pacific during the last 30 kyr. *Earth and Planetary Science Letters*, *368*, 20-32. doi.10.1016/j.epsl.2013.02.028

Perks, H. M., Charles, C. D., and Keeling, R. F. (2002). Precessionally forced production variations across the equatorial Pacific. *Paleoceanography*, *17*(3), 9-1. doi.10.1029/2000PA000603

Pichat, S., Sims, K. W., François, R., McManus, J. F., Brown Leger, S., and Albarède, F. (2004). Lower export production during glacial periods in the equatorial Pacific derived from $(^{231}Pa/^{230}Th)_{xs,0}$ measurements in deep-sea sediments. *Paleoceanography*, *19*(4). doi.10.1029/2003PA000994

Pichevin, L., Reynolds, B. C., Ganeshram, R. S., Cacho, I., Pena, L., Keefe, K., and Ellam, R. M. (2009). Enhanced carbon pump inferred from relaxation of nutrient limitation in the glacial ocean. *Nature*, *459*(7250), 1114-1117. doi.10.1038/nature08101

Ploug, H., Kühl, M., Buchholz-Cleven, B., and Jørgensen, B. B. (1997). Anoxic aggregates-an ephemeral phenomenon in the pelagic environment?. *Aquatic Microbial Ecology*, *13*(3), 285-294. doi.10.3354/ame013285

Putnis, C. V., Kowacz, M., and Putnis, A. (2008). The mechanism and kinetics of DTPA-promoted dissolution of barite. *Applied Geochemistry*, *23*(9), 2778-2788. doi.10.1016/j.apgeochem.2008.07.006

Poggemann, D. W., Hathorne, E. C., Nürnberg, D., Frank, M., Bruhn, I., Reißig, S., and Bahr, A. (2017). Rapid deglacial injection of nutrients into the tropical Atlantic via Antarctic Intermediate Water. *Earth and Planetary Science Letters*, *463*, 118-126. doi.10.1016/j.epsl.2017.01.030

Rafter, P. A., and Charles, C. D. (2012). Pleistocene equatorial Pacific dynamics inferred from the zonal asymmetry in sedimentary nitrogen isotopes. *Paleoceanography*, *27*(3). doi.10.1029/2012PA002367

Rafter, P. A., Sigman, D. M., Charles, C. D., Kaiser, J., and Haug, G. H. (2012). Subsurface tropical Pacific nitrogen isotopic composition of nitrate: Biogeochemical signals and their transport. *Global Biogeochemical Cycles*, *26*(1). doi.10.1029/2010GB003979

Rafter, P. A., and Sigman, D. M. (2016). Spatial distribution and temporal variation

of nitrate nitrogen and oxygen isotopes in the upper equatorial Pacific Ocean. *Limnology and Oceanography*, *61*(1), 14-31. doi.10.1002/lno.10152

Ravelo, A. C., and Hillaire-Marcel, C. (2007). Chapter eighteen the use of oxygen and carbon isotopes of foraminifera in paleoceanography. *Developments in marine geology*, *1*, 735-764. doi.10.1016/S1572-5480(07)01023-8

Richaud, M., Loubere, P., Pichat, S., and Francois, R. (2007). Changes in opal flux and the rain ratio during the last 50,000 years in the equatorial Pacific. *Deep Sea Research Part II: Topical Studies in Oceanography*, *54*(5-7), 762-771. doi.10.1016/j.dsr2.2007.01.012

Rink, S., Kühl, M., Bijma, J., and Spero, H. J. (1998). Microsensor studies of photosynthesis and respiration in the symbiotic foraminifer Orbulina universa. *Marine Biology*, *131*(4), 583-595. doi.10.1007/s002270050350

Rosenthal, Y., and Lohmann, G. P. (2002). Accurate estimation of sea surface temperatures using dissolution-corrected calibrations for Mg/Ca paleothermometry. *Paleoceanography*, *17*(3), 16-1. doi.10.1029/2001PA000749

Rosenthal, Y., Oppo, D. W., and Linsley, B. K. (2003). The amplitude and phasing of climate change during the last deglaciation in the Sulu Sea, western equatorial Pacific.*Geophysical Research Letters*, *30*(8). doi.10.1029/2002GL016612

Rosenthal, Y., Perron-Cashman, S., Lear, C. H., Bard, E., Barker, S., Billups, K., ... and Wilson, P. A. (2004). Interlaboratory comparison study of Mg/Ca and Sr/Ca measurements in planktonic foraminifera for paleoceanographic research. *Geochemistry, Geophysics, Geosystems*, *5*(4). doi.10.1029/2003GC000650

Rushdi, A. I., McManus, J., and Collier, R. W. (2000). Marine barite and celestite saturation in seawater. *Marine Chemistry*, *69*(1-2), 19-31. doi.10.1016/S0304-4203(99)00089-4

Russell, A. D., and Spero, H. J. (2000). Field examination of the oceanic carbonate ion effect on stable isotopes in planktonic foraminifera. *Paleoceanography*, *15*(1), 43-52. doi.10.1029/1998PA000312

Sadekov, A., Eggins, S. M., De Deckker, P., Ninnemann, U., Kuhnt, W., and Bassinot, F. (2009). Surface and subsurface seawater temperature reconstruction using Mg/Ca microanalysis of planktonic foraminifera *Globigerinoides ruber*, *Globigerinoides sacculifer*, and *Pulleniatina obliquiloculata*. *Paleoceanography*, *24*(3). doi.10.1029/2008PA001664

Sarmiento, J. L., Gruber, N., Brzezinski, M. A., and Dunne, J. P. (2004). High latitude controls of thermocline nutrients and low latitude biological production. *Nature*, *427*(6969), 56-60. doi.10.1038/nature02127

Sarnthein, M., Winn, K., Duplessy, J. C., and Fontugne, M. R. (1988). Global variations of surface ocean production in low and mid latitudes: Influence on CO_2 reservoirs of the deep ocean and atmosphere during the last 21,000 years. *Paleoceanography*, *3*(3), 361-399. doi.10.1029/PA003i003p00361

Schiebel, R., and Hemleben, C. (2017). *Planktic foraminifers in the modern ocean* (pp. 1-358). Berlin: Springer.

Schlitzer, R., Anderson, R. F., Dodas, E. M., Lohan, M., Geibert, W., Tagliabue, A.,

... and Lechtenfeld, O. J. (2018). The GEOTRACES intermediate data product 2017. *Chemical Geology*, *493*, 210-223. doi.10.1016/j.chemgeo.2018.05.040

Schlitzer, Reiner, Ocean Data View, https://odv.awi.de, 2020

Schwarz, B., Mangini, A., and Segl, M. (1996). Geochemistry of a piston core from Ontong Java Plateau (western equatorial Pacific): Evidence for sediment redistribution and changes in paleoproduction. *Geologische Rundschau*, *85*(3), 536-545. doi.10.1007/BF02369008

Sigman, D. M., and Boyle, E. A. (2000). Glacial/interglacial variations in atmospheric carbon dioxide. *Nature*, *407*(6806), 859-869. doi.10.1038/35038000

Shackleton, N. J., Hall, M. A., Line, J., and Shuxi, C. (1983). Carbon isotope data in core V19-30 confirm reduced carbon dioxide concentration in the ice age atmosphere. *Nature*, *306*(5941), 319-322. doi.10.1038/306319a0

Smith, M. W., Zeigler Allen, L., Allen, A. E., Herfort, L., and Simon, H. M. (2013). Contrasting genomic properties of free-living and particle-attached microbial assemblages within a coastal ecosystem. *Frontiers in microbiology*, *4*, 120. doi.10.3389/fmicb.2013.00120

Stenni, B., Jouzel, J., Masson-Delmotte, V., Röthlisberger, R., Castellano, E., Cattani, O., ... and Udisti, R. (2004). A late-glacial high-resolution site and source temperature record derived from the EPICA Dome C isotope records (East Antarctica). *Earth and Planetary Science Letters*, *217*(1-2), 183-195. doi.10.1016/S0012-821X(03)00574-0

Spero, H. J., Bijma, J., Lea, D. W., and Bemis, B. E. (1997). Effect of seawater carbonate concentration on foraminiferal carbon and oxygen isotopes. *Nature*, *390*(6659), 497-500. doi.10.1007/978-3-642-58646-0_21

Spero, H. J., and Lea, D. W. (2002). The cause of carbon isotope minimum events on glacial terminations. *Science*, *296*(5567), 522-525. doi.10.1126/science.1069401

Spero, H. J., Mielke, K. M., Kalve, E. M., Lea, D. W., and Pak, D. K. (2003). Multispecies approach to reconstructing eastern equatorial Pacific thermocline hydrography during the past 360 kyr. *Paleoceanography*, *18*(1). doi.10.1029/2002PA000814

Spindler, M., Hemleben, C., Salomons, J. B., and Smit, L. P. (1984). Feeding behavior of some planktonic foraminifers in laboratory cultures. *The Journal of Foraminiferal Research*, *14*(4), 237-249. doi.10.2113/gsjfr.14.4.237

Sternberg, E., Tang, D., Ho, T. Y., Jeandel, C., and Morel, F. M. (2005). Barium uptake and adsorption in diatoms. *Geochimica et Cosmochimica Acta*, *69*(11), 2745-2752. doi.10.1016/j.gca.2004.11.026

Stott, L., Poulsen, C., Lund, S., and Thunell, R. (2002). Super ENSO and global climate oscillations at millennial time scales. *science*, *297*(5579), 222-226. doi.10.1126/science.1071627

Stroobants N., Dehairs F., Goeyens L., Vanderheijden N. and Vangrieken R. (1991). Barite formation in the southern-ocean water column. *Marine Chemistry*. 35, 411–421.

Stuiver, M., Grootes, P.M., 2000. GISP2 oxygen isotope ratios. Quaternary Research

53, 277-284.Suter, E. A., Pachiadaki, M., Taylor, G. T., Astor, Y., and Edgcomb, V. P. (2018).
Free-living chemoautotrophic and particle-attached heterotrophic prokaryotes dominate microbial assemblages along a pelagic redox gradient. *Environmental microbiology*, *20*(2), 693-712. doi.10.1111/1462-2920.13997

Takagi, H., Kimoto, K., Fujiki, T., Saito, H., Schmidt, C., Kucera, M., and Moriya, K. (2019). Characterizing photosymbiosis in modern planktonic foraminifera. *Biogeosciences*, *16*(17), 3377-3396. doi.10.5194/bg-16-3377-2019

Toggweiler, J. R. and Lea, D. (2010). Temperature differences between the hemispheres and ice age climate variability, *Paleoceanography*, 25, PA2212, doi.10.1029/2009PA001758.

Toggweiler, J. R., J. L. Russell, and S. R. Carson (2006), Midlatitude westerlies, atmospheric CO_2, and climate change during the ice ages, *Paleoceanography*, 21, PA2005, doi:10.1029/2005PA001154.

Vetter, L., Spero, H. J., Russell, A. D. and Fehrenbacher, J. S. (2013). LA-ICP-MS depth profiling perspective on cleaning protocols for elemental analyses in planktic foraminifers. *Geochem. Geophys. Geosyst.* 14, 2916–2931. doi.10.1002/ggge.20163

Visser, K., Thunell, R., and Stott, L. (2003). Magnitude and timing of temperature change in the Indo-Pacific warm pool during deglaciation. *Nature*, *421*(6919), 152-155. doi.10.1038/nature01297

Weldeab, S., Lea, D. W., Schneider, R. R., and Andersen, N. (2007a). 155,000 years of West African monsoon and ocean thermal evolution. *science*, *316*(5829), 1303-1307. doi.10.1126/science.1140461

Weldeab, S., Lea, D. W., Schneider, R. R., and Andersen, N. (2007b). Centennial scale climate instabilities in a wet early Holocene West African monsoon. *Geophysical Research Letters*, *34*(24). doi.10.1029/2007GL031898

Winckler, G., Anderson, R. F., Jaccard, S. L., and Marcantonio, F. (2016). Ocean dynamics, not dust, have controlled equatorial Pacific production over the past 500,000 years. *Proceedings of the National Academy of Sciences*, *113*(22), 6119-6124. doi.10.1073/pnas.1600616113

WOCE Hydrographic Programme, WHP (2002): Physical oceanography during Thomas G. Thompson cruise 3250TN026_1 on section P10. PANGAEA, doi.10.1594/PANGAEA.294012

Wolgemuth, K. (1970). Barium analyses from the first Geosecs test cruise. *Journal of Geophysical Research*, *75*(36), 7686-7687. doi.10.1029/JC075i036p07686

Wu, G., and Berger, W. H. (1989). Planktonic foraminifera: Differential dissolution and the Quaternary stable isotope record in the west equatorial Pacific. *Paleoceanography*, *4*(2), 181-198. doi.10.1029/PA004i002p00181

Wu, G., Yasuda, M. K., and Berger, W. H. (1991). Late Pleistocene carbonate stratigraphy on Ontong-Java Plateau in the western equatorial Pacific. *Marine Geology*, *99*(1-2), 135-150. doi.10.1016/0025-3227(91)90087-K

Yu, J., Day, J., Greaves, M., and Elderfield, H. (2005). Determination of multiple element/calcium ratios in foraminiferal calcite by quadrupole ICP-MS. *Geochemistry, Geophysics, Geosystems*, *6*(8). doi.10.1029/2005GC000964

Yu, J., Elderfield, H., Greaves, M., and Day, J. (2007). Preferential dissolution of benthic foraminiferal calcite during laboratory reductive cleaning. *Geochemistry, Geophysics, Geosystems*, *8*(6). doi.10.1029/2006GC001571

Zeebe, R. E., Bijma, J., and Wolf-Gladrow, D. A. (1999). A diffusion-reaction model of carbon isotope fractionation in foraminifera. *Marine Chemistry*, *64*(3), 199-227. doi.10.1016/S0304-4203(98)00075-9

Zhang, R., and Delworth, T. L. (2005). Simulated tropical response to a substantial weakening of the Atlantic thermohaline circulation. *Journal of climate*, *18*(12), 1853-1860. doi.10.1175/JCLI3460.1

Zhang, J., Wang, P., Li, Q., Cheng, X., Jin, H., and Zhang, S. (2007). Western equatorial Pacific production and carbonate dissolution over the last 550 kyr: Foraminiferal and nannofossil evidence from ODP Hole 807A. *Marine Micropaleontology*, *64*(3-4), 121-140. doi.10.1016/j.marmicro.2007.03.003

3.8. Supplementary Information

3.8.1. Mg/Ca SST, $\delta^{18}O$, and species depth habitat reconstructions

3.8.1.1. Reconstructions in the WEP

Mg/Ca and $\delta^{18}O$ IFA measurements fall within the range of bulk foraminifera data for all species in the WEP (Figure S2a and b). Upper water column hydrography and species calcification depths are reconstructed using Mg/Ca-derived temperatures and $\delta^{18}O$ analyses (Figure S3a and b). Mg/Ca ratios are converted to SST using the multi-species equation of Anand et al. (2003; without depth corrections for $\Delta[CO_3^{2-}]$). The Mg/Ca-derived temperature estimates reflect the unique depth habitat of foraminifera species (Anand et al., 2003; Farmer et al., 2007; Elderfield and Ganssen, 2000; Jonkers and Kučera, 2015; Mohtadi et al., 2009). IFA Mg/Ca SST values are ~ 5ºC and 8ºC warmer in surface-dwelling *T. sacculifer* than deeper-dwelling species *N. dutertrei* and *P. obliquiloculata*, respectively. Holocene Mg/Ca-derived temperatures are in general agreement with seasonal modern upper water column SST in the WEP (0 - 200 m, three-month average SST, Levitus and Boyer, 1994; Table S1). A seasonal bias in foraminiferal growth may result in more shells sampled from months within species temperature and salinity preference (Malevich et al., 2019). There is no discernable bias toward a three-month averaged season in our dataset (Figure S3) and annual average is used for depth habitat predictions. Mg/Ca SST reconstructions

using 6GGC and 55GGC cores predict that in the modern ocean, *T. sacculifer* would have calcified between 50 m and 75 m, and *N. dutertrei* and *P. obliquiloculata* would have calcified between 150 m and 200 m (Figure S3a and b). These calcification depths are consistent with previous work that suggests *T. sacculifer* inhabit the upper thermocline (~ 50 - 75 m in the WEP), while *N. dutertrei* and *P. obliquiloculata* calcify within the lower thermocline near the deep chlorophyll maximum (~ 100 - 200 m in the Western Pacific Gyre, e.g., Moutin et al., 2018) (Fairbanks and Wiebe, 1980; Fairbanks et al., 1982).

Mg/Ca-SST IFA predicts depth habitats that are consistent with the depth habitats inferred from IFA $\delta^{18}O$ data (Figure S3a and b). To determine $\delta^{18}O$-based calcification depths, $\delta^{18}O$ measurements in recent samples are compared to equilibrium $\delta^{18}O$ of the modern ocean ($\delta^{18}O_{eq}$), calculated using the Kim and O'Neil, (1997) equation:

$$SST = 14.32 - 4.23 (\delta^{18}O_{eq} - \delta^{18}O_{sw}) + 0.07 (\delta^{18}O_{eq} - \delta^{18}O_{sw})^2$$

where seawater $\delta^{18}O$ is calculated from modern seasonal salinity (three-month average SSS, Levitus and Boyer, 1994) using the relationship of Conroy et al., (2014), and SST is the modern seasonal temperature of the upper water column (Levitus and Boyer, 1994). The approximation of $\delta^{18}O$ ($\delta^{18}O_{eq}$) is useful for comparing measured $\delta^{18}O$ to seawater $\delta^{18}O$ of the modern thermocline. Species-specific factors controlling calcification (biological 'vital' effects) can create offsets depending on ambient temperature (Ravelo and Hillaire-Marcel, 2007 and references therein). However, when we apply *T. sacculifer* (-0.11‰, Spero et al., 2003) and *N. dutertrei* (+0.25‰, Bouvier-Soumagnac and Duplessy, 1985) corrections, our depth habitat interpretations are not impacted; therefore, the values we report are without offset corrections. $\delta^{18}O$ measurements in *T. sacculifer* (-2.2 and -1.2‰) are much lower than *N. dutertrei* (Δ -1.0 and -0.9‰) and *P. obliquiloculata* (Δ -1.25 and -0.55‰ for 6GGC and 55GGC cores, respectively), consistent with *T. sacculifer* calcifying in warmer and/or fresher conditions of the upper thermocline (Farmer et

al., 2007; Elderfield and Ganssen, 2000; Fairbanks et al., 1982; Jonkers and Kučera, 2015; Mohtadi et al., 2009). Our approach (using cores 6GGC and 55GGC) predicts that *T. sacculifer* calcified between 100 - 150 m, and *N. dutertrei* and *P. obliquiloculata* calcified between 150 - 200 m (Figure S1a and b). The calcification depth for *T. sacculifer* is slightly lower than that implied by our Mg/Ca SST data and that of Farmer et al., 2007 (based on $\delta^{18}O$; 50 - 75 m) and Anand et al., 2003 (based on Mg/Ca and $\delta^{18}O$; 50 - 75 m). $\delta^{18}O$ calcification depth reconstructions are consistent with depths predicted with Mg/Ca SST reconstructions.

The shallower 6GGC core is likely to be the better preserved of the OJP cores and is used for the timeseries reconstruction. The bulk shell record from the LGM to the modern indicates a gradual increase in Mg/Ca SST by ~ 3ºC and $\delta^{18}O$ decreases by ~ 1.0‰ (Figure S4a), consistent with other reconstructions in the WEP (Lea et al., 2000; Rosenthal et al., 2003; Stott et al., 2002; Visser et al., 2003; de Garidel-Thoron et al., 2007). Multispecies analysis of Mg/Ca SST and $\delta^{18}O$ could reflect changes in thermocline depth, and differences between upper and lower thermocline dwelling species have been used to track changes in water column stratification (Spero et al., 2003; Sadekov et al., 2009; Mohtadi et al., 2011; Sharri et al., 2013). The difference in IFA Mg/Ca SST between *T. sacculifer* and *N. dutertrei*, and *T. sacculifer* and *P. obliquiloculata* varies by less than 1ºC from the LGM to the Holocene and decreases by ~ 1ºC from the LGM to the deglacial. These values are within the error of the Mg/Ca SST calibration equation (Anand et al., 2003). The difference in IFA $\delta^{18}O$ values between *T. sacculifer* and *N. dutertrei*, and *T. sacculifer* and *P. obliquiloculata* do not change from the LGM to the Holocene. Inconsistently, between the LGM and deglacial, the change in $\delta^{18}O$ values increase between *T. sacculifer* and *N. dutertrei* by ~ 0.1‰, but do not change between *T. sacculifer* and *P. oblquiloculata*. Thermocline reconstructions are inconclusive and suggest little change through the record.

3.8.1.2. *Reconstructions in the EEP*

IFA measurements of Mg/Ca and $\delta^{18}O$ are consistent with bulk foraminifera data for all species in the EEP (Figure S2e and f). Mg/Ca SST and $\delta^{18}O$ data from three species reflect the shallow thermocline of the EEP. The Mg/Ca-derived temperature estimate reflects the unique depth habitat of foraminifera species: IFA Mg/Ca SST reconstructions in the EEP are ~ 6 ºC and 4ºC warmer in surface-dwelling *T. sacculifer* than deeper-dwelling species *N. dutertrei* and *P. obliquiloculata* (at core sites 43JC and 24JC, respectively). Mg/Ca SST reconstructions indicate that *T. sacculifer* and non-spinose species span a depth range of 25 - 50 m at core site 43JC and 20 - 75 m at core site 24JC (Figure S3c and d), with *T. sacculifer* inhabiting the upper thermocline (~ 25 m in the EEP) and *N. dutertrei* and *P. obliquiloculata* calcifying at the base of the thermocline, likely near the deep chlorophyll maximum (~ 50 - 75 m in the EEP, e.g., Pennington et al., 2006).

As in the WEP, $\delta^{18}O$ reconstructions confirm the calcification depths predicted using Mg/Ca SST reconstructions. *Trilobatus sacculifer* IFA $\delta^{18}O$ measurements (-2.3‰ and -1.5‰) are much lower than *N. dutertrei* (Δ -2.2‰ and -1.4‰) and *P. obliquiloculata* (Δ -1.3‰ and -1.4‰ at 43JC and 24C core sites, respectively), consistent with recording conditions of the warmer mixed layer. $\delta^{18}O_{eq}$ predicts *T. sacculifer* calcified between 10 - 25 m, and *N. dutertrei* and *P. obliquiloculata* calcified between 45 - 65 m. We define the calcification depth of *T. sacculifer* as the 'upper thermocline' and the calcification depth of *N. dutertrei* and *P. obliquiloculata* as the 'base of thermocline' for both WEP and EEP regions.

Through the entire record, Mg/Ca SST values for each species gradually increase by approximately 3.0ºC and 1.5ºC, and $\delta^{18}O$ decreases by approximately 1.3‰ and 1.0‰, for 43JC and 24JC core sites, respectively (Figure S4c and d). These values reflect warming since the LGM reported by others; the EEP warm pool is thought to have warmed the same magnitude as in the WEP, and the cold tongue is thought to have warmed less than the warm pool (Lea et al., 2000; Dubois et al., 2009; Ford et al., 2015). The difference in Mg/Ca SST between *T. sacculifer* and *N. dutertrei*, and *T. sacculifer* and *P. obliquiloculata* does not change from the LGM to

the deglacial nor the deglacial to the Holocene at 43JC nor at 24JC core sites. The difference in $\delta^{18}O$ between *T. sacculifer* and *N. dutertrei* increases by 0.4‰ at core site 43JC and decreases by 1.4‰ at core site 24JC between the LGM and the deglacial. $\delta^{18}O$ between *T. sacculifer* and *N. dutertrei* increases by 0.3‰ at 43JC and 24JC core sites between the deglacial and the Holocene, but in contrast, $\delta^{18}O$ between *T. sacculifer* and *P. obliquiloculata* decreases by 0.4‰ at core site 43JC and increases by 0.3‰ at core site 24JC. Overall, our records do not show any consistent changes in the thermocline structure.

3.8.2. $\delta^{13}C$ timeseries reconstructions

$\delta^{13}C$ of foraminiferal calcite reflects $\delta^{13}C$ of seawater DIC as well as biological 'vital' effects. Vital effects are species specific and reflect the influence of photosynthetic symbionts and respiration (Zeebe et al., 1999), as well as the species-specific way that foraminifera respond to $[CO_3^{2-}]$ (Bijma et al., 1999; Spero et al., 1997; Russell and Spero, 2000). While normalization factors are often used to correct for species-specific offsets, we chose to report $\delta^{13}C$ without normalization because it is unclear how $[CO_3^{2-}]$ differences between locations in this study impacts $\delta^{13}C$, and how $[CO_3^{2-}]$ impacts each species. Additionally, if non-spinose foraminifera are calcifying within a POM microhabitat, it is likely that $\delta^{13}C$ of DIC is affected by respiration of and within POM. Indeed, the $\delta^{13}C$ of particulate organic carbon in POM is thought to be distinct from that of seawater and vary through the upper water column (1 - 200 m) by ~ 2‰ (Eadie and Jeffrey, 1973), but it is unclear how the POM isotopic environment effects foraminiferal calcite. Instead of reconstructing thermocline $\delta^{13}C$ of seawater DIC, we evaluate the record of the $\delta^{13}C$ of calcite.

The bulk shell $\delta^{13}C$ and the IFA data are in good agreement (Figure S2). In general, $\delta^{13}C$ gradually increases by ~ 0.5‰ from the LGM to the Holocene at all core sites as recorded by each species, likely recording the signature of increased DIC of seawater over the deglaciation thought to reflect an increase in the size of the terrestrial biosphere (review in Ravelo and Hillaire-Marcel, 2007). A striking feature

of the $\delta^{13}C$ records is the rapid negative excursion during the deglacial, consistent with the results of others (Shackleton et al., 1983; Oppo and Fairbanks, 1989; Spero and Lea, 2002; Anderson et al., 2009; Hayes et al., 2011; Pena et al., 2013; Poggemann et al., 2017). From the LGM to deglacial, $\delta^{13}C$ decreases by 0.2‰ and 0.8‰ in the WEP for *T. sacculifer* and *N. dutertrei*, respectively, and by 0.3‰, 0.4‰, and 0.3‰ in the EEP for *T. sacculifer*, *N. dutertrei*, and *P. obliquiloculata*, respectively (Figure S4). This excursion is distinct from the gradual increase through the record and likely reflects local changes in the $\delta^{13}C$ of seawater DIC at the core locations.

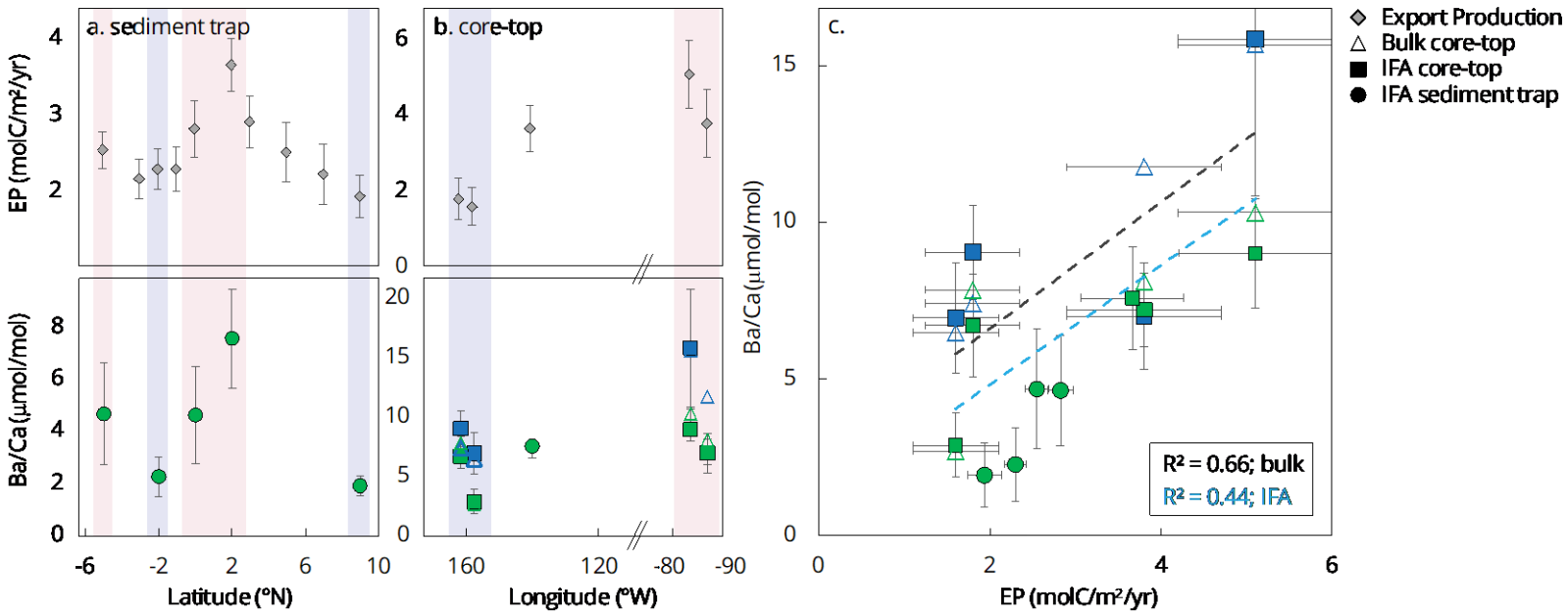

Figure 3.1. a. Ba/Ca ratios and zonal and longitudinal patterns of export production. Mean Ba/Ca ratios (µmol/mol, 1σ) in individual shells (IFA) of sediment trap (circles) *P. obliquiloculata* along a 140°W transect (H. Cynar, Senior Thesis, UC Davis, 2016; JGOFS EqPac Process Study sediment trap, Aug-Sep 1992) and annual average export production (diamonds; EP (molC/m^2/yr); DeVries and Weber, 2017 SIMPLE-TRIM model using NPP from Behrenfeld and Falkowski, 1997 VGPM model); b. Ba/Ca ratios in core-top IFA (squares) and bulk (triangles) *N. dutertrei* and *P. obliquiloculata* from this study, compared to EP. Highest EP and Ba/Ca ratios occur in upwelling zones both latitudinally (a) and longitudinally (b) (shaded in pink); c. correlation between EP and Ba/Ca ratios and coefficient of determination (R^2) for IFA (blue; y = 1.9x + 1.0) and bulk shells (black; y = 2.0x + 2.6). Samples of *N. dutertrei* are in blue and *P. obliquiloculata* are in green.

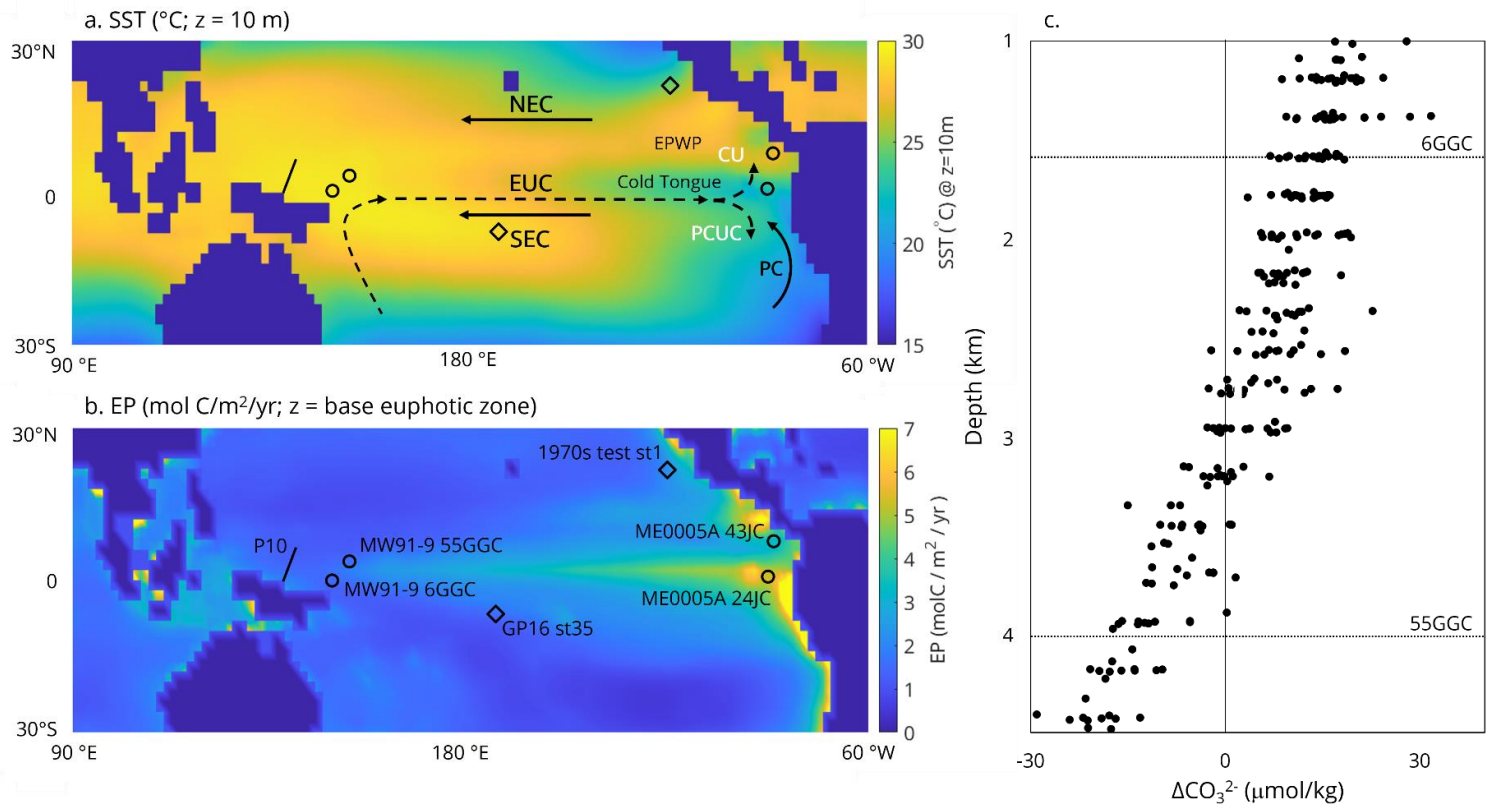

Figure 3.2. Map of core locations (circles), GEOSECS stations used to obtain [Ba] (diamonds), and generalized circulation patterns. a. Modeled Sea Surface Temperature (SST, °C) at 10 m; Currents described are the NEC (North Equatorial Current), the SEC (South Equatorial Current), and the EUC (Equatorial Under Current), which is fed by SAMW (Sub-Antarctic Mode Water, not shown). The EUC bifurcates into the CU (California Undercurrent) and the PCUC (Peru-Chile Under Current) in the eastern equatorial Pacific; b. Annual average export production (EP, mol C/m^2/yr) at the base of the euphotic zone from the SIMPLE-TRIM model (DeVries and Weber, 2017) and core sites MW91-9 6GGC and MW91-9 55GGC on the Ontong Java Plateau and ME0005A-24JC in the Panama Basin and ME0005A-43JC on the Cocos Ridge. c. Profile of $\Delta[CO_3^{2-}]$ from WOCE Cruise P10, station 10 - 40 and ΔCO_3^{2-} calculated from Total Alkalinity, DIC, and other parameters using ODV (equilibrium constants follow Dickson et al., 2007; Schlitzer, 2020). The dotted line shows $\Delta[CO_3^{2-}]$ at the depth of cores 6GGC and 55GGC. The black line defines when $\Delta CO_3^{2-} = 0$. Samples from core 55GGC bathed in water with $\Delta[CO_3^{2-}] < 0$ may experience some calcite dissolution.

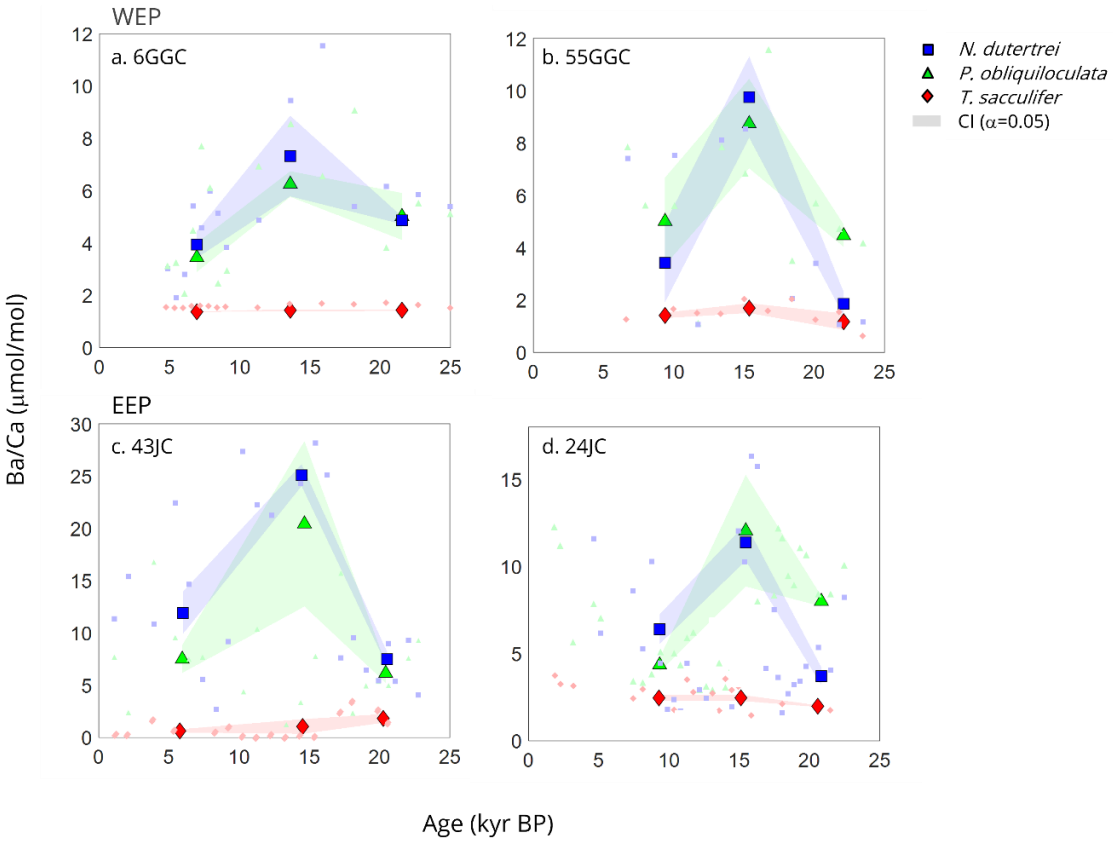

Figure 3.3. Statistical analysis of bulk shell Ba/Ca data. Mean Ba/Ca ratios and 95% confidence interval for the Holocene (~ 5 - 11 ka BP), deglacial (~ 11 - 18 ka BP), and LGM (~ 18 - 25 ka BP) time intervals in cores a. 6GGC; b. 55GGC; c. 43JC; d. 24JC for *N. dutertrei* (blue squares), *P. obliquiloculata* (green triangles), and *T. sacculifer* (red diamonds). All Ba/Ca data points for the timeseries are plotted as smaller shapes. Shaded area is the 95% confidence interval for each time interval. Data from deglacial intervals are significantly different from the Holocene and LGM intervals in all cores within 95% confidence.

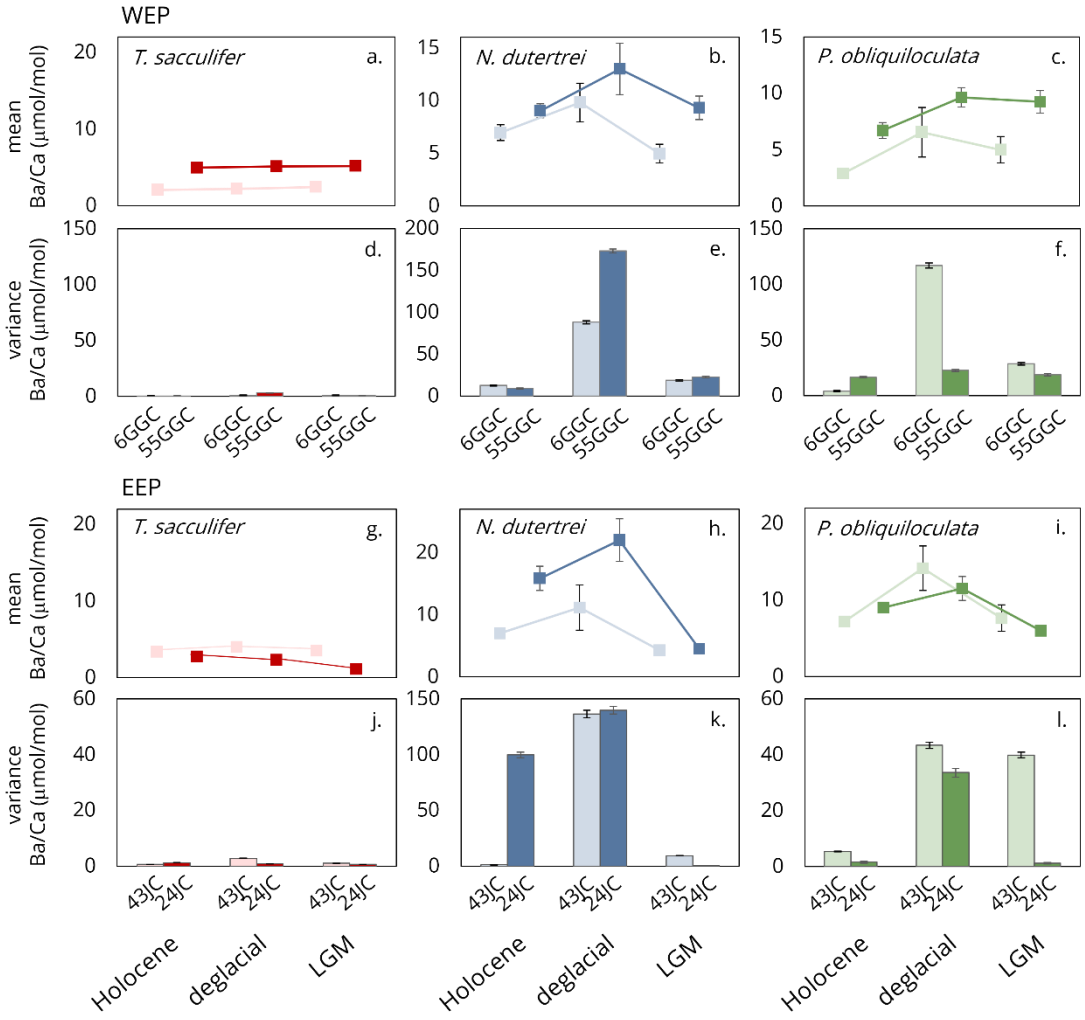

Figure 3.4. Statistical analysis of individual foraminifera Ba/Ca data. Mean individual foraminifera Ba/Ca (µmol/mol) ratios (squares) and 95% confidence intervals (error bars) of *T. sacculifer* (red), *N. dutertrei* (blue), and *P. obliquiloculata* (green) of Holocene (~ 6 ka BP), deglacial (~ 15 ka BP), and LGM (~ 20 ka BP) samples for the WEP (a-c) and EEP (g-i). Variance (bars) is the average intra-shell variance and error bars are ± 5% for the WEP (d-f) and EEP (j-l).

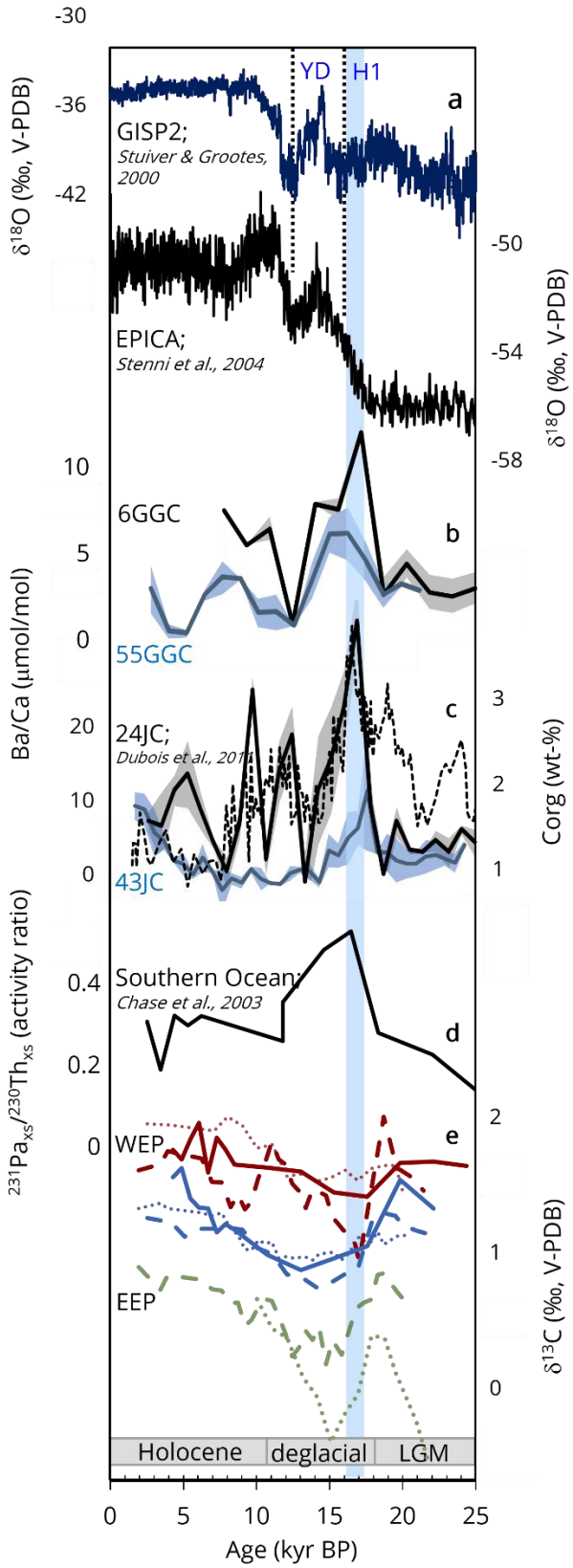

Figure 3.5. Comparison of regional climate and productivity records with foraminifera geochemistry. a. record of $\delta^{18}O$ of the Greenland ice core GISP2 (Stuiver and Grootes, 2000) and of the Antarctica EPICA Dome C (Stenni et al., 2004) as a reference to reflect the northern and southern hemisphere climate signals. Cold time-periods are Heinrich Stadial 1 (H1) and Younger Dryas (YD), and blue band coincides with the productivity peak at ~16 - 17 ka BP; b. average and 1σ compiled *N. dutertrei* and *P. obliquiloculata* Ba/Ca (µmol/mol) from 6GGC (black) and 55GGC (blue) core sites; c. and 24JC (black) and 43JC (blue) core sites with export production (inferred from organic carbon (wt-%)) in 24JC core (Dubois et al., 2011) overlain (dashed line); d. $^{231}Pa_{xs}/^{230}Th_{xs}$ (activity ratio) data from core NBP9802-6PC (61.9ºS, 170ºW; Chase et al., 2003) from the Pacific sector of the Southern Ocean reflecting southern-sourced productivity; e. species specific $\delta^{13}C_c$ (‰, V-PDB) data — *T. sacculifer* (red), *N. dutertrei* (blue), and *P. obliquiloculata* (green) — for 6GGC (solid lines), 24JC (dashed lines), and 43JC (dotted lines). Core sites 43JC and 24JC data is a three-point running mean to show a similar resolution as the 6GGC core site data.

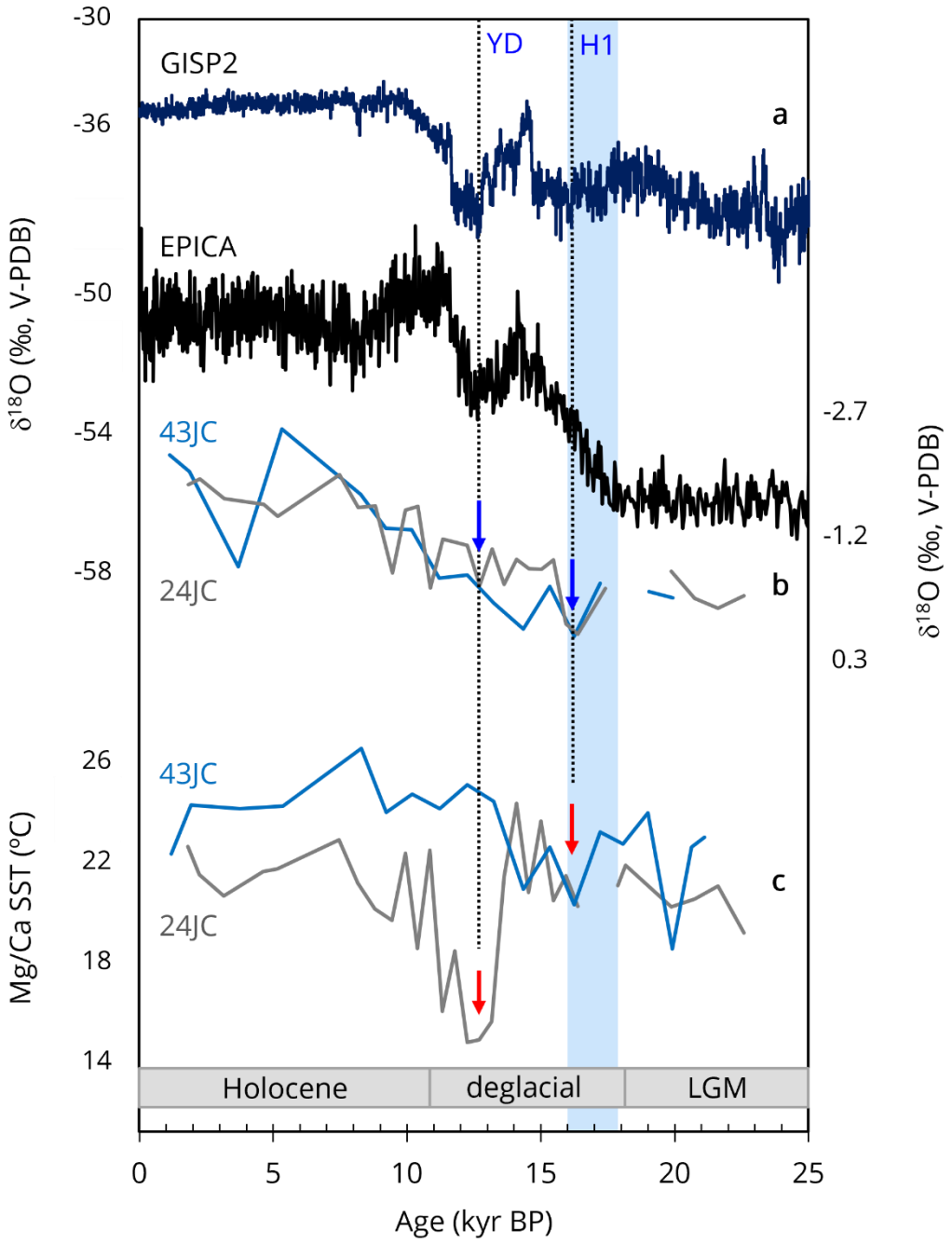

Figure 3.6. The climate and hydrographic record of the EEP. a. record of $\delta^{18}O$ of GISP2 (Stuiver and Grootes, 2000) and EPICA Dome C (Stenni et al., 2004). Cold intervals Heinrich Stadial 1 (H1) and the Younger Dryas (YD), and the productivity peak from Figure 5 (blue box) are indicated; b. *T. sacculifer* $\delta^{18}O$ (‰, V-PDB) from 43JC (blue) and 24JC (grey) core sites; c. *T. sacculifer* Mg/Ca SST (°C) from 43JC and 24JC core sites. Cold intervals lead to surface ocean cooling in the EPP indicated by an increase in $\delta^{18}O$ (blue arrows) and a decrease in Mg/Ca SST (red arrows).

Table 3.1. Surface ocean conditions at core sites. SST and SSS from Levitus and Boyer (1994) three-month seasonal climatology.

Core	Lat, Lon	Water depth (m)	SST (ºC) @UT*	SST (ºC) @BT*	SSS (psu) @UT*	SSS (psu) @BT*	NPP (molC/m^2/yr)**	EP (molC/m^2/yr)***	Ba (nmol/L) @UT*	Ba (nmol/L) @BT*
MW91-9 6GGC	2.02ºS, 156.93ºE	1625	28.9 ± 0.24	22.4 ± 2.56	35.1 ± 0.15	35.5 ± 0.13	17.9 ± 1.9	1.6 ± 1.0	32.6	33.1
MW91-9 55GGC	0.01ºS, 161.77ºE	4024	28.7 ± 0.24	20.8 ± 3.26	35.0 ± 0.16	35.3 ± 0.11	18.7 ± 1.9	1.8 ± 1.1	32.6	33.1
ME0005A-43JC	7.86ºN, 83.6ºW	1364	26.3 ± 1.41	16.1 ± 1.34	33.5 ± 0.47	34.8 ± 0.15	20.2 ± 2.9	3.8 ± 1.8	43.0	50.0
ME0005A-24JC	0.02ºN, 86.5ºW	2941	22.1 ± 1.21	17.0 ± 2.09	34.5 ± 0.28	35.0 ± 0.04	24.4 ± 3.2	5.1 ± 1.8	43.0	50.0

*UT (upper thermoclines) is 50-75m for 6GGC and 55GGC and 10-30m for 43JC and 24JC; BT (base of thermoclines) is 150-200m for 6GGC and 55GGC and 50-100m for 43JC and 24JC. Ba from GEOTRACES cruise GP16 station 35 (10.25°S, 210.00°E; Schlitzer et al., 2018) for 6GGC and 55GGC and GEOSECS 1970 test station (28.48°N, 121.63°W; Wolgemuth, 1970) for 43JC and 24JC.

**NPP (net primary production) from the VGPM model (Behrenfeld and Falkowski, 1997).

***EP, export production at the base of the euphotic zone, as defined in the SIMPLE TRIM model (DeVries and Weber, 2017).

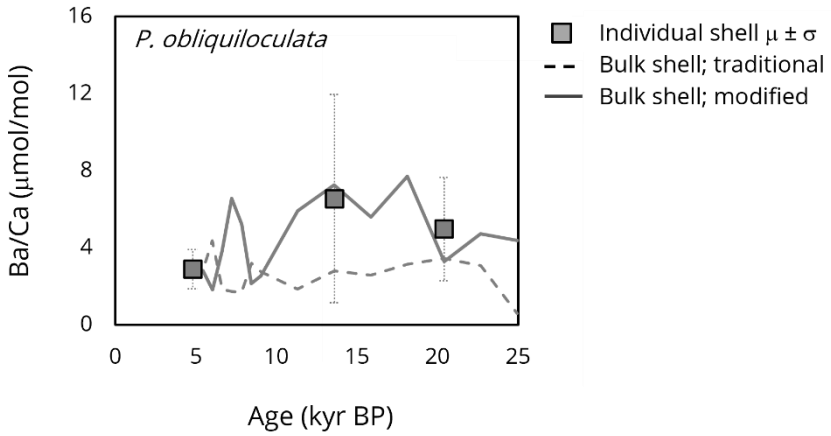

Figure S3.1. Comparison of the mean and standard deviation (1σ) of individual foraminifera (boxes) Ba/Ca (μmol/mol) ratios vs. bulk shell *P. obliquiloculata* that have undergone 'traditional cleaning' (dashed lines) and 'modified cleaning' (solid lines) (after Fritz-Endres & Fehrenbacher, 2020). Results demonstrate that the IFA and bulk data derived following the modified cleaning protocol agree. The shells that were prepared for bulk analysis using the traditional cleaning protocol are lower than the IFA data, likely due to dissolution during the cleaning process. Data is from core site 6GGC.

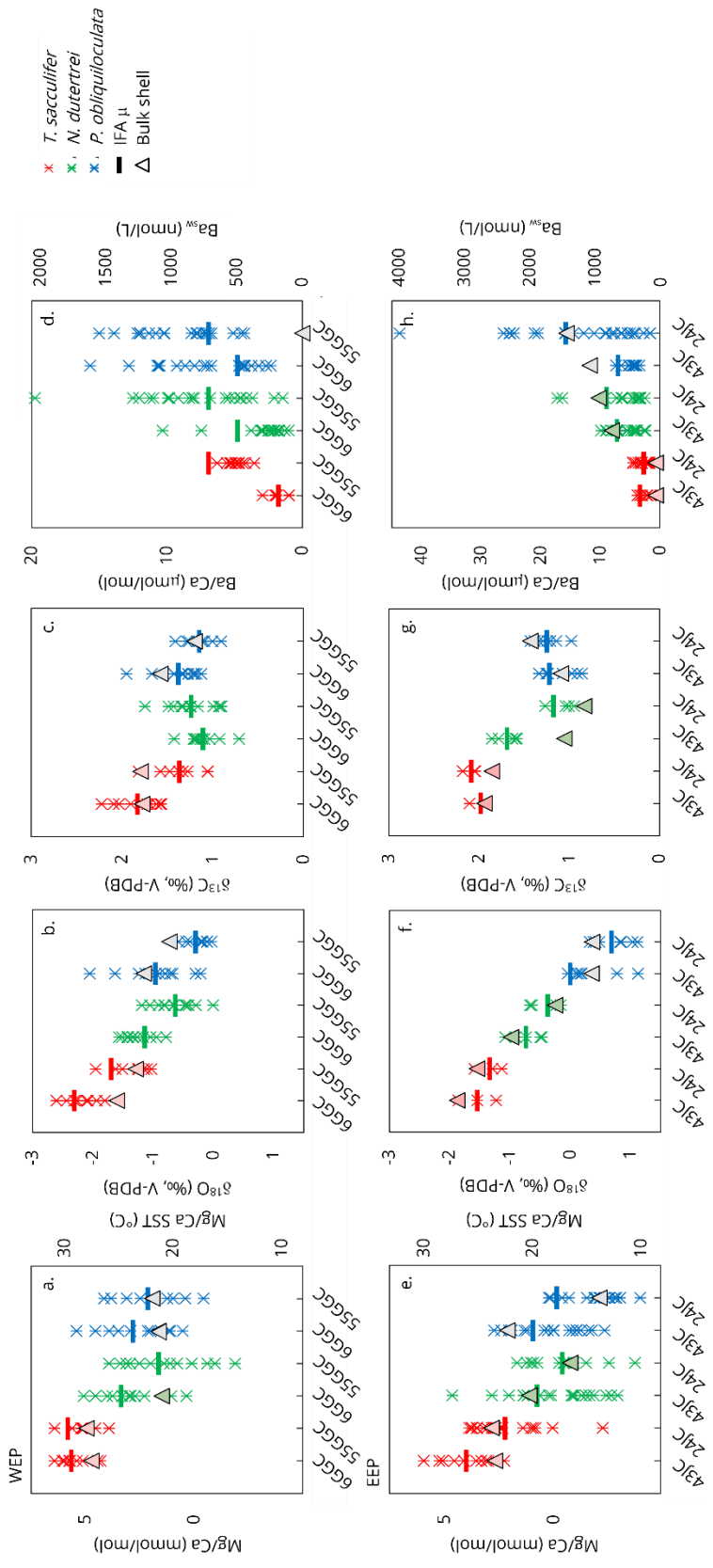

Figure S3.2. Recent (2.3 - 8.2 ka BP) individual foraminifera (stars) and mean individual foraminifera (rectangles) and bulk foraminifera (triangles) data (red is *T. sacculifer*, green is *P. obliquiloculata*, blue is *N. dutertrei*) from WEP cores 6GGC and 55GGC (a-d) and EEP cores 43JC and 24JC (e-f). Mg/Ca (mmol/mol) is converted to Mg/Ca SST using the Anand et al., (2003) multi-species equation, and Ba/Ca (µmol/mol) is used to estimate Ba of seawater (Ba_{sw}, nmol/L) using the relationship for *T. sacculifer* established by Hönisch et al., (2011) and for *N. dutertrei* and *P. obliquiloculata* established by Fehrenbacher et al., (2018).

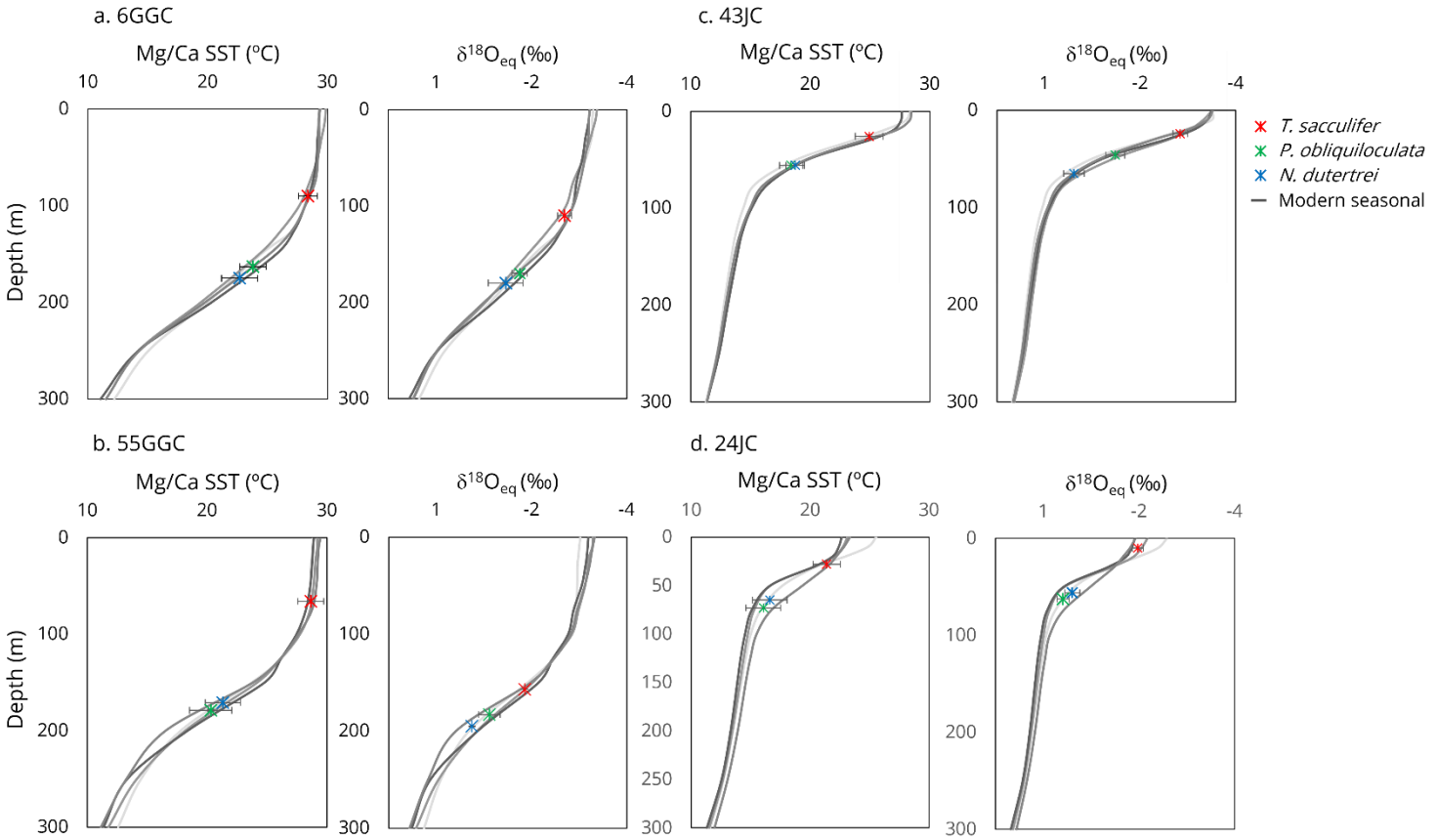

Figure S3.3. Mean individual foraminifera Mg-derived temperature and $\delta^{18}O$ compared to the seasonal (each grey line is three-month mean, e.g., May-June-July) temperatures and calculated seawater $\delta^{18}O$ of the upper 300 m surface ocean for a. 6GGC; b. 55GGC; c. 43JC, and d. 24JC. Estimated $\delta^{18}O$ of the modern ocean ($\delta^{18}O_{eq}$) is derived using the Kim & O'Neil, (1997) equation, where seawater $\delta^{18}O$ is calculated from modern seasonal salinity (Levitus & Boyer, 1994) using the relationship of Conroy et al., (2014), and temperature is that of the upper surface ocean (Levitus & Boyer, 1994).

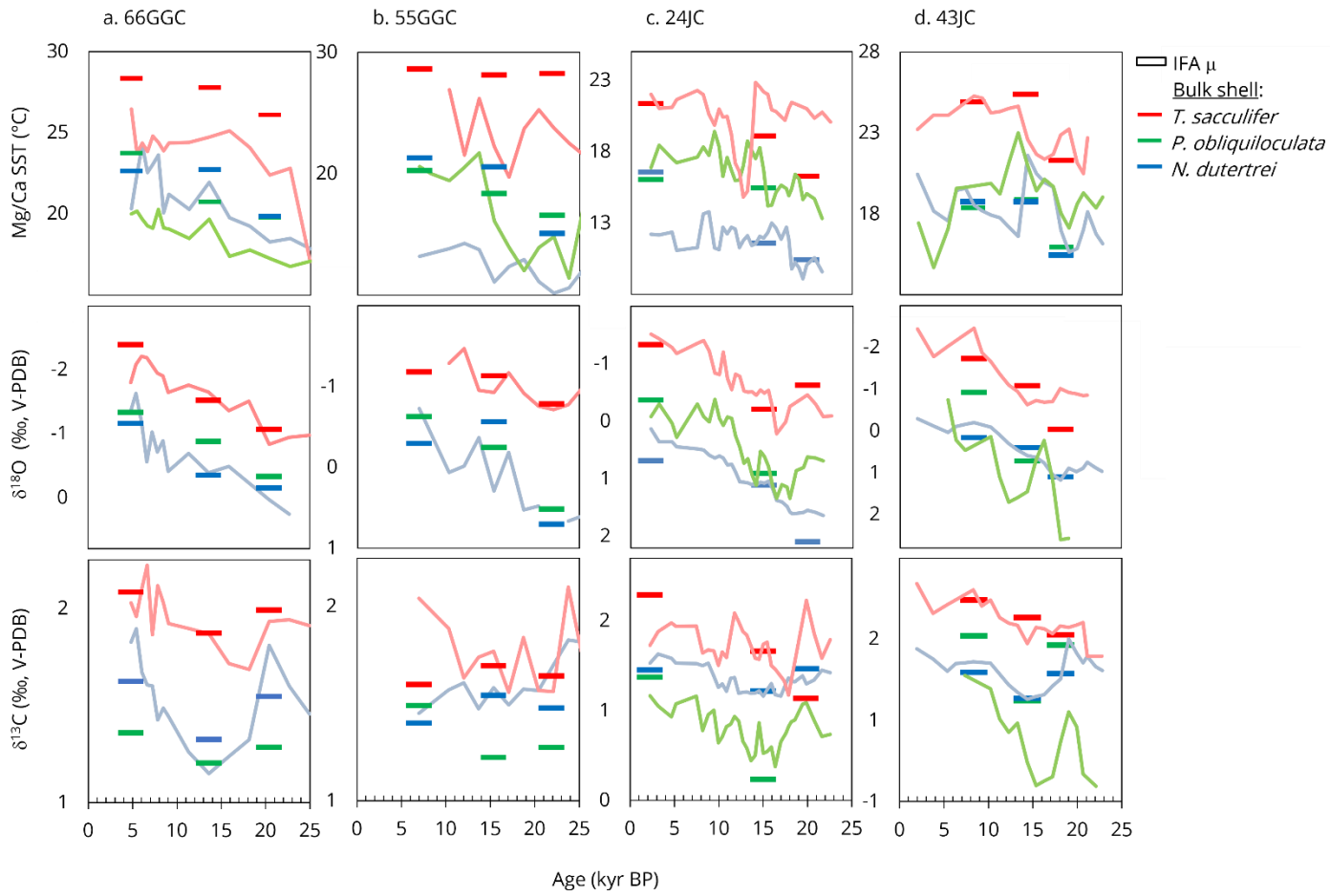

Figure S3.4. Mean individual foraminifera data (bars) and bulk shell data (lines) of *T. sacculifer* (red), *N. dutertrei* (blue), and *P. obliquiloculata* (green). Lines are 2-point running mean for the higher resolution 43JC and 24JC cores. a. 6GGC, b. 55GGC, c. 43JC, and d. 24JC core site data. No bulk shell isotope data exists for *P. obliquiloculata* 6GGC and 55GGC cores.

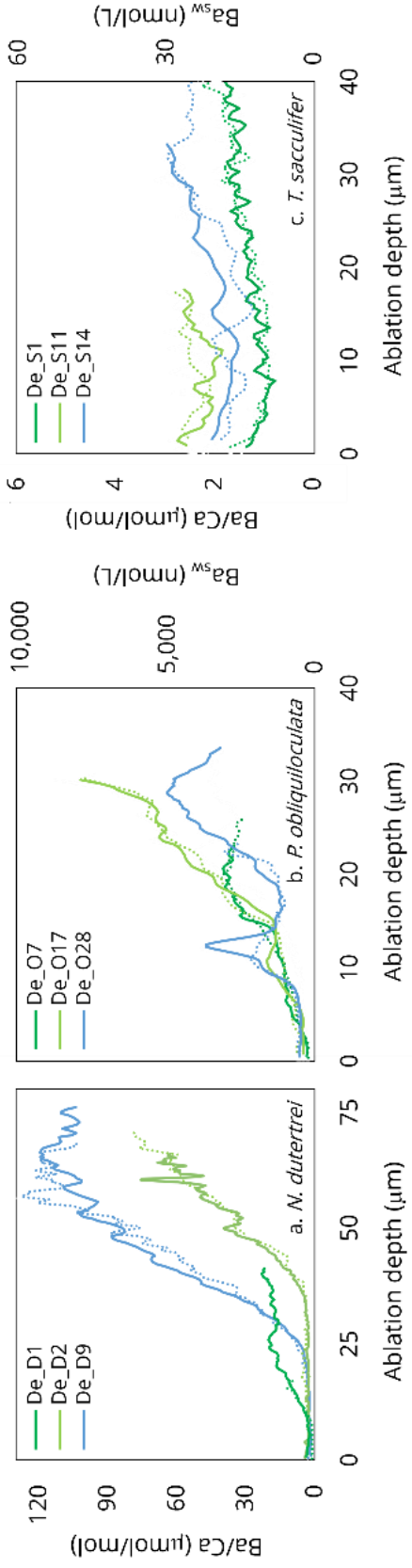

Figure S3.5. Intra-shell laser ablation ICP-MS Ba/Ca (µmol/mol) and estimated Ba_{sw} (nmol/L) ratios in three example specimens of a. *N. dutertrei* b. *P. obliquiloculata*, and c. *T. sacculifer* from core 6GGC. Dashed lines are repeat laser ablation analyses of the solid line of the same color.

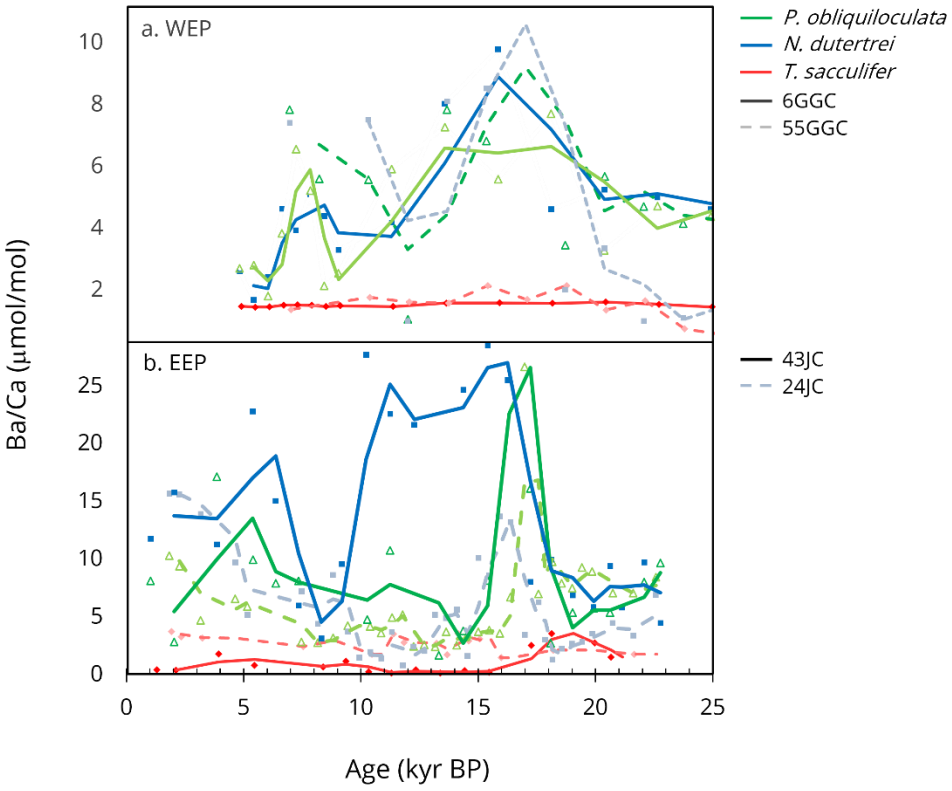

Figure S3.6. Timeseries of bulk shell Ba/Ca (µmol/mol) ratios of the timeseries for a. WEP core sites 6GGC (solid line) and 55GGC (dashed line) and b. EEP core sites 43JC (solid line) and 24JC (dashed line) Ba/Ca *N. dutertrei* (blue) and *P. obliquiloculata* (green) and *T. sacculifer* data. Lines are two-point running mean to highlight major temporal changes. All data are plotted as small shapes for reference.

Table S3.1. Geochemical data of individual foraminifera measured via laser ablation ICP-MS and bulk shells measured via solution ICP-MS from the same intervals.

			Individual shells					Bulk shells				
MW91-9 6GGC		Age (ka BP)	Ba/Ca (μmol/mol)	Mg/Ca (mmol/mol)	Mg/Ca SST* (°C)	$\delta^{18}O$ (VPDB, ‰)	$\delta^{13}C$ (VPDB, ‰)	Ba/Ca (μmol/mol)	Mg/Ca (mmol/mol)	Mg/Ca SST* (°C)	$\delta^{18}O$ (VPDB, ‰)	$\delta^{13}C$ (VPDB, ‰)
	T. sacculifer	4.8	5.2 ± 1.8	4.9 ± 0.7	28.4 ± 1.6	-2.20 ± 0.30	1.83 ± 0.24	1.4	4.29	26.5	-1.60	1.61
		13.6	2.7 ± 1.8	4.6 ± 0.8	27.8 ± 2.0	-1.33 ± 0.46	1.62 ± 0.35	1.5	4.02	24.7	-1.45	1.62
		20.4	3.6 ± 1.1	4.0 ± 0.6	26.1 ± 1.6	-0.87 ± 0.23	1.74 ± 0.22	1.5	3.69	22.4	-0.64	1.68
	N. dutertrei	4.8	6.9 ± 3.5	2.9 ± 0.8	22.7 ± 3.0	-0.96 ± 0.73	1.38 ± 0.23	2.6	1.25	20.2	-1.15	1.58
		13.6	9.8 ± 9.4	2.9 ± 0.9	22.7 ± 4.5	-0.16 ± 0.61	1.08 ± 0.20	8.0	1.31	21.9	-0.19	0.90
		20.4	5.7 ± 4.4	2.3 ± 0.7	19.9 ± 3.5	0.05 ± 0.49	1.30 ± 0.80	5.2	1.03	18.3	0.23	0.90
	P. obliquiloculata	4.8	2.9 ± 2.0	3.2 ± 0.6	23.8 ± 2.2	-1.25 ± 0.33	1.11 ± 0.17	2.7	2.30	20.2	x	x
		13.6	6.5 ± 10.8	2.5 ± 0.7	20.8 ± 3.0	-0.68 ± 0.48	0.96 ± 0.24	7.3	2.23	19.7	x	x
MW91-9 55GGC		20.4	5.0 ± 5.4	2.3 ± 0.5	19.8 ± 2.2	-0.13 ± 0.37	1.04 ± 0.18	3.3	1.80	17.3	x	x
	T. sacculifer	7.0	4.9 ± 0.7	5.0 ± 1.0	28.6 ± 2.2	-1.36 ± 0.41	1.35 ± 0.24	1.3	4.29	26.9	-1.29	1.79
		15.4	4.7 ± 0.8	4.8 ± 0.8	28.1 ± 1.9	-1.14 ± 0.34	1.45 ± 0.19	1.4	3.33	22.2	-0.95	1.49
		20.4	5.2 ± 0.5	4.8 ± 0.9	28.3 ± 2.3	-0.79 ± 0.41	1.39 ± 0.29	1.0	3.23	23.8	-0.76	1.59
	N. dutertrei	7.0	9.0 ± 3.0	2.6 ± 0.7	21.3 ± 2.9	-0.25 ± 0.25	1.15 ± 0.14	7.4	1.25	13.8	-0.73	1.20
		15.4	13 ± 6.6	2.4 ± 0.7	20.6 ± 3.2	-0.57 ± 0.51	1.29 ± 0.26	8.5	1.03	11.1	-0.37	1.33
		20.4	4.8 ± 2.4	1.5 ± 0.4	15.1 ± 3.3	0.70 ± 0.47	1.23 ± 0.33	1.0	0.95	10.2	0.48	1.52
	P. obliquiloculata	7.0	6.7 ± 3.3	2.4 ± 0.7	20.3 ± 3.5	-0.62 ± 0.46	1.24 ± 0.25	7.8	2.42	20.6	x	x
		15.4	9.6 ± 4.8	2.0 ± 0.6	18.4 ± 3.2	-0.25 ± 0.49	0.97 ± 0.20	6.8	1.56	15.7	x	x
ME0005A 43JC		20.4	9.2 ± 4.4	1.7 ± 0.6	16.6 ± 3.8	0.52 ± 1.16	1.03 ± 0.43	4.7	1.34	14.0	x	x
	T. sacculifer	8.3	3.4 ± 0.8	3.7 ± 0.8	24.9 ± 2.3	-1.54 ± 0.31	1.98 ± 0.09	0.8	3.35	24.2	-1.87	1.94
		14.4	4.0 ± 1.7	3.9 ± 1.1	25.4 ± 3.2	-0.89 ± 0.19	1.77 ± 0.43	0.3	2.48	20.85	-0.78	1.50
		18.1	3.5 ± 1.0	2.7 ± 0.7	21.3 ± 2.8	0.16 ± 1.19	1.56 ± 0.27	3.6	2.91	22.63	-0.72	1.65
	N. dutertrei	8.3	7.0 ± 5.0	1.8 ± 0.5	18.7 ± 1.5	0.35 ± 0.43	1.09 ± 0.17	11.8	2.25	19.78	0.11	1.22
		14.4	8.0 ± 10.5	2.2 ± 0.6	18.7 ± 2.2	0.59 ± 0.31	0.77 ± 0.21	24.6	2.66	21.62	0.78	0.77
		18.1	4.3 ± 3.0	1.4 ± 0.5	15.5 ± 1.7	1.29 ± 0.37	1.08 ± 0.25	10.0	1.50	15.24	1.37	1.36
	P. obliquiloculata	8.3	7.2 ± 2.3	1.8 ± 0.3	18.4 ± 1.9	-0.05 ± 0.44	1.69 ± 0.11	8.1	2.11	19.04	0.29	1.05
		14.4	14.1 ± 6.6	2.2 ± 0.3	18.9 ± 1.9	0.91 ± 0.20	1.29 ± 0.08	3.8	2.10	19.00	0.56	-0.57
ME0005A 24JC		18.1	7.6 ± 6.3	1.7 ± 0.4	16.0 ± 2.3	1.20 ± 0.20	1.58 ± 0.06	2.7	1.78	17.13	3.19	0.40
	T. sacculifer	2.3	2.7 ± 0.9	2.7 ± 0.6	21.4 ± 3.0	-1.34 ± 0.23	2.09 ± 0.06	0.7	2.62	21.46	-1.55	1.50
		15.0	2.3 ± 0.8	2.3 ± 0.7	19.1 ± 3.2	-0.22 ± 0.58	1.47 ± 0.64	3.1	3.18	23.60	-0.48	1.76
		19.9	1.1 ± 0.6	1.8 ± 0.7	16.3 ± 3.8	-0.63 ± 0.25	0.94 ± 0.08	2.1	2.34	20.18	-0.46	2.03
	N. dutertrei	2.3	15.8 ± 10.0	1.7 ± 1.7	16.6 ± 2.3	0.68 ± 0.31	1.25 ± 0.14	15.7	1.10	11.80	0.37	1.43
		15.0	18.6 ± 11.0	1.1 ± 1.1	11.6 ± 2.0	1.10 ± 0.32	1.02 ± 0.12	10.3	1.10	11.82	1.11	0.90
		19.9	4.5 ± 0.8	0.8 ± 0.8	10.5 ± 1.0	2.09 ± 0.59	1.27 ± 0.65	3.5	1.02	10.94	1.51	1.00
	P. obliquiloculata	2.3	9.0 ± 3.0	1.6 ± 0.4	16.1 ± 2.9	-0.37 ± 0.26	1.18 ± 0.11	9.4	2.00	18.47	-0.25	0.84
		15.0	11.5 ± 5.8	1.3 ± 0.4	15.5 ± 2.9	0.90 ± 0.79	0.03 ± 0.33	5.2	1.48	15.10	0.87	-0.14
		19.9	6.0 ± 1.2	1.5 ± 0.3	15.0 ± 2.7	0.86 ± 0.20	0.89 ± 0.19	8.9	1.57	15.75	0.85	0.90

*Mg/Ca is converted to SST using the multi-species Anand et al., (2003) equation.

Fossil planktic foraminifera microstructure reflects deep equatorial Pacific carbonate ion saturation since the last glacial

Theresa Fritz-Endres[1]; Jennifer Fehrenbacher[1]

[1]Oregon State University, College of Earth, Ocean, and Atmospheric Sciences, Corvallis, OR 97330

In preparation for submission to: *Geochimica et Cosmochimica Acta*

4. Fossil planktic foraminifera microstructure reflects deep equatorial Pacific carbonate ion saturation since the last glacial

4.1 Abstract

Reconstructing deep ocean carbonate ion saturation (ΔCO_3^{2-}) is critical for investigating carbon reorganization in the climate system on glacial-interglacial timescales. Attempts to reconstruct deep ocean ΔCO_3^{2-} primarily focus on geochemical proxies for calcite dissolution/preservation in sediments. Calcite dissolution/preservation is not straightforward because it reflects processes at the sea surface (calcification intensity) and on the seafloor (dissolution and reprecipitation). We use microCT scans of planktic foraminifera *Trilobatus sacculifer*, *Pulleniatina obliquiloculata*, and *Neogloboquadrina dutertrei* to establish a core-top calibration relating shell density to ΔCO_3^{2-} in the equatorial Pacific. We calculate CT number, a metric related to shell density, from microCT data and develop a CT number calibration for quantifying ΔCO_3^{2-}. We use the calibration to explore changes in preservation since the last glaciation using specimens obtained from a 4.3 km core of the central Pacific. We find that the interior calcite of all three species is better preserved during the deglacial and more poorly preserved during the Holocene and glacial periods. In Holocene and glacial specimens, fragile interior calcite is thin or absent, and blocky exterior calcite crystals that are structurally and geochemically distinct from primary calcite are likely reprecipitated from sediment pore fluids. The deglacial specimens appear relatively well preserved, with intact interior calcite. Converting shell density to ΔCO_3^{2-} suggests that deglacial bottom water ΔCO_3^{2-} in the central Pacific was ~10-15 μmol/kg higher than core-top values. The foraminifera-based reconstruction is consistent with other regional reconstructions of deglacial deepwater ΔCO_3^{2-}, suggesting the proxy may be particularly useful in regions where calcite is heavily dissolved, and proxies are complicated by diagenetic alterations.

4.1. Introduction

Deep ocean carbonate ion concentration ($[CO_3^{2-}]$) is critical for investigating changes to the ocean's carbon cycle over major climate transitions. In the deep ocean, calcite saturation ($\Delta CO_3^{2-} = [CO_3^{2-}]_{in\ situ} - [CO_3^{2-}]_{saturation,}$ where the latter term is the thermodynamic equilibrium for calcite mineral based on temperature, salinity, and pressure) influences the dissolution or preservation of calcium carbonate at depth. Over glacial-interglacial periods, ΔCO_3^{2-} impacts the global ocean alkalinity budget (Sigman et al., 1998) and, in the absence of other feedbacks, shifts the Dissolved Inorganic Carbon (DIC) pool away from or toward aqueous CO_2. This shift increases or decreases dissolved CO_2 in seawater, and consequently, CO_2 exchange with the atmosphere (Sigman and Boyle, 2000). Changes in ΔCO_3^{2-} are compensated on the timescale of a few thousand years by a decrease or increase in calcite burial (i.e., calcite compensation, Broecker and Peng, 1987). Therefore, changes in deep ocean ΔCO_3^{2-} reflect changes in carbonate chemistry due to the uptake or release of CO_2 and calcite compensation feedbacks (Anderson and Archer, 2002; Yu et al., 2014). Deep ocean ΔCO_3^{2-} reflects the balance between surface ocean calcite production and calcite dissolution in regions below the lysocline (the depths over which calcite dissolution intensifies). The equatorial Pacific organic matter export is nearly twice that of higher latitude regions (~10-20 g $CaCO_3/m^2/yr$, in the modern ocean; Milliman, 1993) and slight changes in the lysocline depth (~3.5 km in the modern ocean; Global Ocean Data Analysis Project (GLODAP) data set, Key et al., 2004) promote substantial calcite dissolution, followed by compensation feedbacks (Sigman et al., 1998).

Glacial-interglacial changes in deep ocean ΔCO_3^{2-} are not well constrained, and previous work suggests the Pacific glacial ocean experienced either little change (Anderson and Archer, 2002), increased ΔCO_3^{2-} (Broecker and Clark, 2001a; Wu and Berger, 1989), or decreased ΔCO_3^{2-} (Marchitto et al., 2005; Yu et al., 2010; Fehrenbacher and Martin, 2011; Loubere et al., 2004). Attempts to reconstruct deep ocean ΔCO_3^{2-} mainly rely on calcite preservation/dissolution in sediments (e.g.,

Crowley, 1983; Farrell and Prell, 1989; Le and Shackleton, 1992; Anderson and Archer, 2002) and often on the preservation state of foraminifera shells (e.g., Arrhenius, 1952; Broecker and Clark, 2001a; Qin et al., 2017). The preservation state of foraminifera is based on fragmentation indices (Berger, 1968; Ku and Oba, 1978; Thunell, 1976; Mekik and Francois, 2006), the relative abundance of dissolution resistant and dissolution susceptible species (Berger, 1970), the breakdown of shell surfaces (Henrich, 1989; Dittert et al., 1999), or shell weights (Lohmann, 1995; Broecker and Clark, 2001b; Barker et al., 2004), often normalized by shell size (Barker and Elderfield, 2002; Marshall et al., 2013; Osborne et al., 2016; Osborne et al., 2020). Foraminifera geochemistry has been used to reconstruct deep ocean ΔCO_3^{2-}, including the benthic foraminifera $\delta^{11}B$ (Honisch et al., 2008; Yu et al., 2010, Rae et al., 2011), B/Ca (Yu and Elderfield, 2007; Yu et al., 2010) and Zn/Ca (Marchitto et al., 2000), and the dissolution effect on planktic foraminifera Mg/Ca (Fehrenbacher and Martin, 2011).

Foraminifera dissolution is not straightforward. Shells often dissolve from the inside-out, leaving the exterior calcite intact while the interior calcite may be thin or missing (Brown and Elderfield, 1996; Johnstone et al., 2010). For example, in deep ocean cores from the equatorial Pacific (where ΔCO_3^{2-} is low), the interior calcite of robust/thickly calcified specimens are often completely dissolved, although the shell exterior surfaces appear well preserved (Johnstone et al., 2010). Additionally, deep ocean cores of the central Pacific that underlie productive regions for calcifying organisms accumulate mostly calcific sediments. Dissolution in calcific cores may be accompanied by the formation of crusts and reprecipitates from calcite enriched pore water solutions, which may complicate the interpretation of foraminiferal dissolution-based proxies (Kozdon et al., 2013; Pearson and Burgess, 2008; Edgar et al., 2015).

Calcite dissolution proxies are also complicated by processes at the sea surface (calcification intensity), which adds uncertainty to deep ocean ΔCO_3^{2-} reconstructions. Foraminifera within a population, even a population of the same species within a narrow size range, can have significantly naturally variable shell thickness/mass (Schiebel and Hemleben, 2017). Surface processes that can affect

shell calcification intensity and influence the shell wall thickness and mass include nutrient availability (de Villiers, 2004), calcification temperature (Lombard et al., 2009), and the [CO_3^{2-}] of the seawater in which the shell calcified (Spero et al., 1997; Bijma et al., 1999; Russell et al., 2004; Lombard et al., 2010; Moy et al., 2009; Beer et al., 2010; Aldridge et al., 2012; Manno et al., 2012; Marshall et al., 2013; Osborne et al., 2016, 2020; Iwasaki et al., 2014, 2019). It must be shown that foraminifera dissolution-based proxies are predominantly influenced by post-depositional alterations, not surface ocean growth conditions, for the proxy to be useful for deep ocean ΔCO_3^{2-} reconstructions.

Use micro X-ray computed tomography (microCT) on individual foraminifera shells has recently been investigated to relate shell density to ΔCO_3^{2-}. Preliminary work shows that empirical microCT analysis of core-top specimens (using microCT derived greyscale values) are correlated with deep ocean ΔCO_3^{2-}, despite the likely overprinting of surface ocean effects (Johnstone et al., 2010). A more recent microCT study using plankton tow specimens qualitatively correlated shell density and surface ocean [CO_3^{2-}] by normalizing microCT derived greyscale values to calculate 'CT number' (Iwasaki et al., 2014; 2019). These qualitative methods describe density changes within foraminiferal specimens as they are exposed to progressively lower [CO_3^{2-}] and find a reduction of 1 CT number unit per 1 μmol/kg [CO_3^{2-}] of surface waters (Iwasaki et al., 2019).

Here, we apply the CT number method, for the first time, to examine changes to the density of foraminifera shells obtained from sediment traps (modern) and seafloor (fossil) samples. We first present a regional calibration correlating CT number to ΔCO_3^{2-} across a range of ΔCO_3^{2-}. Sediment trap specimens are used to assess the impact of water column ΔCO_3^{2-} separate from the effects of ΔCO_3^{2-} at the seafloor. We compare the new microCT method for calculating shell density to well-established size normalization methods (Marshall et al., 2013; Osborne et al., 2016). We apply the calibration derived from microCT data to explore changes in ΔCO_3^{2-} in the central equatorial Pacific since the last glacial (core site W8402A-14GC, water depth 4.3 km, modern ΔCO_3^{2-} -20.2 μmol/kg). Core W8402A-14GC is below the

modern lysocline but well above the calcite compensation depth (4.8 km, Berger et al., 1976) and likely experienced variable ΔCO_3^{2-} conditions since the last glacial (Murray, 1987). Waters at this depth are influenced by Antarctic Bottom Water and Circumpolar Deep Water that deliver the Southern Ocean chemical signature. In the modern ocean, these water masses are isolated in the deepest ocean and stratified from overlying water masses (Bostock et al., 2004). Finally, we use laser ablation ICP-MS to examine the intra-shell trace element composition of specimens with suspected diagenetic alterations and demonstrate that shell geochemistry is highly affected by reprecipitation on the seafloor and may not be appropriate for paleoceanographic interpretations.

4.2. Methods

4.2.1. Sample preparation

Core-top sediment samples were obtained from the Ontong Java Plateau, the central Pacific, and the Panama Basin (Figure 1; Table 1). Cores span a calcite saturation gradient from super- to under-saturation (ΔCO_3^{2-} range from 13.8 to -20.2 μmol/kg). We purposefully excluded cores where ΔCO_3^{2-} exceeds 20 μmol/kg, as studies suggest specimens show minor or no discernible signs of dissolution above this value (Berger et al., 1982; Johnstone et al., 2010). Samples of *N. dutertrei* were also obtained from three depths of the PARFLUX Panama Basin sediment traps deployed between December of 1979 and November of 1980 (ΔCO_3^{2-} of 0.5 to -7.7 μmol/kg; Honjo, 1982). Samples were washed with DI water over a 63 μm sieve to remove fines. Approximately 6-10 specimens of *Trilobatus sacculifer, Neogloboquadrina dutertrei*, and *Pulleniatina obliquiloculata* species were picked from the 250-355 μm size fraction of core-top samples, and four *N. dutertrei* were picked from the sediment trap samples (Table 1). Previous studies and preliminary data show that ~6-10 specimens are sufficient to record the relationship between CT metrics and $\Delta[CO_3^{2-}]$ (Iwasaki et al., 2019). Down core samples were obtained from

the central Pacific core 14GC at four intervals: a Holocene interval (7.6 kyr BP), two intervals in the deglacial (14.0 and 18.2 kyr BP), and an interval in the glacial (19.6 kyr BP). The age model used for reconstructions is from Lyle et al., (2002) and based on oxygen isotope stratigraphy using benthic and planktic foraminifera $\delta^{18}O$ measurements correlated to the SPECMAP stack of Imbrie et al. (1984). The average sedimentation rate is 1.9 cm/kyr (range 1.6-2.2 cm/kyr), and the average error of age assignments is ~ ± five kyr. Individual shells were weighed with a Sartorius SE2 Microbalance before microCT analysis. The analytical precision of the weight measurements was ± 0.3 μg (1σ) based on three repeated measurements of each shell.

4. 2.2. MicroCT Analysis

Cleaned shells were placed on carbon tape atop an acrylic peg (~40-80 specimens per peg, Figure S1) and scanned at Oregon State University using a Hamamatsu L10711-19 customized for microCT applications (X-ray tube voltage of 100 kV, target current 20 mA, 0.8 s exposure time, 1800 projections through the helical scanning trajectory). The scanning resolution for four scans was 1-2 μm, allowing us to capture shell micro-porosity. A 213 μm diameter piece of the calcite standard NBS-19 was used for each scan to normalize the density distribution of foraminiferal shells. Customized reconstruction code at OSU was used to correct and reconstruct cross-sections throughout the 3D volume of the shell based on a Katsevich inversion formula (Varslot, 2011).

3D tomographic data reconstructions are used to generate stacks of 8-bit greyscale images (Figure 2a). Greyscale values represent the X-ray attenuation coefficient, a property of the attenuation of a beam of X-rays as it passes through a sample and depends on mineral density, object thickness, and microporosity of the sample material (review in Wildenschild et al., 2002). We use the image processing software imageJ (v1.53, Fiji package, *Schindelin, 2012*) to calculate shell volume and CT number, a normalized measure of density. Image stacks are 'denoised' (Figure 2b, upper panel), and the background is corrected with a rolling-ball background correction (radius of 20 pixels selected to accounts for the size of the topography of

the shell without over correcting) (Figure 2b, lower panel). This type of correction was chosen because it removes complicated background (i.e., air, carbon tape, and sediment infill in shell spaces). Individual shell volume is rendered in imageJ (3D object counter plugin v2.0.1) and is subsequently converted to μm^3 using the known resolution of the reconstruction (Figure 2c). To calculate 'volume density' (size-normalized shell weight using volume), individual shell weight is divided by the reconstructed shell volume. ImageJ is also used to render the image stacks as a 3D object (3D Viewer plugin, the threshold is pixel intensity of 20 with no resampling factor) by creating a border between the object and the background based on the selected threshold and a modified 'marching cubes' algorithm extracts an isosurface from the volume data.

CT number is calculated using the greyscale value after Iwasaki et al., 2014 (Figure 2d).

$$Eq.1. \qquad CT\ number = \left[\frac{\mu_{\text{sample}} - \mu_{background}}{\mu_{standard} - \mu_{background}}\right] * 1000$$

where μ_{sample}, $\mu_{background}$, $\mu_{standard}$ are the X-ray attenuation coefficients of a sample, background (air, carbon tape, sediment infill etc.), and calcite standard (NBS-19). The mean greyscale value of voxels (3D pixels) of the sample, background, and standard is used to calculate the X-ray attenuation coefficients. The histogram of greyscale values for each species from each core-top/time interval was compiled, and the mean CT number calculated as

$$Eq.2. \qquad mean\ CT\ number\ = \frac{1}{T} \sum_{n=mean_{background}}^{mean_{standard}} nT_n$$

where n is CT number of the voxel, T_n is total number of voxels with a CT number of n, T is total number of voxels in the shell, $mean_{standard}$ is the mean CT number of the calcite standard, and the $mean_{background}$ is the mean CT number of the background. Because the summation is between the $mean_{background}$ and the $mean_{std}$, the mean CT number represents shell and excludes values of background and other material besides calcite (e.g., sediment infill).

To compare volume density and CT number to size normalization methods, we calculate size normalized shell weight using shell area after Marshall et al. (2013). Individual shells were photographed umbilical side up using a Leica M125 stereomicroscope with a DMC 4500 mounted camera system. ImageJ was used to measure the longest shell diameter and the 2D surface area or silhouette area. Pixel measurements are converted to length (μm) and surface area (μm^2) by calibrating an image taken at the same magnification and working distance as the shell images. Area density was calculated by dividing shell weight by shell surface area.

4.2.3. SEM analysis

Following microCT analysis, individual shells were adhered to an SEM pin stub sample mount with aluminum backed carbon tape and imaged on a FEI Quanta 300 environmental SEM at OSU (high voltage 15 kv, spot size 2-4, pressure 90-100 Pa, working depth 9-10 mm). The SEM images were used to visually assess the effect of variable ΔCO_3^{2-} on shell preservation and microstructure. Representative shells were selected for each of the three species used in this study for each location or time interval. Shells were gently cracked open with a scalpel, and fragments were oriented such that the exterior calcite of at least one fragment faced the detector and interior calcite of at least one fragment faced the detector so that interior and exterior calcite could be imaged for each shell.

4.3. Results

4.3.1 Shell microstructure changes with ΔCO_3^{2-}

4.3.1.1 Core-top *N. dutertrei*

SEM and microCT derived images demonstrate the impact of progressive dissolution on shell microstructure. In *N. dutertrei* specimens bathed in seawater with a ΔCO_3^{2-} of 13.8 μmol/kg, the shell interior appears well preserved with regularly spaced round to funneled pores, smooth inter-pore areas, preserved shell layers, and

sharp edges of crystal structures (Figure 3a). On shell exteriors, pores are surrounded by high ridges, and blocky euhedral calcite is present but does not dominate shell thickness (Figure 3b). Pores are visible, and shells appear opaque under a light microscope (Figure 3c). CT numbers are high through the shell wall, and 3D reconstructions show that inner chambers are intact (Figure 3d). A histogram of the pooled *N. dutertrei* CT number data is bimodal and has a broader peak at higher CT numbers, likely reflecting separations between interior and exterior calcite and more exterior calcite present in the shell (Figure 7a, purple curve). Specimens bathed in seawater with a ΔCO_3^{2-} of 4.3 μmol/kg show signs of dissolution, including funneled pores in shell interiors (Figure 3e) and eroded ridges and crystal surfaces on shell exteriors (Figure 3f). The shell exteriors appear well preserved when viewed under a light microscope (Figure 3g). Exterior calcite has high CT numbers, interior calcite has low CT numbers, and inner chambers appear thin in the 3D reconstructions (Figure 3h). In the histogram, the higher CT number peak is dampened, and values shift toward the lower CT number peak, reflecting a change in both the interior and exterior calcite material (Figure 7a, light blue curve). There is substantial interior calcite dissolution in specimens bathed in seawater with a ΔCO32- of -14.7 μmol/kg. Specimens have cracked and disintegrated interior calcite layers, funneled pores (Figure 3i), and eroded ridges and crystal surfaces on the shell exterior (Figure 3j). Under a light microscope, shell exteriors appear well preserved (Figure 3k), although several shells appear slightly 'sugary' (i.e., altered, Sexton et al., 2006). Inner chambers are thin or are completely missing in the 3D reconstructions (Figure 3l). The higher value peak is muted in the histogram of CT numbers (Figure 7a, olive curve). In shells bathed in seawater with a ΔCO_3^{2-} of -20.2 μmol/kg, the calcite appears reprecipitated; interior calcite appears non-primary with irregular and non-crystalline structures (Figure 3m), and the exterior calcite crystals are large, blocky, and euhedral and dominate the shell wall (Figure 3n). Under a light microscope, the surface texture appears moderately to very sugary (Figure 3o). 3D reconstructions reveal that interior calcite is absent, exterior calcite thickens, and specimens have only low CT numbers (Figure 3p). In the histogram, CT numbers are only low

(<1000), reflecting an impact to the shell material through the shell, including the robust exterior calcite (Figure 7a, yellow curve).

4.3.1.2 Sediment trap *N. dutertrei*

Sediment trap *N. dutertrei* specimens bathed in seawater with a range of ΔCO_3^{2-} appear well preserved with no visible preservation differences despite residing in seawaters with different ΔCO_3^{2-}. The interior pores are rounded and evenly spaced, and the interior of the shell walls are smooth (Figure 4a,e, i). Exterior calcite is thickly calcified but does not contain euhedral crystals like the W8402A-14GC core-top samples (Figure 4b,f,j). Under a light microscope, shells appear well preserved with visible pores and a more translucent shell than opaque fossil specimens (Figure 4c,g,k). Inner chambers walls are intact in the 3D reconstructions (Figure 4d,h,l).

Specimens exposed to different water column ΔCO_3^{2-} have similar CT numbers through the shell. Histograms reveal that sediment trap *N. dutertrei* specimens contain a range of CT numbers, indicating the presence of both interior and exterior calcite (Figure 7b, dark blue, light blue, and turquoise curves). The shapes of the histograms are mostly normally distributed and not bimodal, indicating that there is no separation between the interior and exterior calcite. There is no significant difference in the mean or standard deviation (1σ) between specimens bathed in seawater with different ΔCO_3^2 (t-test, two-tailed, two-sample assuming equal variances, all sample sets p-value < 0.01).

4.3.1.2 Core-top *P. obliquiloculata*

Specimens of *P. obliquiloculata* bathed in seawater with ΔCO_3^{2-} of 13.8 μmol/kg have round, evenly spaced pores, a smooth inner surface (Figure 5a), and a smooth micro-perforate exterior 'cortex' (Figure 5b). The shell cortex appears 'glassy' under a light microscope (i.e., well preserved, Sexton et al., 2006). The shell interior has visible pores between high ridges (Figure 5c), and the chamber walls are intact and have high CT numbers (Figure 5d). In the histogram, the distribution is centered around higher CT numbers (Figure 7b, purple and dark blue curves). In these

specimens, low CT numbers are distinct from high CT numbers, and the shape of the histogram is bimodal, indicating a separation of interior calcite layers from the cortex. In specimens bathed in seawater with ΔCO_3^{2-} of 4.3 μmol/kg, interior calcite appears more dissolved: pores are funneled, and inner pore areas are corroded (Figure 5e). Exterior calcite does not appear altered, but interior calcite layers are delaminated from the cortex in a few regions of the shell (Figure 5f). Under a light microscope, specimens appear glassy. Inner chambers are visible (Figure 5g) but thin and contain low CT numbers (Figure 5h). High CT numbers shift lower in the histogram, and the mean and standard deviation are reduced (Figure 7b, light blue curve). In specimens bathed in seawater with ΔCO_3^{2-} of -14.7 μmol/kg, inner calcite is severely cracked, pores are heavily funneled, and there is a void between interior and exterior calcite (Figure 5i). The cortex does not appear altered, but sheets away from the interior calcite (Figure 5j). Shells appear glassy to opaque under a light microscope, and inner chambers are missing (Figure 5k). The whole shell is thin and contains low CT numbers within the shell wall with voids (Figure 5l). In the histogram, low CT numbers dominate (Figure 7b, olive curve). In specimens bathed in seawater with ΔCO_3^{2-} of -20.2 μmol/kg, interior calcite is severely altered (Figure 5m), while the cortex does not appear altered. However, there are distinct divisions between the cortex and interior calcite, and portions of interior calcite layers are removed (Figure 5n). For the majority of the specimens, interior calcite is completely absent. Under a light microscope, shells appear opaque to 'frosty,' and upon cracking open the shell, it is evident that inner chambers are absent (Figure 5o). CT numbers are low through the shell wall (Figure 5p). In the histogram, all shell material contains lower CT numbers, and the mean and standard deviation is reduced (Figure 7b, yellow curve).

4.3.1.3 Core-top *T. sacculifer*

Specimens of *T. sacculifer* bathed in seawater with ΔCO_3^{2-} of 13.8 μmol/kg appear well preserved. Interior calcite contains rounded to slightly funneled pores and smooth shell surfaces (Figure 6a), and the exterior calcite contains high ridges between pore spaces (Figure 6b). Under a light microscope, specimens have visible

pores and appear well preserved (Figure 6c). Inner chambers are intact in the 3D reconstructions and contain high CT numbers (Figure 6d). The histogram of CT numbers is bimodal, indicating a distinction between interior and exterior calcite (Figure 5d, purple and dark blue curves). In specimens bathed in seawater with ΔCO_3^{2-} of 4.3 μmol/kg, pores are more funneled, interior calcite is cracked and dissolved (Figure 6e), and exterior calcite surfaces have reduced ridges between the pores (Figure 6f). Specimens appear well preserved under the light microscope (Figure 6g); however, 3D reconstructions show that inner chambers are very thin or missing and have low CT numbers (Figure 6h). In the histogram, CT numbers are mostly low, and the mean and standard deviation is reduced, indicating that specimens are heavily dissolved even above the lysocline (Figure 5d, light blue curve). Specimens bathed in seawater with ΔCO_3^{2-} of -14.7 μmol/kg have heavily dissolved interior calcite (Figure 6i), and the exterior calcite has severely eroded ridges (Figure 6j). Specimens appear well preserved to slightly sugary under a light microscope (Figure 6k). However, the 3D reconstructions indicate that specimens have experienced significant dissolution: inner chambers are almost completely missing, and all parts of the shell have low CT numbers (Figure 6l). In the histogram, CT numbers peak at low values (Figure 5d, olive curve). In specimens bathed in seawater with ΔCO_3^{2-} of -20.2 μmol/kg, interior calcite appears 'powdery' (Figure 6m), and the exterior calcite has severely eroded ridges (Figure 6n). Shells appear sugary under a light microscope, and 3D reconstructions show that inner chambers are absent. Low CT numbers dominate the remaining shell wall (Figure 6p), and all CT numbers of the histogram are low (Figure 5d, yellow curve).

4.3.2 Correlating mean CT number and volume density to ΔCO_3^{2-}

The shell density (mean CT number, Eq 2.) progressively decreases with decreasing calcite saturation state and is strongly correlated with ΔCO_3^{2-} ($R^2 = 0.92$, 0.97, 0.77, for *N. dutertrei*, *P. obliquiloculata*, and *T. sacculifer*, respectively, Figure 8). The linear relationship weakens when sediment trap specimens are included in the regression (blue line, $R^2 = 0.48$). The slope of the correlation between mean CT

number and $\Delta[CO_3^{2-}]$ differs between non-spinose and spinose species. Mean CT number decreases by ~13 per unit ΔCO_3^{2-} (μmol/kg) in *N. dutertrei* and *P. obliquiloculata* specimens and by ~3 per unit ΔCO_3^{2-} (μmol/kg) in *T. sacculifer* specimens. Specimens of *T. sacculifer* have a much shallower slope (y = 3.3x + 718), likely because values are low even in well-preserved specimens (see section 4.4.1).

Volume density (shell weight normalized by the shell volume) of *N. dutertrei* specimens has a weaker linear relationship but is still correlated with ΔCO_3^{2-} (R^2 = 0.75; Figure 6a). The linear relationship is weaker when sediment trap specimens are included in the regression (blue line, R^2 = 0.63). The correlation with P. obliquiloculata and T. sacculifer specimens is significant (R^2 = 0.72, Figure 6b and R^2 = 0.81, Figure 6c, respectively). The slope of the relationship between volume density and ΔCO_3^{2-} is similar for all three species (indicating a decrease in volume density of ~0.02 g/cm^2 per 1 μmol/kg ΔCO_3^{2-}), despite species differences in the dissolution susceptibility of the shell. Because volume density to ΔCO_3^{2-} and CT number/volume density to ΔCO_3^{2-} when using the species *T. sacculifer* have weaker relationships, these metrics are not used to generate calibrations.

4.3.3 Shell microstructure changes with ΔCO_3^{2-}

All specimens from time intervals of the W8402A-14GC core have been impacted by dissolution. However, SEM images suggest shells were better preserved during the deglacial compared to the Holocene and glacial intervals (Figure 9). Specimens from the deglacial interval retain some rounded pores and smooth inter-pore areas (Figure 9g) and contain some inner chamber material (Figure 9h). In contrast, *N. dutertrei* specimens from Holocene and glacial intervals show signs of significant dissolution (Figure 9a and i), lack inner chambers, and specimens have low CT numbers through the shell wall (Figure 9b and m). Histograms of CT numbers show that deglacial (Figure 10a, light blue and turquoise curves) *N. dutertrei* specimens have a higher mean and standard deviation than Holocene (dark blue curve), core-top (purple curve), or glacial (yellow curve) specimens, indicating the preservation of fragile interior calcite.

P. obliquiloculata from deglacial intervals also retain interior calcite and inner chambers and have higher CT numbers in both the exterior and interior calcite than other intervals (Figure 9i-9j). In contrast, the *P. obliquiloculata* from Holocene and glacial intervals contain interior calcite delaminated from the cortex and is heavily altered or absent (Figure 9c and n). Inner chambers are absent (Figure 9d and o). Histograms of CT numbers show that deglacial (Figure 10b, light blue and turquoise curves) *P. obliquiloculata* specimens have a higher mean and standard deviation than other intervals: Holocene (dark blue curve) and core-top (purple curve) specimens contain lower CT numbers (Figure 10b). Glacial (yellow curve) specimens have the lowest CT numbers.

The deglacial interval is the only interval where *T. sacculifer* specimens have preserved pores (Figure 9k) and inner chambers (Figure 9l). In Holocene and glacial *T. sacculifer*, interior calcite is severely altered (Figure 9e and p), and inner chambers are missing or thin. They have only very low CT numbers (Figure 9f and q). Histograms of CT numbers show that deglacial (Figure S2a, light blue and turquoise curves) *T. sacculifer* specimens have a higher mean and standard deviation than Holocene (dark blue curve) and modern (purple curve) intervals, and the core-top interval has a histogram that shifts dramatically toward the lowest CT numbers. Glacial (yellow curve) specimens have slightly lower CT numbers than deglacial specimens.

4.4. Discussion

4.4.1 CT number reflects bottom water saturation state

We find that shell microstructure is impacted by dissolution at the seafloor. This is true even in regions where reprecipitation accompanies dissolution (section 4.4.2), and even though water column (section 4.4.3) and surface ocean ΔCO_3^{2-} changes may influence the initial shell structure (e.g., Spero et al., 1997; Bijma et al., 1999; Russell et al., 2004). The central Pacific core W8402A-14GC is well below the

regional lysocline, and it is likely that dissolution in deep waters and in sediments, not surface ocean calcification conditions, dominates shell density. The central Pacific is a region of relatively stable hydrography, and surface water pCO_2 levels have been in approximate equilibrium with atmospheric pCO_2 since the last glacial (Douville et al., 2010; Kubota et al., 2014). If our records had been affected by changing surface ocean [CO_3^{2-}], we would see a declining trend since the last glacial in response to increasing atmospheric pCO_2 (Henehan et al., 2013; Yu et al., 2013b). Yet, our records show an increase from the glacial to deglacial and then a decrease into the Holocene, indicating that deep ocean ΔCO_3^{2-} is likely the dominant signal.

Species specific equations of mean CT number are generated using mean CT numbers of *N. dutertrei*

$$Eq.\,3. \qquad y = 12.7x + 956 \pm 31;\ R^2 = 0.92$$

and *P. obliquiloculata*

$$Eq.\,4. \qquad y = 13.1x + 1000 \pm 30;\ R^2 = 0.97$$

and used to reconstruct ΔCO_3^{2-} (± uncertainties are 95% confidence intervals). The equations accurately reconstruct modern ΔCO_3^{2-} conditions of -20.2 μmol/kg (GLODAP cruise 31WT station 91; Key et al., 2004) within error of ΔCO_3^{2-} measurements (modern $\Delta[CO_3^{2-}]$ reconstructed as -20.0 and -20.3 μmol/kg using *N. dutertrei* and *P. obliquiloculata*, respectively). Mean CT numbers are strongly correlated with ΔCO_3^{2-}, and the implications are that a decrease/increase in deep ocean ΔCO_3^{2-} through time likely impacts microCT derived density in shells from the deep central Pacific.

4.4.2 Bottom water ΔCO_3^{2-} conditions since the last glacial

We use these calibration equations to reconstruct bottom water ΔCO_3^{2-} since the last glacial using samples from core W8402A-14GC of the central equatorial Pacific. Results suggest better preservation during the deglacial (Figure 9). Shell density, inferred from the mean CT number, is significantly higher than other intervals. Reconstructed ΔCO_3^{2-} using deglacial specimens is higher than all time intervals (shaded areas) and higher than the core-top (‘modern,’ dashed line), within

95% confidence (e.g., the confidence interval around deglacial mean does not intersect other confidence intervals, Figure 10c and d). Both *N. dutertrei* and *P. obliquiloculata* specimens reconstruct this trend. Reconstructions indicate ΔCO_3^{2-} was 10-15 μmol/kg higher during the deglacial compared to the glacial and Holocene intervals (Figure 10c and d). Results suggest the deglacial may have been a period of greater calcite preservation in seafloor sediments, and the glacial may have been a period of calcite preservation conditions more like that of the Holocene.

To evaluate the accuracy of our reconstructions, we compare our results to other regional reconstructions. Because of generally poor preservation, few dissolution-based reconstructions have been conducted in bottom waters of the central Pacific, and we compare our results to reconstructions in the western and eastern equatorial Pacific (EEP) and shallower depths than the W8402A-14GC core site. While our results are in contrast with the long held belief that the glacial was a period of better preservation on the OJP (Berger, 1970, 1973; Broecker, 1971; Broecker and Broecker, 1974; Peterson and Prell, 1985; Farrell and Prell, 1989; Wu and Berger, 1989; Broecker and Clark, 2001a; Anderson and Archer, 2002), they are consistent with more recent work inferred from decreased percent carbonate content (Wu et al., 1991), reduced shell weight (Broecker and Clark, 2003), and an increased dissolution effect on foraminifera geochemistry (Yu and Elderfield, 2007; Yu et al., 2010; Yu et al., 2013a; Fehrenbacher and Martin, 2011). In the EEP, $^{230}Th_{ex}$-normalized calcite flux supports decreased glacial preservation (Loubere, 1999, 2001; Loubere et al., 2004), and a Zn-CO_3^{2-} proxy suggests slightly lower glacial ΔCO_3^{2-} (Marchitto et al., 2005). Our glacial ΔCO_3^{2-} reconstruction is consistent with the emerging picture of decreased preservation in the deep Pacific during the glacial relative to the deglacial that followed.

Various estimates of deglacial ΔCO_3^{2-} suggest deep water ΔCO_3^{2-} was between 10-15 μmol/kg (Fehrenbacher and Martin, 2011; Yu et al., 2010; Loubere, 1999, 2001; Loubere et al., 2004) to 25-30 μmol/kg (Marchitto et al., 2005; Broecker and Peng, 1987; Boyle, 1988) higher than Holocene ΔCO_3^{2-}. Our reconstruction supports the smaller estimate of ΔCO_3^{2-} during the deglacial. This may be because

our core site resides in bottom waters isolated by stratification from intermediate water masses (Bostock et al., 2004). The shallower water depths of all the reconstructions mentioned here (~3-4 km water depth) are likely to experience greater ΔCO_3^{2-} variability in response to circulation changes during the deglacial period, which were namely a shoaling and greater mixing of Circumpolar Deep Water and Antarctic Bottom Water into intermediate waters (Bostock et al., 2004; Yu et al., 2010).

During the transition between the deglacial to the late Holocene (~14-10 ka BP), our data suggest that the lysocline likely shoaled, as is indicated by records on the OJP. OJP records support a decrease in carbonate flux in sediments (Berger, 1973; Pisias and Rea, 1988; Farrell and Prell, 1989; Stephens and Kadko, 1997; Loubere et al., 2004) and an increased dissolution effect on more dissolution susceptible foraminifera species and on foraminifera geochemistry (Wu and Berger, 1989; Fehrenbacher and Martin, 2011). In the EEP, $^{230}Th_{ex}$-normalized calcite flux and shell fragmentation suggest that calcite preservation began to decrease at ~10 ka BP and continued falling through the Holocene (Loubere, 1999, 2001; Loubere et al., 2004).

Our estimates support an increase in ΔCO_3^{2-} of the deep Pacific during the deglacial, which is thought to be the result of circulation changes – i.e., enhanced Antarctic Bottom Water formation (Bostock et al., 2004; Menviel et al., 2015) or enhanced deep water formation in the North Pacific (Okazaki et al., 2010; Wan and Jian, 2014) – and the transfer of deep ocean CO_2 of the Southern Ocean or North Pacific into intermediate water depths and eventually into the atmosphere (Monnin et al., 2001; Smith et al., 1999; Galbraith et al., 2007; Marchitto et al., 2007; Sigman et al., 2010). The timing of the deep Pacific ΔCO_3^{2-} increase we observe between ~18 and 14 ka BP is somewhat consistent with the record of others. Deep Pacific ΔCO_3^{2-} increase is thought to have begun early during the deglacial, producing a maximum at ~17 ka BP (Loubere, 1999, 2001; Loubere et al., 2004), or may have occurred later in the deglacial between ~14-10 ka BP (Yu et al., 2010). Our age model supports estimates of an earlier rise in deep ocean ΔCO_3^{2-} directly linked to the initiation of

increasing atmospheric pCO_2 at ~18 ka BP that peaked between 14-10 ka BP (Monnin et al., 2001; Lüthi et al., 2008). However, the error of the age model (±5 kyr, Lyle et al., 2002) means that our reconstruction cannot confidently assess the timing of the ΔCO_3^{2-} peak. It may be that our reconstruction captures the earlier signal of circulation changes and CO_2 release at the deepest depths before the signal entrains into shallower waters.

Our record supports the hypothesis that ΔCO_3^{2-} declined through the Holocene in the deep central pacific, likely caused by a decrease in oceanic alkalinity. Deglacial increase in ΔCO_3^{2-} and greater calcite preservation in response to deep ocean pCO_2 release during the early-late deglacial period likely led to a decrease in alkalinity and a plateau in deep ocean ΔCO_3^{2-} (Yu et al., 2010). ΔCO_3^{2-} is thought to have eventually decreased into the Holocene associated with alkalinity depletion and carbonate compensation, which likely brought ΔCO_3^{2-} back down to its pre-peak value (Broecker and Peng, 1987; Yu et al., 2010). In addition, high sea level stand following the glacial may have promoted coral reef buildup on shelves, contributing to the removal of alkalinity and a decrease in ΔCO_3^{2-} of the whole ocean (Opdyke and Walker, 1992). The decline in alkalinity likely reduced seawater CO_2 solubility and contributed to increasing atmospheric pCO_2 in the Holocene (Opdyke and Walker, 1992; Lüthi et al., 2008), and our data supports the link between bottom water ΔCO_3^{2-} and atmospheric pCO_2.

4.4.4 Caveats: Species and location specific dissolution/reprecipitation susceptibility

4.4.4.1 Species specific effects

The slopes of the mean CT number vs. ΔCO_3^{2-} and volume density vs. ΔCO_3^{2-} relationships are species-specific, reflecting species differences in dissolution susceptibility. The slopes decrease in the order *P. obliquiloculata* > *N. dutertrei* > *T. sacculifer*, which is consistent with the dissolution susceptibility ranking of Berger (1970). The slope of the *T. sacculifer* relationship is shallower than the other species. This represents the greater density loss with decreasing ΔCO_3^{2-} of *N. dutertrei* and *P. obliquiloculata* because *T. sacculifer* are fragile thin-walled species at the time of

shell formation and have less density to lose during dissolution (Berger, 1968). Because *T. sacculifer* is thought to only show the early stages of dissolution before they are completely dissolved, studies have questioned the reliability of this species as a dissolution indicator (Wu and Berger, 1989; Johnstone et al., 2010). *Trilobatus sacculifer* lack the robust exterior calcite of *N. dutertrei* and *P. obliquiloculata*. Furthermore, *T. sacculifer* are thin or completely absent in sediment core assemblages well below the lysocline (Bonneau et al., 1980; Brown and Elderfield, 1996). We find that *T. sacculifer* dissolution progresses rapidly as sites approach the lysocline. Inner chambers begin to dissolve at cores sites above the lysocline, and there is severe interior calcite dissolution and some dissolution of exterior calcite below the lysocline. In specimens bathed in seawater with ΔCO_3^{2-} below 4.3 μmol/kg, CT numbers are low, and CT number histograms are hard to separate from the background, which increases the uncertainty of these interpretations. While *T. sacculifer* show a relationship between mean CT number or volume density-and ΔCO_3^{2-} (R^2=0.47 and R^2=0.29, respectively, Figure 7d), the relationship is weaker compared to *N. dutertrei* and *P. obliquiloculata* specimens, likely because of the greater dissolution susceptibility of *T. sacculifer*, and we suggest they not be used for ΔCO_3^{2-} reconstructions.

4.4.4.2 Evidence of reprecipitation in the deep Central Pacific

Specimens from the central Pacific core W8402A-14GC contain reprecipitated crystallites that appear non-primary and may be inorganic (Rosenthal et al., 2007; Edgar et al., 2015; Gibson et al., 2016). Micro-scale euhedral reprecipitates cover the ridges and pores of the interior shell wall, and large randomly oriented crystals that appear ‘sugary’ under a light microscope dominate the shell exterior (Pearson and Burgess, 2008; Sexton et al., 2006; Figure 3m-p and Figure 5m-p). The primary (biogenic) well-oriented micro-granular crystals typical of shell surfaces are absent. Specimens of *T. sacculifer*, the most poorly preserved species used in this study, are ‘chalky’ and appear opaque/‘frosty’ under a light microscope (Sexton et al., 2006; Figure 6m-p).

The reprecipitated shells have altered trace element compositions compared to well-preserved shells. Reprecipitated shells have lower trace element concentration and lack the variable trace element banding common in unaltered specimens (Figure S4). Mean Mn/Ca ratios are higher, Ba/Ca and Zn/Ca ratios are similar, and Mg/Ca and Sr/Ca ratios are lower than ratios measured in well-preserved specimens (Table S1). These results are consistent with other studies that found that Mg/Ca and Sr/Ca ratios are low compared to primary calcite (Branson et al., 2014), even though inorganic reprecipitates in seawater-like solutions have Mg/Ca ratios orders of magnitude higher than primary calcite (de Nooijer et al., 2014; Mucci, 1987). Additionally, reprecipitates are thought to offset shell $\delta^{18}O$ by ~ +2.5‰, likely due to calcite growth in colder waters at the seafloor (Edgar et al., 2015; Kozdon et al., 2011; Pearson et al., 2001; Sexton et al., 2006). In our data, reprecipitated shells have $\delta^{18}O$ offset by +0.5-1‰ compared to well-preserved specimens, likely in part due to diagenesis (Table S1). Previous work has proposed that reprecipitates calcify in either a 'closed,' 'open,' or 'semi-closed' system relative to seawater (Branson et al., 2014; Edgar et al., 2015). Our observations of low Mg/Ca and small (+0.5-1‰) $\delta^{18}O$ offsets relative to bottom water supports reprecipitation occurring in a 'semi-closed' system that is relatively isolated from bottom water pore fluids, and that reprecipitates form in part from the dissolution of the foraminiferal shell itself (Pearson and Burgess, 2008; Kozdon et al., 2013; Branson et al., 2014; Edgar et al., 2015). Reprecipitates would reflect the geochemical signature of the dissolved pool surrounding the shell; i. e., supersaturated in Ca, depleted in Mg and Sr and enriched in $\delta^{18}O$ relative to seawater (Branson et al., 2014), consistent with our results.

Dissolution/reprecipitation is potentially localized and gradual, and several rounds of dissolution and reprecipitation may result in a kind of Rayleigh distillation of some trace elements (Pearson and Burgess, 2008), potentially enriching Mn, Ba, and Zn. Further work is needed to understand shell geochemical alterations before specimens from this site can be used for paleoceanographic interpretations.

The dissolution and reprecipitation of calcite may introduce some nonlinearity and weaken the correlation between mean CT number/volume density and ΔCO_3^{2-}.

Shells from core W8402A-14GC likely experienced severe dissolution and should be composed of low-density calcite (i.e., more porous). Inorganic reprecipitates, which are likely to be denser than foraminiferal calcite (Böhm et al., 2012), would thus add uncertainty to the regression as shells from core W8402A-14GC would contribute a 'robust calcite' data point to the regression. However, the addition of core W8402A-14GC *N. dutertrei* specimens to the regression increases the correlation (R^2 = 0.86 and 0.71 without; R^2 = 0.92 and 0.75 with; for mean CT number and volume density, respectively) and the addition of *P. obliqiloculata* and *T. sacculifer* W8402A-14GC specimens does not change the strength of the relationship. Using microCT, we see that dissolution impacts the shell structure by creating micro-scale airspaces (e.g., Figures 3p). These airspaces are present through the shell wall and result in lower density calcite (Figure 7, yellow curves). The reprecipitation process is poorly understood, but the process likely involves both dissolution and reprecipitation repeatedly (Pearson and Burgess, 2008). The end state is thought to dissolve organic lining and leave empty spaces (Sexton et al., 2006), and replace primary calcite with calcite containing loosely packed blocky crystals (Pearson and Burgess, 2008). This may result in the whole shell density decrease that we observe. The implications are that the regression using CT metrics can be applied to reconstruct ΔCO_3^{2-} at the W8402A-14GC core site.

4.4.4.3 Sediment trap samples

The sediment trap *N. dutertrei* specimens appear well preserved, and CT numbers are not significantly different between the shallow and deep trap depths. ΔCO_3^{2-} likely impacts specimens collected in the water column very differently than specimens on the seafloor. The main differences are the dissolution time (one year in sediment traps vs. decades to centuries in sediments) and environment (exposure to sediments and seawater conditions of the sample cup vs. exposure to calciferous sediments and pore waters). Results suggest that microCT metrics capture dissolution of the seafloor, not dissolution in the water column. These results also indicate that

sediment trap samples should not be included in the regression correlating CT metrics to deep water ΔCO_3^{2-}.

4.4.5 CT methods may be a better proxy for bottom-water ΔCO_3^{2-} than size normalization methods

Size normalization methods are commonly used to investigate the impact of ΔCO_3^{2-} on shell growth in the surface ocean (Marshall et al., 2013; Osborne et al., 2016; Osborne et al., 2020) and shell preservation in the deep ocean (e.g., Barker and Elderfield, 2002). These methods are useful because they are straightforward and do not require specialized instruments. For example, area density is calculated by dividing individual foraminifera shell weight by their 'silhouette area' and only requires accurate shell weight measurements and a 2D image of the shell. However, these methods do not always account for the variable ways that dissolution impacts the shell. Specimens used in this study were obtained from core-tops that span a wide range of ΔCO_3^{2-}, including far below the lysocline where reprecipitation accompanies dissolution. Our data includes species with different dissolution resistance and specimens from sediment traps and the seafloor. When we include all specimens, the correlation between shell weight/length and ΔCO_3^{2-} is weak for *N. dutertrei* (R^2 = 0.32 and 0.55 for shell weight and length, respectively, Figure S3b) and *P. obliquiloculata* (R^2 = 0.26 and 0.12 for shell weight and length, respectively, Figure S3a) specimens. When sediment trap *N. dutertrei* are included in the regression, the correlation weakens further (R^2 = 0.01 and 0.45 for shell weight and length, respectively, Figure S3a). Shell weight/length is not correlated with ΔCO_3^{2-} using *T. sacculifer* specimens (R^2 = 0.01 and 0.02 for shell weight and length, respectively, Figure S3c). Furthermore, the relationship between area density and ΔCO_3^{2-} is negative or non-existent for all species (Figure S3g-i). The poor correlation is in part due to the higher than expected sediment-trap derived *N. dutertrei* values (Figure S3a,d,g, triangles) and inclusion of the central Pacific site with ΔCO_3^{2-} of -20.2 μmol/kg. Reprecipitates result in shell thickening and greater length and surface area, which may drive area density values to be higher than expected, given the poor

preservation of shells at the central Pacific site. Poor correlation using *T. sacculifer* specimens may be driven by high variability in individual shell weight, length, and area density. Shell normalization methods also do not correlate with mean CT number nor volume density (Figure S4), likely driven by poor correlation when sediment trap specimens, specimens with reprecipitates, and *T. sacculifer* specimens are included.

4.5. Conclusions

Foraminifera dissolution-based proxies using microCT derived data reconstruct the seafloor calcite saturation state (ΔCO_3^{2-}). MicroCT scans record structural changes in foraminifera shells at the microscale and reflect shell density. In a core-top calibration from the equatorial Pacific that spans a ΔCO_3^{2-} gradient, microCT metrics are strongly correlated with the ΔCO_3^{2-} of the deep ocean. The regional calibration equation is applied to reconstruct bottom water ΔCO_3^{2-} of the central equatorial Pacific through the glacial period. Results suggest the deglacial period samples are better preserved, and ΔCO_3^{2-} was 10-15 μmol/kg higher than the Holocene and last glacial. Results are comparable to other regional reconstructions and support existing estimates of ΔCO_3^{2-} changes and the hypothesis that these changes are linked to the atmospheric pCO_2 rise over the record. Because of poor preservation, few reconstructions have been conducted at this depth, and our dataset adds valuable regional information about the bottom ocean ΔCO_3^{2-} state since the last glacial.

4.6 Acknowledgements

Core samples were obtained from WHOI and OSU MARSSAM. Sediment trap samples are obtained from USC. Jim Kelly, Faith Shell, and Grace Meyer helped pick, clean, mount, and process many samples. We are grateful for the guidance of Dorthe Wildenschild, Doug Meisenheimer, and Maoz Dor at the microCT facility and

Teresa Sawyer at the EM facility at OSU. This work is based on financial support from an OSU Learning Innovation Grant.

4.7 References

Aldridge, D., Beer, C. J., and Purdie, D. A. (2012). Calcification in the planktonic foraminifera Globigerina bulloides linked to phosphate concentrations in surface waters of the North Atlantic Ocean. *Biogeosciences*, *9*(5), 1725-1739. doi.10.5194/bg-9-1725-2012

Anderson, D. M., and D. Archer (2002), Glacial-interglacial stability of ocean pH inferred from foraminifer dissolution rates, Nature, 416, 70–73, doi.10.1038/416070a.

Arrhenius, G., Sediment cores from the East Pacific: Properties of the sediments, Rep. swed. *Deep Sea Exped*., 1951-1952, 1-227, 1952.

Barker, S. and Elderfield, H. Foraminiferal calcification response to glacial/interglacial changes in atmospheric CO2. *Science* 297, 833–836 (2002).

Barker, S., Kiefer, T., and Elderfield, H. (2004). Temporal changes in North Atlantic circulation constrained by planktonic foraminiferal shell weights. *Paleoceanography*, *19*(3). doi.10.1029/2004PA001004

Beer, C. J., Schiebel, R., and Wilson, P. A. (2010). Testing planktic foraminiferal shell weight as a surface water [CO32−] proxy using plankton net samples. *Geology*, *38*(2), 103-106. doi.10.1130/G30150.1

Berger, W. H. (1968). Planktonic foraminifera: selective solution and paleoclimatic interpretation. In *Deep Sea Research and Oceanographic Abstracts* (Vol. 15, No. 1, pp. 31-43). Elsevier. doi.10.1016/0011-7471(68)90027-2

Berger, W. H., Planktonic foraminifera: Selective solution and the lysocline, Mar. Geol., 8, 111-138, 1970.

Berger, W. H., Deep-sea carbonates: Pleistocene dissolution cycles, 3. Foraminiferal Res., 3, 187-195, 1973.

Berger, W. H., Adelseck Jr, C. G., and Mayer, L. A. (1976). Distribution of carbonate in surface sediments of the Pacific Ocean. *Journal of Geophysical Research*, *81*(15), 2617-2627. doi.10.1029/JC081i015p02617

Berger, W. H., Bonneau, M. C., and Parker, F. L. (1982). Foraminifera on the deep sea floor-lysocline and dissolution rate. *Oceanologica Acta*, *5*(2), 249-258.

Bijma, J., Spero, H. J. and Lea, D. W. in *Use of Proxies in Paleoceanography: Examples from the South Atlantic* (eds Fisher, G. and Wefer, G.) 489–512 (Springer, 1999). doi.10.1007/978-3-642-58646-0_20

Böhm, F., Eisenhauer, A., Tang, J., Dietzel, M., Krabbenhöft, A., Kisakürek, B., and Horn, C. (2012). Strontium isotope fractionation of planktic foraminifera and inorganic calcite. *Geochimica et Cosmochimica Acta*, *93*, 300-314. doi.10.1016/j.gca.2012.04.038

Bonneau, M. C., Vergnaudgrazzini, C., and Berger, W. H. (1980). Stable isotope fractionation and differential dissolution in recent planktonic-foraminifera from Pacific box-cores. *Oceanologica Acta*, *3*(3), 377-382.

Bostock, H. C., Opdyke, B. N., Gagan, M. K., and Fifield, L. K. (2004). Carbon isotope evidence for changes in Antarctic Intermediate Water circulation and ocean ventilation in the southwest Pacific during the last deglaciation. *Paleoceanography*, *19*(4). doi.10.1029/2004PA001047

Boyle, E. A. (1988). Cadmium: Chemical tracer of deepwater paleoceanography. *Paleoceanography*, *3*(4), 471-489. doi.10.1029/PA003i004p00471

Branson, O., Read, E., Redfern, S. A., Rau, C., and Elderfield, H. (2015). Revisiting diagenesis on the Ontong Java Plateau: Evidence for authigenic crust precipitation in *Globorotalia tumida*. *Paleoceanography*, *30*(11), 1490-1502. doi.10.1002/2014PA002759

Broecker, W. S., Calcite accumulation rates and glacial to interglacial changes in ocean mixing, The Late Cenozoic Glacial Ages, edited by K. K. Turekian, pp. 239-265, Yale University Press, New Haven, Conn., 1971.

Broecker, W. S., and S. Broecker, Carbonate dissolution on the western flank of the East Pacific Rise, Studies in Paleo-oceanography, edited by W. W. Hay, Spec. Pub l., Soc. Econ. Palaeontol. Mineral., 20, 44-57, 1974.

Broecker, W. S., and E. Clark (2001a), Glacial-to-Holocene redistribution of carbonate ion in the deep sea, Science, 294, 2152–2155, doi.10.1126/science.1064171.

Broecker, W., and Clark, E. (2001b). An evaluation of Lohmann's foraminifera weight dissolution index. *Paleoceanography*, *16*(5), 531-534. doi.10.1029/2000PA000600

Broecker, W. S., and Clark, E. (2003). Glacial-age deep sea carbonate ion concentrations. *Geochemistry, Geophysics, Geosystems*, *4*(6). doi.10.1029/2003GC000506

Broecker, W. S., and Peng, T. H. (1987). The role of CaCO3 compensation in the glacial to interglacial atmospheric CO2 change. *Global Biogeochemical Cycles*, *1*(1), 15-29. doi.10.1029/GB001i001p00015

Brown, S. J., and Elderfield, H. (1996). Variations in Mg/Ca and Sr/Ca ratios of planktonic foraminifera caused by postdepositional dissolution: Evidence of shallow Mg-dependent dissolution. *Paleoceanography*, *11*(5), 543-551. doi.10.1029/96PA01491

Crowley, T. J. (1983). Calcium-carbonate preservation patterns in the central North Atlantic during the last 150,000 years. *Marine Geology*, *51*(1-2), 1-14. doi.10.1016/0025-3227(83)90085-3

Curve fitting toolbox : for use with MATLAB® : user's guide. (2001). Natick, MA :MathWorks,

Dittert, N., Baumann, K. H., Bickert, T., Henrich, R., Huber, R., Kinkel, H., and Meggers, H. (1999). Carbonate dissolution in the deep-sea: methods, quantification and paleoceanographic application. In *Use of proxies in paleoceanography* (pp. 255-284). Springer, Berlin, Heidelberg. doi.10.1007/978-3-642-58646-0_10

de Nooijer, L. J., Spero, H. J., Erez, J., Bijma, J., and Reichart, G. J. (2014). Biomineralization in perforate foraminifera. *Earth-Science Reviews*, *135*, 48-58. doi.10.1016/j.earscirev.2014.03.013

de Villiers, S. (2004). Optimum growth conditions as opposed to calcite saturation as a control on the calcification rate and shell-weight of marine foraminifera. *Marine Biology*, *144*(1), 45-49. doi. 10.1007/s00227-003-1183-8

Douville, E., M. Paterne, G. Cabioch, P. Louvat, J. Gaillardet, A. Juillet-Leclerc, and L. Ayliffe (2010), Abrupt sea surface pH change at the end of the Younger Dryas in the central sub-equatorial Pacific inferred from boron isotope abundance in corals (Porites), Biogeosciences, 7(8), 2445 -2459, doi.10.5194/bg-7-2445-2010.

Edgar, K. M., Anagnostou, E., Pearson, P. N., and Foster, G. L. (2015). Assessing the impact of diagenesis on $\delta^{11}B$, $\delta^{13}C$, $\delta^{18}O$, Sr/Ca and B/Ca values in fossil planktic foraminiferal calcite. *Geochimica et Cosmochimica Acta*, *166*, 189-209. doi.10.1016/j.gca.2015.06.018

Farrell, J. W., and W. L. Prell (1989), Climatic change and CaCO3 preservation: An 800,000 year bathymetric reconstruction from the central equatorial Pacific Ocean, Paleoceanography, 4, 447–466, doi.10.1029/PA004i004p00447.

Fehrenbacher, J., and P. Martin (2011). Western equatorial Pacific deep water carbonate chemistry during the Last Glacial Maximum and deglaciation: Using planktic foraminiferal Mg/Ca to reconstruct sea surface temperature and seafloor dissolution. Paleoceanography, 26(2). doi.10.1029/2010PA002035.

Galbraith, E. D., S. L. Jaccard, T. F. Pedersen, D. M. Sigman, G. H. Haug, M. Cook, J. R. Southon, and R. Francois (2007), Carbon dioxide release from the North Pacific abyss during the last deglaciation, Nature, 449, 890–893, doi.10.1038/nature06227.

Gibson, K. A., Thunell, R. C., Machain-Castillo, M. L., Fehrenbacher, J., Spero, H. J., Wejnert, K., ... and Tappa, E. J. (2016). Evaluating controls on planktonic foraminiferal geochemistry in the Eastern Tropical North Pacific. *Earth and Planetary Science Letters*, *452*, 90-103. doi.10.1016/j.epsl.2016.07.039

Imbrie,J ., J. D. Hays,D . G. MartinsonA, . Mcintyre,A . C. Mix, J. J. Morley, N. G. Pisias, W. L. Prell, and N.J. Shackleton, The Orbital theory of Pleistocene climate: support from a revised chronology of the marine $\delta^{18}O$ record, Milankovitch and Climate. part I, edited by A. L. Berger, pp. 269-305, D. Reidel, Hingham, Mass., 1984.

Henehan, M.J., J. Rae, G.L. Foster, J. Erez, K.C. Prentice, M. Kucera, H.C. Bostock, M.A. Martinez-Boti, J.A. Milton, P.A. Wilson, and others. (2013). Calibration of the boron isotope proxy in the planktonic foraminifera *Globigerinoides ruber* for use in palaeo-CO_2 *Oceanography* | March 2014 25 reconstruction. *Earth and Planetary Science Letters* 364:111–122, doi.10.1016/j.epsl.2012.12.029.

Henrich, R., Kassens, H., Vogelsang, E., and Thiede, J. (1989). Sedimentary facies of glacial-interglacial cycles in the Norwegian Sea during the last 350 ka. *Marine Geology*, *86*(4), 283-319. doi.10.1016/0025-3227(89)90090-X

Hönisch, B., Bickert, T., and Hemming, N. G. (2008). Modern and Pleistocene boron isotope composition of the benthic foraminifer Cibicidoides wuellerstorfi. *Earth and Planetary Science Letters*, *272*(1-2), 309-318. doi.10.1016/j.epsl.2008.04.047

Honjo, S. (1982). Seasonality and interaction of biogenic and lithogenic particulate flux at the Panama Basin. *Science*, *218*(4575), 883-884. doi.10.1126/science.218.4575.883

Iwasaki, S. et al. Observation of the dissolution process of *Globigerina bulloides* tests (planktic foraminifera) by X-ray microcomputed tomography. Paleoceanography 30, 317–331 (2014). doi.10.1002/2014PA002639

Iwasaki, S., Kimoto, K., Okazaki, Y., and Ikehara, M. (2019). Micro-CT Scanning of Tests of Three Planktic Foraminiferal Species to Clarify Dissolution Process and Progress. *Geochemistry,Geophysics, Geosystems*, *20*(12), 6051-6065.

Johnstone, H. J., Schulz, M., Barker, S., and Elderfield, H. (2010). Inside story: An X -ray computed tomography method for assessing dissolution in the tests of planktonic foraminifera. *Marine Micropaleontology*, *77*(1-2), 58-70.

Key, R.M., et al., 2004. A global ocean carbon climatology: Results from GLODAP. Global Biogeochemical Cycles, 18(4). doi.10.1029/2004GB002247.

Kozdon, R., Kelly, D. C., Kitajima, K., Strickland, A., Fournelle, J. H., and Valley, J. W. (2013). In situ $\delta^{18}O$ and Mg/Ca analyses of diagenetic and planktic foraminiferal calcite preserved in a deep-sea record of the Paleocene-Eocene thermal maximum. *Paleoceanography*, *28*(3), 517-528. doi.10.1002/palo.20048

Kozdon R., Kelly D. C., Kita N. T., Fournelle J. H. and Valley J. W. (2011) Planktonic foraminiferal oxygen isotope analysis by ion microprobe technique suggests warm tropical sea surface temperatures during the early paleogene. Paleoceanography 26, PA3206.

Ku, T. L., and Oba, T. (1978). A Method for Quantitative Evaluation of Carbonate Dissolution in Deep-Sea Sediments and Its Application to Paleoceanographic Reconstruction1. *Quaternary Research*, *10*(1), 112-129. doi.10.1016/0033-5894(78)90016-9

Kubota, K., Y. Yokoyama, T. Ishikawa, S. Obrochta, and A. Suzuki (2014), Larger CO_2 source at the equatorial Pacific during the last deglaciation, Sci. Rep., 4, doi.10.1038/srep05261.

Lombard, F., da Rocha, R. E., Bijma, J., and Gattuso, J. P. (2010). Effect of carbonate ion concentration and irradiance on calcification in planktonic foraminifera. *Biogeosciences*, *7*(1), 247-255. doi.10.5194/bg-7-247-2010

Le, J., and Shackleton, N. J. (1992). Carbonate dissolution fluctuations in the western equatorial Pacific during the late Quaternary. *Paleoceanography*, *7*(1), 21-42. doi.10.1029/91PA02854

Lohmann, G. P. (1995). A model for variation in the chemistry of planktonic foraminifera due to secondary calcification and selective dissolution. *Paleoceanography*, *10*(3), 445-457. doi.10.1029/95PA00059

Lombard, F., Labeyrie, L., Michel, E., Spero, H.J., Lea, D.W., 2009. Modelling the

temperature dependent growth rates of planktic foraminifera. Mar. Micropaleontol. 70,1–7. doi.10.1016/j.marmicro.2008.09.004.

Loubere, P. (1999). A multiproxy reconstruction of biological production and oceanography in the eastern equatorial Pacific for the past 30,000 years. *Marine micropaleontology*, *37*(2), 173-198. doi.10.1016/S0377-8398(99)00013-4

Loubere, P. (2001). Nutrient and oceanographic changes in the eastern equatorial Pacific from the last full glacial to the present. *Global and Planetary Change*, *29*(1-2), 77-98. doi.10.1016/S0921-8181(00)00085-0

Loubere, P., Mekik, F., Francois, R., and Pichat, S. (2004). Export fluxes of calcite in the eastern equatorial Pacific from the Last Glacial Maximum to present. *Paleoceanography*, *19*(2). doi.10.1029/2003PA000986

Lüthi, D., Le Floch, M., Bereiter, B. *et al.* High-resolution carbon dioxide concentration record 650,000-800,000 years before present. *Nature* 453, 379–382 (2008). doi.org/10.1038/nature06949

Lyle, M., Mix, A., and Pisias, N. (2002). Patterns of CaCO3 deposition in the eastern tropical Pacific Ocean for the last 150 kyr: Evidence for a southeast Pacific depositional spike during marine isotope stage (MIS) 2. *Paleoceanography*, *17*(2), 3-1. doi.10.1029/2000PA000538

Manno, C., Morata, N., and Bellerby, R. (2012). Effect of ocean acidification and temperature increase on the planktonic foraminifer Neogloboquadrina pachyderma (sinistral). *Polar Biology*, *35*(9), 1311-1319. doi.10.1007/s00300-012-1174-7

Marshall, B. J., Thunell, R., Hennehan, M., Astor, Y. and Wejnert, K. Planktonic foraminiferal area density as a proxy for carbonate ion concentration: a calibration study using the Cariaco Basin ocean time series. *Paleoceanography* 28, 363–376 (2013).

Marchitto Jr, T. M., Curry, W. B., and Oppo, D. W. (2000). Zinc concentrations in benthic foraminifera reflect seawater chemistry. *Paleoceanography*, *15*(3), 299-306. doi.10.1029/1999PA000420

Marchitto, T. M., Lynch-Stieglitz, J., and Hemming, S. R. (2005). Deep Pacific $CaCO_3$ compensation and glacial-interglacial atmospheric CO2. *Earth and Planetary Science Letters*, *231*(3-4), 317-336. doi.10.1016/j.epsl.2004.12.024

Marchitto, T. M., S. J. Lehman, J. D. Ortiz, J. Flückiger, and A. van Geen (2007), Marine radiocarbon evidence for the mechanism of deglacial atmospheric CO_2 rise, Science, 8, 1456–1459, doi.10.1126/science.1138679.

Mekik, F., and François, R. (2006). Tracing deep-sea calcite dissolution: Agreement between the Globorotalia menardii fragmentation index and elemental ratios (Mg/Ca and Mg/Sr) in planktonic foraminifers. *Paleoceanography*, *21*(4). doi.10.1029/2006PA001296

Menviel, L., Spence, P., and England, M. H. (2015). Contribution of enhanced Antarctic Bottom Water formation to Antarctic warm events and millennial-scale atmospheric CO2 increase. *Earth and Planetary Science Letters*, *413*, 37-50. doi.10.1016/j.epsl.2014.12.050

Milliman, J. D. (1993). Production and accumulation of calcium carbonate in the

ocean: Budget of a nonsteady state. *Global Biogeochemical Cycles*, *7*(4), 927-957. doi.10.1029/93GB02524

Monnin, E., A. Indermühle, A. Dällenbach, J. Flückiger, B. Stauffer, T. F. Stocker, D. Raynaud, and J. M. Barnola (2001), Atmospheric CO2 concentrations over the last glacial termination, Science, 291, 112–114, doi.10.1126/science.291.5501.112.

Moy, A. D., Howard, W. R., Bray, S. G., and Trull, T. W. (2009). Reduced calcification in modern Southern Ocean planktonic foraminifera. *Nature geoscience*, *2*(4), 276-280. doi.10.1038/NGEO460

Mucci, A. (1987). Influence of temperature on the composition of magnesian calcite overgrowths precipitated from seawater. *Geochimica et Cosmochimica Acta*, *51*(7), 1977-1984. doi.10.1016/0016-7037(87)90186-4

Murray, D. W. (1987). Spatial and temporal variations in sediment accumulation in the central tropical Pacific.

Okazaki, Y., Timmermann, A., Menviel, L., Harada, N., Abe-Ouchi, A., Chikamoto, M. O., ... and Asahi, H. (2010). Deepwater formation in the North Pacific during the last glacial termination. *Science*, *329*(5988), 200-204. doi.10.1126/science.1190612

Opdyke, B.N., and J.C.G. Walker. 1992. Return of the coral reef hypothesis: Basin to shelf partitioning of $CaCO_3$ and its effect on atmospheric CO2. *Geology* 20:733–736, doi.10.1130/0091-7613(1992)020<0733:ROTCRH>2.3.CO;2.

Osborne, E. B. et al. Calcification of the planktonic foraminifera *Globigerina bulloides* and carbonate ion concentration: results from the Santa Barbara Basin. *Paleoceanography* 31, 1083–1102 (2016).

Osborne, E. B., Thunell, R. C., Gruber, N., Feely, R. A., and Benitez-Nelson, C. R. (2020). Decadal variability in twentieth-century ocean acidification in the California Current Ecosystem. *Nature Geoscience*, *13*(1), 43-49. doi.10.1038/s41561-019-0499-z

Pearson, P. N., and C. E. Burgess (2008), Foraminifer test preservation and diagenesis: Comparison of high latitude Eocene sites, in *Biogeochemical Controls on Palaeoceanographic Environmental Proxoes*, vol. 303, edited by W. E. N. Austin and R. H. James, pp. 59–72, London.

Pearson P. N., Ditchfield P. W., Singano J., Harcourt-Brown K. G., Nicholas C. J., Olsson R. K., Shackleton N. J. and Hall M. A. (2001) Warm tropical sea surface temperatures K.M. Edgar et al. / Geochimica et Cosmochimica Acta 166 (2015) 189–209 207 in the Late Cretaceous and Eocene epochs. Nature 413, 481–487.

Peterson, L. C., and Prell, W. L. (1985). Carbonate dissolution in recent sediments of the eastern equatorial Indian Ocean: preservation patterns and carbonate loss above the lysocline. *Marine Geology*, *64*(3-4), 259-290. doi.10.1016/0025-3227(85)90108-2

Pisias, N. G., and Rea, D. K. (1988). Late Pleistocene paleoclimatology of the central equatorial Pacific: Sea surface response to the southeast trade winds. *Paleoceanography*, *3*(1), 21-37. doi.10.1029/PA003i001p00021

Qin, B., T. Li, Z. Xiong, T. J. Algeo, and F. Chang (2017), Deepwater carbonate ion

concentrations in the western tropical Pacific since 250 ka: Evidence for oceanic carbon storage and global climate influence, Paleoceanography, 32, 351–370. doi.10.1002/2016PA003039.

Rae, J. W., Foster, G. L., Schmidt, D. N., and Elliott, T. (2011). Boron isotopes and B/Ca in benthic foraminifera: Proxies for the deep ocean carbonate system. *Earth and Planetary Science Letters*, *302*(3-4), 403-413. doi.10.1016/j.epsl.2010.12.034

Rosenthal, S. J., McBride, J., Pennycook, S. J., and Feldman, L. C. (2007). Synthesis, surface studies, composition and structural characterization of CdSe, core/shell and biologically active nanocrystals. *Surface science reports*, *62*(4), 111-157. doi.10.1016/j.surfrep.2007.02.001

Russell, A. D., Hönisch, B., Spero, H. J., and Lea, D. W. (2004). Effects of seawater carbonate ion concentration and temperature on shell U, Mg, and Sr in cultured planktonic foraminifera. *Geochimica et Cosmochimica Acta*, *68*(21), 4347-4361. doi.10.1016/j.gca.2004.03.013

Schiebel, R., and Hemleben, C. (2017). *Planktic foraminifers in the modern ocean* (pp. 1-358). Berlin: Springer.

Schindelin, J., Arganda-Carreras, I., Frise, E., Kaynig, V., Longair, M., Pietzsch, T., ... and Cardona, A. (2012). Fiji: an open-source platform for biological-image analysis. *Nature methods*, *9*(7), 676-682. doi.10.1038/nmeth.2019

Sexton P. E., Wilson P. A. and Pearson P. N. (2006) Microstructural and geochemical perspectives on planktic foraminiferal preservation: “Glassy” versus “Frosty”. *Geochem. Geophys. Geosyst.*

Sigman, D. M., and Boyle, E. A. (2000). Glacial/interglacial variations in atmospheric carbon dioxide. *Nature*, *407*(6806), 859-869. doi.10.1038/35038000

Sigman, D. M., Hain, M. P., and Haug, G. H. (2010). The polar ocean and glacial cycles in atmospheric CO 2 concentration. *Nature*, *466*(7302), 47-55. doi.10.1038/nature09149

Sigman, D. M., McCorkle, D. C., and Martin, W. R. (1998). The calcite lysocline as a constraint on glacial/interglacial low-latitude production changes. *Global Biogeochemical Cycles*, *12*(3), 409-427. doi.10.1029/98GB01184

Smith, H. J., Fischer, H., Wahlen, M., Mastroianni, D., and Deck, B. (1999). Dual modes of the carbon cycle since the Last Glacial Maximum. *Nature*, *400*(6741), 248-250. doi.10.1038/22291

Spero, H. J., Bijma, J., Lea, D. W. and Bemis, B. E. Effect of seawater carbonate concentration on foraminiferal carbon and oxygen isotopes. *Nature* 390, 497–500 (1997). doi.org/10.1038/37333

Stephens, M. P., and Kadko, D. C. (1997). Glacial-Holocene calcium carbonate dissolution at the central equatorial Pacific seafloor. *Paleoceanography*, *12*(6), 797-804. doi.10.1029/97PA02271

Thunell, R. C. (1976). Optimum indices of calcium carbonate dissolution, in deep-sea sediments. *Geology*, *4*(9), 525-528. doi.10.1130/0091-7613(1976)4<525:OIOCCD>2.0.CO;2

Varslot, T., Kingston, A., Myers, G., and Sheppard, A. (2011). High-resolution

helical cone-beam micro CT with theoretically-exact reconstruction from experimental data. *Medical physics*, *38*(10), 5459-5476.

Wan, S., and Jian, Z. (2014). Deep water exchanges between the South China Sea and the Pacific since the last glacial period. *Paleoceanography*, *29*(12), 1162-1178. doi.10.1002/2013PA002578

Wildenschild, D., Vaz, C. M. P., Rivers, M. L., Rikard, D., and Christensen, B. S. B. (2002). Using X-ray computed tomography in hydrology: systems, resolutions, and limitations. *Journal of Hydrology*, *267*(3-4), 285-297. doi.10.1016/S0022-1694(02)00157-9

WOCE Hydrographic Programme, WHP (2002): Physical oceanography during Thomas G. Thompson cruise 3250TN026_1 on section P10. PANGAEA, doi.10.1594/PANGAEA.294012

Wu, G., and Berger, W. H. (1989). Planktonic foraminifera: differential dissolution and the Quaternary stable isotope record in the west equatorial Pacific. *Paleoceanography*, *4*(2), 181-198. doi.10.1029/PA004i002p00181

Wu, G., Yasuda, M. K., and Berger, W. H. (1991). Late Pleistocene carbonate stratigraphy on Ontong-Java Plateau in the western equatorial Pacific. *Marine Geology*, *99*(1-2), 135-150. doi.10.1016/0025-3227(91)90087-K

Yu, J. M., and H. Elderfield (2007), Benthic foraminiferal B/Ca ratios reflect deep water carbonate saturation state, Earth Planet. Sci. Lett., 258, 73–86, doi.10.1016/j.epsl.2007.03.025.

Yu, J., W. Broecker, H. Elderfield, Z.D. Jin, J. McManus, and F. Zhang. 2010. Loss of carbon from the deep sea since the Last Glacial Maximum. *Science* 330:1,084–1,087, doi.10.1126/science.1193221.

Yu, J., R.F. Anderson, Z.D. Jin, J. Rae, B.N. Opdyke, and S. Eggins (2013a). Responses of the deep ocean carbonate system to carbon reorganization during the Last Glacial–interglacial cycle. Quaternary Science Reviews 76:39–52, doi.10.1016/j.quascirev.2013.06.020.

Yu, J., D.J.R. Thornalley, J. Rae, and I.N. McCave. (2013b). Calibration and application of B/Ca, Cd/Ca, and $\delta^{11}B$ in *Neogloboquadrina pachyderma* (sinistral) to constrain CO_2 uptake in the subpolar North Atlantic during the last deglaciation. *Paleoceanography* 28:237–252, doi.org/10.1002/palo.20024.

Yu, J., R.F. Anderson, and E.J. Rohling (2014). Deep ocean carbonate chemistry and glacial-interglacial atmospheric CO_2 changes. Oceanography 27(1):16–25, doi.10.5670/oceanog.2014.04.

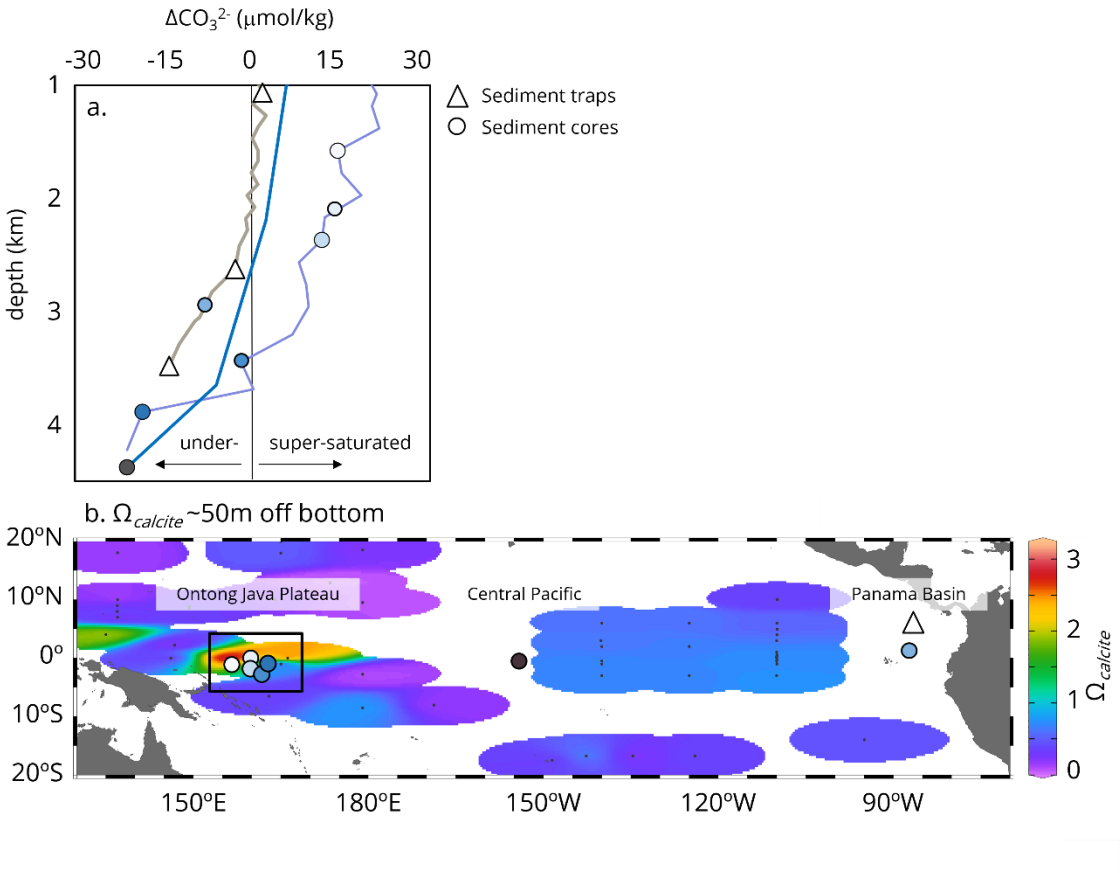

Figure 4.1. a. Profile of ΔCO_3^{2-} for the Ontong Java Plateau (WOCE Cruise P10 station 24; WHP, 2002), the Central Pacific (GLODAP cruise 31WT station 91; Key et al., 2004), and the Panama Basin (GLODAP cruise 316N station 385; Key et al., 2004). ΔCO_3^{2-} was calculated from Total Alkalinity, DIC, and other parameters using ODV (equilibrium constants follow Dickson et al., 2007; Schlitzer, 2020). The black line defines when $\Delta CO_3^{2-} = 0$. Specimens from core material bathed in seawater with $\Delta CO_3^{2-} < 0$ are under-saturated, and with $\Delta CO_3^{2-} > 0$ are super-saturated with respect to calcite. b. Colormap of Ω (degree of calcite saturation) of deep ocean ~50 m above the seafloor (map generated using ODV, Schlitzer, 2020; data from GLODAP, Key et al., 2004) and locations of core and sediment traps used in this study on the Ontong Java Plateau, Central Pacific, and the Panama Basin.

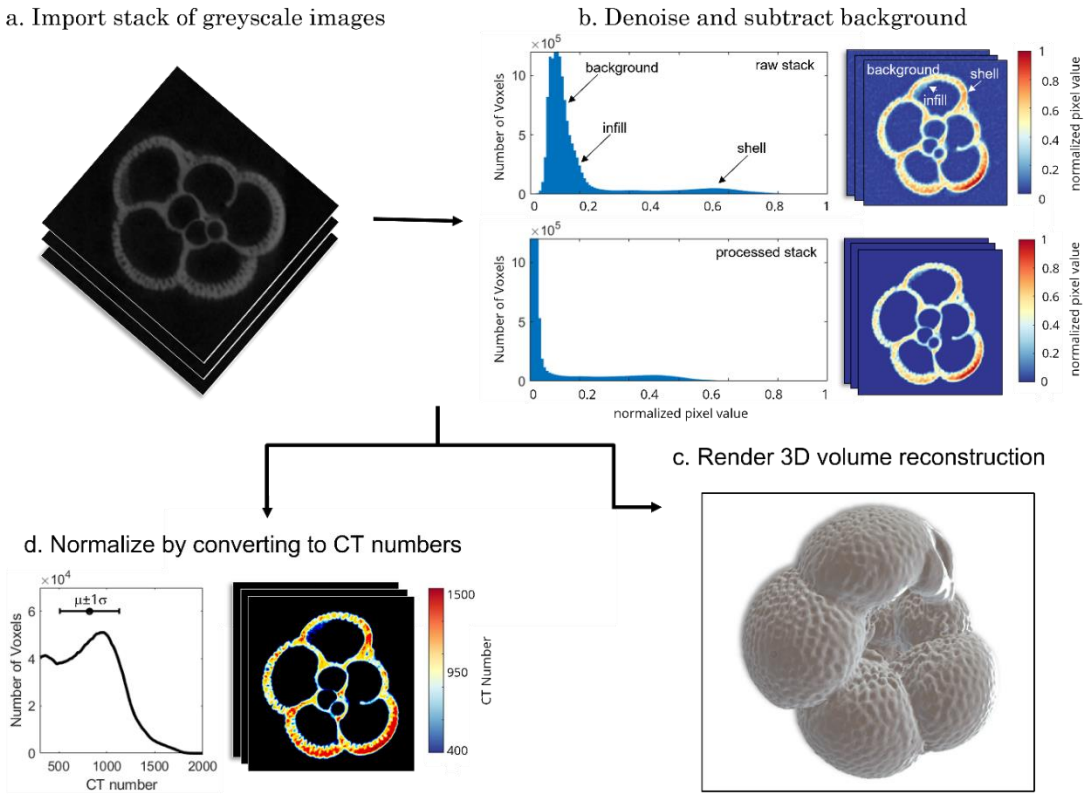

Figure 4.2. Methods for performing microCT data processing. a. stacks of 8-bit greyscale images (that reconstruct 3D tomographic data) are imported into imageJ software. b. Image stacks are processed with a denoising filter and the background subtracted. c. 3D rendering of shell volume from stack of images. d. greyscale values of stack of images are converted to CT number to normalize shell values (after Iwasaki et al., 2014).

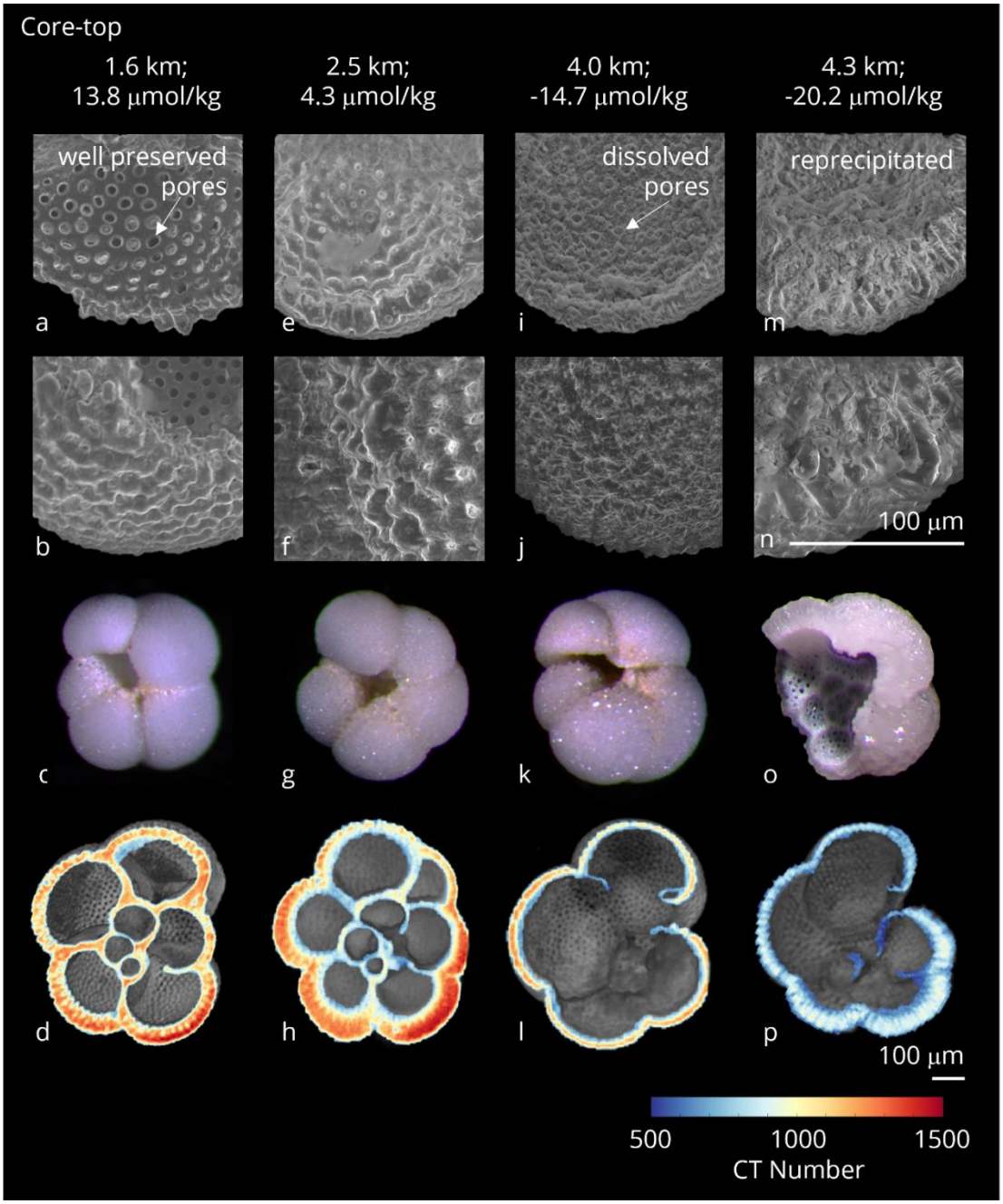

Figure 4.3. Representative microCT scanned and SEM imaged core-top *N. dutertrei* specimens from four core depths and deep ocean ΔCO_3^{2-} values. Top row are SEM images of interior calcite, second row are SEM images of exterior calcite, third row are light microscope images, and fourth row are cross sections of 3D renderings of shell volume overlaid with a CT number cross-section image.

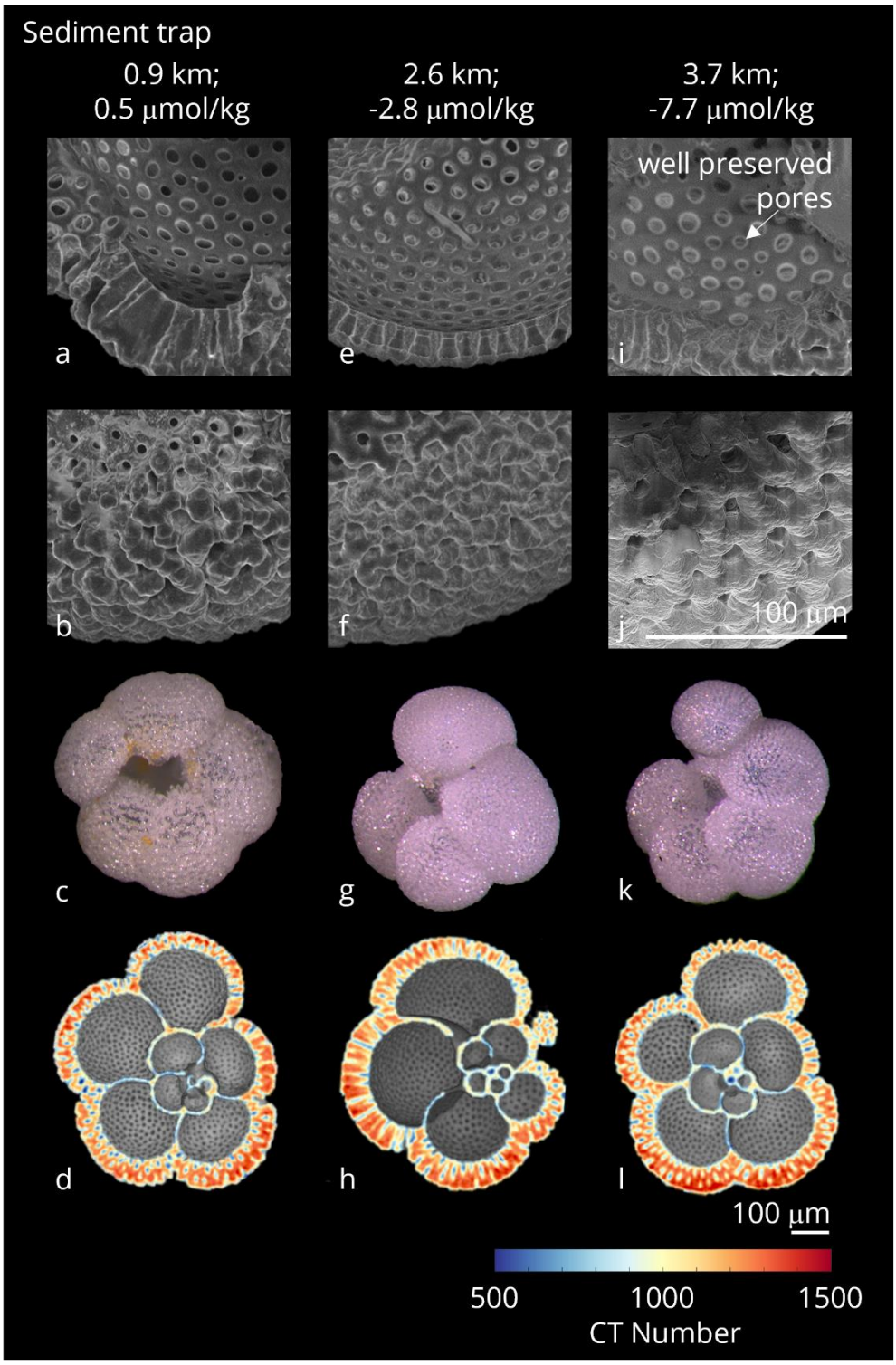

Figure 4.4. The same as with Figure 4.3, but with representative sediment trap *N. dutertrei* specimens.

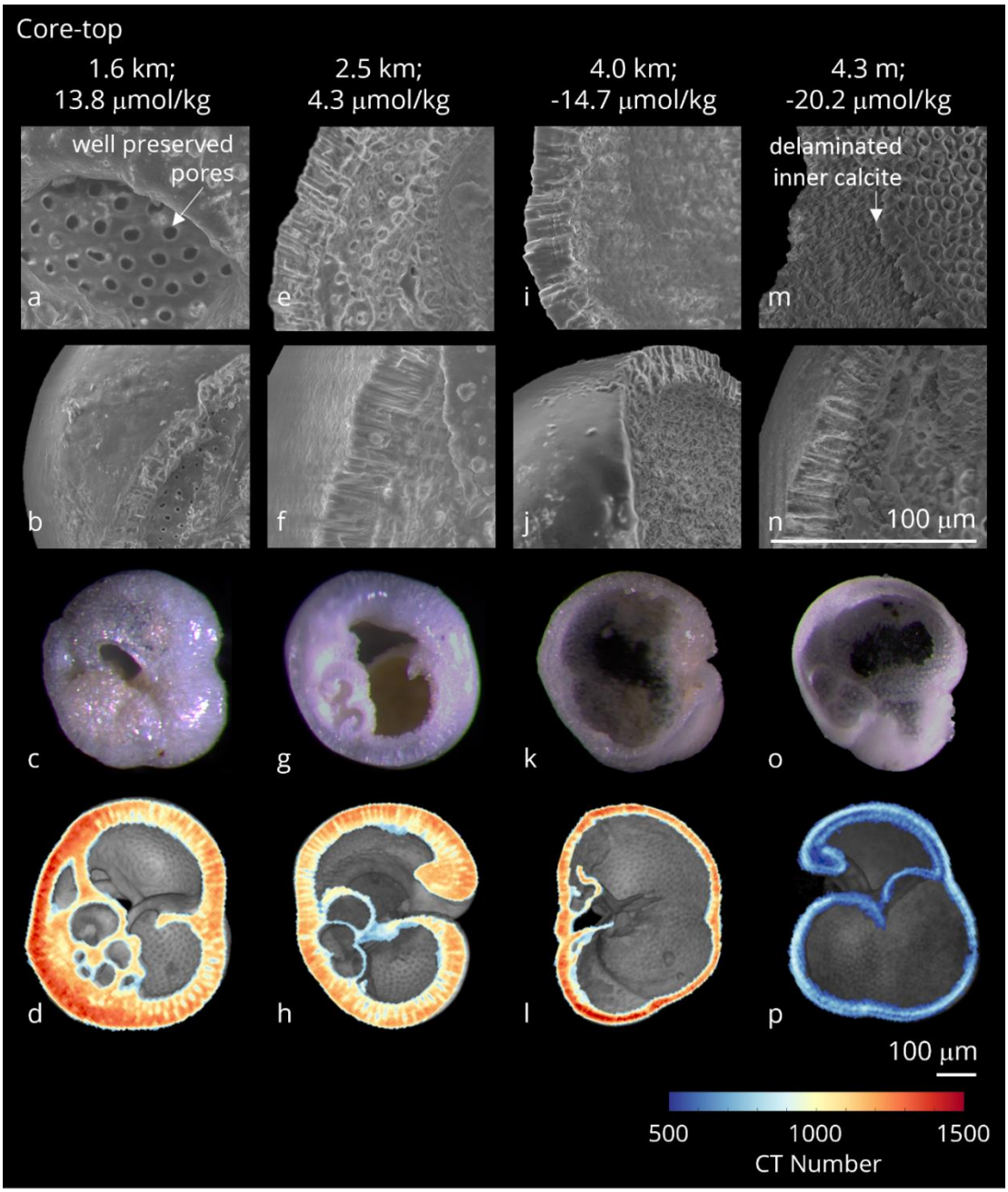

Figure 4.5. The same as with Figure 4.3, but with representative *P. obliquiloculata* specimens.

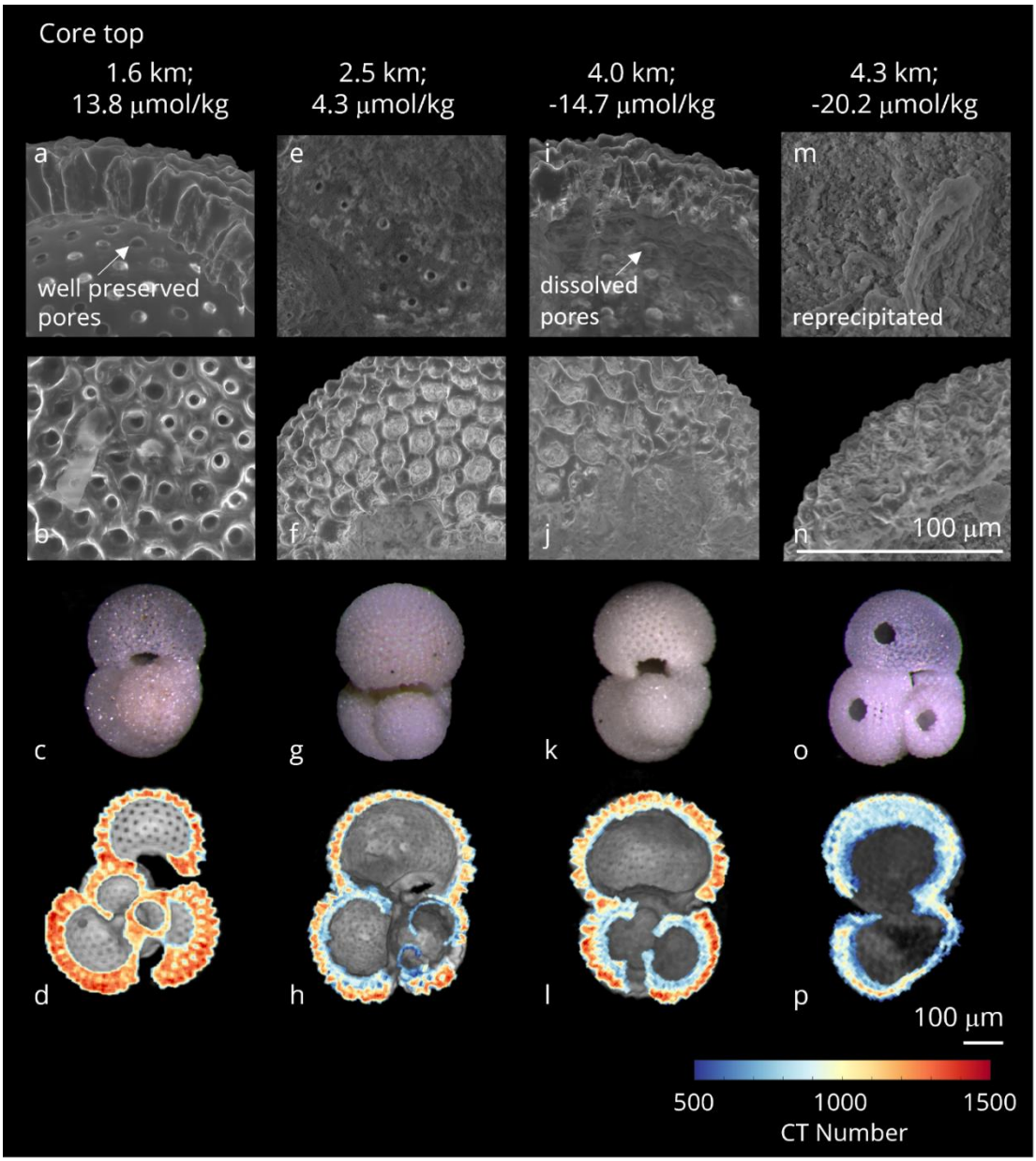

Figure 4.6. The same as with Figure 4.3, but with representative *T. sacculifer* specimens.

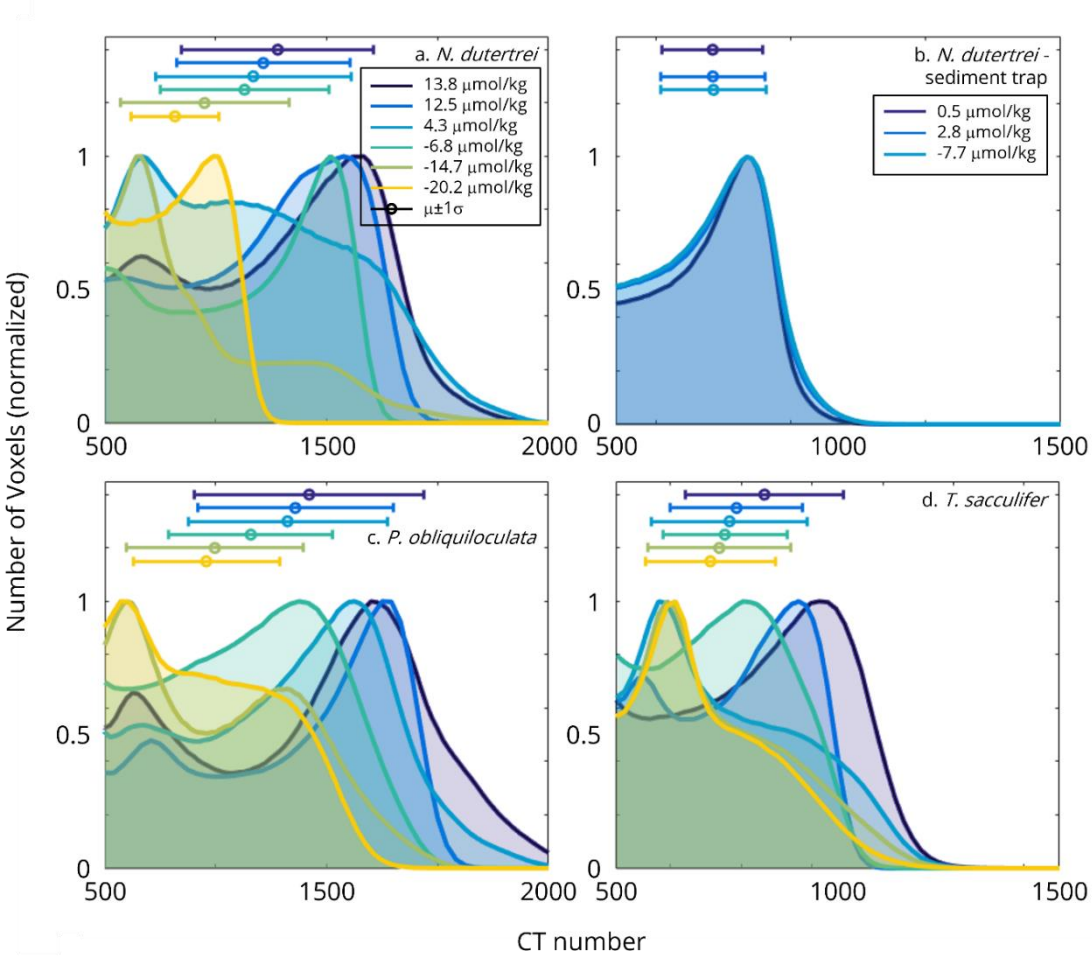

Figure 4.7. Histograms are the compilation of CT numbers of voxels (normalized) of 6-10 specimens at each ΔCO_3^{2-} value in µmol/kg (purple, dark blue, light blue, turquoise, olive, and yellow) for a. core-top *N. dutertrei*, b. sediment trap *N. dutertrei*, c. core-top *P. obliquiloculata*, and d. core-top *T. sacculifer*. Histograms show that exposure to progressively lower ΔCO_3^{2-} shifts the mean CT numbers to lower values (decreasing shell density).

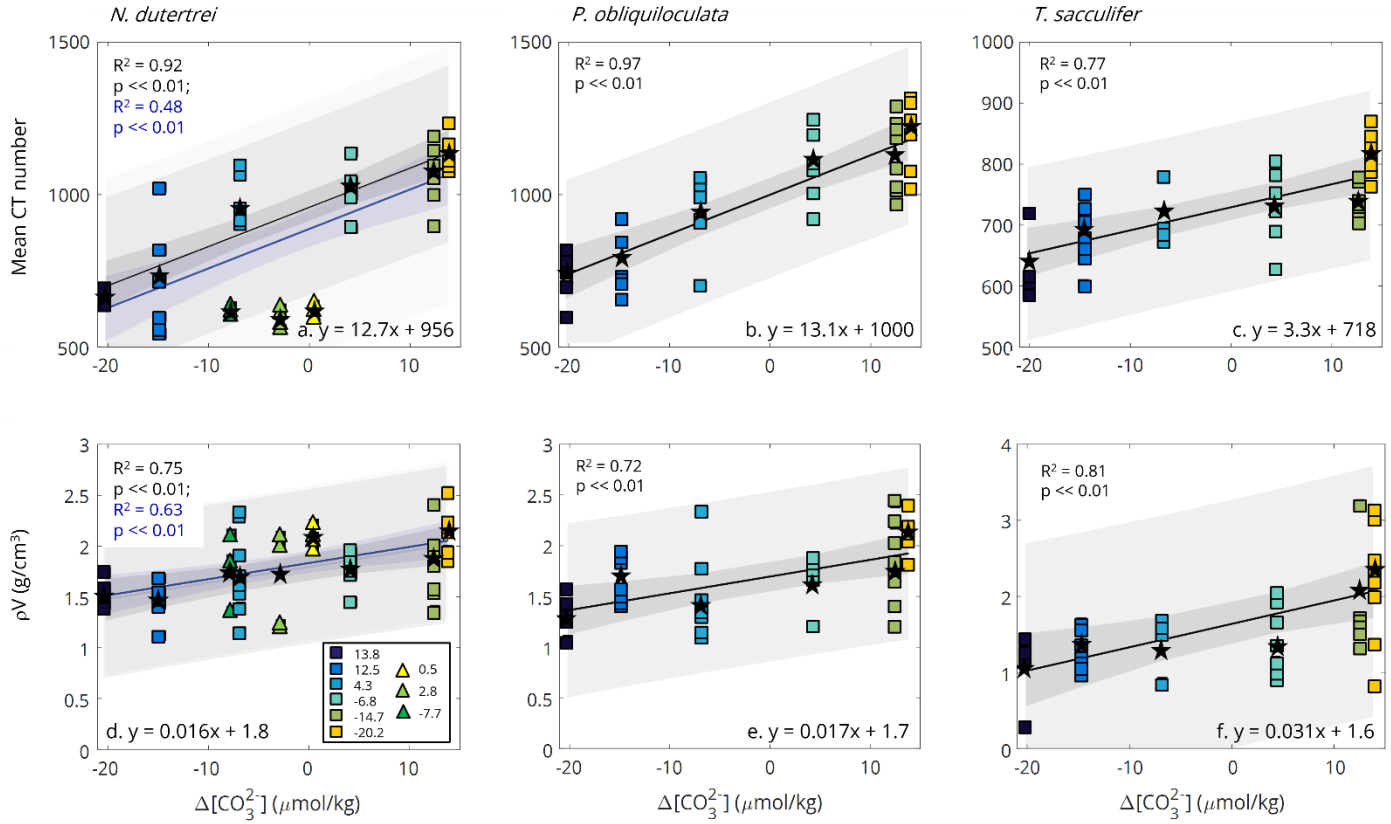

Fig 4.8. Correlation plot of a-c. mean CT number and d-f. volume density against ΔCO_3^{2-} for core-top (squares) and sediment trap (triangles) derived specimens. Correlation coefficient, p-value, and regression equation indicated based on mean values (black stars). Shaded areas are prediction bounds (simultaneous, for functional (darker area) and for observational (lighter area) results; Matlab Curve Fitting Toolbox, 2001). Volume density and mean CT number are strongly correlated with ΔCO_3^{2-} of the deep oceans where specimens resided.

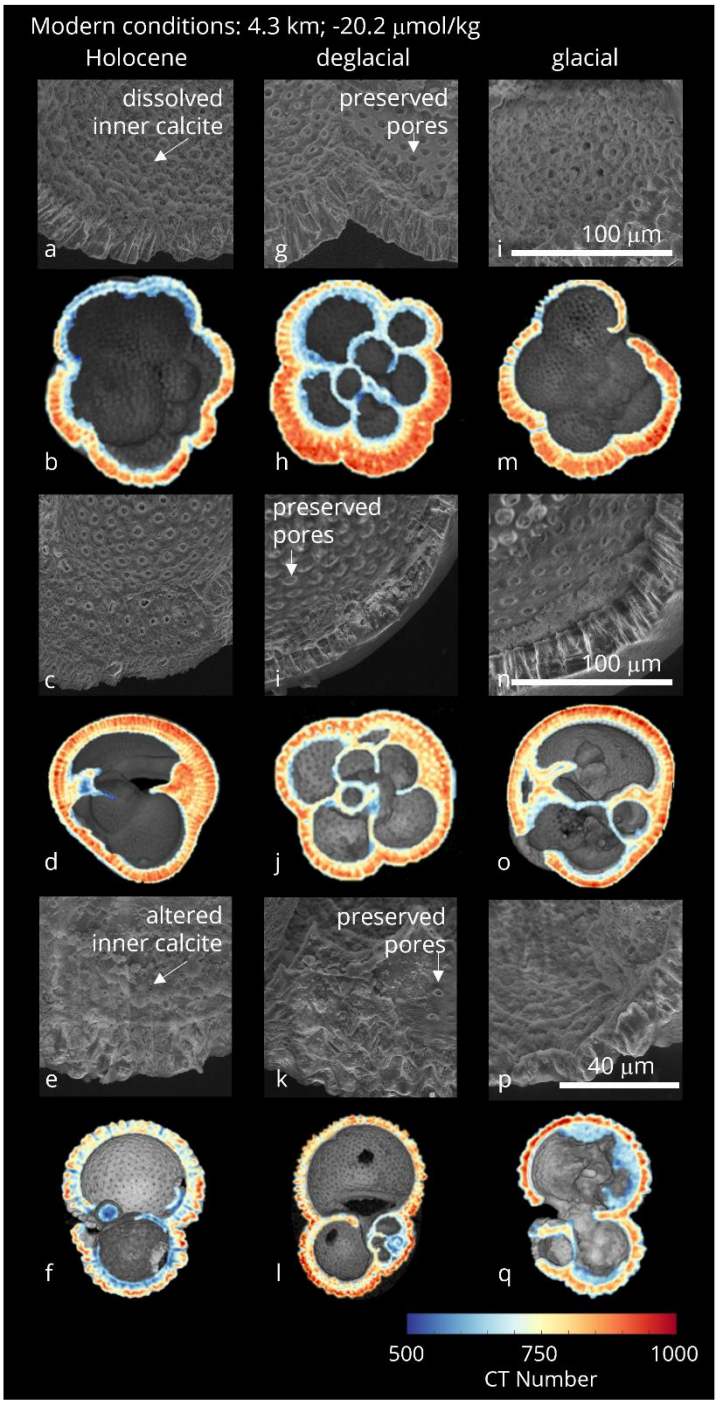

Figure 4.9. Representative microCT scanned and SEM imaged specimens from Holocene (7.6 ka BP), deglacial (14.0 ka BP), and glacial (19.6 ka BP) intervals. Top row are SEM images of interior calcite of *N. dutertrei*, second row are CT number cross-sections of *N. dutertrei*, third row are SEM images of interior calcite of *P. obliquiloculata*, forth row are CT number cross-sections of *P. obliquiloculata*, fifth row are SEM images of interior calcite of *T. sacculifer*, sixth row are CT number cross-sections of *T. sacculifer*.

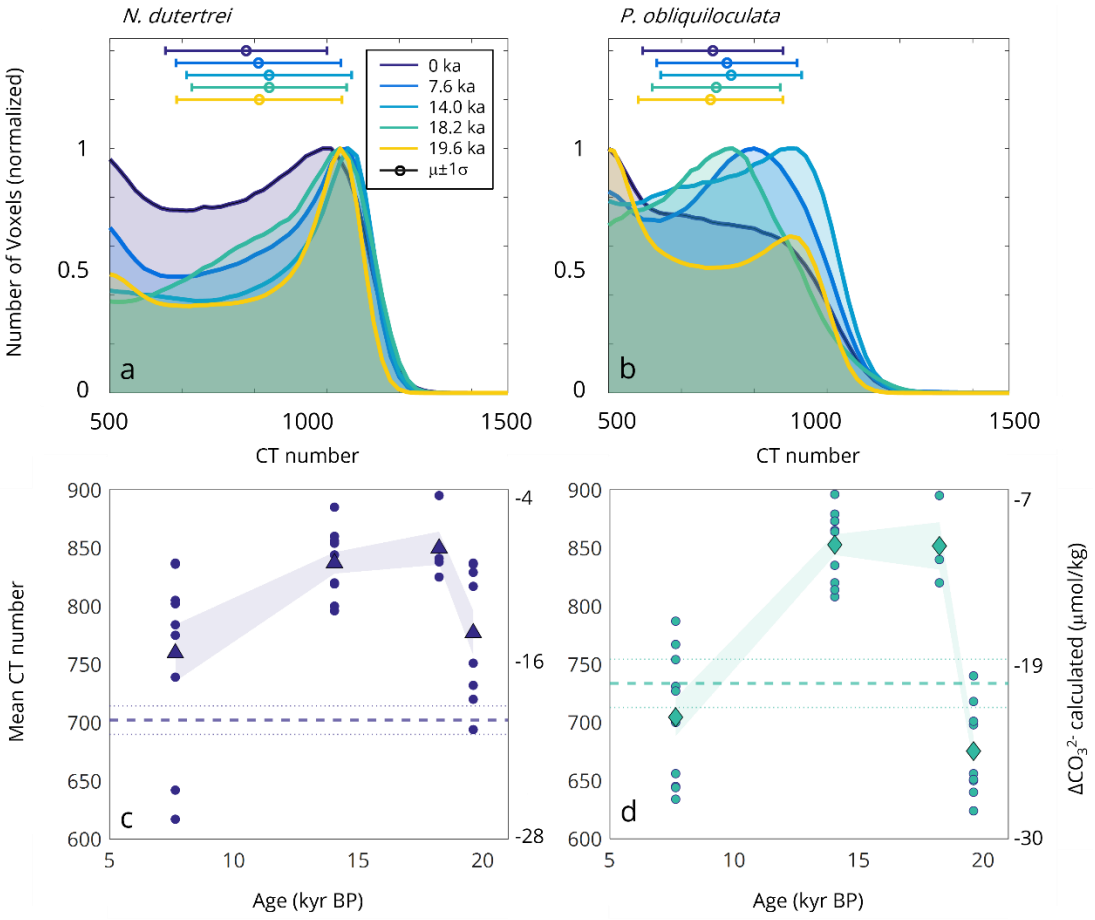

Figure 4.10. Histograms of the compiled CT number data (normalized) of 6-10 shells at each time interval in ka BP (purple, dark blue, light blue, turquoise, and yellow; a. *N. dutertrei* and b. *P. obliquiloculata*). Mean CT number and calculated ΔCO_3^{2-} using species specific equations for c. *N. dutertrei* and d. *P. obliquiloculata* are plotted as a dashed line and 95% confidence interval for the core-top is plotted as a dotted line. Shaded area is the 95% confidence interval for each time interval. Mean CT number and calculated $\Delta[CO_3^{2-}]$ for the deglacial time interval are significantly different from the Holocene and glacial time intervals within 95% confidence.

Table S4.1 Hydrographic conditions and number of specimens used for analysis from each location. ΔCO_3^{2-} based on GLODAP cruise data and calculated from Total Alkalinity, DIC, and other parameters using ODV (equilibrium constants follow Dickson et al., 2007; Schlitzer, 2020). Age model for 14GC core is from Lyle et al. (2002).

Core	Type	Location	Water Depth (m)	ΔCO_3^{2-} (µmol/kg)	Core Interval (cm)	Age (kyr BP)	Species	N
Panama Basin								
PB2-S2	Sediment trap	5.22°N, 85.35°W	890	0.5	-	0	*N. dutertrei*	4
PB2-S3	Sediment trap	5.22°N, 85.35°W	2560	-2.8	-	0	*N. dutertrei*	4
PB2-S4	Sediment trap	5.22°N, 85.35°W	3680	-7.7	-	0	*N. dutertrei*	4
ME0005A-24JC	Core-top	0.01°N, 86.30°W	2941	-6.79	0-2	0	*N. dutertrei* *P. obliquiloculata* *T. sacculifer*	8 8 8
Ontong Java Plateau								
MW91-9 6GGC	Core-top	2.21°S, 156.97°E	1625	13.8	8-10		*N. dutertrei* *P. obliquiloculata* *T. sacculifer*	6 6 9
MW91-9 34GGC	Core-top	0.49°S, 157.84°E	2022	12.5	0-2	0	*N. dutertrei* *P. obliquiloculata* *T. sacculifer*	8 8 7
MW91-9 38GGC	Core-top	0.01°N, 159.37°E	2456	4.3	0-2	0	*N. dutertrei* *P. obliquiloculata* *T. sacculifer*	5 6 8
MW91-9 55GGC	Core-top	0.01°S, 161.77°E	4024	-14.7	0-2	0	*N. dutertrei* *P. Obliquiloculata* *T. sacculifer*	7 5 9
Central Pacific								
W8402A-14GC	Core-top	1.09°N, 139.53°W	4287	-20.2	0-3	0	*N. dutertrei* *P. obliquiloculata* *T. sacculifer*	6 6 4
	Core interval			-15.5* -22.6*	12-13	7.6	*N. dutertrei* *P. obliquiloculata* *T. sacculifer*	9 10 6
				-9.4* -11.2*	24-25	14.0	*N. dutertrei* *P. obliquiloculata* *T. sacculifer*	9 10 9
				-8.4* -11.3*	33-34	18.2	*N. dutertrei* *P. obliquiloculata* *T. sacculifer*	4 3 6
				-14.2 -24.8	36-37	19.6	*N. dutertrei* *P. obliquiloculata* *T. sacculifer*	8 8 8

*calculated using species specific equations for *N. dutertrei* (y = 12.7x + 956±31; R^2=0.92) and *P. obliquiloculata* (y = 13.1x + 1000±30; R^2=0.97)

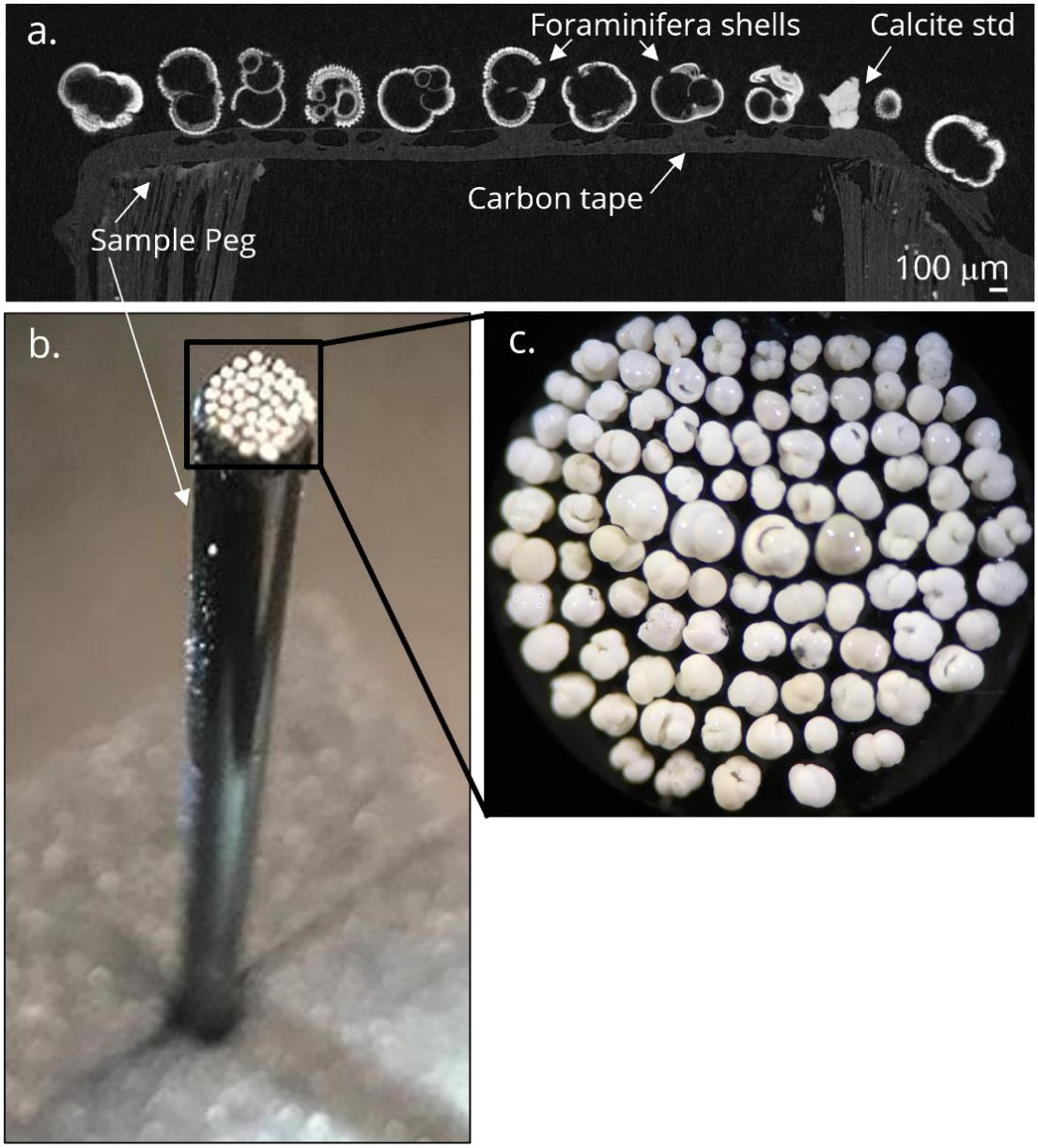

Figure S4.1. ~40-80 foraminifera specimens per scan are placed on carbon tape atop a dense plastic peg (b and c) and scanned using a Hamamatsu L10711-19 at Oregon State University, customized for micro-scale analysis, to generate tomographs (a). Scanning resolution was 1 - 2 µm.

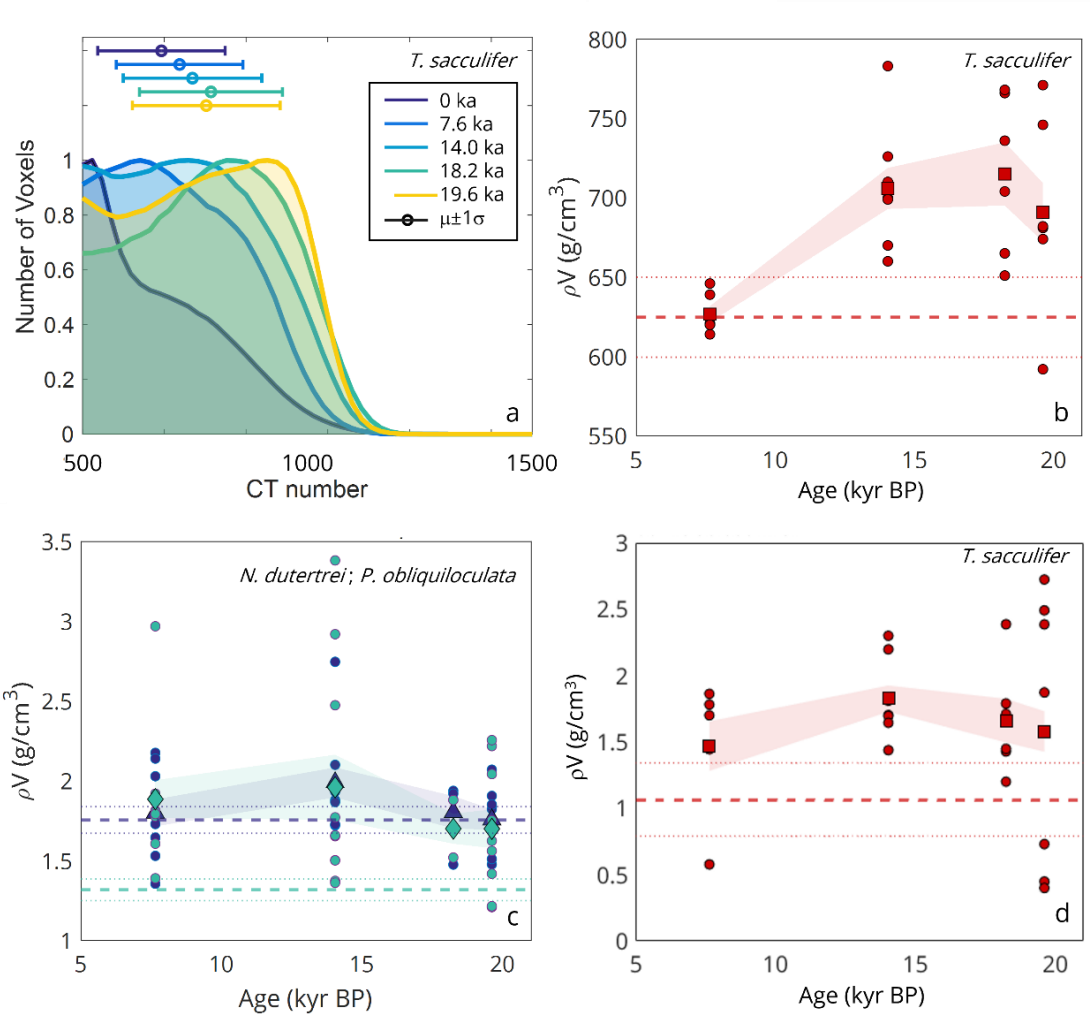

Figure S4.2. Histograms of the compilation of CT numbers of voxels (normalized) of 6-10 shells at each time interval in ka BP (purple, dark blue, light blue, turquoise, and yellow; a. *T. sacculifer*). Mean CT number for b. *T. sacculifer* and volume density for c. *N. dutertrei* (blue) and *P. obliquiloculata* (purple), and d. *T. sacculifer* (red) plotted as a dashed line and 95% confidence interval for the core-top is plotted as a dotted line. Shaded area is the 95% confidence interval for each time interval. Mean CT number for the deglacial time interval are significantly different from the Holocene time interval within 95% confidence.

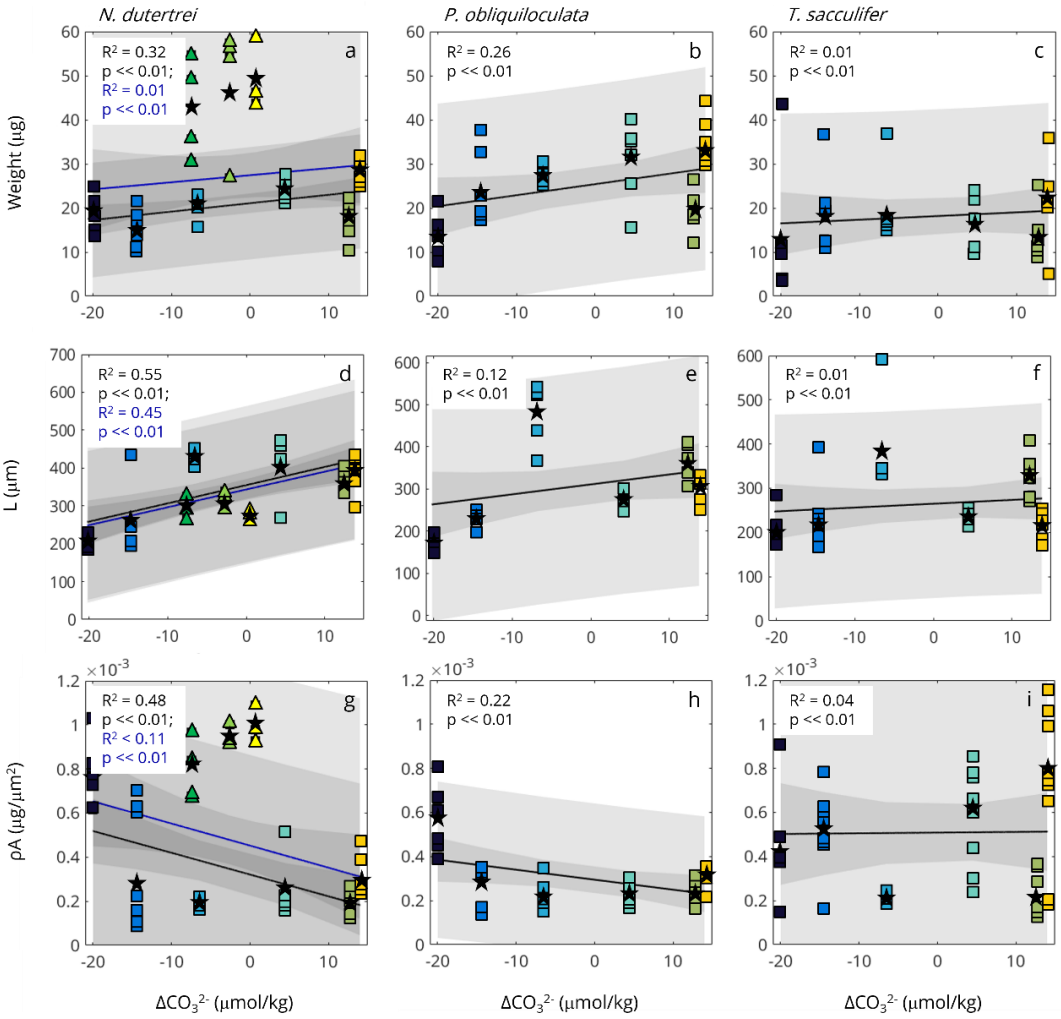

Figure S4.3. Correlation plot of shell weight (µg; top row), length (L, µm; second row), and area density (ρA, µg/µm^2; third row), against ΔCO_3^{2-} for a. *N. dutertrei* (core-top derived specimens are plotted with squares and sediment trap derived specimens are plotted with triangles), b. *P. obliquiloculata*, and c. *T. sacculifer*.

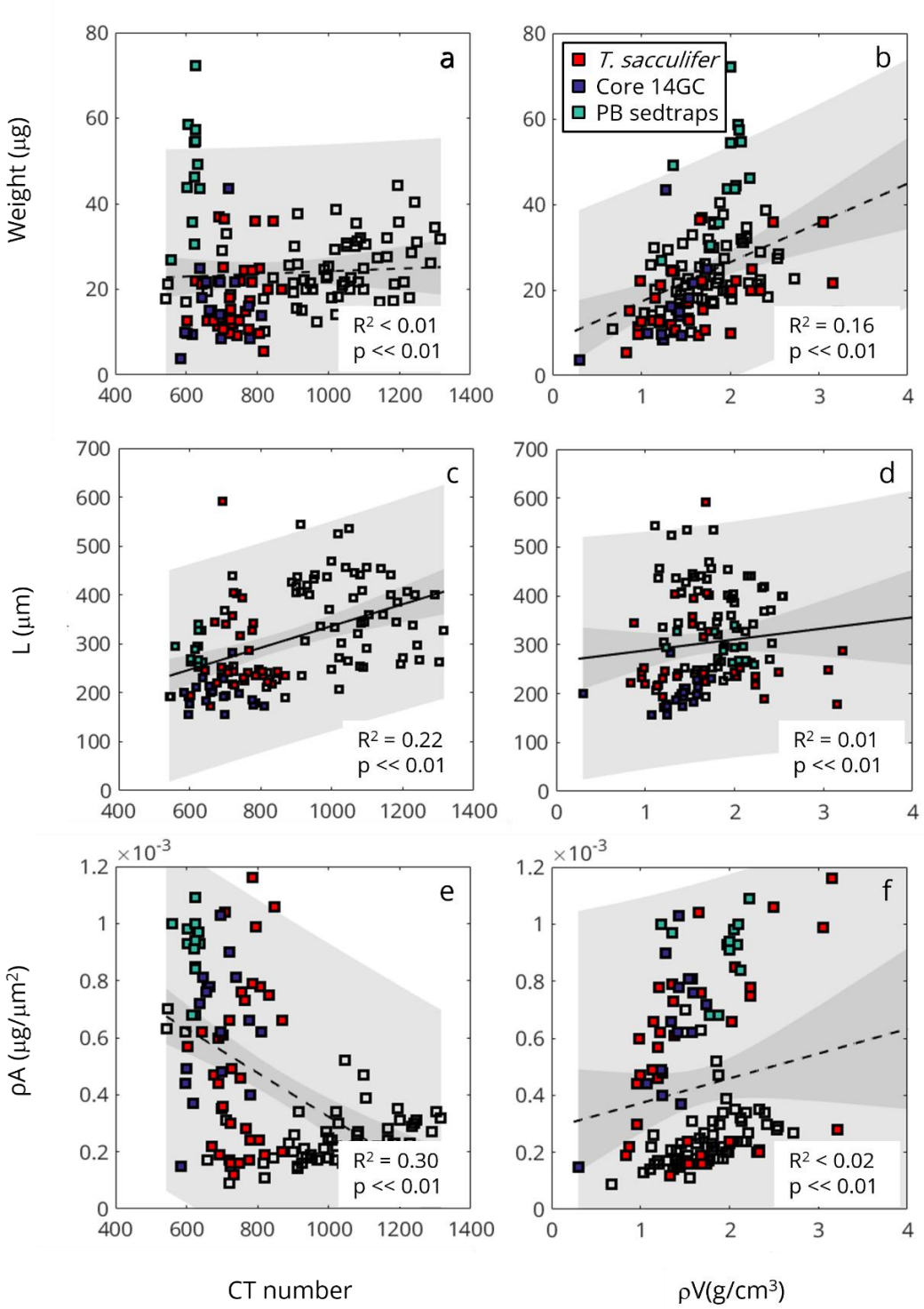

Figure S4.4. Correlation plot of shell weight (µg; top row), length (L, µm; second row), area density (ρA, µg/µm^2; third row), against mean CT number and volume density (g/cm^3). Values are indicated for *T. sacculifer* specimens (red), deep central Pacific core specimens (purple), and sediment trap specimens (green).

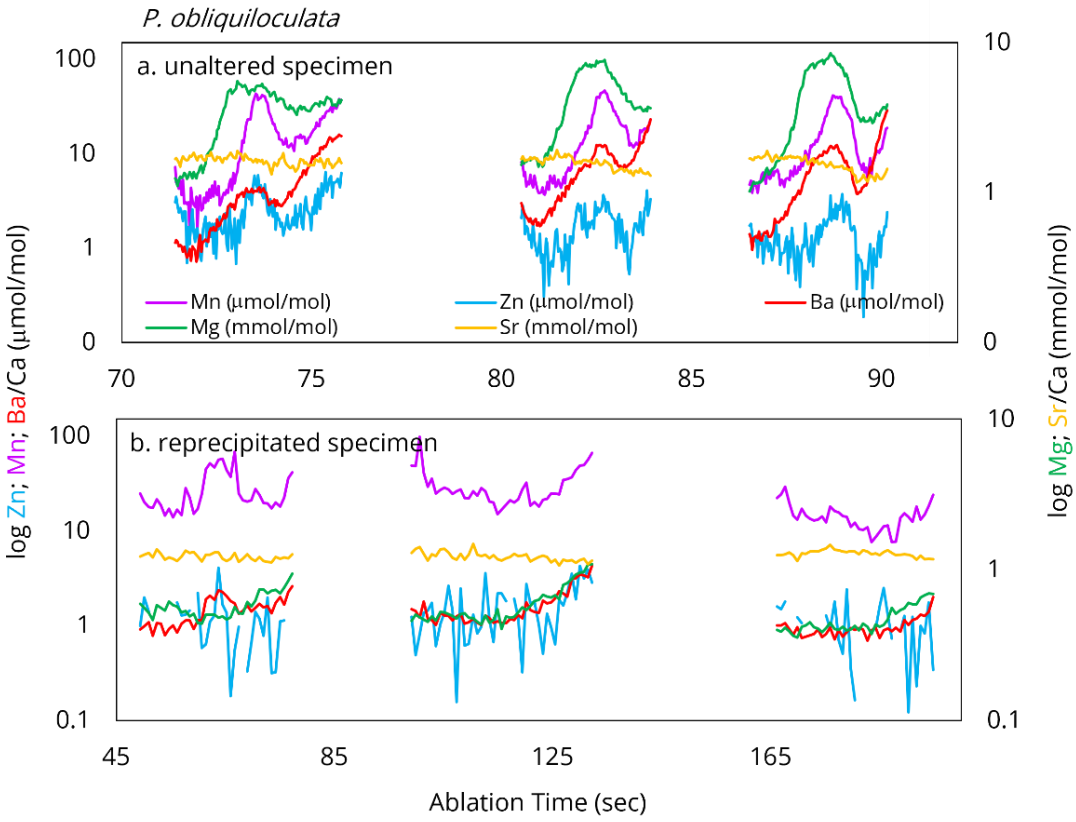

Figure S4.5. Example laser ablation trace element profiles of *P. obliquiloculata* from, a. well preserved specimen from the 6GGC core at 1.6 km water depth, and b. a specimen that is likely to contain post-depositional alterations from the 14GC core at 4.3 km water depth.

Table S4.1. Average individual shell trace element and $\delta^{18}O$ data from *N. dutertrei*, *P. obliquiloculata*, and *T. sacculifer* core-top specimens from core 6GGC that are well preserved and core 14GC that likely contain post-depositional alterations.

		6GGC core (1.6 km w.d.)	14GC core (4.3 km w.d.)
Mg/Ca (mmol/mol)	*N. dutertrei*	2.9	1.4
	P. obliquiloculata	3.2	1.7
	T. sacculifer	4.9	2.6
Sr/Ca (mmol/mol)	*N. dutertrei*	1.6	25.1
	P. obliquiloculata	1.5	17.8
	T. sacculifer	1.5	8.7
Mn/Ca (μmol/mol)	*N. dutertrei*	20.6	137.6
	P. obliquiloculata	10.3	152.9
	T. sacculifer	12.5	72.5
Zn/Ca (μmol/mol)	*N. dutertrei*	3.3	110.4
	P. obliquiloculata	2.3	66.4
	T. sacculifer	4.3	34.1
Ba/Ca (μmol/mol)	*N. dutertrei*	6.9	34.3
	P. obliquiloculata	2.9	15.2
	T. sacculifer	5.2	19.8
$\delta^{18}O$ (‰, VPDB)	*N. dutertrei*	-0.96	-0.18
	P. obliquiloculata	-1.14	-0.79
	T. sacculifer	-2.20	-1.20

CHAPTER 5: CONCLUSION

5.1. Research importance

The unifying goals of the research of this dissertation were to 1) Establish new foraminifera-based proxies that trace critical parameters of the marine carbon system, 2) Test the use of these proxies in regions that are globally important to carbon production and carbon storage, 3) Place the reconstructions in the context of hydrographic changes over climate transitions. This work focused on the equatorial Pacific, where extensive carbon production is countered by widespread carbon dissolution, and the transition between the Last Glacial Maximum and the Holocene when global changes impacted the carbon cycle.

Despite significant efforts by the oceanographic community to reconstruct carbon production and carbon storage in the equatorial Pacific over glacial-interglacial transitions (e.g., Arrhenius, 1952; Broecker, 1982; Gottschalk et al., 2019), there remains little consensus on the relative changes in the organic (Costa et al., 2017) and inorganic carbon (Yu et al., 2017) systems. These uncertainties are in part due to the fact that diagenetic processes may alter proxies. To address these uncertainties and achieve my research goals, I explored new proxies hosted by non-spinose foraminifera using high spatial resolution techniques that allow for the careful consideration of diagenetic processes. I then compared these results to well-established regional reconstructions. The primary conclusion from this work is that non-spinose foraminifera-based proxies add valuable insight to reconstructions of surface ocean production and deep ocean calcite preservation, particularly in regions where diagenetic processes may alter other commonly used proxies.

I explore new foraminifera-based proxies within non-spinose deeper dwelling species. Non-spinose foraminifera are adapted to colder deeper environments and offer the potential to reconstruct conditions of their calcification environment at the base of the thermocline. However, the trace element geochemistry of these species is complex. Trace elements are often higher and more variable both through the shell and from specimen-to-specimen than the more commonly used spinose species. For

this reason, trace element proxies hosted within non-spinose species are underutilized in paleoceanography.

To develop the use of trace element proxies in non-spinose species, individual foraminifera shells are carefully assessed with high-resolution techniques (Evans et al., 2016; Jonkers et al., 2012; Marr et al., 2013; Wit et al., 2010). Individual foraminifera analysis (IFA) allows for considerations of non-primary geochemical signals that reside on shell surfaces that impact the primary signal (e.g., Rongstad et al., 2017; Vetter et al., 2013). I first assess the distribution of trace elements (Ba, Mg, Mn, and Zn) in non-spinose species using laser ablation ICP-MS. Results show that elements are elevated in the inner calcite and not just on shell surfaces. This suggests high trace element concentrations are not the result of diagenetic alterations. Furthermore, the inner calcite is preferentially dissolved, and shell-bound trace elements are lowered when traditional shell cleaning protocols designed to remove contamination are used. I establish cleaning methods that remove shell contaminant phases but minimize shell dissolution and the loss of shell-bound trace elements. I then apply non-spinose foraminifera trace element proxies using the new cleaning methods.

The field application of the research was focused on the equatorial Pacific, where high organic and inorganic carbon production in the surface ocean is counteracted by organic carbon remineralization and calcite dissolution in the deep ocean. Changes to the amount of production of organic matter in the surface ocean and strength of the biologic pump, which sequesters carbon from the atmosphere and transports and stores some of this carbon to the deep ocean, in part driving atmospheric pCO_2 changes on glacial-interglacial timescales (Broecker, 1982; Sigman and Boyle, 2000). Extensive research has been conducted in the equatorial Pacific to resolve production changes over glacial-interglacial transitions (Pedersen et al., 1983; Perks et al., 2002; Loubere et al., 2004; Pichat et al., 2004; Dubois et al., 2011; Costa et al., 2017). To date, paleoceanographic reconstructions have explored the contribution of organic carbon from the surface and its storage at depth and generally rely on the use of flux proxies that reconstruct the accumulation rate of

biogenic materials in sediments. Many reconstructions disagree, in part, because the array of commonly used proxies record fundamentally different aspects of production, and all contain their own assumptions (Berger et al., 1994; Bordiga et al., 2013). Additionally, nearly all production proxies are subject to alteration in the water column and seafloor (diagenetic processes). Therefore, they are linked to multiple counteracting processes such as organic carbon production and deep ocean calcite preservation. As a result, many production reconstructions differ in their interpretation of the timing and magnitude of change.

Over climate transitions, even small changes in inorganic carbon preservation in the deep ocean can impact global carbon partitioning between the atmosphere and ocean. However, glacial-interglacial changes in the calcite saturation state of the deep ocean and the depth of the lysocline (the depths over which calcite dissolution in sediments intensifies) are not well constrained. Previous work suggests the Pacific glacial ocean was a period of either little change (Anderson and Archer, 2002), better preservation conditions (Broecker and Clark, 2001), or decreased preservation (Marchitto et al., 2005; Yu et al., 2010; Fehrenbacher and Martin, 2011; Loubere et al., 2004). Reconstructions of deep ocean calcite saturation mainly rely on calcite preservation/dissolution in sediments (e.g., Anderson and Archer, 2002) and often on the preservation state of the calcite shells of foraminifera (e.g., Arrhenius, 1952; Broecker and Clark, 2001; Qin et al., 2017), which is complicated by the fact that calcite dissolution is not straightforward and is often accompanied by reprecipitation. In this dissertation, I attempt to address these uncertainties using new tools for reconstructing aspects of the carbon system.

5.2. Chapters summary

Chapter 2 explores trace element variability within individual foraminifera shells and demonstrates that Ba, Mn, and Zn are lattice bound, incorporated into the shell during calcification, and elevated in the early ontogenic calcite in the non-spinose foraminifera species *Neogloboquadrina dutertrei* and *Pulleniatina*

obliquiloculata. Traditionally, aggressive cleaning was used to lower these elements under the premise that they represented contaminant phases (e.g., Lea and Boyle, 1991). However, the aggressive cleaning also preferentially removes the early ontogenetic calcite and favors the low trace element outer calcite. Thus, preferential loss of the early ontogenetic calcite significantly decreases these trace elements in *N. dutertrei* and *P. obliquiloculata* shells. This biases foraminiferal trace element ratios toward lower values and may yield problematic data for reconstructions that use these trace elements as proxies. Modified cleaning techniques developed in chapter 2 minimize early ontogenetic calcite dissolution and retain the primary trace element signal. This improves the utility of trace element proxies in non-spinose foraminifera for paleo-reconstructions.

Chapter 3 explores using Ba/Ca in the shells of the non-spinose species *N. dutertrei* and *P. obliquiloculata* as a proxy for paleo-production. Elevated Ba/Ca in *N. dutertrei* and *P. obliquiloculata* species likely record the Ba-enriched conditions within the particulate organic matter of the microhabitat in which the foraminifera calcified (Fehrenbacher et al., 2018). This hypothesis explains high Ba/Ca ratios and the high specimen-to-specimen and intra-shell Ba/Ca variability, as each specimen would record its own microhabitat. Ba/Ca ratios in sediment trap and core-top specimens reflect the production gradient across the modern equatorial Pacific surface ocean and support the hypothesis that Ba/Ca ratios in *N. dutertrei* and *P. obliquiloculata* can serve as a proxy for surface ocean production. The downcore record of Ba/Ca reproduces the deglacial (~16-17 ka BP) peak recorded by other regional paleo-production proxies (Schwarz et al., 1996; Winckler et al., 2016, Pichat et al., 2004; Bradmiller et al., 2006; Richaud et al., 2007; Anderson et al., 2009; Pichevin et al., 2009; Hayes et al., 2011; Kienast et al., 2006; Dubois et al., 2011). A deglacial peak in production is consistent with atmospheric and oceanic reorganizations and is consistent with the hypothesis that production changes were sparked by southern-sourced nutrient enrichment delivered to the equatorial thermocline by an intensification of intermediate water circulation (Dubois et al., 2011). Careful analysis of the Ba/Ca proxy in regions impacted by diagenetic

alterations (sediment focusing and dissolution) indicates that the Ba/Ca proxy may be a valuable tool in locations where other production proxies are poorly preserved.

Chapter 4 explores foraminiferal shell density changes with increased water depth and correlates shell density with changes to bottom water carbonate saturation state. Carbonate ion saturation state (ΔCO_3^{2-}) decreases with increased water depth and causes foraminifera shells to dissolve. Micro-computer tomography (microCT) scans of specimens obtained from a depth transect are used to determine shell density. A core-top calibration conducted across the equatorial Pacific shows that the microCT derived metrics, 'CT number' (after Iwasaki et al., 2014, 2019) and 'volume density,' reflect shell density and are strongly correlated with the ΔCO_3^{2-} of the deep ocean. I apply the calibration equation to a downcore reconstruction of bottom water (4.2 km water depth) ΔCO_3^{2-} in the central equatorial Pacific. Results indicate carbonate ion concentration during deglacial time intervals is 10-15 □mol/kg higher, and shells are better preserved than the Holocene and glacial time periods (where ΔCO_3^{2-} are similar to modern values, -20.2 μmol/kg). Results are comparable to other regional reconstructions and support estimates of deep ocean ΔCO_3^{2-} change since the last glacial and an increase in deglacial deep ocean ΔCO_3^{2-} linked to the transfer of pCO_2 from the deep ocean to the atmosphere. Because of poor preservation, few reconstructions have been conducted at this depth. My dataset adds valuable information about changes in the lysocline in the Pacific Ocean since the last glacial.

5.3. Key reflections

Elderfield (2002) summarized the 'proxy scientific maturation process' as beginning with an 'optimistic phase' when limited evidence suggests a new proxy has a high potential, moving through a 'pessimistic phase' when analytical challenges, competing environmental controls, or preservation issues cause a drop in confidence, and then finally arriving at a 'realism phase' where the limits of the proxy are identified, and interpretations can be stated with appropriate confidence (Elderfield, 2002). In this dissertation, I worked to advance the utility of new foraminiferal

proxies. I explored caveats and shortcomings of new proxies and focused on arriving at a 'realism phase.' Using high-resolution techniques, paired IFA-bulk shell analysis, sediment traps and core-tops, and multi-proxy reconstructions, I worked to discover the limitations and develop the use of new proxies.

High-resolution techniques on individual foraminifera, including laser ablation depth profiling elemental analysis, microCT, and scanning electron microscopy (SEM), improve our understanding of the nature of shell material (i.e., improved assessment of diagenetic alterations that impact the proxy). Using high-resolution techniques, I showed that trace elements like Ba and Mn are highest in the inner calcite and are incorporated when the foraminifera calcified in the surface ocean and are not due to sediment contamination. These results are site-specific. High-resolution techniques should be conducted in complex regions such as redox sensitive basins (Pena et al., 2005, 2008) or organic matter rich environments (Guo et al., 2019) to indicate the presence or absence of diagenetic overgrowths or contaminant infill. If careful and high-resolution analysis reveals that contaminants affect foraminifera proxies, new methods need to be developed to remove contaminations while retaining the primary signal of the foraminifera geochemical composition (Yu et al., 2007; Koho et al., 2015; Gibson et al., 2016; Fritz-Endres and Fehrenbacher, 2020). High-resolution techniques employed in this study reveal that Ba, Mn, and other trace elements in non-spinose foraminifera that have long been interpreted as contamination are likely a primary signal, incorporated at the time of calcification and my findings may increase the utility of these trace elements in paleo-reconstructions.

Using high-resolution techniques, I also showed that shells from the deepest central pacific could not be used for geochemical reconstructions because of severe alterations to the shell chemistry. However, these shells can be used with new microCT techniques to reflect the deep ocean calcite saturation state and create ΔCO_3^{2-} reconstructions. These shells provide valuable information about the deepest part of the Pacific, where few reconstructions currently exist because of extensive dissolution.

Paired IFA laser ablation depth profiling and bulk shell elemental analysis offers the opportunity to reconstruct individual shell and population variability with average shell values of the timeseries. I explored appropriate cleaning methods to prepare samples for trace element analysis by using paired IFA and bulk shell analysis. Specifically, I showed that cleaning processes considerably affect Ba/Ca timeseries reconstructions by measuring Ba/Ca in individual shells in three time intervals and through the entire timeseries using bulk shells. The two analyses are done using the same species and in the same core intervals and should match. However, the Ba/Ca recorded in individual shells is not replicated by bulk solution when traditional cleaning steps are used. When I use the modified cleaning techniques developed in this study, the bulk shell results are consistent with the individual shell results. This suggests that the signal is no longer cleaned away. I recommend these techniques when non-spinose species Ba/Ca reconstructions are generated in the future. Given that high-resolution techniques are more costly and labor-intensive, these techniques could be employed for key time intervals while still relying on traditional (i.e., bulk solution) analyses for higher resolution timeseries reconstructions. Previously published trace element reconstructions using non-spinose species that have produced contradictory results could be reinterpreted.

The use of sediment traps and core-tops from the same location as downcore reconstructions offers valuable insight for foraminifera-based proxy development. Specimens from sediment traps and core-tops are relatively young and are calcified in oceanographic conditions most like modern conditions. I compare the geochemistry and microstructure of these specimens to conditions of the modern ocean to establish calibrations and develop new proxies. I find that Ba/Ca in sediment trap and core-top derived specimens of non-spinose foraminifera species from a productivity transect in the equatorial Pacific reflect the pattern of surface ocean export production. This indicates that the Ba/Ca proxy likely records the equatorial Pacific surface ocean production. The Ba/Ca proxy appears to reflect the production of the surface ocean, not just what is transported to and accumulated on the seafloor, as is the case with most bulk sediment proxies, making this proxy uniquely valuable. Paired with

appropriate bulk sediment records, the Ba/Ca proxy may offer the opportunity to reconstruct the amount of organic carbon raining from the surface ocean that accumulates and is sequestered in sediments. Furthermore, this study establishes the utility of the Ba/Ca proxy in complex environments. The eastern equatorial Pacific (EEP) is a high sedimentation environment with variable topography and some evidence for re-sedimentation (Lyle et al., 2005). Ba/Ca ratios in non-spinose specimens from the core-tops of the EEP cores used in this study follow the expected surface ocean export production pattern. I also test the Ba/Ca proxy using core-tops of deep core on the OJP that may experience dissolution that alters the preservation of shells and their trace element composition (Berger et al. 1982; Zhang et al., 2007). The Ba/Ca proxy is consistent between a deep core that is likely to experience calcite dissolution and a nearby shallow core where dissolution is unlikely to impact shells. This indicates that the Ba/Ca signal is retained, despite some dissolution of shells derived from deep cores with variable preservation.

In the future, core-top and sediment trap analysis paired with microCT analysis may be useful to quantify the contributions of surface ocean controls like temperature and [CO_3^{2-}] on shell density (Iwasaki et al., 2019). MicroCT scans of foraminifera shells that I explore as a deep ocean dissolution proxy may be complicated by surface ocean growth conditions, particularly when attempting to reconstruct deep ocean dissolution conditions over time periods and in regions where surface ocean conditions have not been stable (e.g., Spero et al., 1997; Bijma et al., 1999; Russell et al., 2004). Once surface ocean controls are well defined, the contributions of deep ocean controls on shell density may be better constrained.

Careful assessment of foraminiferal proxies with multiple and high-resolution techniques and in complex environments help to establish the use and appropriate confidence in interpreting carbon reconstructions using these new proxies. Further development of the foraminiferal proxies I assessed in this dissertation offers the opportunity to elucidate key understandings of surface ocean organic carbon production and deep ocean calcite preservation. Because of the strong link between these aspects of the carbon cycle and atmospheric CO_2, these pursuits are critical to

understanding the mechanisms that control the global climate in light of modern CO_2 emissions and climate warming.

5.4. References

Anderson, D. M., and D. Archer (2002), Glacial-interglacial stability of ocean pH inferred from foraminifer dissolution rates, Nature, 416, 70–73, doi.10.1038/416070a.

Anderson, R. F., S. Ali, L. Bradtmiller, S. H. H. Nielson, M. Q. Fleisher, B. E. Anderson, and L. H. Burckle (2009), Wind-driven upwelling in the Southern Ocean and the deglacial rise in atmospheric CO_2, *Science*, 323, 1443-1448. doi.org/10.1126/science.1167441

Arrhenius, G. (1952). Sediment cores from the eastern Pacific. Swedish Deep-Sea Exped.(1947-1948) Rept. *Hedwigia, Beihft.*, *53*, 323-354.

Berger, W. H., Bonneau, M. C., and Parker, F. L. (1982). Foraminifera on the deep sea floor-lysocline and dissolution rate. *Oceanologica Acta*, *5*(2), 249-258.

Berger, W. H., Herguera, J. C., Lange, C. B., and Schneider, R. (1994). Paleoproduction: flux proxies versus nutrient proxies and other problems concerning the Quaternary production record. In *Carbon cycling in the glacial ocean: Constraints on the ocean's role in global change* (pp. 385-412). Springer, Berlin, Heidelberg.

Bijma, J., Spero, H. J. and Lea, D. W. in *Use of Proxies in Paleoceanography: Examples from the South Atlantic* (eds Fisher, G. and Wefer, G.) 489–512 (Springer, 1999). doi.10.1007/978-3-642-58646-0_20

Bordiga, M., Beaufort, L., Cobianchi, M., Lupi, C., Mancin, N., Luciani, V., ... and Sprovieri, M. (2013). Calcareous plankton and geochemistry from the ODP site 1209B in the NW Pacific Ocean (Shatsky Rise): New data to interpret calcite dissolution and paleoproduction changes of the last 450 ka. *Palaeogeography, Palaeoclimatology, Palaeoecology*, *371*, 93-108. doi.10.1016/j.palaeo.2012.12.021

Bradtmiller, L. I., Anderson, R. F., Fleisher, M. Q., and Burckle, L. H. (2006). Diatom production in the equatorial Pacific Ocean from the last glacial period to the present: A test of the silicic acid leakage hypothesis. *Paleoceanography*, *21*(4). doi.10.1029/2006PA001282

Broecker, W. S., and E. Clark (2001), Glacial-to-Holocene redistribution of carbonate ion in the deep sea, Science, 294, 2152–2155, doi.10.1126/science.1064171.

Costa, K. M., Jacobel, A. W., McManus, J. F., Anderson, R. F., Winckler, G., and Thiagarajan, N. (2017). Production patterns in the equatorial Pacific over the last 30,000 years. *Global Biogeochemical Cycles*, *31*(5), 850-865. doi.10.1002/2016GB005579

Dubois, N., Kienast, M., Kienast, S., Normandeau, C., Calvert, S. E., Herbert, T. D.,

and Mix, A. (2011). Millennial-scale variations in hydrography and biogeochemistry in the Eastern Equatorial Pacific over the last 100 kyr. *Quaternary Science Reviews*, *30*(1-2), 210-223. doi.10.1016/j.quascirev.2010.10.012

Elderfield H (2002) Foraminiferal Mg/Ca paleothermometry: expected advances and unexpected consequences. Geochimica et Cosmochimica Acta 66, Supplement 1: A213

Evans, D., Erez, J., Oron, S., and Müller, W. (2015). Mg/Ca-temperature and seawater-test chemistry relationships in the shallow-dwelling large benthic foraminifera *Operculina ammonoides*. *Geochimica et Cosmochimica Acta*, *148*, 325-342. doi.10.1002/2015GC005822

Fehrenbacher, J., and P. Martin (2011). Western equatorial Pacific deep water carbonate chemistry during the Last Glacial Maximum and deglaciation: Using planktic foraminiferal Mg/Ca to reconstruct sea surface temperature and seafloor dissolution. Paleoceanography, 26(2) doi.10.1029/2010PA002035

Fehrenbacher, J. S., Russell, A. D., Davis, C. V., Spero, H. J., Chu, E., and Hönisch, B. (2018). Ba/Ca ratios in the non-spinose planktic foraminifer *Neogloboquadrina dutertrei*: Evidence for an organic aggregate microhabitat. *Geochimica et Cosmochimica Acta*, *236*, 361-372. doi.10.1016/j.gca.2018.03.008

Gottschalk, J., Battaglia, G., Fischer, H., Frölicher, T. L., Jaccard, S. L., Jeltsch -Thömmes, A., ...and Stocker, T. F. (2019). Mechanisms of millennial-scale atmospheric CO_2 change in numerical model simulations. *Quaternary science reviews*, *220*, 30-74. doi.10.1016/j.quascirev.2019.05.013

Guo, X., Xu, B., Burnett, W. C., Yu, Z., Yang, S., Huang, X., ... and Sun, F. (2019). A potential proxy for seasonal hypoxia: LA-ICP-MS Mn/Ca ratios in benthic foraminifera from the Yangtze River Estuary. *Geochimica et Cosmochimica Acta*, *245*, 290-303. doi.10.1016/j.gca.2018.11.007

Hayes, C. T., Anderson, R. F., and Fleisher, M. Q. (2011). Opal accumulation rates in the equatorial Pacific and mechanisms of deglaciation. *Paleoceanography*, *26*(1). doi.10.1029/2010PA002008

Iwasaki, S. et al. Observation of the dissolution process of *Globigerina bulloides* tests (planktic foraminifera) by X-ray microcomputed tomography. Paleoceanography 30, 317–331 (2015). doi.10.1002/2014PA002639

Iwasaki, S., Kimoto, K., Okazaki, Y., and Ikehara, M. (2019). Micro-CT Scanning of Tests of Three Planktic Foraminiferal Species to Clarify Dissolution Process and Progress. *Geochemistry, Geophysics, Geosystems*, *20*(12), 6051-6065. doi.10.1029/2019GC008456

Johnstone, H. J., Schulz, M., Barker, S., and Elderfield, H. (2010). Inside story: An X ray computed tomography method for assessing dissolution in the tests of planktonic foraminifera. *Marine Micropaleontology*, *77*(1-2), 58-70.

Jonkers, L., De Nooijer, L. J., Reichart, G. J., Zahn, R., and Brummer, G. J. (2012).

Encrustation and trace element composition of *Neogloboquadrina dutertrei* assessed from single chamber analyses implications for paleotemperature estimates. *Biogeosciences*, *9*(11), 4851-4860. doi.10.5194/bg-9-4851-2012

Kienast, S. S., Kienast, M., Mix, A. C., Calvert, S. E., and François, R. (2007). Thorium-230 normalized particle flux and sediment focusing in the Panama Basin region during the last 30,000 years. *Paleoceanography*, *22*(2). doi.10.1029/2006PA001357

Lea, D. W., and Boyle, E. A. (1991). Barium in planktonic foraminifera, *Geochim. Cosmochim. Acta*, 55(11), 3321–3331.

Loubere, P., Mekik, F., Francois, R., and Pichat, S. (2004). Export fluxes of calcite in the eastern equatorial Pacific from the Last Glacial Maximum to present. *Paleoceanography*, *19*(2). doi.10.1029/2003PA000986

Lyle, M., Mitchell, N., Pisias, N., Mix, A., Martínez, J. I., and Paytan, A. (2005). Do geochemical estimates of sediment focusing pass the sediment test in the equatorial Pacific? *Paleoceanography*, *20*(1). doi.10.1029/2004PA001019

Marchitto, T. M., Lynch-Stieglitz, J., and Hemming, S. R. (2005). Deep Pacific $CaCO_3$ compensation and glacial–interglacial atmospheric CO2. *Earth and Planetary Science Letters*, *231*(3-4), 317-336. doi.10.1016/j.epsl.2004.12.024

Marr, J. P., Carter, L., Bostock, H. C., Bolton, A., and Smith, E. (2013). Southwest Pacific Ocean response to a warming world: Using Mg/Ca, Zn/Ca, and Mn/Ca in foraminifera to track surface ocean water masses during the last deglaciation. *Paleoceanography*, *28*(2), 347-362. doi.10.1002/palo.20032

Qin, B., Li, T., Xiong, Z., Algeo, T. J., and Chang, F. (2017). Deepwater carbonate ion concentrations in the western tropical Pacific since 250 ka: Evidence for oceanic carbon storage and global climate influence. *Paleoceanography*, *32*(4), 351-370. doi.10.1002/2016PA003039

Pedersen, T. F. (1983). Increased production in the eastern equatorial Pacific during the last glacial maximum (19,000 to 14,000 yr BP). *Geology*, *11*(1), 16-19. doi.10.1130/0091-7613(1983)

Pena, L. D., Calvo, E., Cacho, I., Eggins, S., and Pelejero, C. (2005). Identification and removal of Mn Mg rich contaminant phases on foraminiferal tests: Implications for Mg/Ca past temperature reconstructions. *Geochemistry, Geophysics, Geosystems*, *6*(9). doi.10.1029/2005GC000930

Pena, L. D., Cacho, I., Calvo, E., Pelejero, C., Eggins, S., and Sadekov, A. (2008). Characterization of contaminant phases in foraminifera carbonates by electron microprobe mapping. *Geochemistry, Geophysics, Geosystems*, *9*(7). doi.10.1029/2008GC002018

Perks, H. M., Charles, C. D., and Keeling, R. F. (2002). Precessionally forced production variations across the equatorial Pacific. *Paleoceanography*, *17*(3), 9-1. doi.10.1029/2000PA000603

Pichat, S., Sims, K. W., François, R., McManus, J. F., Brown Leger, S., and Albarède, F. (2004). Lower export production during glacial periods in the equatorial Pacific derived from $(^{231}Pa/^{230}Th)_{xs,0}$ measurements in deep-sea sediments. *Paleoceanography*, *19*(4). doi.10.1029/2003PA000994

Pichevin, L., Reynolds, B. C., Ganeshram, R. S., Cacho, I., Pena, L., Keefe, K., and

Ellam, R. M. (2009). Enhanced carbon pump inferred from relaxation of nutrient limitation in the glacial ocean. *Nature*, *459*(7250), 1114-1117. doi.10.1038/nature08101

Richaud, M., Loubere, P., Pichat, S., and Francois, R. (2007). Changes in opal flux and the rain ratio during the last 50,000 years in the equatorial Pacific. *Deep Sea Research Part II: Topical Studies in Oceanography*, *54*(5-7), 762-771. doi.10.1016/j.dsr2.2007.01.012

Rongstad, B. L., Marchitto, T. M., and Herguera, J. C. (2017). Understanding the effects of dissolution on the Mg/Ca paleothermometer in planktic foraminifera: Evidence from a novel individual foraminifera method. *Paleoceanography*, *32*(12), 1386-1402. doi.10.1002/2017PA003179

Schwarz, B., Mangini, A., and Segl, M. (1996). Geochemistry of a piston core from Ontong Java Plateau (western equatorial Pacific): Evidence for sediment redistribution and changes in paleoproduction. *Geologische Rundschau*, *85*(3), 536-545. doi.10.1007/BF02369008

Russell, A. D., Hönisch, B., Spero, H. J., and Lea, D. W. (2004). Effects of seawater carbonate ion concentration and temperature on shell U, Mg, and Sr in cultured planktonic foraminifera. *Geochimica et Cosmochimica Acta*, *68*(21), 4347-4361. doi.10.1016/j.gca.2004.03.013

Spero, H. J., Bijma, J., Lea, D. W. and Bemis, B. E. Effect of seawater carbonate concentration on foraminiferal carbon and oxygen isotopes. *Nature* 390, 497–500 (1997). doi.10.1038/37333

Vetter, L., Spero, H. J., Russell, A. D. and Fehrenbacher, J. S. (2013). LA-ICP-MS depth profiling perspective on cleaning protocols for elemental analyses in planktic foraminifers. *Geochem. Geophys. Geosyst.* 14, 2916–2931. doi.10.1002/ggge.20163

Winckler, G., Anderson, R. F., Jaccard, S. L., and Marcantonio, F. (2016). Ocean dynamics, not dust, have controlled equatorial Pacific production over the past 500,000 years. *Proceedings of the National Academy of Sciences*, *113*(22), 6119-6124. doi.10.1073/pnas.1600616113

Wit, J. C., Reichart, G. J., A Jung, S. J., and Kroon, D. (2010). Approaches to unravel seasonality in sea surface temperatures using paired single-specimen foraminiferal $\delta^{18}O$ and Mg/Ca analyses. *Paleoceanography*, *25*(4). doi.10.1029/2009PA001857

Yu, J., W. Broecker, H. Elderfield, Z.D. Jin, J. McManus, and F. Zhang. 2010. Loss of carbon from the deep sea since the Last Glacial Maximum. *Science* 330:1,084–1,087 doi.10.1126/science.1193221

Yu, J., R.F. Anderson, Z.D. Jin, J. Rae, B.N. Opdyke, and S. Eggins (2013). Responses of the deep ocean carbonate system to carbon reorganization during the Last Glacial interglacial cycle. Quaternary Science Reviews 76:39–52, doi.10.1016/j.quascirev.2013.06.020.

Zhang, J., Wang, P., Li, Q., Cheng, X., Jin, H., and Zhang, S. (2007). Western equatorial Pacific production and carbonate dissolution over the last 550 kyr: Foraminiferal and nannofossil evidence from ODP Hole 807A. *Marine Micropaleontology*, *64*(3-4), 121-140. doi.10.1016/j.marmicro.2007.03.003